LBL-29112

Lawrence Berkeley Laboratory
UNIVERSITY OF CALIFORNIA

Materials & Chemical
Sciences Division

Nitrogen Dioxide Fluorescence Following Photolysis in a Supersonic Jet

W.N. Sisk
(Ph.D. Thesis)

May 1990

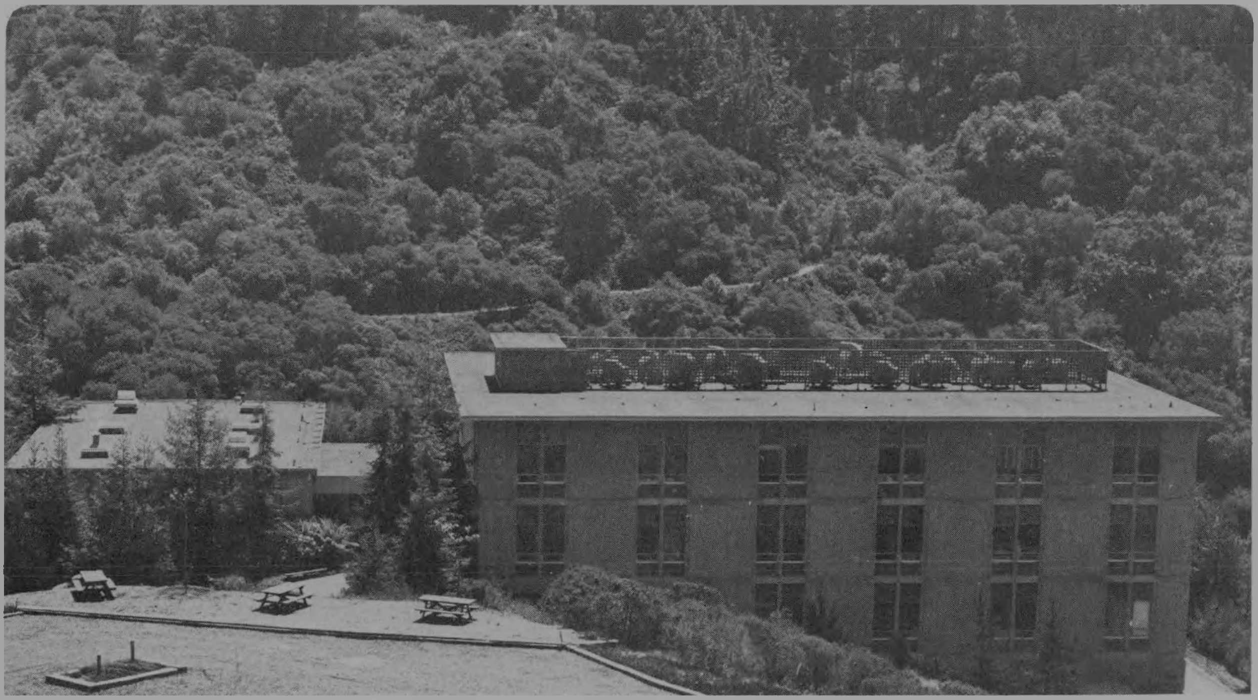

Prepared for the U.S. Department of Energy under Contract Number DE-AC03-76SF00098.

LBL--29112

DE90 014164

Nitrogen Dioxide Fluorescence Following Photolysis in a Supersonic Jet

Wade Napoleon Sisk
Ph.D. Thesis

Materials and Chemical Sciences Division
Lawrence Berkeley Laboratory
University of California
Berkeley, CA 94720

May 1990

This work was supported by the Director, Office of Energy Research, Office of Basic Energy Sciences, Chemical Sciences Division of the U.S. Department of Energy under Contract No. DE-AC03-76SF00098.

ACKNOWLEDGEMENTS

Many people have participated in one form or another in the development of this thesis and I congratulate them all. I would like to extend a warm thanks to my research advisor Professor Harold Johnston for his wise counsel and willingness to " hear me out ". I truly appreciate his effort in expediting the production of this thesis by taking the time to advise the construction of this thesis in the midst of bearing other responsibilities such as reading the dissertations of other graduate students and trying to meet the needs of his undergraduate students.

I would also like to thank Charles Miller who has worked with me in performing these experiments in the supersonic beam. His help in carrying out many of the late night experiments and in the analysis and interpretation of the data is commendable. Ken Patten, Jr. is to be thanked for the development of the Fortran PIF fitting program which greatly facilitated the PIF data analysis and for his " optomistic and positive attitude " about laser service. I would also like to thank the following individuals who assisted me in some fashion: Dr. Anthony Young, Dr. Doug Kinnison, Phil Hunter, Bongsoo Kim, and Joel Burley. Thanks should also be extended to members of the machine shop, Andy and George, for their input in modifying the molecular beam machine.

I would like to thank my parents, James and Naomi Sisk,

and grandparents, Rev. Elick and Rachel Patterson, who have always been a source of strength and inspiration. Also a special thanks to my brother Chet for the long, uplifting phone conversations.

This work was supported by the Director, Office of Energy Research, Office of Basic Energy Sciences, Chemical Sciences Division of the U.S. Department of Energy under contract number DE-AC03-76SF00098.

TABLE OF CONTENTS

CHAPTER 1. NO_2 Fluorescence Following N_2O_4 Photolysis

ABSTRACT

A supersonic jet of N_2O_4 has been photolyzed at three wavelengths: 193, 248 and 351 nm. The resultant fluorescence of NO_2 was dispersed, and from this the energy distribution of fluorescent NO_2 has been determined by the Photolysis Induced Fluorescence (PIF) scheme. The spread of the energy distribution increased with decreasing photolysis wavelength. These results have been compared to Kawasaki's time of flight translational energy distributions at 193 and 248 nm.[1] We conclude from these complementary measurements that the most probable N_2O_4 photodissociation channels are:

$$N_2O_4 + h\nu\ (351) \rightarrow NO_2(^2B_1, v_2 = 3 \text{ to } 4) + NO_2(^2A_1)$$

$$N_2O_4 + h\nu\ (248) \rightarrow NO_2(^2B_1) + NO_2(^2B_2)$$

$$N_2O_4 + h\nu\ (193) \rightarrow NO_2(^2B_2) + NO_2(^2B_2)$$

INTRODUCTION

The prompt fluorescence of NO_2 following UV photolysis of N_2O_4 has been examined in a number of previous studies.[1,2,3,] The N_2O_4 groundstate is planar symmetric D_{2h} with an exceptionally long N-N bond length (1.75 - 1.78 Å[4-6]) as illustrated in Figure 1.1. The correspondingly weak bond dissociation energy is estimated to be 12.69 Kcal/mol (4437.7 cm^{-1}) by Hisatsune[7], or 12.88 kcal/mol (4504.1 cm^{-1}) by Giauque[8] at 0 K and 13.64 kcal/mol (4770 cm^{-1}) at 300 K by Hisatsune. The ultraviolet absorption cross sections are large, as indicated in Figure 1.2. When N_2O_4 is photolyzed by UV radiation the NO_2 fragments are produced in the excited state, emitting visible radiation with lifetimes from 60 to 100 microseconds.[9] The NO_2^* producing channels with the thermodynamic threshold wavelengths are:[1,10]

$N_2O_4 + h\nu \rightarrow$ $NO2(^2B_2) + NO_2(^2A_1)$ $\lambda < 699$ nm (a)
$NO2(^2B_1) + NO2(^2A_1$ $\lambda < 516$ nm (b)
$NO_2(^2B_2) + NO_2(^2B_2)$ $\lambda < 416$ nm (c)
$NO_2(^2B_1) + NO_2(^2B_2)$ $\lambda < 344$ nm (d)
$NO_2(^2A_2) + NO_2(^2B_2)$ $\lambda < 327$ nm (e)
$NO_2(^2B_1) + NO_2(^2B_1)$ $\lambda < 293$ nm (f)
$NO_2(^2A_2) + NO_2(^2B_1)$ $\lambda < 281$ nm (g)
$NO_2(^2B_2) + NO + O$ $\lambda < 253$ nm (h)
$NO_2(^2B_1) + NO + O$ $\lambda < 225$ nm (i)

In previous studies the emphasis was on fluorescence quantum yields and translational energy distributions.[1,2] Although the NO_2^* fluorescence continuum was observed, very little information was obtained from this. The flow cell work of Inoue et. al.[2] suggests that channel (a) above is responsible for the fluorescence, following excitation in the range 295-365 nm. Photolysis of a neat supersonic jet of N_2O_4 has been carried out by Kawasaki and coworkers[1] with the subsequent determination of the TOF translational energy distribution. There was no evidence of significant NO production at 193 and 248 nm photolysis of N_2O_4; thus they concluded that channel (b) was the predominant channel for 193 and 248 nm photolysis. This is very surprising since there should be ample available energy to initiate NO production.

We have previously reported the determination of the NO_2^* energy distribution, following N_2O_5 and NO_2Cl photolysis, by a deconvolution scheme which exploits the information available in a dispersed NO_2 fluorescence spectrum.[11,12] Mcleod and coworkers have applied this scheme in a less rigorous fashion to study the energy profile of the fluorescing NO_2 following peroxynitric acid photolysis.[13] This deconvolution model is based on the hypothesis that an NO_2^* emission profile, independent of its history of production, may be represented by a linear combination of monoenergetically excited NO_2 emission profiles. This was termed the Photolysis Induced Fluorescence (PIF) deconvolution scheme, because it was originally applied to NO_2^* fluorescence following the photolysis of the precursor.

Nitrogen tetroxide presents a very interesting case for study. The primary reason for N_2O_4 PIF is to test the PIF deconvolution scheme when there exists the possibility of two fluorescing fragments. The other less obvious motivation is the possibility of observing discrete features in the NO_2^* emission profile. There has been some discussion in other groups that discrete features were observed in the prompt fluorescence of NO_2 following N_2O_4 photolysis, just as Donnelly observed in the NO_2 LIF.[14]

EXPERIMENTAL

A. Methods

1. NO_2 Prompt Fluorescence Detection

Nitrogen dioxide fluorescence from the low lying electronic states following UV laser photolysis of a precursor takes place in the visible region of the spectrum, allowing for easy dispersion and detection. A GaAs or multialkali photomultiplier tube is appropriate for collecting this fluorescence, which is scanned from 375 nm to 825 nm. The signal was taken at delay times of 400 and 1500 nanoseconds after the laser pulse, ensuring collection of nascent fluorescence (NO_2 lifetimes are ~ 100 microseconds[9]). This also allowed us to note if there were any major changes in the spectrum with time due to post photolysis collisions, and to obtain RF noise-free spectra. Once this fluorescence is collected and processed, it may be fitted by the PIF deconvolution scheme, resulting in an NO_2 internal energy distribution.

2. Supersonic Cooling

In contrast to the previous PIF experiments[12] this experiment employed a supersonic expansion to cool the translational and rotational modes, and to a lesser extent the vibrational modes, of the precursor.[15] These beams are referred to as supersonic because the Mach number, the ratio of the speed of mass flow to the local speed of sound, is greater than 1. This is acheived not because of the high speed of mass flow, which will not exceed 2 x 10^5 centimeters per second for helium as compared to 1.3 x 10^5 centimeters per second at 300 K, but rather it is due to the dramatic decrease in the local speed of sound which is proportional to the square root of temperature. Thus, it is this decrease in temperature which is responsible for Mach numbers greater than 1. The expansion of a gas from a high pressure region across an orifice into a vacuum causes the molecules to undergo many collisions which bring about this cooling. These collisions cause the random thermal motion to convert into directed mass flow in front of the nozzle. Thus, the cooling mechanism depends on how well the molecule's various degrees of freedom can convert energy into bulk directed translation. The advantage of this cooling for purposes of PIF studies is that it removes a large fraction of the Boltzmann internal energy present at 300 K, thus allowing for a more precise account of the energy partitioning. Another advantage is that the expansion helps push the, equilibrium, $N_2O_4 \rightarrow 2NO_2$ to the left. In the present experiment 300 torr of helium is passed over a trap of NO_2/N_2O_4 in a carbon tetrachloride/liquid nitrogen low temperature bath at -23° C, giving rise to a total pressure of 50 torr, of which 16 torr (32%) should be N_2O_4 according to the equilibrium constant of Bass.[2] An interpolation of the quasi-diatomic model by Wren and coworkers[16] estimates a neat NO_2/N_2O_4 beam at 298 K to be 81% N_2O_4. The model predicts that this fraction will rise with seeding since seeding, provides for three body collision needed to stabilize a complex; thus the 32% N_2O_4 would rise to a larger fraction.

B. Apparatus

1. Molecular Beam Chamber / Vacuum

Figure 1.3 illustrates the experimental arrangement for studying photolysis induced fluorescence of nitrogen tetroxide. A close up view depicting how the sample gas and laser light cross in the vacuum chamber is shown in Figure 1.4. The chamber body was made of stainless steel. The volume of the chamber was approximately .03 cubic meters. One interesting feature of the chamber is the recessed flange; this is used to increase the detection solid angle when observing total fluorescence. This recess also supports an adjustable lens external to the vacuum. The sample gas enters the chamber via a Newport Research Corporation, NRC, BV-100V pulsed valve. This valve was operated in a fashion different from that suggested by the manual. One chamber of the pulsed valve held 350 torr of He/N_2O_4, counterbalanced with vacuum on the other side instead of the recommended equal pressure. This allowed for greater pulse intensity, while yet maintaining a pulse-to-pulse reproducibility within five percent. There is the possibility that this might distort the time profile of the pulse, but that is of no consequence for fluorescence detection experiments, although it might cause difficulties for mass spectrometric detection. The chamber was pumped by a Norton VHS-6 diffusion pump operating with DOW Corning 705 allowing for an ultimate vacuum of less than $1x10^{-6}$ torr. Under normal operating conditions of pulsing at 10 hertz with 400 microsecond pulses the steady state reading on the Veeco ion gauge was $4x10^{-5}$ torr. This air-calibrated gauge measures the positive ion current from helium ions but the ionization potential of helium is greater than that for air, thus the reading must be multiplied by 6.8 to give a steady state pressure of $2.7x10^{-4}$ torr.[17] The chamber was pumped with a liquid nitrogen baffled 6" diffusion pump leading to a liquid nitrogen trap before entering the Edwards M-18 two stage mechanical pump. The liquid nitrogen delivery to the baffle was controlled by an Opto-Electronic LN_2 Level Controller. This device measures the resistence difference between two thermistors, one inside the baffle and one at room temperature, and completes a circuit supplying current across a resistor which in turn increases the pressure in a dewar to pump liquid nitrogen to the baffle.

In the initial arrangement the laser is guided through the high vacuum chamber by two right angle suprasil prisms such that the laser light, and thus the fluorescent volume, runs parallel to the entrance slit of the monochromator. The final prism guides the laser light to a Scientech Model 360001 power meter, the output of which is fed to an IBM AT computer. Later, when we decided to carry out the 248 nm photolysis, the fluorescent signal was much lower as expected due to a smaller absorption cross section.[18] When the PMT bias voltage was increased and the laser light was focused in an effort to increase the signal, a relatively significant fluorescent spectrum was observed in the absence of pulsing sample. This background fluorescence is probably attributed to the impurities in the Suprasil window or to pump oil or other materials adsorbed on the windows. Quartz is known to fluoresce in the visible after 193 nm excitation.[19] This empty chamber fluorescence is illustrated in Figures 1.5 and 1.6. To rectify this problem, the laser light was directed through baffled side windows and the monochromator was rotated 90° for alignment with the fluorescent volume. Even in this new configuration, this focused light caused the Suprasil windows to become less efficient in transmitting UV light with time and it was discovered that color centers had been produced. This process was decelerated by keeping the windows warm (~373K) with heating wrapped tape around the outer edge of the flanges in which the windows were housed. Eventually, after a week of experiments these windows had to be removed. The windows could be recovered by heating overnight at 500° C; after which time the transmission would return to a reasonable level prior to the formation of color centers.

The pressure behind the nozzle is ˜300 Torr of helium and 45 - 50 torr of the sample gas . For 50 torr of N_2O_4/NO_2 at 298 Kelvin this leads to an equilibrium mixture of ˜ 16 Torr of N_2O_4.[2] The pressure in the foreline behind the nozzle is measured with a MKS Baratron Model 220-2A6-1000 capacitance manometer. Initially the plan was to photolyze a neat beam of N_2O_4 to provide greater signal intensity and for a direct comparison against Kawasaki's experiments.[1] This was abandoned when the Viton o-rings decomposed upon reaction with liquid N_2O_4. The o-rings, were changed to Butyl o-rings as recommended by the chemical compatiblity from the Parker Seals O-Ring Handbook ord-5700. These also decomposed, thus it was necessary to seed the N_2O_4 in helium. One obvious advantage was that the pulse-to-pulse reproducibilty was far better for the seeded beam than the neat beam. This is probably because the seeded beam prevents condensation at the nozzle tip. The laser crosses the emitted gas 8 mm downstream of the nozzle (orifice of 0.5 or 1 mm) where the concentration along the expansion axis is estimated at 1.3×10^{15} molecules/cc.[3] Even with the large steady state background pressure of 2.7×10^{-4} torr, this interaction region is in a collisionless regime due to the shock front.[20] If the pressure P_0 behind the nozzle relative to the steady state pressure P is large enough along with a large orifice diameter d, then the gas behind the shock wave behaves like a free jet expanding in a vacuum and is unaffected by the background gas. The shock front distance of the nozzle, l , may be calculated from the formula:

$$l = 0.67d\left(\frac{P_o}{P}\right)^{\frac{1}{2}} \qquad \textbf{(1.1)}$$

Thus, for the present conditions, the shock front is 36 cm for the 500 micron orifice.

2. Photolysis Source

The photolysis source was a Questek Model 2210 excimer laser. The energy spread of the laser pulse is $\sim$160 cm^{-1}. The duration of each pulse is 17 ns. The laser operated on ArF, KrF, and XeF for 193, 248, and 351 nm wavelengths of excitation respectively. A plot of the absorption cross section for NO_2 and N_2O_4 is shown in Figure 1.2 adapted from Bass et. al.[18] Note that the N_2O_4 absorption cross section rise by a factor of 2 from 351 to 248 nm, but change by a factor of 45 from 248 to 193 nm. Thus, for the 248 and 351 nm experiments, a long focal length lens was placed in front of the laser output to make a more tightly collimated beam with slight focusing to obtain higher signal. The laser power and beam dimensions at the interaction are listed below in Table 1.1.

3. Optics/Detection

The fluorescence signal was collected with a 7.6 cm focal length f/1 lens 18 cm from the interaction region equipped with a cardboard mask with a 2 x 2 cm^2 aperture to prevent the collection of scattered light. This image was focused on the entrance slit of a 0.3m McPherson monochromator (model 218) which utilized a 1200 lines/mm grating blazed at 5000 Å. The slits were typically set at 500 μm and the scanning speed 100 Å/min. One hundred shots were fired between data points, of which the last 50 were collected at a laser repetition rate of 10 hertz, corresponding to a resolution of 2.13 nm per data point. The monochromator was run with a home built controller which allowed the monochromator to scan continously, as opposed to stepping in defined intervals. The monochromator entrance slit was equipped with a f/4.65 Suprasil lens to maximize the image on the back mirror and a corning 0-52 (effectively cuts out all radiation below 380 nm) filter to prevent laser scatter light from entering the chamber. A f/4.25 glass lens was placed at the exit slit leading to a f/2 glass reduction lens to effectively reduce the image to fit onto the active element of the RCA 4832 (GaAs) or Hamamatsu R1477 (multialkali) visible photomultiplier tube.

The signal from the PMT was amplified by an Avantek 120 gain amplifier (model GPD460). The amplified signal was sent to an SRS gated integrator/boxcar and this signal was stored in an IBM AT computer. The boxcar integrator sampled the fluorescent signal at two different delay times, 400 ns and 1500 ns, with a gate width of 100 ns. The fluorescent signal was corrected for laser power and the nonuniform responsivity of the system by use of a tungsten lamp and monochromator (see appendix A). The lamp's emission was directed through the same optical train (monochromator, lenses, filetrs, ect.) as the NO_2^* fluorescence ending at the photomultiplier tube. By comparing the experimental lamp emission profile and the theoretical lamp profile as found in the literature[21], a response profile describing the relative efficiency for each photon may be determined.

4. Triggering Scheme

The triggering scheme was designed such that a signal generator operating at 10 Hz played the role of the initiator. This signal was fed to an EH Generation model G710 Pulse Generator used to place a delay between the laser and pulsed valve. The pulse generator has two outputs: 1. The trigger output which is a TTL pulse mirroring the input pulse from the signal generator and 2. the normal output which produces a pulse after the desired delay has been established on the pulse generator. The delay was set by optimizing the fluorescence signal viewed on an oscilliscope with the monochromator fixed for 600 nm. The trigger output triggered the BV-100D NRC beam valve driver, whereas the normal output triggered the laser. The laser was placed in a shielded room (Faraday cage) to reduce RF noise, and the input trigger line traversed an opto-isolator to minimize noise feedback from the excimer. Scattered light from the steering optics impinged on a photodiode which served as a trigger for the boxcar integrators. The computer operated in a passive mode by only controlling the time in which the appropriate A/D ports would be sampled for the data collection (boxcars and power meter). The computer also controlled the monochromator scanning via outputting TTL pulses to a control unit. The data collection programs were written with the software package ASYST[22], which allowed in situ plotting of both the 400 and 1500 ns fluorescence spectra.

C. Gases

The NO_2 was supplied in the liquid/gas phase from Matheson and purified by reiterative sequences of freeze, pump, and thaw. When not in use, the NO_2 was stored in liquid nitrogen. This was to prevent the decomposition and to prevent N_2O_4 from reacting with the Viton o-rings, and thus allowing contaminants from the atmosphere to enter the sample vessel. The gases for the laser were obtained from the Airco Co. with the following purity levels: Helium

99.9999%, Xenon 99.9%, Fluorine 5% in Helium, Argon 99.9995%, and Krypton 99.995%.

RESULTS

A. Mathematical Derivation of PIF Equations

As demonstrated in Figure 1.7 The complicated NO_2 absorption and fluorescence spectra defy quantum state assignments. Demtröder and coworkers[23] have recently reported that the spectrum is chaotic and follows a Wigner type distribution. They conclude that this is a manifestation of the nonadiabatic vibronic coupling which destroys the Born-Oppenheimer description of the molecular eigenstates. The coupling is thought to be so extensive that only energy and angular momentum remain good "quantum numbers" of the system. Thus, there was no attempt to derive a quantum state distribution of NO_2^* photofragments following an R-NO_2 photodissociation; rather, the PIF scheme makes use of dispersed NO_2 fluorescence. In this scheme the cumulative sum of the data are least squares fitted to a semi empirical fitting function. By fitting the cumulative sum of the data rather than data itself, the entire spectrum, including the discrete features, are taken into account.

1. NO_2 LIF Fitting Function

The analysis of the PIF spectra was carried out by the PIF deconvolution scheme described previously.[24] At the heart of the analysis is the following assumption. The dispersed emission of NO_2 following N_2O_4 photolysis may be represented by a linear combination of dispersed emission from monoenergetically excited NO_2. The NO_2 LIF profiles near room temperature were characterized by an analytical function which depends only on the laser excitation energy.

$$L(X,X_L) = CZ^2EXP(-Z) \qquad \textbf{(1.2)}$$

$$Z = \frac{(x_L+\Delta X-X)}{(X_L+\Delta X)\,a} = \frac{(B-X)}{Ba} \qquad (1.3)$$

B = $X_L + \Delta X$

X_L = laser excitation energy in wavenumbers

X = observation energy in wavenumbers

ΔX = 1000 cm^{-1}

threshold energy (highest observed fluorescence energy) minus X_L: this agrees with the room temperature boltzmann rovibrational population spread

c = amplitude factor: computed by normalizing the area under the curve of the fit to that of the data.

a = fitting parameter

This NO_2 fitting function, **L**, may be integrated in a cumulative fashion to give a function **I**, which is the running sum of **L**, as shown below in Figure 1.8. The cumulative sum of the data is least squares fitted to **L** by varying the fitting parameter **a**. This was done to account for the sharp features in the NO_2 fluorescence as described in the previous report.[24]

$$I(X',X_L) = \int_{X'}^{B} L(X,X_L)\,dX \qquad (1.4)$$

$$I(X',X_L) = Bac[2-(2+2Z+Z^2)EXP(-Z)] \qquad (1.5)$$

X' is a particular value of X, the observation energy. This was done for 22 values of X_L between 399.8 to 672.6 nm. The resulting 22 values of **a** were fitted against X_L via an exponential function.

$$a(X_L) = EXP(7.293*10^{-5}X_L-2.9861) \qquad (1.6)$$

With $\mathbf{a(X_L)}$ as a closed function, it is possible generate NO_2 fluorescence profiles anywhere in the visile region of the spectrum.

2. Basis Set: Normalization of $L(X,X_L)$

In order for the absolute intensity of each LIF curve to be suitable as a basis element, the curve's $\{L(X,X_L)\}$ area must be proportional to the radiative rate constant

$(1/\tau)$ and to the total number of molecules in the excited state for the particular laser excitation energy. Each LIF profile, $L(X,X_L)$, is corrected by normalizing its area to equal the inverse of its total fluorescence lifetime at excitation energy X_L (actually in practice the area is normalized to unity, which is later multiplied by the inverse lifetime) the corresponding coefficient of the basis element is proportional to the number of molecules with excitation energy X_L. The unit-area normalized fluorescence profile, $L_D(X,X_L)$, given by the following formula.

$$L_D(X,X_L) = \frac{L(X,X_L)}{\int_0^{\min(B,D_0)} L(X,X_L)\,dX} \quad (1.7)$$

D_0 = NO_2 dissociation threshold[25] ≈ 25137 cm^{-1}

$\min(B,D_0)$ = The minimum of B and D_0

Due to the fact that the fluorescence may not exceed the thermodynamic NO_2 dissociation threshold, the limits of integration for the above equation are listed in Table 1.2.

$$L_D(X,X_L)\,dX = \frac{Z^2 EXP(-Z)\,dX}{a(X_L+\Delta X)\left[(2+2Z_{LL}+Z_{LL}^2)\,e^{Z_{LL}} - \left(2+\frac{2}{a}+\left(\frac{1}{a}\right)^2\right)e^{-\frac{1}{a}}\right]}$$

(1.8)

3. Fitting PIF Profile

The assumption that the PIF spectrum following photolysis is a linear combination of NO_2 LIF spectra is expressed mathematically as:

$$P(X) = \sum_{X_L = X - \Delta X}^{D_0} L_D(X, X_L)\, F(X_L)\, \Delta X_L \quad \mathbf{(1.9)}$$

P(X) = NO_2 fluorescence intensity at energy X calculated by the PIF deconvolution

$\{F(X_L)\}$ = laser excitation coefficients "weighting" function

The running sum of the PIF spectrum was fit to the running sum of **P(X)**, **ΣP(X)**, serving the same purpose as fitting the **I** function for NO_2 LIF basis elements; namely, to take the sharp features into account. A mulplicative constant (amplitude factor) for **P(X)** was determined by setting the last points of the fit, **ΣP(X)**, equal to the last point of the cumulative sum of the PIF spectrum. The last point is equal to the area of the PIF spectrum; thus the PIF spectrum and the P(X) function are normalized to equal area. Once the fit is computed, **P(X)** is generated and plotted against the PIF spectrum. Two weighting functions were employed in the deconvolution, the kernel of the Gamma function and the

Gaussian function. Thus the NO_2 laser induced fluorescence (LIF) profiles constitute the basis set.

(1) The Gamma Fitting function

$$\Gamma\ kernel: F(X) = (M-X_L)^n EXP\left(-\frac{(M-X_L)}{s}\right) \qquad (1.10)$$

M = Maximum available internal energy for NO_2 based on the photon energy and bond dissociation energy difference.

n,s = adjustable fitting parameters

This may be expressed in variable Y_{max} = ns

$$F(X_L) = \left(\frac{M-X_L}{Y_{max}} EXP\left[-\frac{M-X_L}{Y_{max}}\right]\right)^n \qquad (1.11)$$

The Gaussian function

$$F(X_L) = \frac{EXP\left(-\frac{(X_L-\mu)^2}{2\sigma^2}\right)}{(2\pi\sigma^2)^{\frac{1}{2}}} \qquad (1.12)$$

μ,σ = fitting parameters

Both functions produce similar fits, but the " M " value of the kernel of the Gamma function makes it the more physically relevant function.

Once $\{F(X_L)\}$ is obtained two corrections, boltzmann energy spread and fluorescence lifetime, are made to compute the population.

$$POP(X) = \sum_{X_L=0}^{X} F(X_L)\,\tau(X_L)\,BOL(X_L)\,\Delta X_L \quad \textbf{(1.13)}$$

The lower limit utilized in the above integral was actually 9710 cm^{-1} ($^2B_2$ orgin)[26] instead of 0. This approximation was empirically valid, in that the integral changed by less than a fraction of a percent around the 9710 cm^{-1} region.

τ = Fluorescence lifetime at zero pressure in seconds

$$\tau^{-1}(X_L) = 0.335(X_L-9710)+9350 \quad (1.14)$$

$BOL(X,X_L)$ = boltzmann rovibrational NO_2 function

$$BOL(X,X_L) = \left(\frac{X-X_L}{kT}\right) EXP\left[-\frac{(X-X_L)}{kT}\right] \quad \textbf{(1.15)}$$

This function computes the rovibrational population of NO_2 as a function of temperature.

B. DATA

1. PIF Spectra and Fits to $\Sigma P(X)$

The 1500 ns delay PIF spectra corrected for system response and laser power is shown in Figures 1.9-1.11 for 193, 248, and 351 nm photolysis wavelengths respectively. These are displayed because the signal to noise ratio is better at

1500 ns than at 400 ns due to less interference from RF noise. The Gamma Kernel fits to the cumulative sum of the data and the resulting **P(X)** plotted against the PIF spectra are illustrated in Figures 1.12-1.17. Table 1.3 lists the Gamma Kernel fitting parameters for the N_2O_4 PIF files. Note that the parameters are widely varying even for similar fits. This occurs because the least squares error minimization may select any one of several equivalent sets of parameters that give the same error within the specified tolerance. The different system response files for the PIF files are also listed in Table 1.3. The response profiles corresponding to the system response files are displayed in Appendix A.

2. Internal Energy Distribution from PIF Method

The resultant populations of these fits are displayed in Figures 1.18-1.20. The populations resulting from the 193 nm photolysis are pretty much in agreement except for the WSE98F data. This is probably due to the CCl_4 slush bath warming up and/or some other inexplicable changes that caused concentration fluctuations. The 248 nm populations also show a wide variance with the WSE290D result being the possible result of concentration fluctuation. The 351 nm populations seemed very consistent. Statistical measures of the populations such as the mean energy, the most probable energy the root mean squared energy, and the standard deviation are listed below in Table 1.4. Note that the mean and rms values are pretty consistent for a particular wavelength. The standard deviation decreases with increasing wavelength indicating a more defined distribution for less available energy.

The populations obtained from Gamma Kernel fitting function versus those obtained from the Gaussian fitting function are illustrated in Figures 1.21-1.23. It is readily apparent that the differences between the populations from the two functions is within the population reproducibility error within trials of the Gamma Kernel function.

C. Direct Interpretation of Data

1. Prior Distribution Comparison

The PIF distribution may be compared with a statistical distribution, the results of which may yield information about the dynamics of dissociation. The PIF results at 248 nm and 193 nm aren't well suited for phase space calculations, because these allow for the three body product channel: NO_2 + NO + O. For such a channel it is very difficult to obtain the product state density. On the other hand the 351 nm photolysis results do not allow access to the NO production channel, assuming very few molecules contain more than 1200 cm^{-1} of thermal energy.

The prior distribution was the statistical model employed to calculate the internal energy distribution of NO_2^* from N_2O_4 photolysis at 351 nm.[27] The prior distribution of states of the products has the relative probabilty for the product state proportional to the statistical weight, the number of different ways the energy may distributed among the internal modes of the product and translation. Unlike phase space calculations in where there are two constraints, angular momentum and energy conservation, the prior distribution operates solely under the constraint of energy conservation. To simplify the calculation the probability was calculated only for $NO_2^*(\alpha)$ for the rotationless levels ($J=0$), but the rotational degeneracy due to the $NO_2(\beta)\,[^2A_1]$ fragment was taken into account. Restricting the values of J to 0 neglects the subsequent Coriolis mixing which could lead to a different weighting for the vibrational quantum number, dependent on the value of the coupling constant. The statistical weight for the $NO_2^*(\alpha)$ fragment containing vibrational energy $E_v(\alpha)$ is given by:

$$P_\alpha(E_v(\alpha), J=0) = \frac{\sum_{E_v(\beta)=0}^{E-E_v(\alpha)} \sum_{J_\beta=0}^{J_{\beta\,max}} \rho\; g_v(\beta)\, g_v(\alpha)\, (2J_\beta+1)}{\sum_{E_v(\alpha)=0}^{E} \sum_{E_v(\beta)=0}^{E-E_v(\alpha)} \sum_{J_\beta=0}^{J_{\beta\,max}} \rho\; g_v(\beta)\, g_v(\alpha)\, (2J_\beta+1)} \qquad (1.16)$$

E = The available energy after dissociation = $E_{PHOTON} - E_{BOND}$

$E_v(\alpha)$ = The vibrational energy in α NO_2 fragment

$E_v(\beta)$ = The vibrational energy in β NO_2 fragment

$g_v(\alpha)$ = The vibrational density of states for α NO_2 fragment

$g_v(\beta)$ = The vibrational density of states for β NO_2 fragment

ρ = $[E-E_v(\alpha)-E_v(\beta)]^{.5}$ proportional to translational density of states

When one applies the prior model to photodissociation, the electronic states of product and reactants must be specified. Table 1.5 lists the NO_2 parameters employed. Figure 1.24 shows the experimental 351 nm PIF $P(E_{NO2})$ and the prior distributions calculated for NO_2 $^2B_2$, $^2B_1$, and $^2A_2$ excited electronic states. Clearly the $^2B_2$ prior distribution disagrees with the PIF $P(E_{NO2})$. The $^2B_1$ and $^2A_2$ prior distributions resemble $P(E_{NO2})$ much more closely, but still display significant discrepancies in overall contour and the energy of the distribution maximum. Noting the marked geometrical difference between the linear $^2B_1$ and bent $^2A_2$ states, the similarity of the prior distributions for these states result from the close proximity of their electronic term values. The $^2B_1$ state is the most likely possibility although the $P(E_{NO2})$ via PIF doesn't match very well in Figure 1.24. IF the linear $NO_2(^2B_1)$ is born with 3 or 4 nascent quanta of ν_2 in $^2B_1$ state and the energy is allowed to statistically distribute after this point the prior distribution and the 351 nm PIF internal energy distribution agree very well as illustrated in Figure 1.25. The prior distribution model was adjusted to account for this by allowing the $^2B_1$ electronic origin to assume a new value of $^2B_1+v_2$, where v_2 is the vibrational quantum numbers of the bending mode within the $^2B_1$ electronic state. There is good reason to expect nascent ν_2 excitation in the Franck-Condon formation of bent $^2B_1$, which has a linear equilibrium structure.[28] From the above discussion we conclude:

$$N_2O_4 + h\nu(351\ \text{nm}) \rightarrow NO_2(^2A_1) + NO_2(^2B_1,\ v_2 = 3\ \text{to}\ 4)$$

2. Translational Energy Distribution Comparison

Kawasaki and coworkers[1] have photolyzed a molecular beam of N_2O_4 and monitored the TOF of the NO_2 fragment to obtain a translational energy distribution. Care must be taken in comparing Kawasaki's translational energy distribution to the translational energy distribution derived from our PIF results. Subtracting the PIF internal energy from the total available energy doesn't yield the translational energy. This is because the translational energy stated by Kawasaki is the **total** translational energy correlated to the **total** internal energy of the two post-photolysis NO_2 fragments. The PIF energy of the fluorescing NO_2 fragments does not correlate the two resultant NO_2 fragments. Note in the PIF model the internal energy distribution may not exceed 25137 cm^{-1}, the dissociation threshold of NO_2. Thus, to restate the above argument another way: The internal energy distribution from Kawasaki's TOF results is for the two correlated NO_2 fragments, which may exceed 25137 cm^{-1}; the internal energy from PIF is not necessarily correlated for NO_2 fragments from the same parent.

We have attempted to obtain the translational energy from PIF results as follows. We can designate the correlated NO_2 (NO_2 fragments from N_2O_4 parent) as α and β. The primary assumption of this model is that both NO_2 fragments (α and β) have the same energy distribution. This is describing the distribution of the fragments in a statistical sense and does not say that both fragments from a particular N_2O_4 have the same energy distribution. The probability of a particular translational energy is the sum of the number of ways $NO_2(\alpha)$ and $NO_2(\beta)$ may possess particular energies within the constraint of the conservation of energy.

$$P(E_{trans}) = \sum_{E_{NO_2(\alpha)}=0}^{E_{avai}-E_{trans}} P(E_{NO_2(\alpha)})\,P(E_{NO_2(\beta)}) \tag{1.17}$$

$$p(E_{trans}) = \sum_{E_{NO_2}=0}^{E_{avai}-E_{trans}} P(E_{NO_2})\,P(E_{avai}-E_{trans}-E_{NO_2}) \tag{1.18}$$

$P(E_{NO2})$ is the probability that an NO_2 fragment has internal energy E_{NO2} obtained from the PIF populations. Figures 1.26 and 1.27 show the comparison between Kawasaki's translational energy distribution and that derived from PIF.

The agreement between the calculated and observed translational energy distributions of NO_2 following the 193 nm photolysis of N_2O_4 (Figure 1.26) confirms the postulate that both NO_2 fragments from N_2O_4 at 193 nm have the same energy distribution. On the other hand, the disagreement between the calculated and observed translational energies for NO_2 produced by N_2O_4 photolysis at 248 nm (Figure 1.27) refutes the postulate the the internal energy distributions are the same for $NO_2(\alpha)$ and $NO_2(\beta)$.

Two other facets of the PIF spectra that were studied include the appearance of discrete features in the 351 and 248 nm data and the onset of fluorescence as an indicator of the N-N bond dissociation energy for the 351 nm PIF. These are discussed in Appendicies B and C.

DISCUSSION

A. N_2O_4 Electronic Structure

Understanding the N_2O_4 electronic structure will be crucial to our analysis of the its photodissociation dynamics. Therefore, we briefly review the pertinant experimental and theoretical information. As our development of the N_2O_4 photodissociation process requires more specific molecular orbital descriptions, we will introduce it based on the groundwork supplied in this section.

1. The N_2O_4 Absorption Spectrum

The N_2O_4 absorption spectrum, shown in Figure 1.2, extends continuously from 370 nm to below 180 nm.[18] The spectrum is everywhere diffuse, suggesting that all of the transitions terminate in dissociative states. (Howell and Van Wazer's[29] ab initio calculations, which show the first four π states are dissociative, support this conclusion.) The spectrum divides into two distinct regions. The first portion of the spectrum is a broad, single, low intensity feature stretching from 300 to 370 nm with a maximum at 340 nm (σ = 8.28E-19 cm^2). An intense absorption feature with a maximum at 187 nm (σ = 5.58E-17 cm^2) and a shoulder near 265 nm (σ = 8.62E-19 cm^2) dominate the spectrum at shorter wavelengths. The two absorption bands are separated by a shallow minimum between 285 and 310 nm. The shoulder near 268 nm is in a region consistent with $n \rightarrow \pi^*$ transition localized on the NO_2 group found in other R-NO_2 molecules.[30,31] Likewise, the intense feature peaked at 186 nm usually receives a $\pi \rightarrow \pi^*$ assignment for nitroalkanes although this was assigned to $\sigma \rightarrow \sigma^*$ for N_2O_4 by Mason.[32] (again localized on the NO_2 chromophore).

N_2O_4 photodissociation experiments provide additional information about the absorption spectrum's underlying transitions. Inoue et al.[2] concluded from fluorescence quantum yield measurements that excitation into the first absorption feature (295 - 365 nm) creates one NO_2 fragment electronically excited and one electronically "cold". Kawasaki et al.[1] determined from the angular anisotropy of the NO_2 fragment distributions that the transitions excited at 248 and 193 nm both have parallel transition dipole moments; these are Z-polarized and have b_{1u} symmetry in the D_{2h} point group.

2. Molecular Orbital Theory

When discussing the molecular orbitals of N_2O_4/NO_2 it is very helpful to specify the choice of axis. The convention chosen here is that utilized by von Niessen[33], Alrichs[34], Pulay[35], and Bauschlicher[36].

$D_{2h} \rightarrow C_{2v}$: $Z \rightarrow Z$, $Y \rightarrow X$

N_2O_4 is in XZ plane with the Z axis parallel to the N-N bond. NO_2 is in the YZ plane with the Z axis equal to the C_2 axis. The N_2O_4 groundstate electron configuration is

$$....(4b_{2u})^2(4b_{3g})^2(1b_{1g})^2(1a_u)^2(6a_g)^2.$$

Its geometry resembles that of two free NO_2 molecules bound by a particularly long N-N bond (Figure 1.1), leading to its description as an NO_2 dimer. The geometries and electronic configurations of the excited states are unknown.

Ab initio characterizations of the N_2O_4 electronic structure have focussed primarily on the electron deficient N-N bond and planarity of the groundstate. However, these studies have revealed substantial information about the nature of the low energy excited electronic configurations, since a single configuration SCF wavefunction incorrectly understimates the N-N bondlength by 0.2 Å.[29,33,34,36] Kvick et al. found that calculations including the $6b_{1u}(\sigma^*)$ virtual orbital in a two state configuration wavefunction predict a more correct 1.80 Å N-N bondlength.[6]

Bauschlicher et al.[36] and Pulay and Hamilton[35] expanded the N_2O_4 active configuration space to include the $2b_{2u}$ and $2b_{3g}$ virtual π^* orbitals in their calculations. These calculations demonstrated that the π framework and 1,4 interactions between the oxygen atoms maintain the molecule's planarity.

There are three other theoretical investigations of the N_2O_4 system which should be mentioned before proceeding. The disputed assignment of the N_2O_4 photoelectron spectrum was addressed by the ab initio calculations of von Neissen et.al.[33] This group used a Green's function many-body perturbation procedure to optimize the calculated ionization potentials. It is interesting to note that the many body correlations reordered the ionization energies, moving the $3b_{2g}(3b_{3g})$ to lesser energy than the $1b_{1g}/1_{au}$ pair of oxygen lone pair orbitals which are calculated to be at higher energy in the N_2O_4 groundstate valence shell. Additionally, this paper provides a quantitative estimation of the virtual orbital energies. Mason[32] attempted to describe the transitions which produce the N_2O_4 UV absorption spectrum using CNDO techniques. This is the only theoretical prediction of its kind, but the CNDO approximation is not very rigorous. They may prove useful as a guideline. Kishner's CNDO/BW calculations[37] serve as a guide for the comparison of Mason's predictions to the ab initio results.

Alrichs et.al.[34], Bauschlicher et.al.[36] , Howell et.al.[29] , and Pulay et.al.[35] all conducted ab initio calculations to ascertain the nature of the unusually long N-N bond and the reason for the seemingly unstable planarity of the N_2O_4 groundstate. A Green's function perturbation approach was used by von Neissen et.al[33] to optimize their ab initio calculations and explain the disputed ordering of the ionization potentials from the N_2O_4 photoelectron spectrum. Kishner et.al.[37] conducted a less rigorous CNDO/BW calculation obtained molecular orbital energies in qualitative agreement with ab initio results. Mason[32] also used CNDO techniques in an attempt to explain the N_2O_4 UV absorption spectrum. Figure 1.28 shows a molecular orbital correlation diagram for $NO_2 + NO_2 \rightarrow N_2O_4$.

B. N_2O_4 Photodissociation Dynamics

One general remark should be made before treating specific photodissociation experiments: $N_2O_4 + h\nu \rightarrow NO_2 + NO_2$ is a symmetric reaction. Thus the wavefunction of the product states of the system for channel 6 (Figure 1.29) may be represented as:

$$\Psi=\psi(\alpha,{}^2B_1)\psi(\beta,{}^2B_2)+\psi(\alpha,{}^2B_2)\psi(\beta,{}^2B_1)$$

1. 351 nm Excitation

In an attempt to determine the product electronic states of NO_2 following N_2O_4 photolysis at 351 nm excitation we make use of the previously discussed prior distribution results and the dissociation channels listed in Figure 1.29.

The prior distribution strongly showed channel 3 to be the preferred dissociaton channel. This result is compatible with Inoue's conclusion of only one NO_2 electronic excited state when N_2O_4 is excited in the 296-365 nm range. If the thermal energy of N_2O_4 is considered, channels 1-6 of Figure 1.29 are the only channels energetically possible at 351 nm excitation. Channels 6 and 5 are eliminated by Inoue's conclusion, whereas channels 1 and 4 are eliminated due to lack of electric dipole moment (zeroth order) to allow fluorescence. Of the remaining channels (2 and 3), channel 3 was conclusively chosen over channel 2 in the prior distribution comparison.

The electronic transition compatible with the assigning $^2B_1$ as the electronic state of NO_2^* may be determined from the N_2O_4/NO_2 correlation diagram, Figure 1.28, based on the molecule orbital ordering of von Niessen et al.[33] (This ordering is utilized rather than the more conventional ordering which places the $6b_{1u}$ molecular orbital as the LUMO because these authors are the only group to report quantitative energies and the ordering of the virtual orbitals.) Depending on the ordering of the virtual orbitals and their interactions under various geometrical configurations, there are three possibilities for the lowest energy N_2O_4 electronic transition: $6a_g \rightarrow 6b_{1u}$, $6a_g \rightarrow 2b_{2u}$, or $1a_u \rightarrow 6b_{1u}$. The $6a_g \rightarrow 6b_{1u}$ $\sigma \rightarrow \sigma^*$ transition correlates to $^2A_1$ + $^2A_1$ products. The $1a_u \rightarrow 6b_{1u}$ $n \rightarrow \sigma^*$ transition transition is not symmetry allowed (transition moment = b_{1g}) and the products correlate to $^2A_2$ + $^2A_1$. The $6a_g \rightarrow 2b_{2u}$ $\sigma \rightarrow \pi^*$ transition posesses a Y/b_{2u} transition moment and correlates to the desired $^2B_1$ + $^2A_1$ products. The calculations of von Neissen et.al.[33] predict this to be the HOMO-LUMO transition.

While an experimental $P(E_{trans})$ distribution for the 351 nm N_2O_4 photodissociation is not available, the characteristics of such a distribution may be inferred from the PIF $P(E_{NO2})$. Assuming minimal internal excitation of the $NO_2(\beta)$ fragment, the TOF spectrum is predicted to show a maximum translational energy release corresponding to about $E_{trans(max)}$ ~ 9000 cm^{-1} (E_{aval} - $^2B_1$ promotion energy = 23,890 - 14,700 = 9190 cm^{-1}; Figure 1.30 shows the $P(E_{trans} + E_{NO2(\beta)})$ composite distribution calculated from the PIF $P(E_{NO2}) = P(E_{NO2(\alpha)})$ distribution. Difference between $P(E_{trans} + E_{NO2(\beta)})$ and $P(E_{trans})$ is expected to be minimal. The symmetry arguments mentioned above suggest that angular distribution measurements of the photofragments from excitation into the first absorption band will probably reflect contributions from predominantly perpendicular transitions.

The impulsive model is a nonstatistical model by which to compare the 351 nm photolysis results.[37] This model assumes the dissociation is direct such that there is little time for the equilibration of internal energy. According to this model the amount of translational energy for the 351 nm photolysis should be $(m_N/m_{NO2})E_{avai} = 7270$ cm^{-1} which leaves 16619 cm^{-1} to be distributed among the internal modes of both fragments. This does not agree with the PIF distributions which is peaked at energies about 3000 cm^{-1} higher than 16619 cm^{-1}.

2. 193 nm N_2O_4 Photodissociation

As mentioned earlier, the 193 nm used in implementing Eqs. 1.18 and 1.19 for translational energy and $P(E_{NO2}(\beta))$ internal energy distributions imply similar energy distributions for the two correlated NO_2 fragments $E_{NO2}(\alpha) = E_{NO2}(\beta)$ (postulate (i)). Although channels 1-14 (Figure 1.29) are all energetically available only channels 1,5,9, and 11 obey this conditon of postulate (i). Of these four channels only channels 5 and 9 are electric dipole allowed to fluoresce. The TOF results yield a value of 26,164 cm^{-1} for the maximum translational energy, $E_{trans(max)}$, which accounts for only 55% of the available energy as listed in Table 1.6. The minimum internal energy, $E_{int(min)}$, determined by subtracting $E_{trans(max)}$ from E_{aval} is 20,969 cm^{-1}. The channel(s) that satisfy these criteria as well as having it's threshold below that of $E_{int(min)}$ (193) is channel 5 ($^2B_2$ + $^2B_2$).

The energy difference between $E_{int(min)}$ and $^2B_2$ + $^2B_2$

formation (20,969 - 19500 = 1469 cm^{-1}) is 1469 cm^{-1}. Dividing this energy evenly between the NO_2 fragments places 735 cm^{-1} in each NO_2. This energy coincides almost exactly with the ν_2 bending frequency in $^2B_2$ NO_2. Such a dynamic motion is expected in the formation of $^2B_2$ NO_2 fragments, since the bond ONO bond angles in groundstate N_2O_4 are about 135 degrees(same as $^2A_1$) and the bond angle in $NO_2(^2B_2)$ is a more constricted 102 degrees.[39]

The molecular orbital correlation diagram in conjunction with the TOF angular distribution from Kawasaki may be used to determined the molecular orbitals which correspond to channel 5 ($^2B_2$ + $^2B_2$). The large absorption cross section at 193 nm is indicative of an electric dipole allowed transition.[18] From the anisotropy of the NO_2 photofragments Kawasaki and coworkers[1] determined the transition to be Z polarized (b_{1u} symmetry in D_{2h}). The only electronic transition of b_{1u} symmetry involving the outer valence orbitals is the $6a_g \rightarrow 6b_{1u}$ $\sigma \rightarrow \sigma^*$ transition.

Mason[32] has ascribed the 186 nm transition to $\sigma(a_g) \rightarrow \sigma(b_{1u})$. Several additional arguments support this assignment despite the fact that this transition correlates to $^2A_1$ + $^2A_1$ products. It is the only $\sigma \rightarrow \sigma^*$ transition available among the low energy eletronic transitions possessing the proper transition symmetry. The calculations of von Neissen et al.[33] mark the $6a_g \rightarrow 6b_{1u}$ promotion as the second lowest energy symmetry allowed transition (not as the HOMO-LUMO transition as several groups claim[6,29]), making this assignment consistent with the absorption spectrum and the $6a_g \rightarrow 2b_{2u}$ assignment made for the 351 nm dissociation above.

An attempt must be made to resolve the apparent discrepancy between the $6a_g \rightarrow 6b_{1u}$ $\sigma \rightarrow \sigma^*$ ($^2A_1$ + $^2A_1$ products) assignment which was based on theoretical N_2O_4 electronic structure, and the $^2B_2$ + $^2B_2$ product channel assigned on the basis of $P(E_{NO2})$, $P(E_{trans})$, and energetic considerations. The most probable explanation is that the potential energy surfaces (PES) correlating to ($^2A_1$ + $^2A_1$) (Channel 1/PES 1) and ($^2B_2$ + $^2B_2$) (Channel 5/PES 5) products intersect (see Figure 1.31). These surfaces must cross somewhere if the $6a_g \rightarrow 6b_{1u}$ transition is excited at 193 nm. The $^2A_1$ and $^2B_2$ NO_2 PES's cross for C_{2v} configurations with bond angles near 108 degrees[39,40].

It is possible that the predicted crossing of N_2O_4 PES 1 and PES 5 occurs when the ONO angles approach 108 degrees as in NO_2. If the intersection occurs near the Franck-Condon region of 193 nm transition, the probability for the dissociating N_2O_4 system to cross onto PES 5 ($^2B_2$ + $^2B_2$ products) would be enhanced.

3. 248 nm N_2O_4 Photodissociation

Again as in the 193 nm case the pool of possible product channels may be narrowed by the results of Eqs. 1.18 and 1.19 and a close inspection of Kawasaki's transaltional energy distribution. Postulate (ii) $E_{NO2}(\alpha) \neq E_{NO2}(\beta)$ is inferred from the 248 nm implementation of Eqs. 1.18 and 1.19. At 248 nm the $E_{int(min)}$ (Table 1.6) is 24733 cm^{-1}. Only channels 1-12 may be considered due to E_{aval} = 35,640 cm^{-1}. The $E_{int(min)}$ value of 24,733 cm^{-1} eliminates channels 9-12 from consideration since these channels lie above this minimum to a significant degree even when the initial thermal energy of the precursor is considered. No nitric oxide was detected by Kawasaki in the 248 TOF experiment, implying that the NO producing channels and channels with only one excited NO_2 are not very significant (channels 1-4, 7). Channel 5 is eliminated by postulate (ii).

The remaining choices consist of Channel 6 ($^2B_1$ + $^2B_2$), or Channel 8 ($^2B_2$ + $^2A_2$). Note from Figure 1.29 that the value for $E_{int(min)}$ (24,733 cm^{-1}) agrees almost exactly with the threshold energy for Channel 6 ($^2B_1$ + $^2B_2$) (24,450 cm^{-1}) leading us to believe this to be the dominant channel at 248 nm photolysis of N_2O_4.

The molecular orbital correlation diagram (Figure 1.28) along with the TOF and PIF information may be utilized to determine which molecular orbitals correspond to channel 6 ($^2B_1$ + $^2B_2$). Kawasaki's TOF angular distribution of N_2O_4 at 248 nm reveals a Z-polarized (b_{1u} in D_{2h}) parallel transition. There are three possible transitions from the $4b_{2g}/4b_{3u}$ orbitals to the $2b_{2u}/2b_{3g}$ orbitals which may correlate to $^2B_1$ + $^2B_2$.

The lowest energy transition in this group is $4b_{2g} \rightarrow 2b_{2u}$. Von Neissen et al.[33] have calculated that the ionization of $4b_{2g}$ orbital occurs at lower energies than that of either the $1a_u$ or $1b_{1g}$ orbitals which have higher calculated valence energies. This reordering of valence orbital energies may occur during electronic transitions.

This transition is electronically forbidden. When the vibrational modes, as discussed by Bibart et al.[41] and Snyder et al.[42], are investigated for the possibility of vibronically allowed transitions no vibrational modes were found of the proper symmetry (b_{1g}), after converting the axis convention from their papers (N_2O_4 in YX plane: Y axis parallel to N-N bond) to the axis convention utilized for this discussion.

The $4b_{2g} \rightarrow 2b_{3g}$ transition, while also electric dipole forbidden, produces an interesting vibronic transition. This transition requires an A_u vibrational mode to occur via a b_{1u} transition dipole moment. There is only one N_2O_4 groundstate vibration with this symmetry: the ν_4 torsional bending mode. This is intriguing since the torsional motion destroys the planarity of the N_2O_4 molecule and takes it toward a staggered configuration (D_{2d}). Such a possibility is also very likely, since ν_4 has a very low frequency (70 [Snyder[42]] or 79 cm^{-1} [Bibart[41]]) and the torsional barrier is only 800 - 1000 cm^{-1} [Snyder and Bibart]. N_2O_4 dissociation from a non-planar geometry also has some interesting dynamical implications. However, von Neissen et al.[33] calculated that the $2b_{3g}$ orbital lies 1.86 eV above the $2b_{2u}$ orbital, thus this transition seems less likely although still possible.

The $4b_{3u} \rightarrow 2b_{2u}$ transition becomes a b_{1u} allowed transition through the same torsional motions as the $4b_{2g} \rightarrow 2b_{3g}$ transition. The $4b_{3u} \rightarrow 2b_{3g}$ transition requires the same vibronic coupling as the $4b_{2g} \rightarrow 2b_{2u}$ transition. The major difference between considering transitions originating from the $4b_{3u}$ orbital and the $4b_{2g}$ orbital is that MO calculations indicate the $4b_{3u}$ transitions require about 2 eV more energy, which probably places them above the 248 nm photon energies.

Thus at 248 nm the specific molecular orbitals corresponding to the product channel $NO_2(^2B_1) + NO_2(^2B_2)$ is most likely from the group $4b_{2g}/4b_{3u} \rightarrow 2b_{2g}/2b_{3g}$. However, there is not enough evidence to decide exclusively on one of the three possible assignments.

4. N_2O_4 Photodissociation Wavelength Comparison

A few points can be made in comparing the photodissociation at the three photolysis wavelengths. The reason why the 193 nm PIF population profile has a lower internal energy peak than the 248 nm profile may be due to the resultant NO_2 electronic states. The fact that the 193 nm photolysis produces NO_2 in the $^2B_2 + {}^2B_2$ state whereas the 248 nm photolysis produces NO_2 in the $^2B_1 + {}^2B_2$ state leads to the 248 nm population having a larger value for most probable internal energy value if the superposition of the NO_2 population in each electronic state is considered. The 351 nm results has a much larger portion of its available energy residing in the internal modes of NO_2. The TOF distributions are reversed of what would be expected: the 248 nm might release less proportional E_{trans} because it is not as high up a repulsive wall as the 193 excitation. This is reasonable due to the energies of the separated fragments.

The internal energy distribution of NO_2 obtained from the PIF deconvolution clearly show a broadening of the width as the photolysis energy increases. This could be due to a statistical contribution such that an increase in the photolysis energy would increase the number of ways the energy can be distributed between internal modes of NO_2 and translation thus broadening the distribution.

Figures 1.32-1.34 depict the comprehensive energy level diagrams for the NO_2 populations for all photolysis wavelengths.

CONCLUSION

The laser photolysis of N_2O_4 and subsequent fluorescence of NO_2 has been studied at three wavelengths: 193, 248, and 351 nm. Upon application of the PIF deconvolution scheme the internal energy distribution of the fluorescent NO_2 was obtained. The peak and spread of the internal energy distribution increased with increasing photolysis energy. The 351 nm photolysis modeled by a prior distribution had the following as the most probable production of excited state NO_2.

$$N_2O_4 + h\nu(351) \rightarrow NO2^*(B^2B_1, v_2 = 3 \text{ to } 4) + NO_2(X^2A_1)$$

The 193 and 248 nm results were compared with Kawasaki's TOF results leading to:

$$N_2O_4 + h\nu\ (248) \rightarrow NO_2^*(^2B_1) + NO_2^*(^2B_2)$$

$$N_2O_4 + h\nu\ (193) \rightarrow NO_2^*(^2B_2) + NO_2^*(^2B_2)$$

The discrete features apparent in the 248 and 351 nm PIF might also come into play spectra are manifestations of a more condensed energy distribution in NO_2 relative to the 193 nm case. Dinitrogen tetroxide PIF should be exploited as means of increasing the body of knowledge of NO_2 spectroscopy.

REFERENCES

[1] M. Kawasaki, K. Kasatani, and H. Sato, Chemical Physics **78**, 65 (1983).

[2] G. Inoue, Y. Nakata, Y. Usui, H. Akimoto, and M. Okuda, J. Chem. Phys. **70**, 3689 (1979).

[3] J. V. Auwera and M. Herman, J. Photochem. **38**,15 (1987).

[4] D.W. Smith and K. Hedberg, J. Chem. Phys. **25** 1282 (1956).

[5] B.W. McClelland, G. Gundersen, and K. Hedberg, J. Chem. Phys. **56**, 4541 (1956).

[6] A. Kvick, R.K. McMullan, and M.D.Newton, J. Chem. Phys. **76** 3754 (1982).

[7] I.C. Hisatsune, J. Phys. Chem., **65**, 2249 (1961).

[8] W.F. Giaque and J.D. Kemp, J. Chem. Phys. **6** 781 (1938). 12.88 kcal/mol

[9] K. Patten, J. Burley, H.S. Johnston accepted for publication J. Phys. Chem.

[10] D.L. Baulch, R.A. Cox, R.F. Hampson,Jr., J.A. Kerr, J. Troe, and R.T. Watson, J. Phys. Chem. Ref. Data, **9**, 467 (1980).

[11] D. Oh, W. Sisk, A. Young, and H.S. Johnston, J. Chem. Phys. **85**, 7146 (1986).

[12] D. OH, Ph.D. Thesis, University of California, Berkeley 1988.

[13] H. Mcleod, G.P. Smith, and D. Golden, J. Geophys. Res. **93**, 3813 (1988).

[14] V.M. Donnelly, D.G. Keil, and F. Kaufman, J. Chem. Phys. **71**, 659 (1979).

[15] C.B. Moore **Chemical and Biochemical Applications of Lasers** (Academic Press, New York, 1977).

[16] D.J. Wren and M. Menzinger, Chemical Physics **66**, 85 (1982).

[17] J. H. Moore, C. Davis, and M. Coplan, **Building Scientific Apparatus** (Addison-Wesley Publishing Company, Inc., New York, 1989), p. 83.

[18] A. Bass, A.E. Ledford, Jr., and A.H. Laufer, J. Res. Natl. Bureau Stands. **80**, 143 (1975).

[19] D.J. Wren, Applied Spectroscopy **34**, 627 (1980).

[20] R. Campargue and A. Lebehot, in **Rarefied Gas Dyn. Proc. Int. Symp. 2**, C11-1 (1974).

[21] J.C. DeVos, Physica, XX, 690 (1954).

[22] ASYST version 2.1, Macmillan Software Co., 1985.

[23] W. Demtröder, R. Duchowicz, J. Gress, H.J. Forth, R. Kullmer, G. Persch, and M. Schwarz, Physica Scripta. **T23**, 176 (1988).

[24] D. Oh, W.N. Sisk, K. Patten, H.S. Johnston manuscript in preparation.

[25] C.H. Chen, D.W. Clark, M.G. Payne, and S.D. Kramer, Optics Communications **32**, 391 (1980).

[26] A. Weaver, R.B. Metz, S.E. Bradforth and D.M. Nuemark, J. Chem. Phys. **90**, 2070 (1989).

[27] E. Zamir and R.D. Levine, Chem. Phys. **52**, 253 (1980)

[28] J.L. Hardwick and J.C.D. Brand **21**, 458 (1973)

[29] J.M. Howell and J.R. Van Wazer, J. Am. Chem. Soc. **96**, 7902 (1974).

[30] G.D. Greenblatt, H. Zuckerman, and Y. Haas, Chem. Physics Letters **134**, 593 (1988).

[31] J.C. Mialocq and J.C. Stephenson, Chem. Phys. **106**, 281 (1986).

[32] J. Mason, J. Chem. Soc. Dalton Trans. I, 19 (1985).

[33] W. von Niessen, W. Domcke, L.S. Cedarbaum, and J. Schirmer, Far. Trans. II **74**, 1550 (1978).

[34] R. Alrichs and F. Keil, J. Am. Chem. Soc. **96** 7615 (1974).

[35] P. Pulay and T.P. Hamilton, J. Chem. Phys. **88** 4926 (1988).

[36] C.W. Bauschlicher, Jr., A. Komornicki, and B. Roos. J. Am. Chem. Soc. **105**, 745 (1983).

[37] S. Kishner, M.A. Whitehead, and M.S. Gopinathan. J. Am. Chem. Soc. **100**, 1365 (1978).

[38] G.E. Busch and K.R. Wilson, J. Chem. Phys., **56**, 3627

(1972).

[39] C.F. Jackels and E.R. Davidson, J. Chem. Phys. **64**, 2908 (1976).

[40] G. Persch, E. Mehdizadeh, W. Demtröder, Th. Zimmermann, H. Köppel, and L.S. Cederbaum, Ber. Bunsenges. Phys. Chem. **92**, 312 (1988).

[41] C.H. Bibart and G.E. Ewing. J. Chem. Phys. **61** 1284 (1974).

[42] R.G. Snyder and I.C. Hisatsune, J. Mol. Spectrosc. **1**, 139 (1957).

Laser Fluence for N_2O_4 PIF

FILENAME	λ (NM)	ENERGY MJ/PULSE	DIMENSIONS CM X CM	FLUENCE MJ/CM^2
WSE98- WSE99-	193	15	.318 X 1.91	25.6
WSE237- WSE238-	248	30	.2 X .55	273.
WSE290-	248	10	.2 X .55	90.9
WSE288- WSE289-	351	7.0	.2 X .55	63.

Table 1.1

Integration Limits X→Z (Equation 1.7→1.8)

X_L Range	X Integration Limit	Z Integration Limit
$D_0 > X_L > D_0 - \Delta X$	$0 , D_0$	$(B-D_0)/(aB)=Z_{LL}, 1/a$
$D_0 - \Delta X > X_L$	$0 , X_L + \Delta X$	$0 = Z_{LL}, 1/a$

Table 1.2

D_0 = The NO_2 disssociation threshold
X_L = The laser exciation energy
X = The observation energy
B = Energy denoting the onset of fluorescence
Z_{LL} = The lower limit of the integration expressed in terms of variable Z

Table 1.3. Gamma Kernel Fitting Parameters for N_2O_4

FILE NAME	SPECIES	λ nm	τ_{ns} DEL	M	n	Y_{max}	SYSTEM RESPON
WSE98A	N_2O_4	193	400	47213	8.675	2.0582E4	WSE 43BD
WSE98B			1500		1.4675E1	2.3715E4	
WSE98C *			400		3.25E1	2.3938E4	
WSE98D			1500		5.675E1	2.5377E4	
WSE98E			400		1.1719E-2	9.4299E1	
WSE98F			1500		1.0E1	2.0816E4	
WSE99A			400		2.8E1	2.4115E4	
WSE99B			1500		3.35E1	2.4982E4	
WSE237A *		248	400	35723	2.0275E2	1.2938E4	WSE219 AV.SYS
WSE237B			1500		5.875E1	1.3002E4	
WSE237C *			400		2.2075E2	1.285E4	
WSE237D *			1500		9.575E1	1.294E4	
WSE290A			400		3.100E1	1.365E4	WSF3AV SYS
WSE290B			1500		2.3375E1	1.3773E4	
WSE290C			400		4.375	9.1445E3	
WSE290D			1500		6.625	1.1457E4	
WSE290E			400		4.375E1	1.3541E4	

FILE NAME	SPECIES	λ nm	τ_{ns} DEL	M	n	Y_{max}	SYSTEM RESPON
WSE290F			1500		3.625E1	1.3771E4	
WSE288A	N_2O_4	351	400	23890	1.975E1	4.6426EE3	WSF3AVSYS
WSE288B			1500		8.9375	4.6426E3	
WSE288C			400		1.2563E1	4.5283E3	
WSE288D			1500		5.0938	4.5342E3	
WSE288G			400		2.275E1	4.7031E3	
WSE288H			1500		1.0063E1	4.7959E3	

Table 1.3

Table 1.4. Population Statistics for N_2O_4 Gamma Kernel Fits

FILE NAME	SPECIES	λ nm	τ_{ns} DEL	MEAN	MOST PROB	RMS	σ
WSE98A	N_2O_4	193	400	1.8545E4	2.5107E4	1.8894E4	3.6152E3
WSE98B			1500	1.8394E4	2.2819E4	1.8730E4	3.5366E3
WSE98C *			400	1.9703E4	2.3171E4	1.9974E4	3.2740E3
WSE98D			1500	1.9844E4	2.1904E4	2.0068E4	2.9910E3
WSE98E			400	1.8620E4	2.5107E4	1.8988E4	3.7219E3
WSE98F			1500	1.8709E4	2.5107E4	1.9053E4	3.6038E3
WSE99A			400	1.9294E4	2.2906E4	1.9587E4	3.3719E3
WSE99B			1500	1.9138E4	2.2146E4	1.9424E4	3.3203E3
WSE237B		248	1500	2.2321E4	2.3081E4	2.2380E4	1.6182E3
WSE290A			400	2.0930E4	2.2310E4	2.1071E4	2.4343E3
WSE290B			1500	2.0303E4	2.2146E4	2.0494E4	2.7883E3
WSE290C			400	1.9808E4	2.5107E4	2.0115E4	3.4976E3
WSE290D			1500	1.9376E4	2.4100E4	1.9685E4	3.4730E3
WSE290E			400	2.1515E4	2.2477E4	2.1610E4	2.0253E3
WSE290F			1500	2.1041E4	2.2228E4	2.1165E4	2.2900E3
WSE288A	N_2O_4	351	400	1.9183E4	1.9551E4	1.9218E4	1.1609E3
WSE288B			1500	1.8741E4	1.9551E4	1.8824E4	1.7711E3
WSE288C			400	1.9149E4	1.9680E4	1.9203E4	1.4316E3

FILE NAME	SPECIES	λ nm	τ_{ns} DEL	MEAN	MOST PROB	RMS	σ
WSE288D			1500	1.8284E4	1.9616E4	1.8423E4	2.2583E3
WSE288G			400	1.9239E4	1.9551E4	1.9269E4	1.0777E3
WSE288H			1500	1.8652E4	1.9425E4	1.8731E4	1.7113E3

Table 1.5.
Electronic Origins and Vibrational Frequencies for NO_2

STATE	ORGIN	ω_1	ω_2	ω_3
$^2A_1$	0	1320	750	1617
$^2B_2$	9710^a	1461	739	1225_b
$^2B_1$	14748_b	1192	960	1277^c
$^2A_2$	16293_a	1360	798	1350^c

* All energy entries are in units of wavenumbers

References:

Unless otherwise specified the energy values are obtained from:

W.L. Lafferty and R.L. Sams J. Mol. Spectrosc. 66, 478 (1977)

a This value obtained from:

A. Weaver, R.B. Metz, S.E. Bradforth and D.M. Neumark, J. Chem. Phys. 90, 2070 (1989)

b This value obtained from:

K.K. Innes, J. Mol. Spectrosc. 96, 331 (1982)

c This value obtained from: ω_3 estimated from

$[(\omega_1\omega_2\omega_3)_{2A1}+(\omega_1\omega_2\omega_3)_{2B2}]$ / $[2(\omega_1\omega_2)_{[2B1 \text{ or } 2A1]}]$

Table 1.6
Time of Flight Energy Terms for N_2O_4 Photolysis

	193.3 nm	248.5 nm	351 nm
hν	51733	40240	28490
E_I	890	890	890
D_0	4600	4600	4600
E_{aval} $(h\nu+E_I-D_0)$	48023	36530	24780
$E_{trans(max)}$	26164	10867	
$E_{trans(peak)}$	3510	4180	
$E_{int(min)}$ $(E_{aval}-E_{trans(max)})$	21859	25663	
$E_{int(peak)}$ $(E_{aval}-E_{trans(peak)})$	44513	32350	
$E_{trans(max)}/E_{aval}$ %	54.4	29.7	
$E_{trans(peak)}/E_{aval}$ %	7.3	11.4	
$h\nu - 4600 = E'$	47133	35640	23890
$E' - E_{trans(max)}$	20969	24773	
$E' - 4200$		31440	
$E_{trans(max)} / E'$ %	55.51	30.49	

Figure 1.1

The planar D_{2h} structure of N_2O_4.

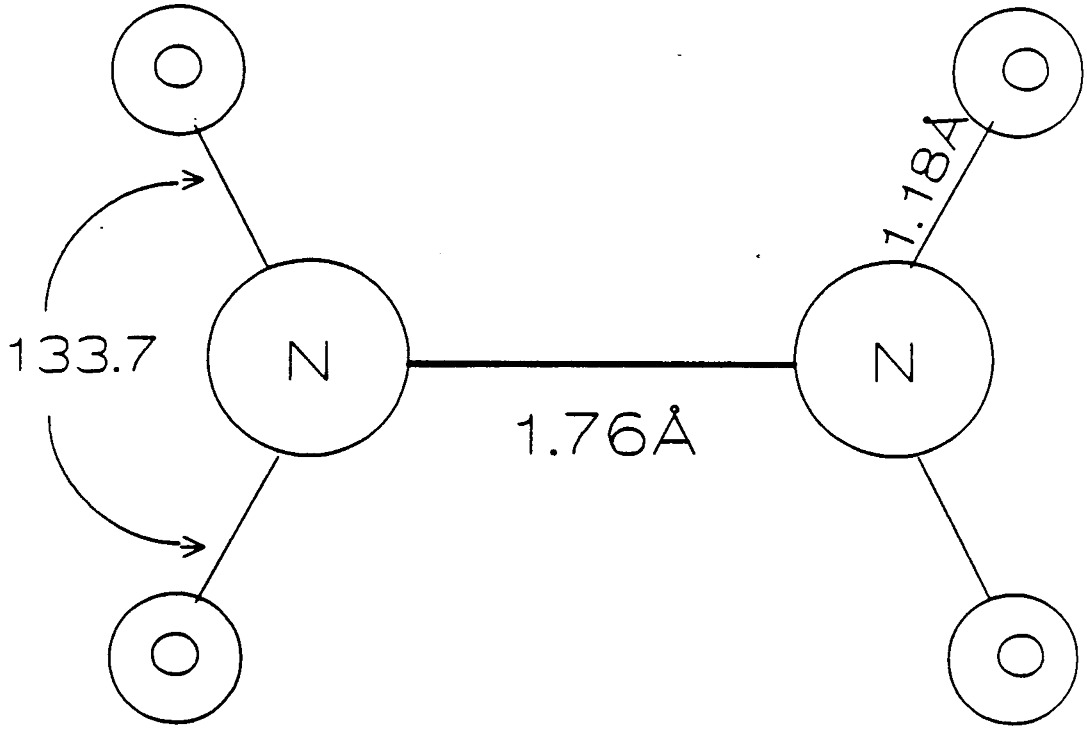

Figure 1.1

Figure 1.2

The absorption cross sections of NO_2 and N_2O_4 adapted from Ref. 18.

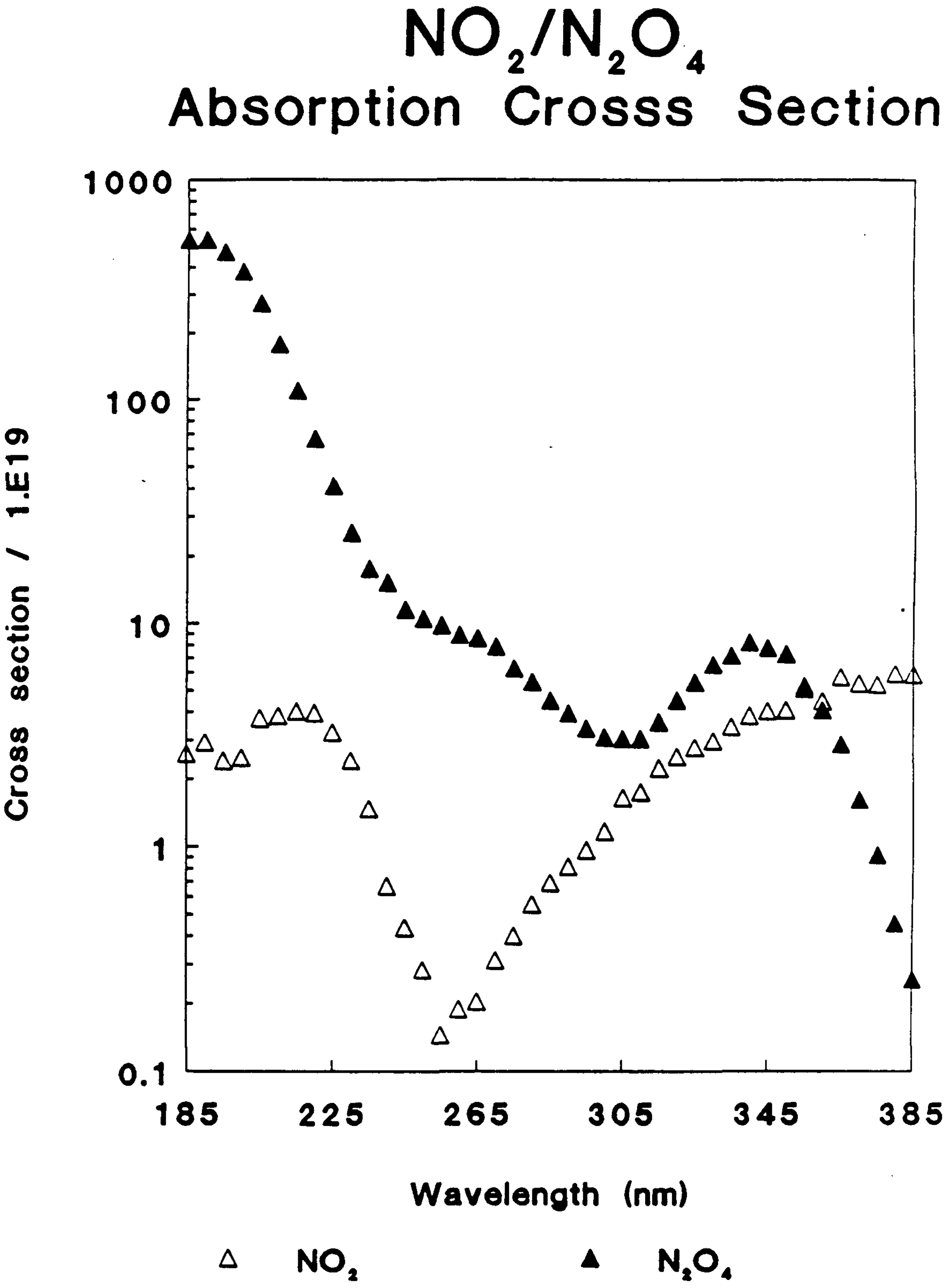
NO_2/N_2O_4
Absorption Crosss Section
Cross section / 1.E19
1000
100
10
1
0.1
185
225
265
305
345
385
Wavelength (nm)
△ NO_2
▲ N_2O_4

Figure 1.2

Figure 1.3

Schematic experimental arrangement for N_2O_4 PIF in a supersonic jet.

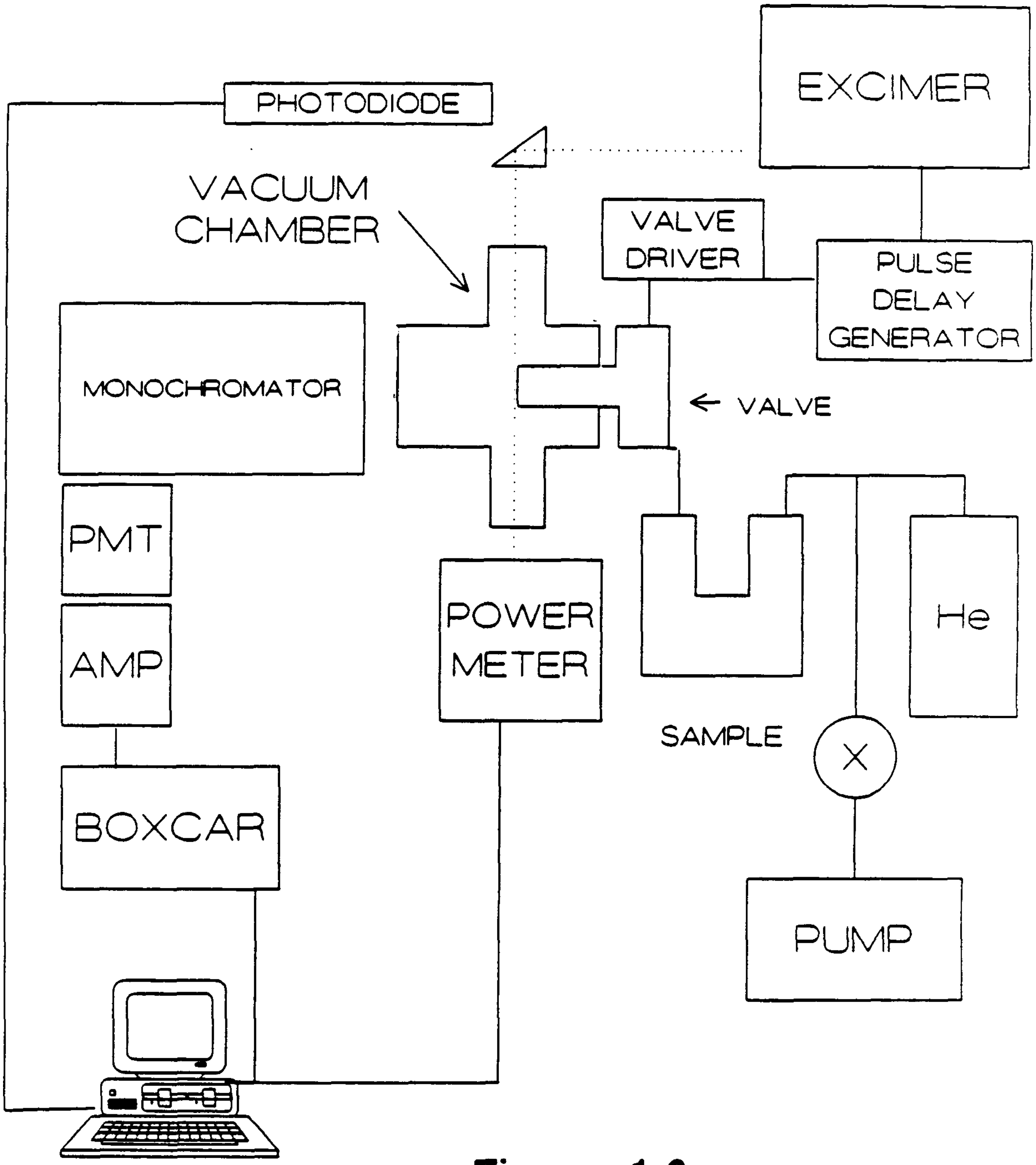
PHOTODIODE
EXCIMER
VACUUM CHAMBER
VALVE DRIVER
PULSE DELAY GENERATOR
MONOCHROMATOR
VALVE
PMT
AMP
POWER METER
He
SAMPLE
BOXCAR
PUMP

Figure 1.3

Figure 1.4

Expanded view of the molecular beam chamber utilized in the N_2O_4 PIF experiments

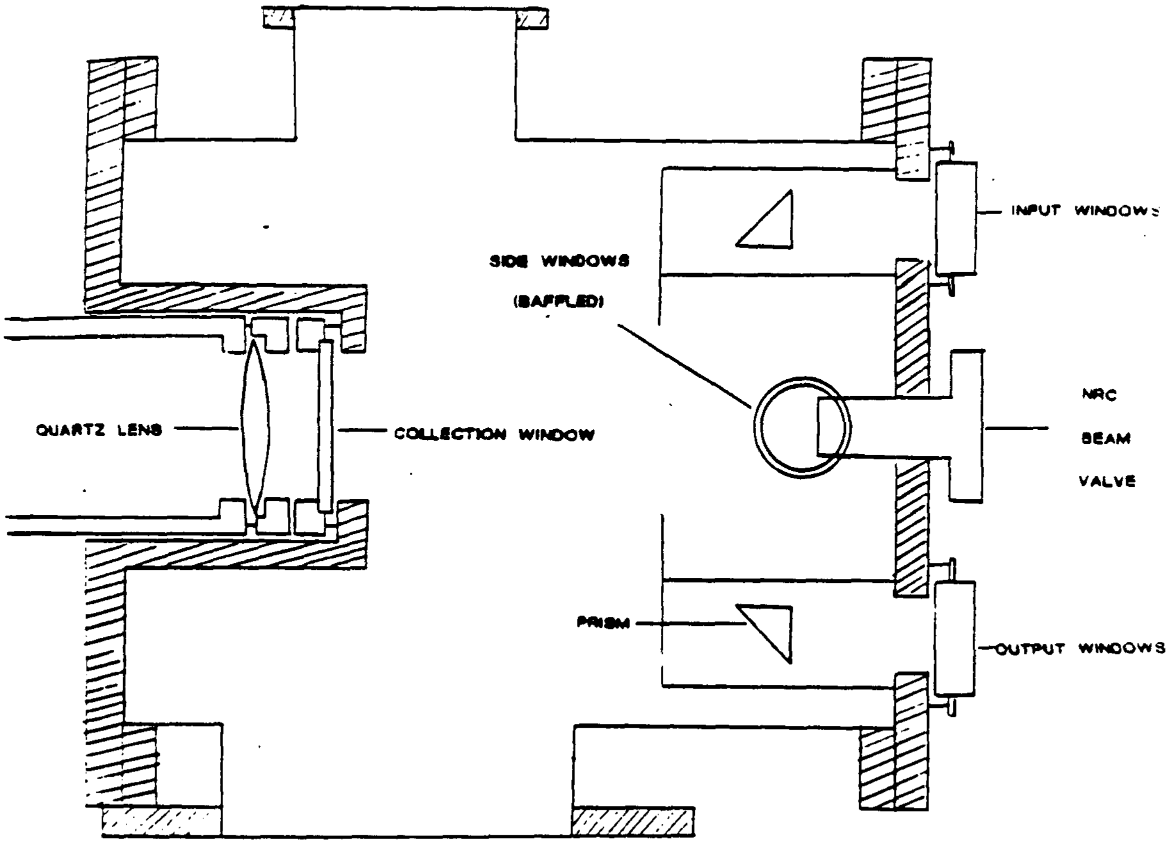
INPUT WINDOWS
SIDE WINDOWS
(BAFFLED)
NRC
BEAM
VALVE
QUARTZ LENS
COLLECTION WINDOW
PRISM
OUTPUT WINDOWS

Figure 1.4

Figure 1.5

Fluorescence of windows at 400 ns delay.

Figure 1.6

Fluorescence of windows at 1500 ns delay.

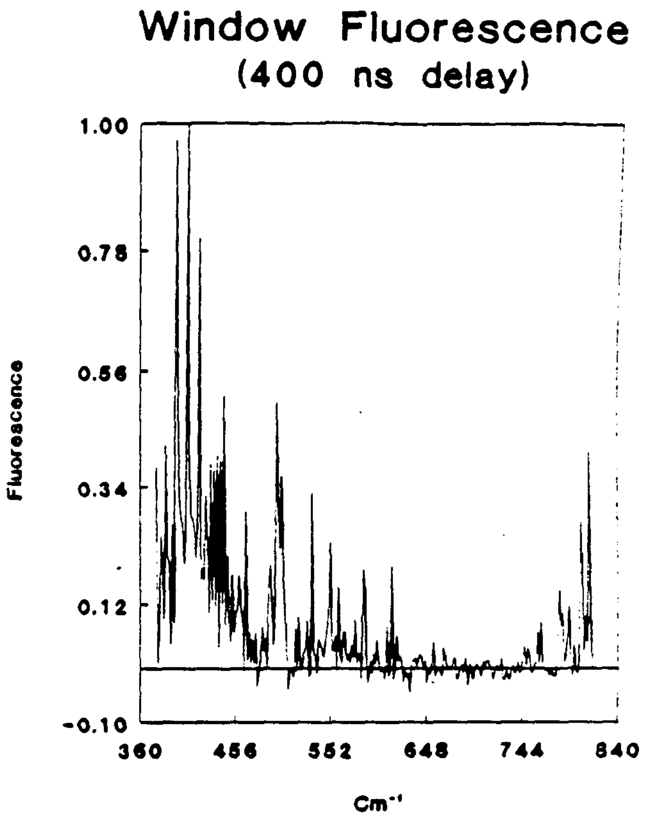

Figure 1.5

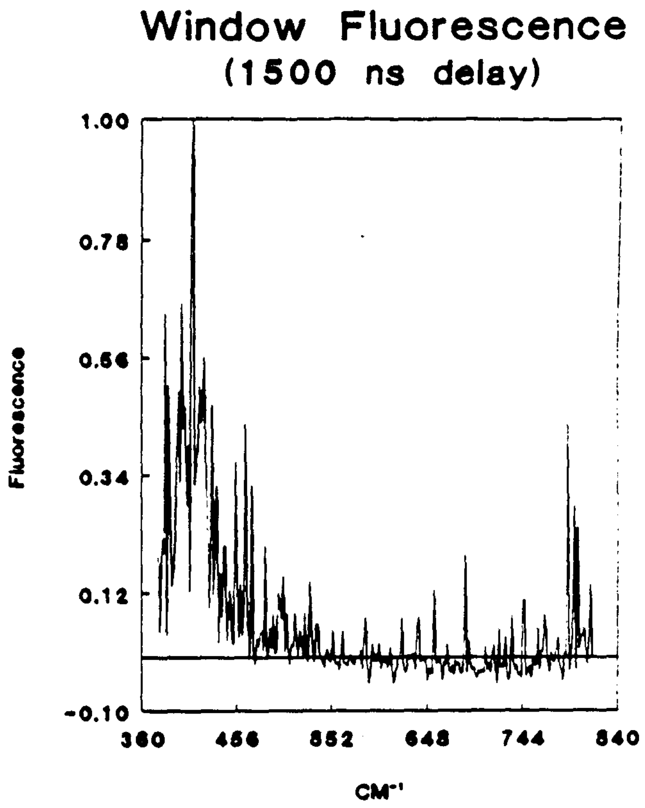

Figure 1.6

Figure 1.7

Nascent laser induced fluorescence spectrum of NO_2 at 298 K excited at 449.9 nm.

Figure 1.8

Running sum of the 449.9 nm LIF spectrum (solid curve) fitted by the running sum function I (dotted curve).

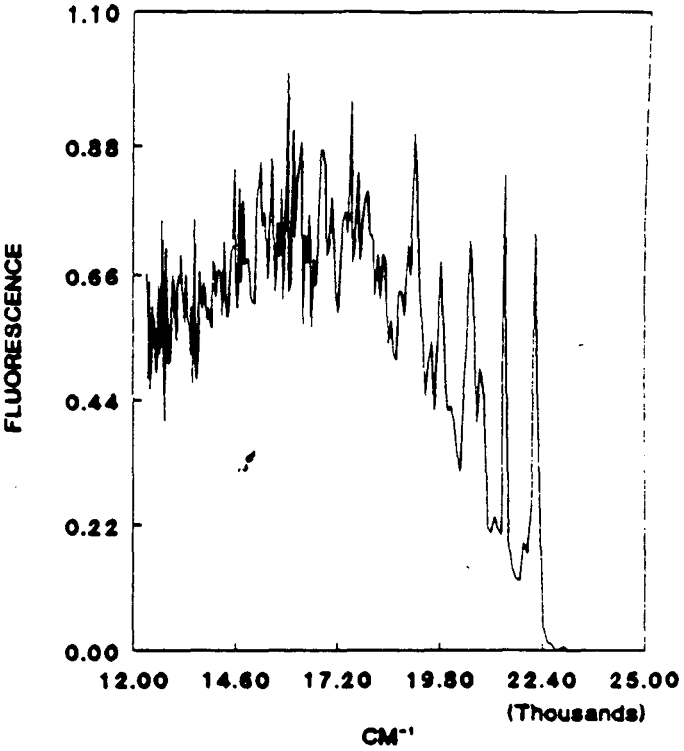

NO$_2$ 449.9 nm LIF

Figure 1.7

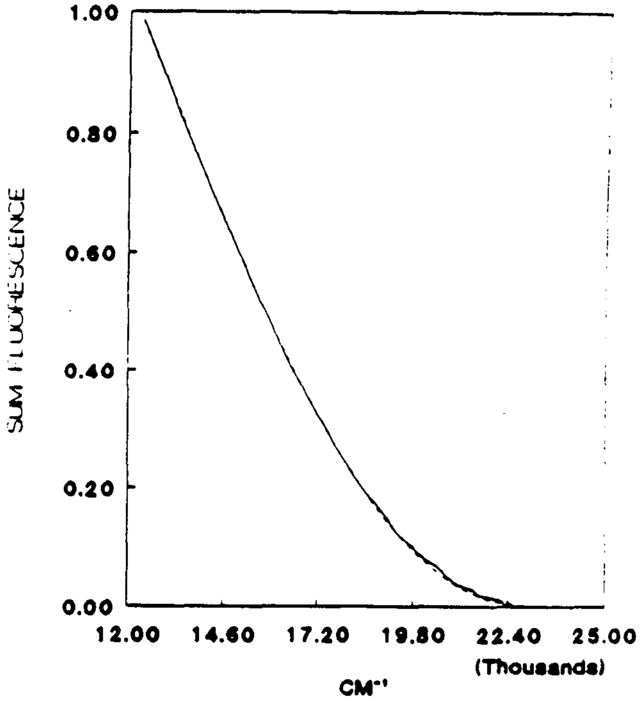

(Fit to Sum)

Figure 1.8

Figure 1.9

PIF spectra of the N_2O_4 at 193 nm excitation.

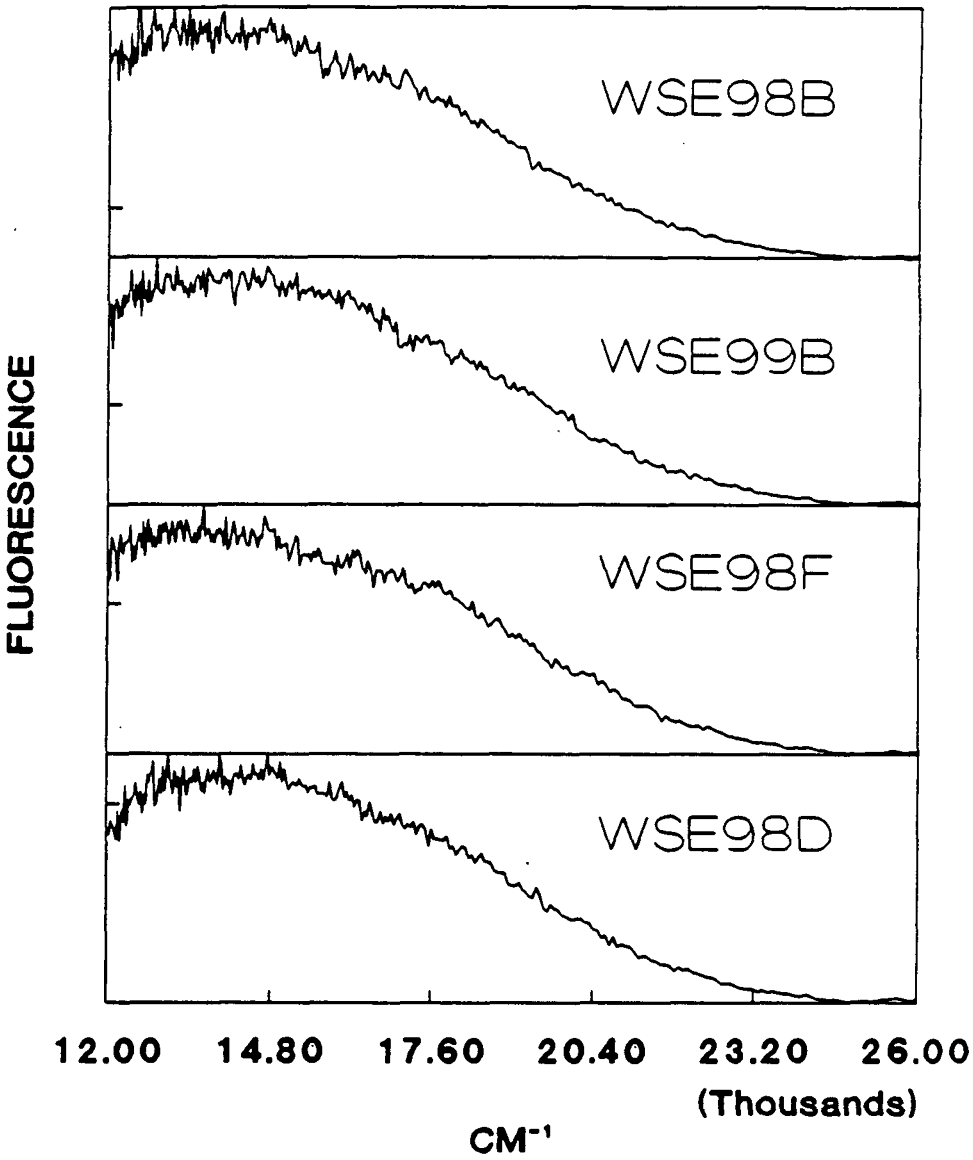

FLUORESCENCE PROFILES

193 NM

Figure 1.9

Figure 1.10

PIF spectra of N_2O_4 at 248 nm excitation.

FLUORESCENCE PROFILES

248 NM

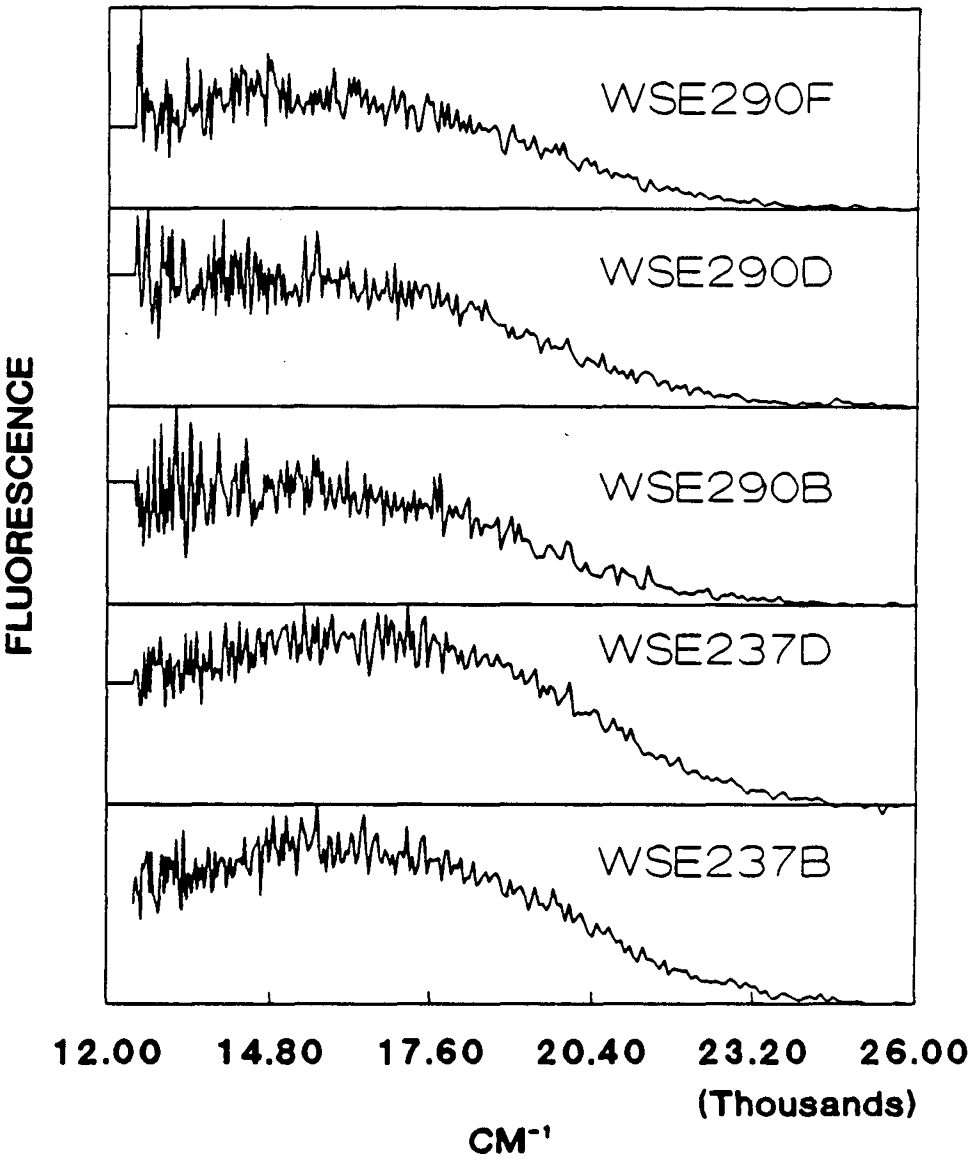

Figure 1.10

Figure 1.11

PIF spectra of N_2O_4 at 351 nm excitation.

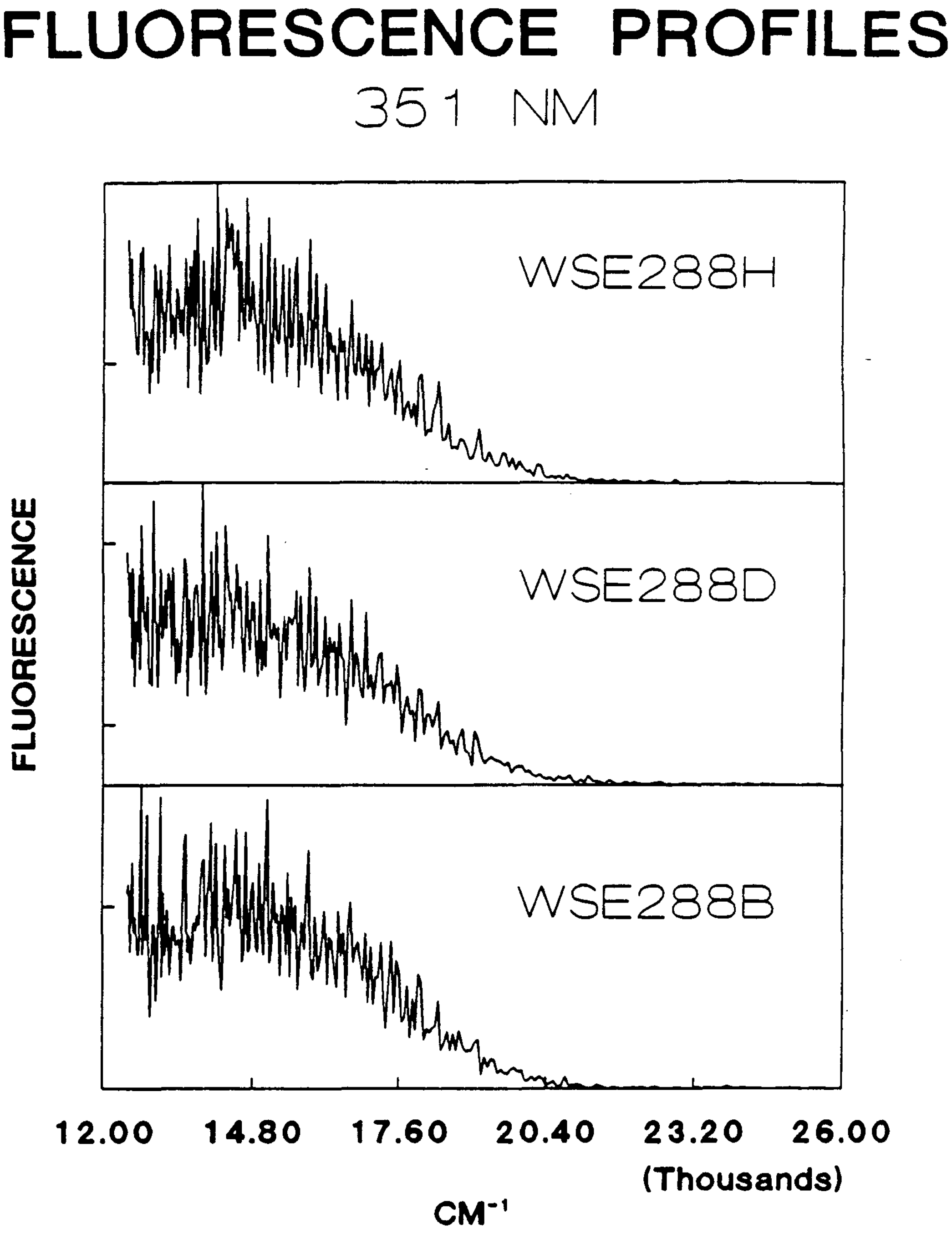
FLUORESCENCE PROFILES
351 NM
WSE288H
WSE288D
WSE288B
FLUORESCENCE
12.00
14.80
17.60
20.40
23.20
26.00
(Thousands)
CM-1

Figure 1.11

Figure 1.12

Cumulative sum, **ΣP**, fit (dotted curve), to the cumulative sum of the N_2O_4 193 nm PIF data (solid curve).

Figure 1.13

N_2O_4 193 nm spectrum plotted against **P(X)**.

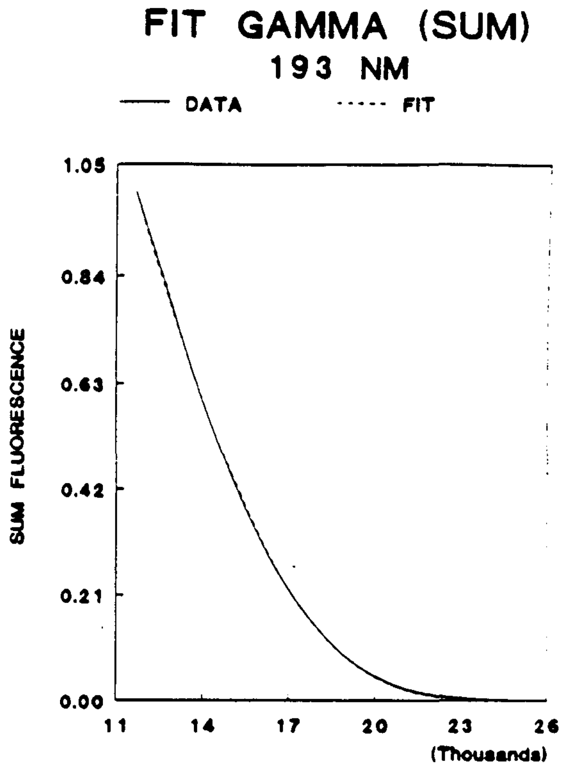

Figure 1.12

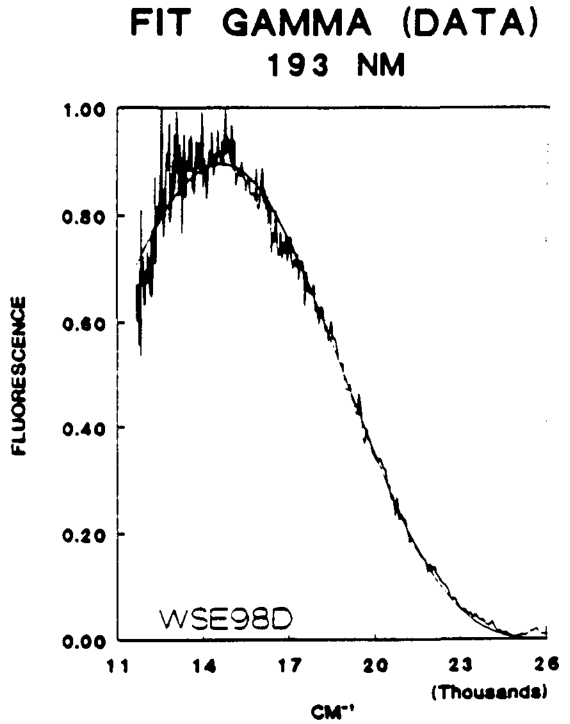

Figure 1.13

Figure 1.14

Cumulative sum, **ΣP**, fit (dotted curve), to the cumulative sum of the N_2O_4 248 nm PIF data (solid curve).

Figure 1.15

N_2O_4 248 nm spectrum plotted against **P(X)**.

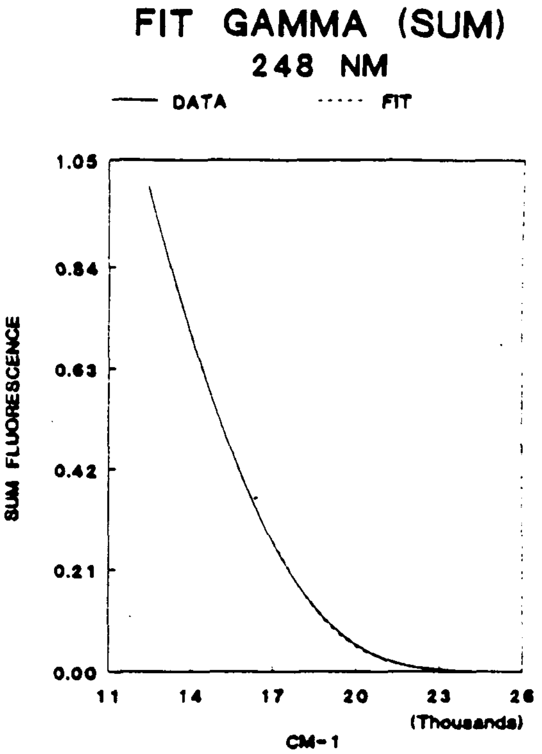

Figure 1.14

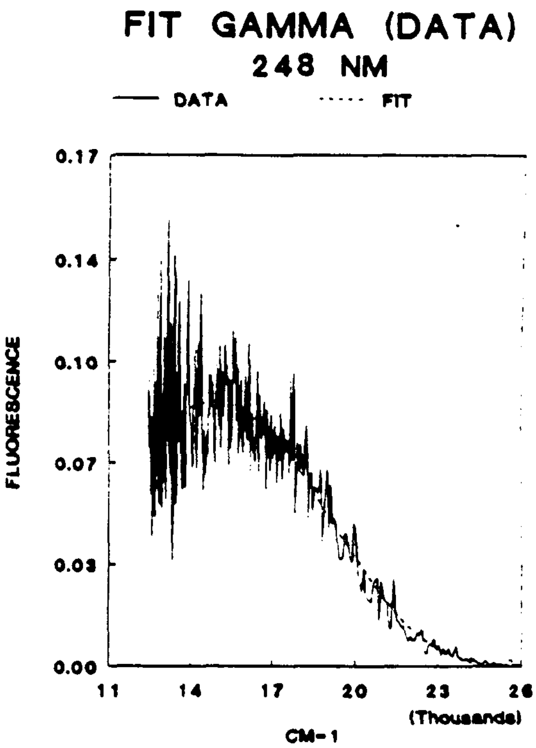

Figure 1.15

Figure 1.16

Cumulative sum, **ΣP**, fit (dotted curve), to the cumulative sum of the N_2O_4 351 nm PIF data (solid curve).

Figure 1.17

N_2O_4 351 nm spectrum plotted against **P(X)**.

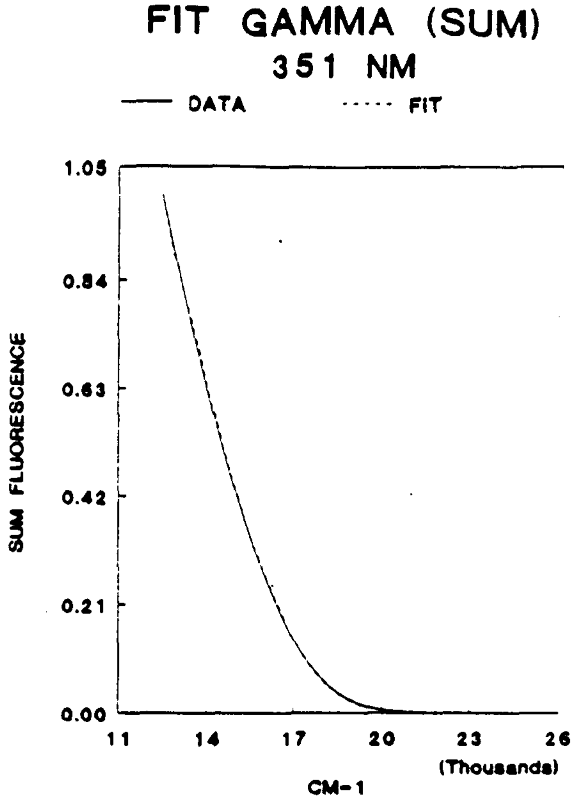

Figure 1.16

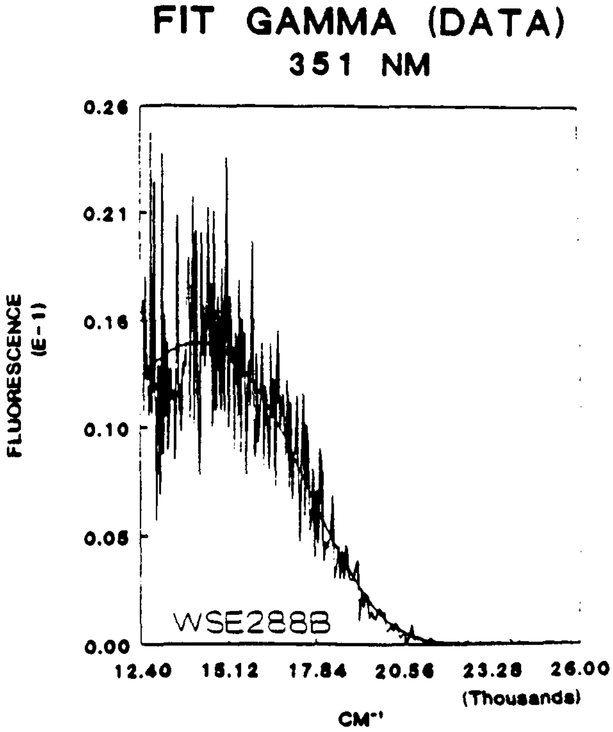

Figure 1.17

Figure 1.18

NO_2 internal energy distribution for 193 nm N_2O_4 PIF computed from Equation 1.9 utilizing the Gamma Kernel function, Equation 1.10.

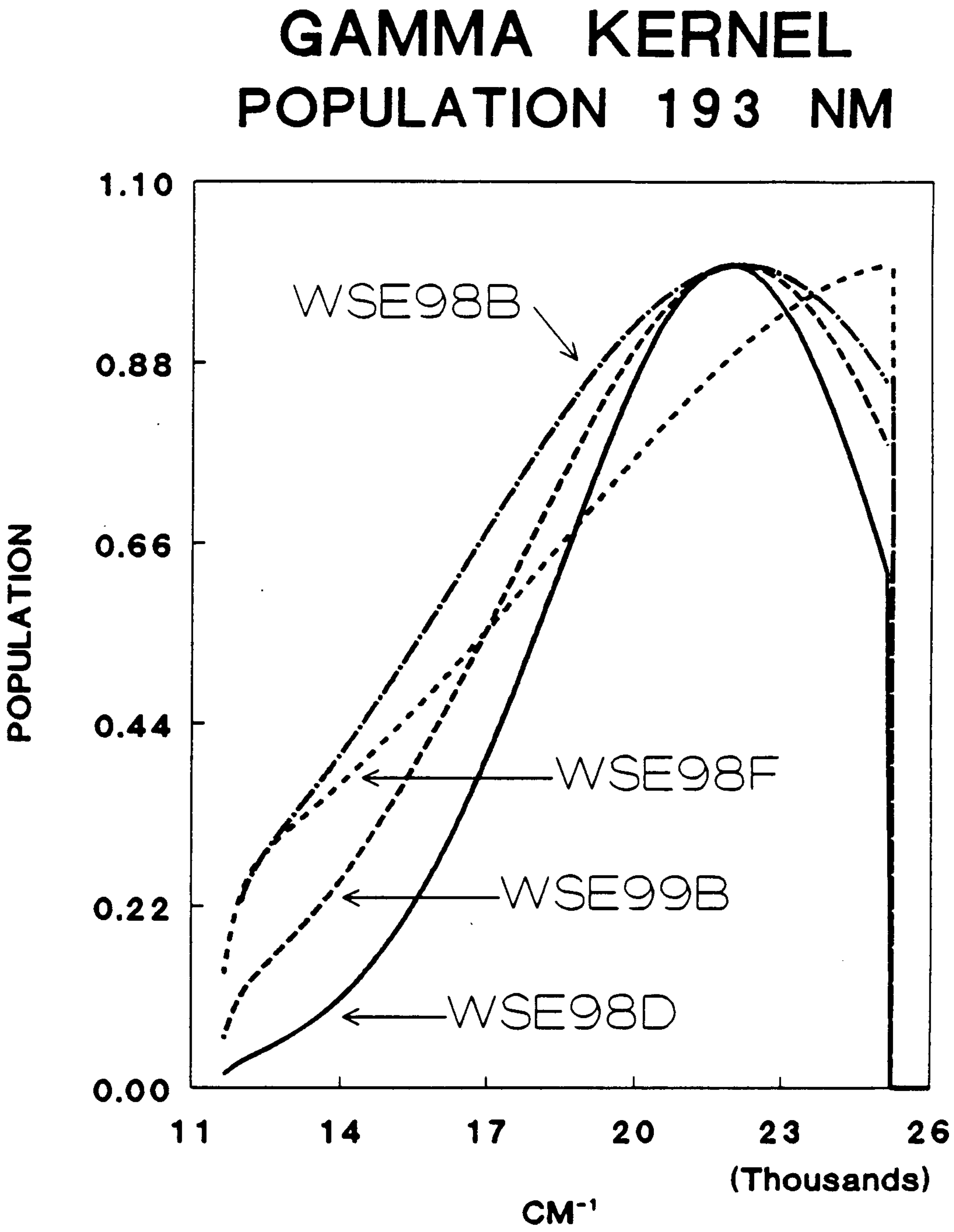
GAMMA KERNEL
POPULATION 193 NM
POPULATION
1.10
0.88
0.66
0.44
0.22
0.00
11
14
17
20
23
26
(Thousands)
CM⁻¹
WSE98B
WSE98F
WSE99B
WSE98D

Figure 1.18

Figure 1.19

NO_2 internal energy distribution for 248 nm N_2O_4 PIF computed from Equation 1.9 utilizing the Gamma Kernel function, Equation 1.10.

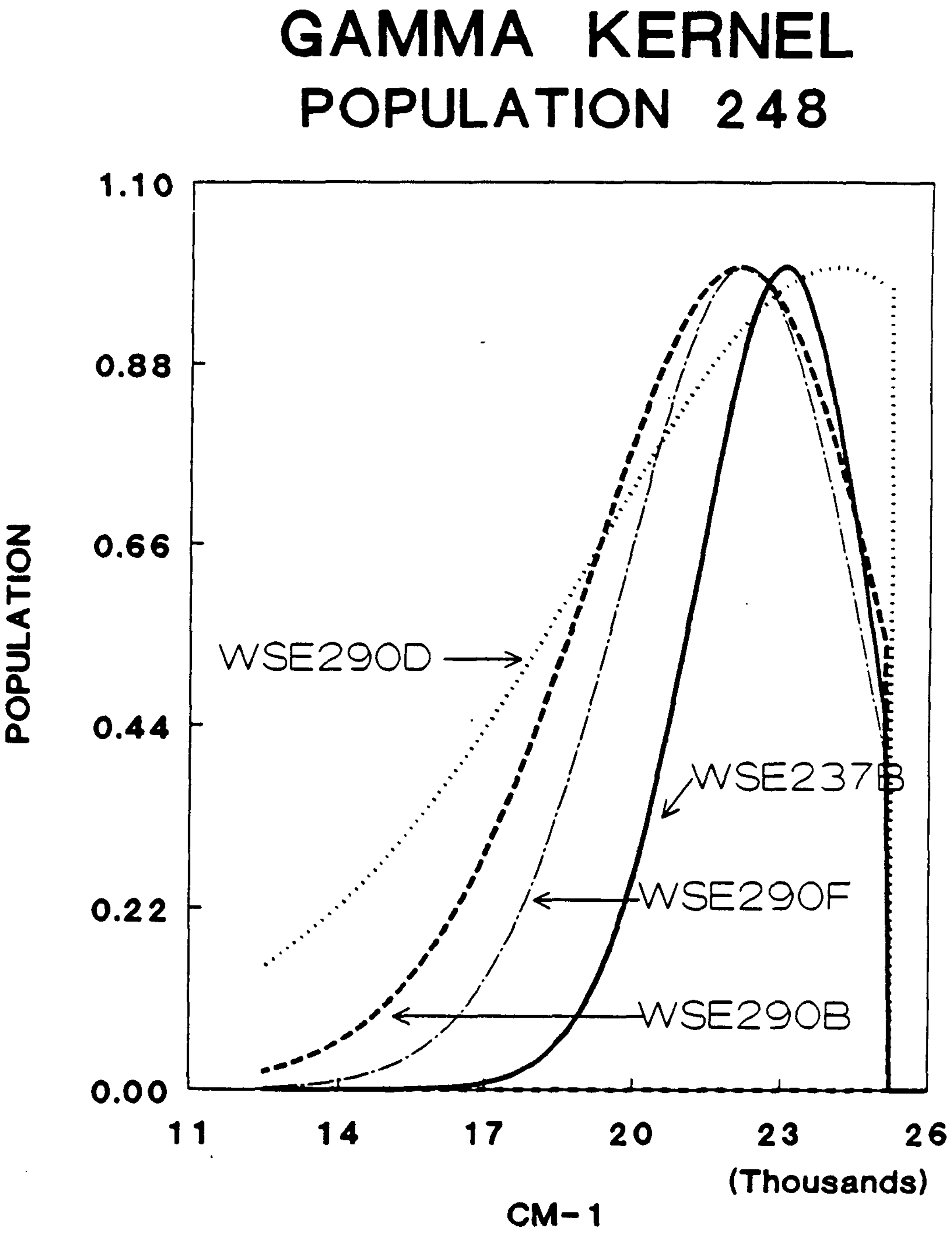
GAMMA KERNEL
POPULATION 248
POPULATION
1.10
0.88
0.66
0.44
0.22
0.00
11
14
17
20
23
26
(Thousands)
CM-1
WSE290D
WSE237B
WSE290F
WSE290B

Figure 1.19

Figure 1.20

NO_2 internal energy distribution for 351 nm N_2O_4 PIF computed from Equation 1.9 utilizing the Gamma Kernel function, Equation 1.10.

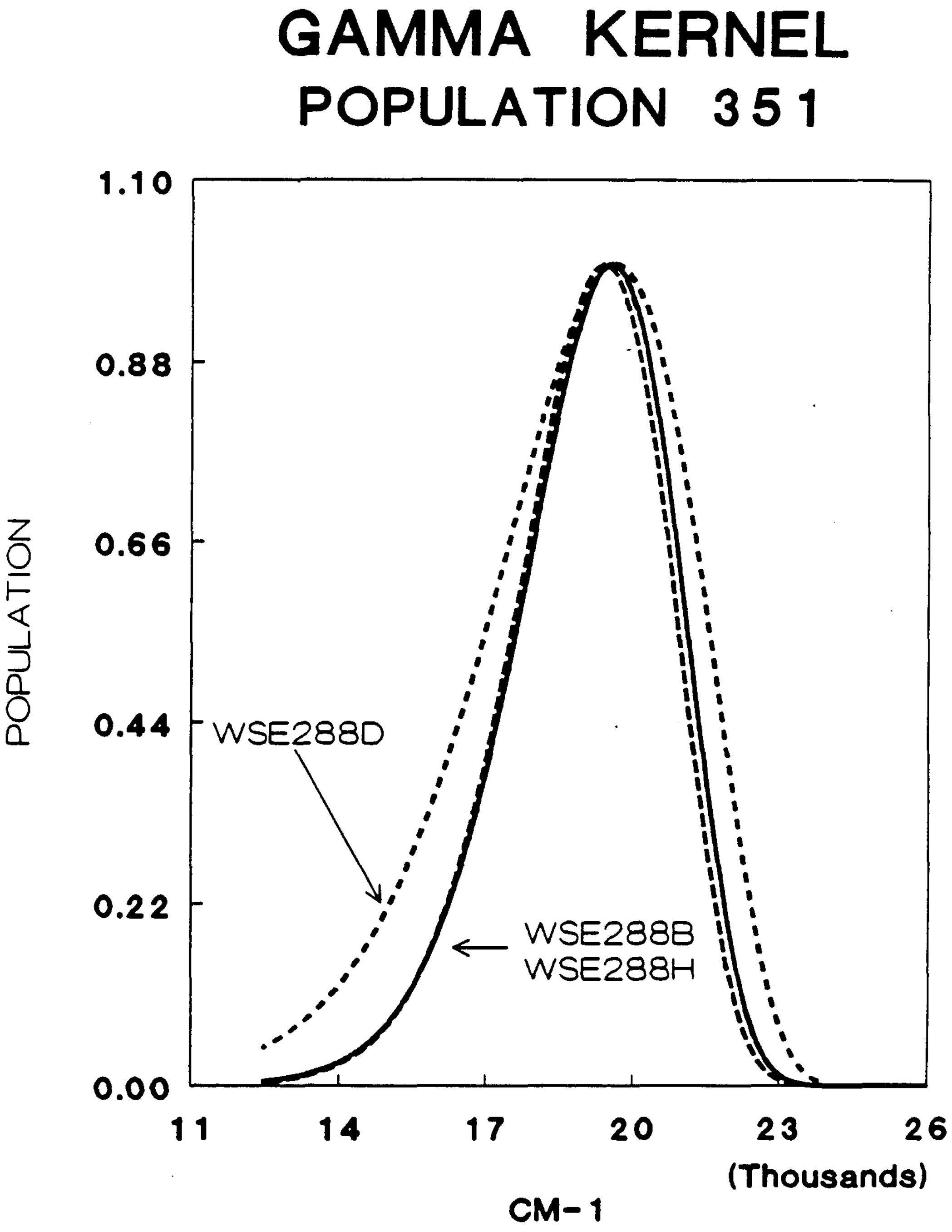
GAMMA KERNEL
POPULATION 351
POPULATION
1.10
0.88
0.66
0.44
0.22
0.00
11
14
17
20
23
26
(Thousands)
CM-1
WSE288D
WSE288B
WSE288H

Figure 1.20

Figure 1.21

Comparison of the **P(X)** for the 193 nm N_2O_4 PIF utilizing the Gamma Kernel function (Equation 1.10) and the Gaussian function (Equation 1.12).

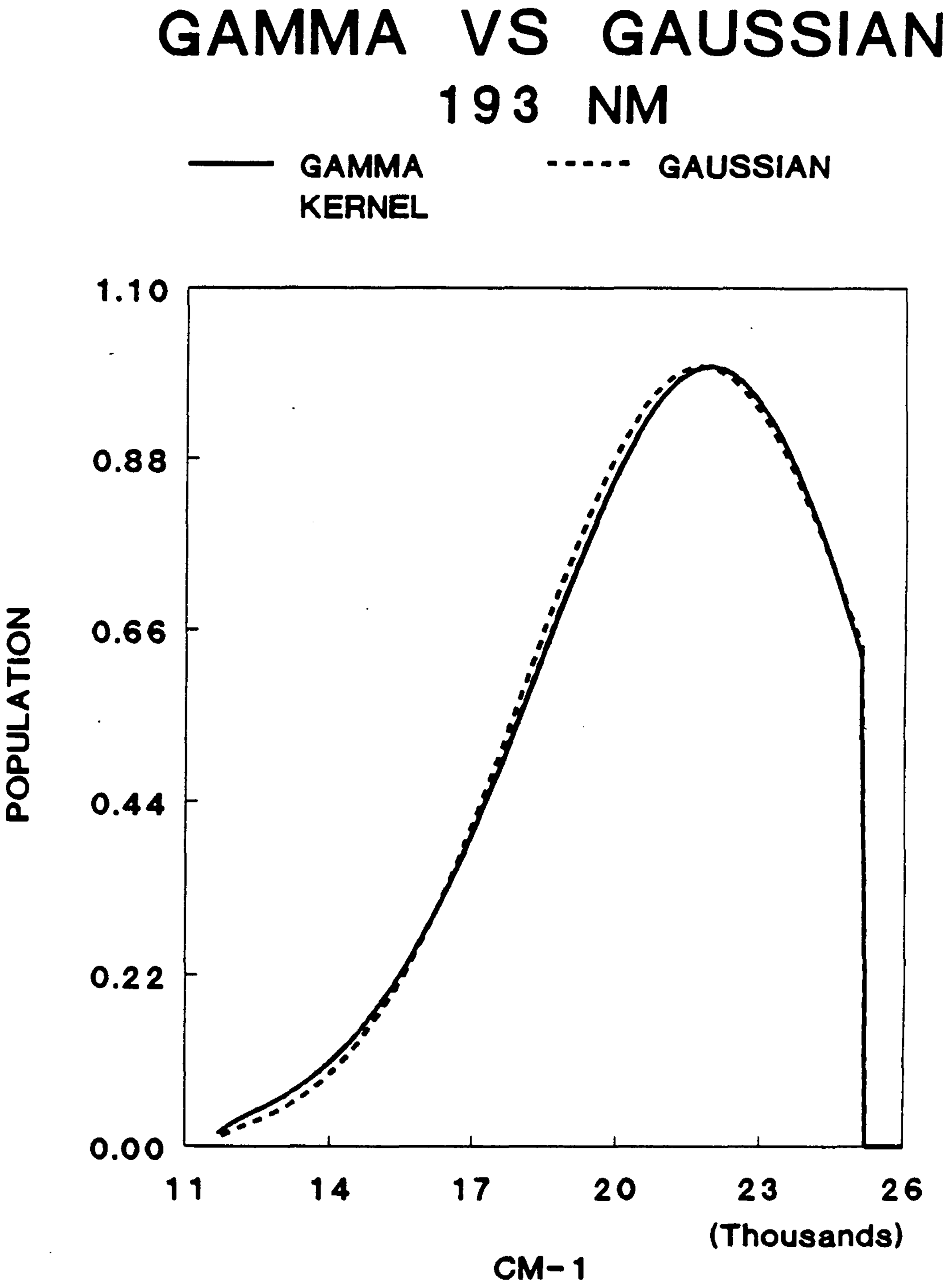
GAMMA VS GAUSSIAN
193 NM
GAMMA KERNEL
GAUSSIAN
POPULATION
1.10
0.88
0.66
0.44
0.22
0.00
11
14
17
20
23
26
(Thousands)
CM-1

Figure 1.21

Figure 1.22

Comparison of the **P(X)** for the 248 nm N_2O_4 PIF utilizing the Gamma Kernel function (Equation 1.10) and the Gaussian function (Equation 1.12).

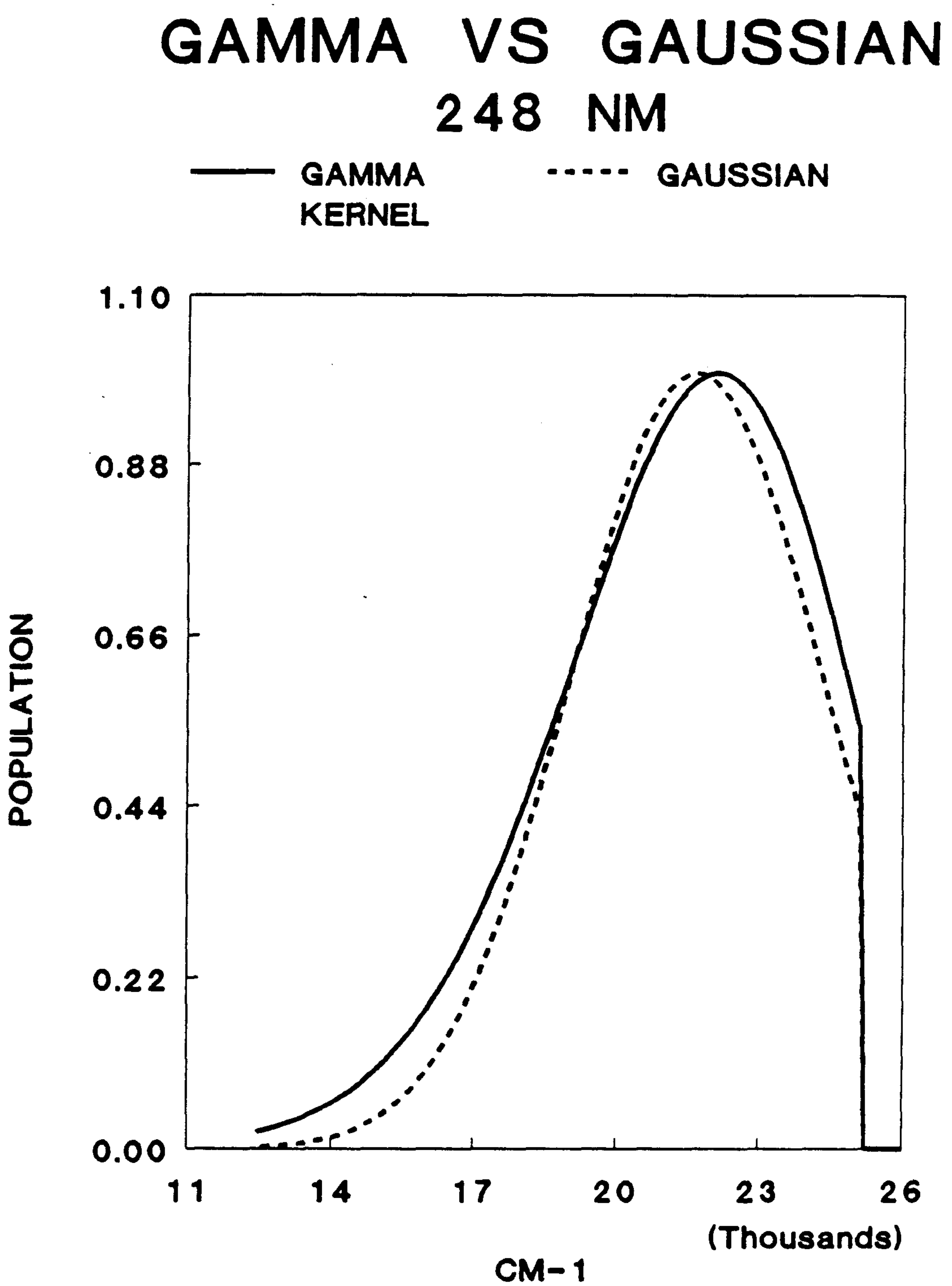
GAMMA VS GAUSSIAN
248 NM
GAMMA KERNEL
GAUSSIAN
POPULATION
1.10
0.88
0.66
0.44
0.22
0.00
11
14
17
20
23
26
(Thousands)
CM-1

Figure 1.22

Figure 1.23

Comparison of the P(X) for the 351 nm N_2O_4 PIF utilizing the Gamma Kernel function (Equation 1.10) and the Gaussian function (Equation 1.12).

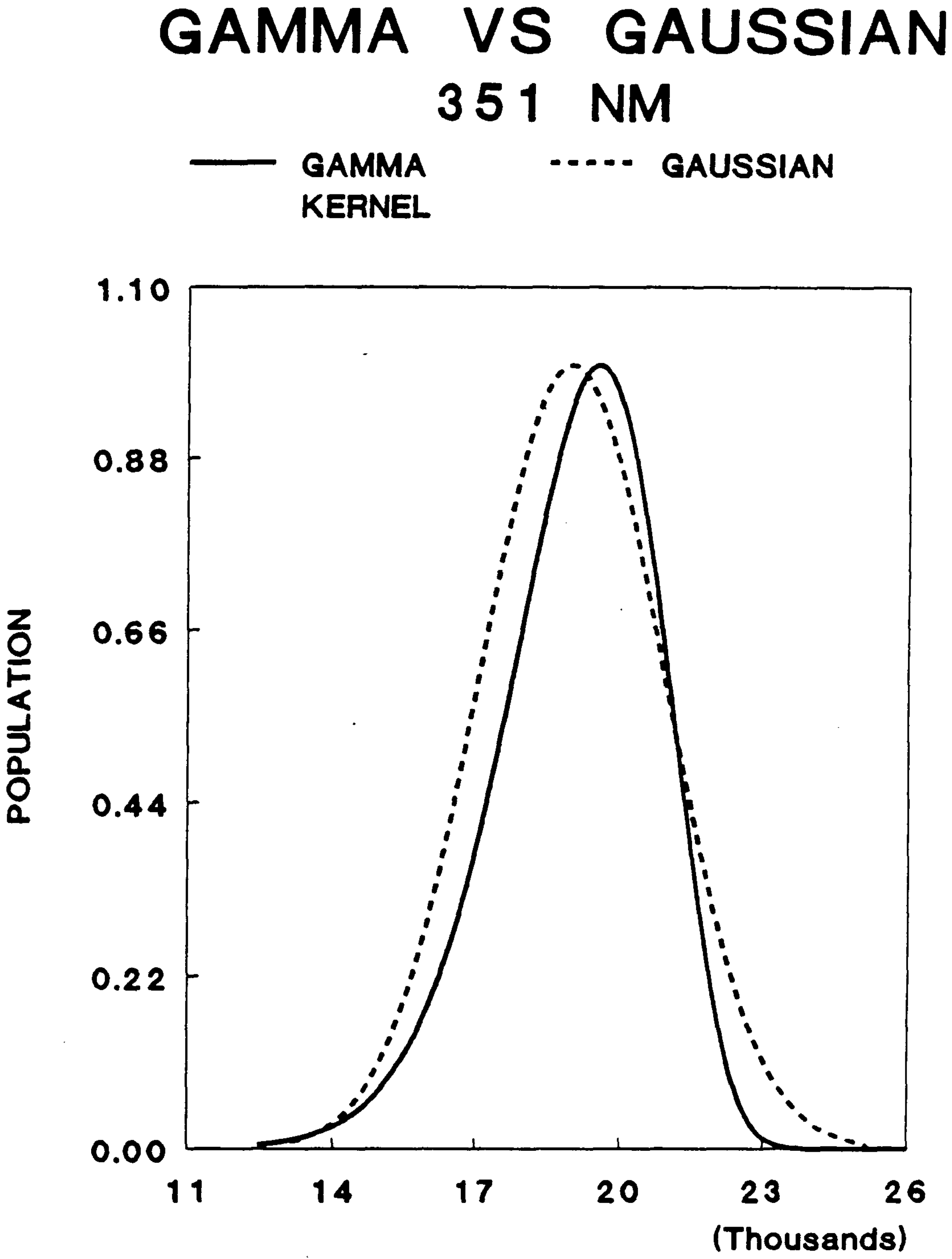
GAMMA VS GAUSSIAN
351 NM
GAMMA KERNEL
GAUSSIAN
POPULATION
1.10
0.88
0.66
0.44
0.22
0.00
11
14
17
20
23
26
(Thousands)
CM-1

Figure 1.23

Figure 1.24

The NO_2 internal energy distribution from 351 nm PIF plotted against the prior distribution results assuming $^2B_2$, $^2B_2$, or $^2A_2$ electronic excited states. These prior results are computed from equation 1.16.

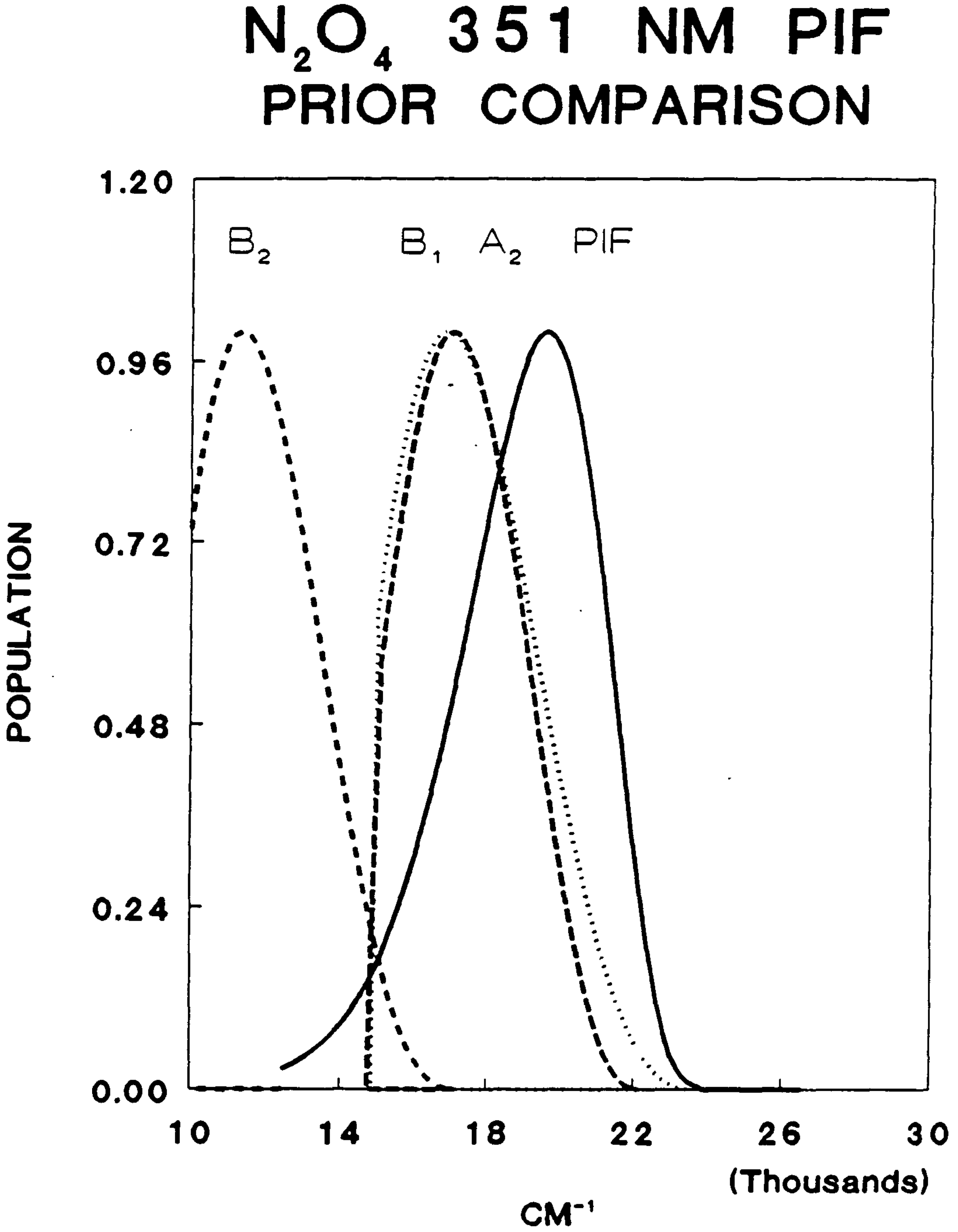
N_2O_4 351 NM PIF
PRIOR COMPARISON
B_2
B_1
A_2
PIF
POPULATION
1.20
0.96
0.72
0.48
0.24
0.00
10
14
18
22
26
30
(Thousands)
CM^{-1}

Figure 1.24

Figure 1.25

The NO_2 internal energy distribution from 351 nm PIF plotted against various prior distribution curves assuming the NO_2 electronic state is $^2B_1$ and the amount of bending quanta is v_2 (v_2 = 2 , 3, 4, 5, or 6).

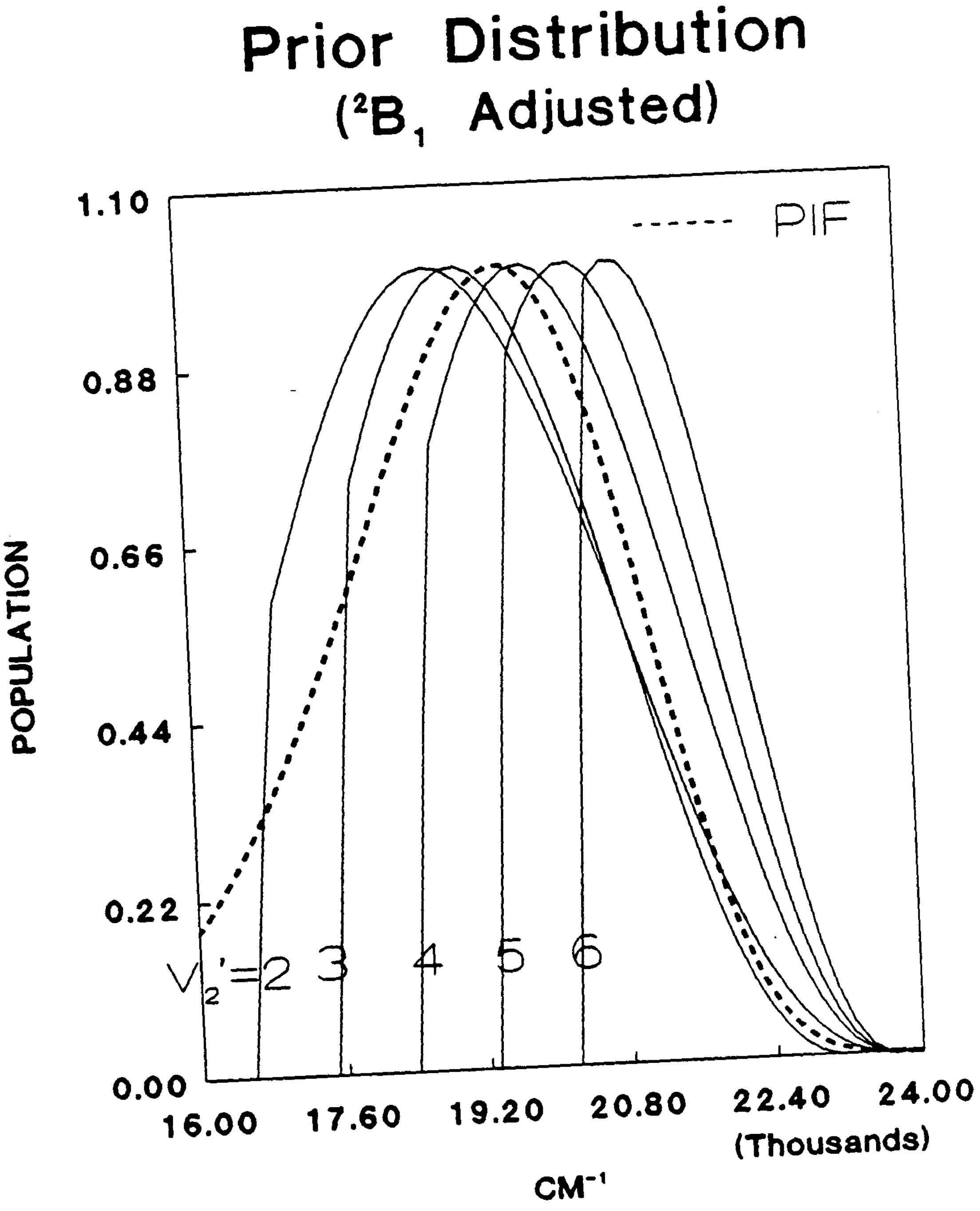
Prior Distribution
($^2B_1$ Adjusted)
PIF
POPULATION
1.10
0.88
0.66
0.44
0.22
0.00
$V_2'=2$
3
4
5
6
16.00
17.60
19.20
20.80
22.40
24.00
(Thousands)
CM^{-1}

Figure 1.25

Figure 1.26

NO_2 translational energy distribution from Kawasaki (Ref. 1, solid curve) plotted against the translational energy derived from N_2O_4 193 nm PIF utilizing Equation 1.17 (dotted/dashed curves), on the assumption that both $NO_2(\alpha)$ and $NO_2(\beta)$ have equivalent internal energy distributions. The agreement between the calculated and observed translational energies confirms the postulate of equal internal energy distribution in the two NO_2 molecules produced by the photolysis of N_2O_4 at 193 nm.

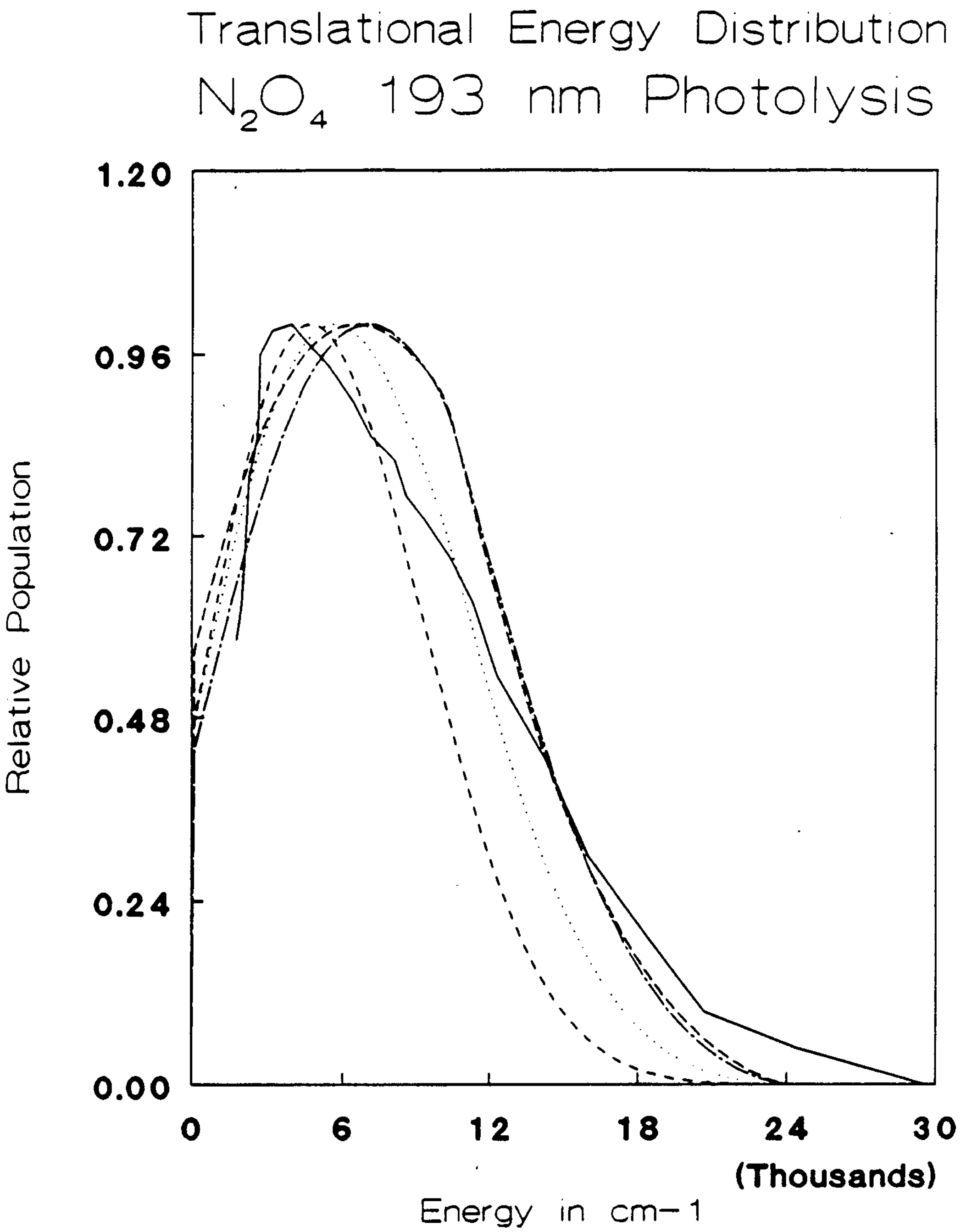
Translational Energy Distribution
N_2O_4 193 nm Photolysis
1.20
0.96
0.72
0.48
0.24
0.00
Relative Population
0
6
12
18
24
30
(Thousands)
Energy in cm-1

Figure 1.26

Figure 1.27

NO_2 translational energy distribution from Kawasaki (Ref. 1, solid curve) plotted against the translational energy derived from N_2O_4 248 nm PIF utilizing Equation 1.17, on the assumption that both $NO_2(\alpha)$ and $NO_2(\beta)$ have equivalent internal energy distributions. The disagreement between the calculated and observed translational energies rejects the postulate of equal internal energy distribution in the two NO_2 molecules produced by the photolysis of N_2O_4 at 248 nm.

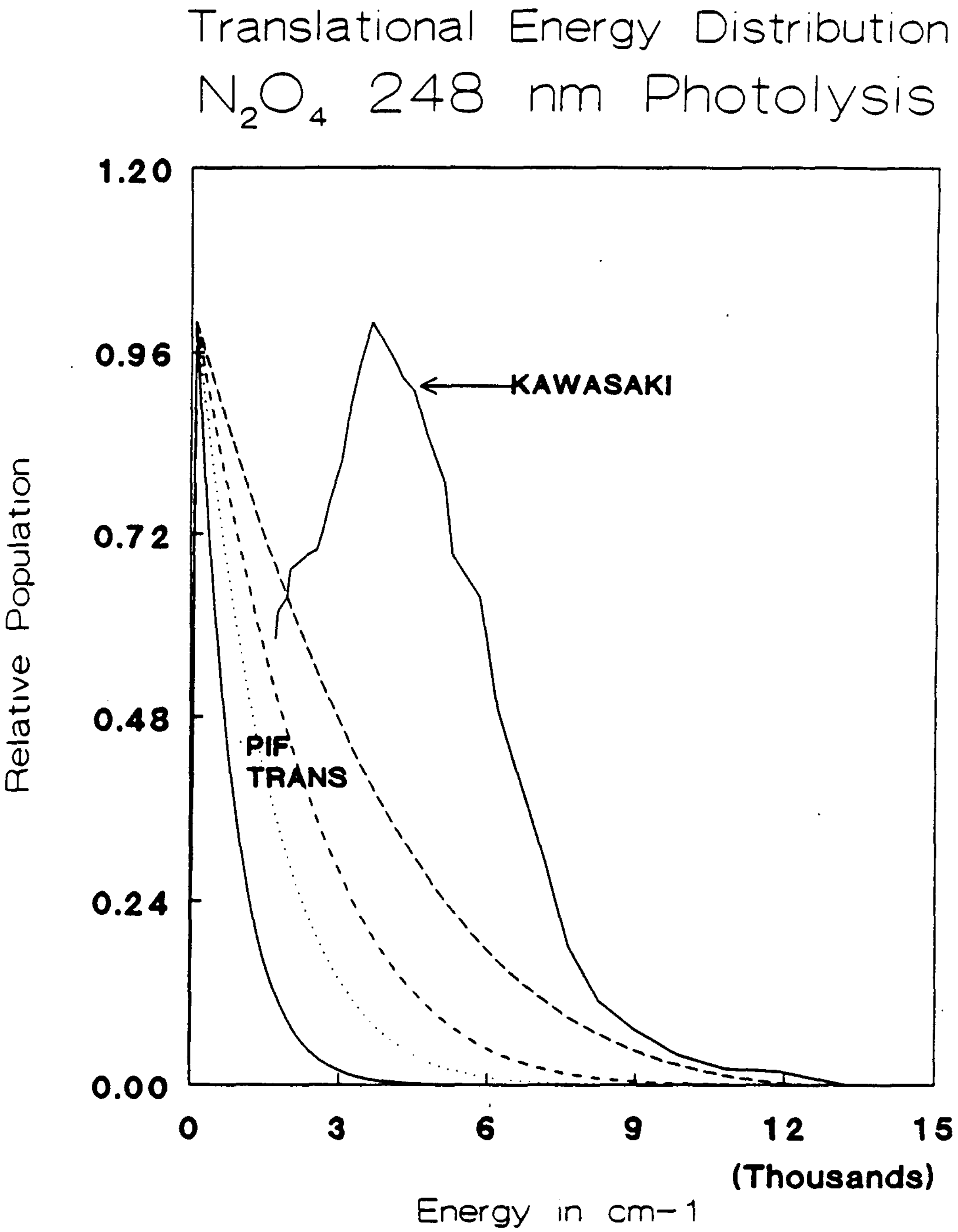
Translational Energy Distribution
N_2O_4 248 nm Photolysis
Relative Population
1.20
0.96
0.72
0.48
0.24
0.00
0
3
6
9
12
15
(Thousands)
Energy in cm-1
KAWASAKI
PIF
TRANS

Figure 1.27

Figure 1.28

N_2O_4/NO_2 correlation diagram based on von Niessen's results (Ref. 33).

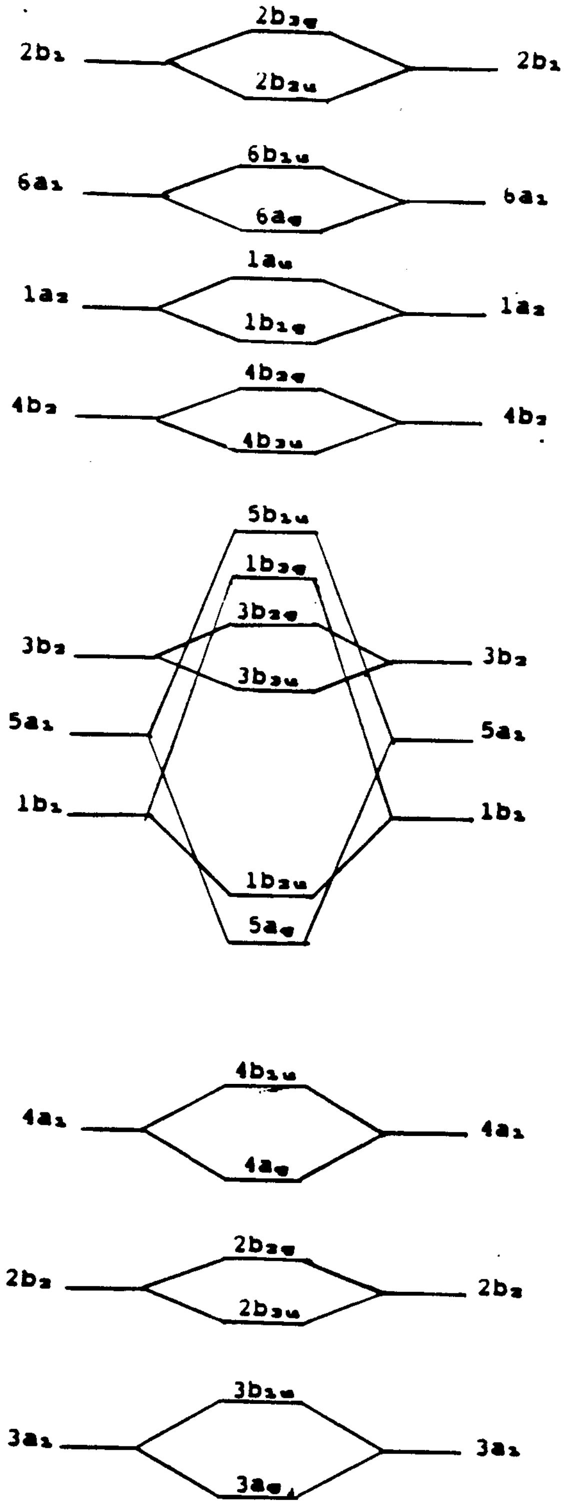
$2b_1$
$2b_{3g}$
$2b_{2u}$
$2b_1$
$6a_1$
$6b_{1u}$
$6a_g$
$6a_1$
$1a_2$
$1a_u$
$1b_{1g}$
$1a_2$
$4b_2$
$4b_{2g}$
$4b_{3u}$
$4b_2$
$5b_{1u}$
$1b_{3g}$
$3b_{2g}$
$3b_2$
$3b_{3u}$
$3b_2$
$5a_1$
$5a_1$
$1b_1$
$1b_1$
$1b_{2u}$
$5a_g$
$4b_{1u}$
$4a_1$
$4a_g$
$4a_1$
$2b_{2g}$
$2b_2$
$2b_{3u}$
$2b_2$
$3b_{1u}$
$3a_1$
$3a_g$
$3a_1$

Figure 1.28

Figure 1.29

Thermodynamic thresholds for various N_2O_4 dissociation channels.

Energetics

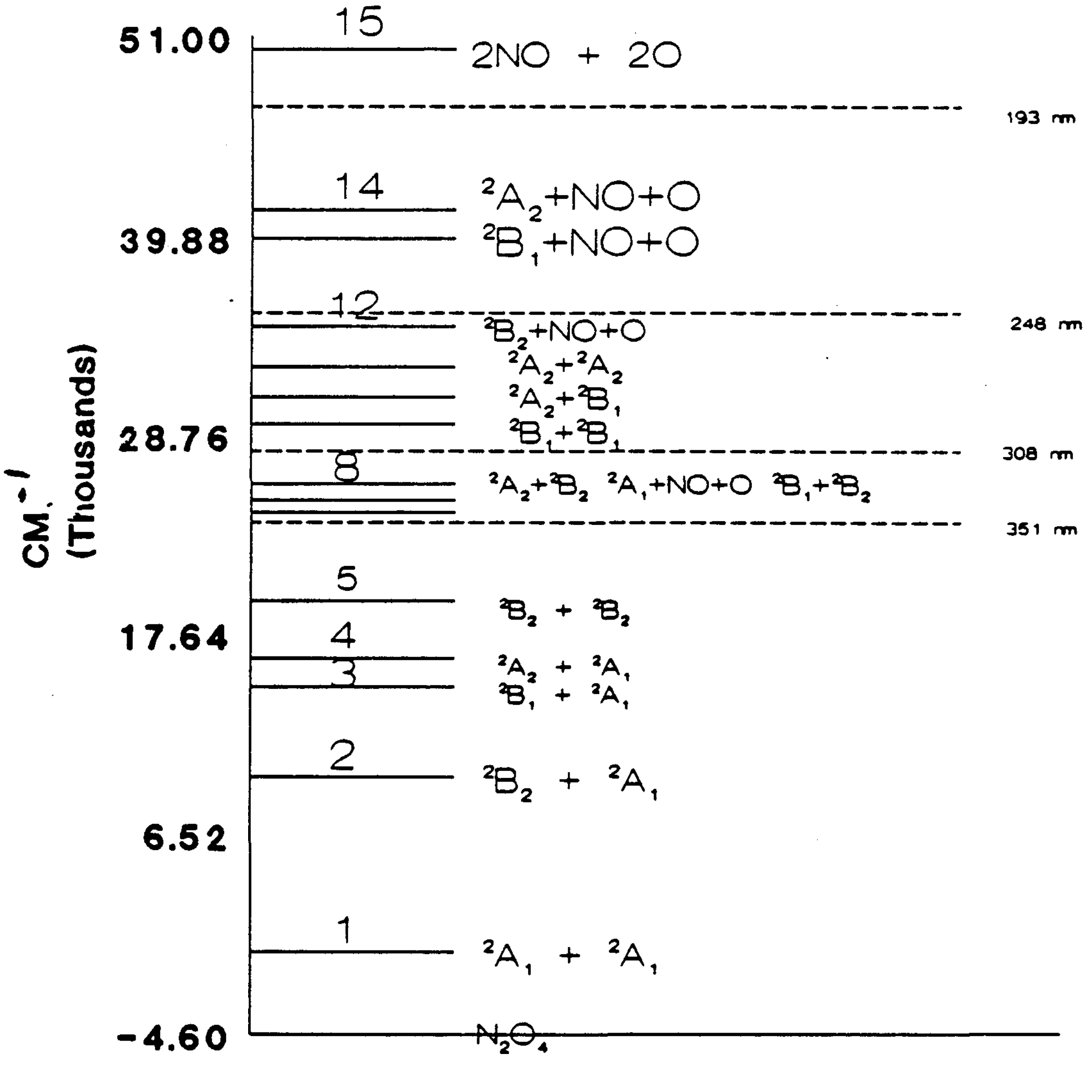

Figure 1.29

Figure 1.30

Predicted NO_2 translational energy distribution (including a small contribution from the nonfluorescing $NO_2(\beta)$) following photolysis of N_2O_4 at 351 nm. This computed by subtracting the PIF $E_{NO2}(\alpha)$ from the total available energy.

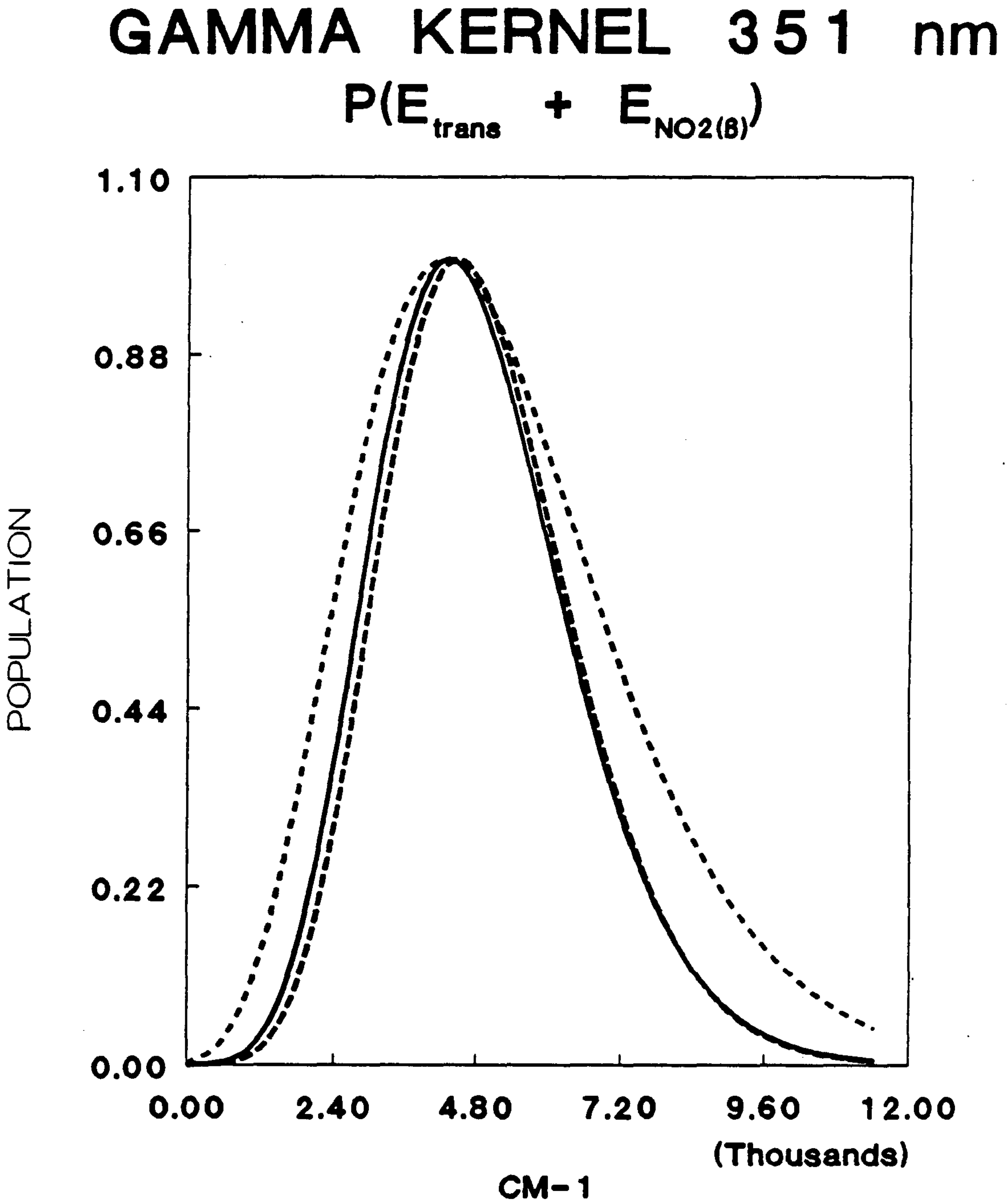
GAMMA KERNEL 351 nm
$P(E_{trans} + E_{NO2(B)})$
1.10
0.88
0.66
0.44
0.22
0.00
POPULATION
0.00
2.40
4.80
7.20
9.60
12.00
(Thousands)
CM-1

Figure 1.30

Figure 1.31

Proposed product curves following N_2O_4 photolysis at 193 nm illustrating the potential for curve crossing.

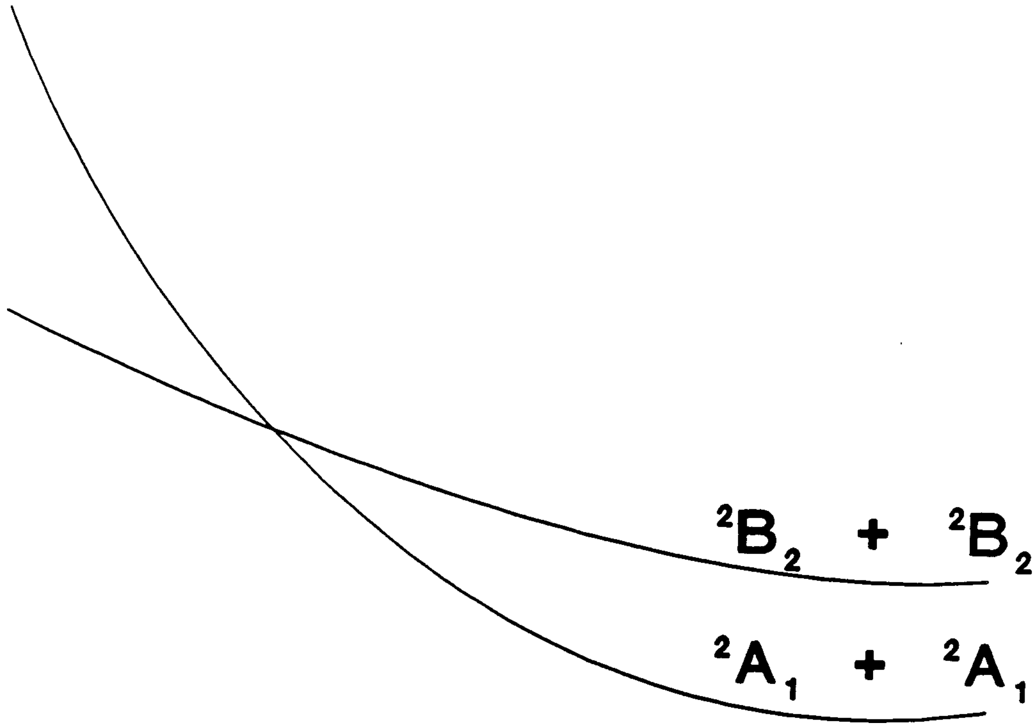

Figure 1.31

Figure 1.32

N_2O_4 351 nm PIF comprehensive energy diagram

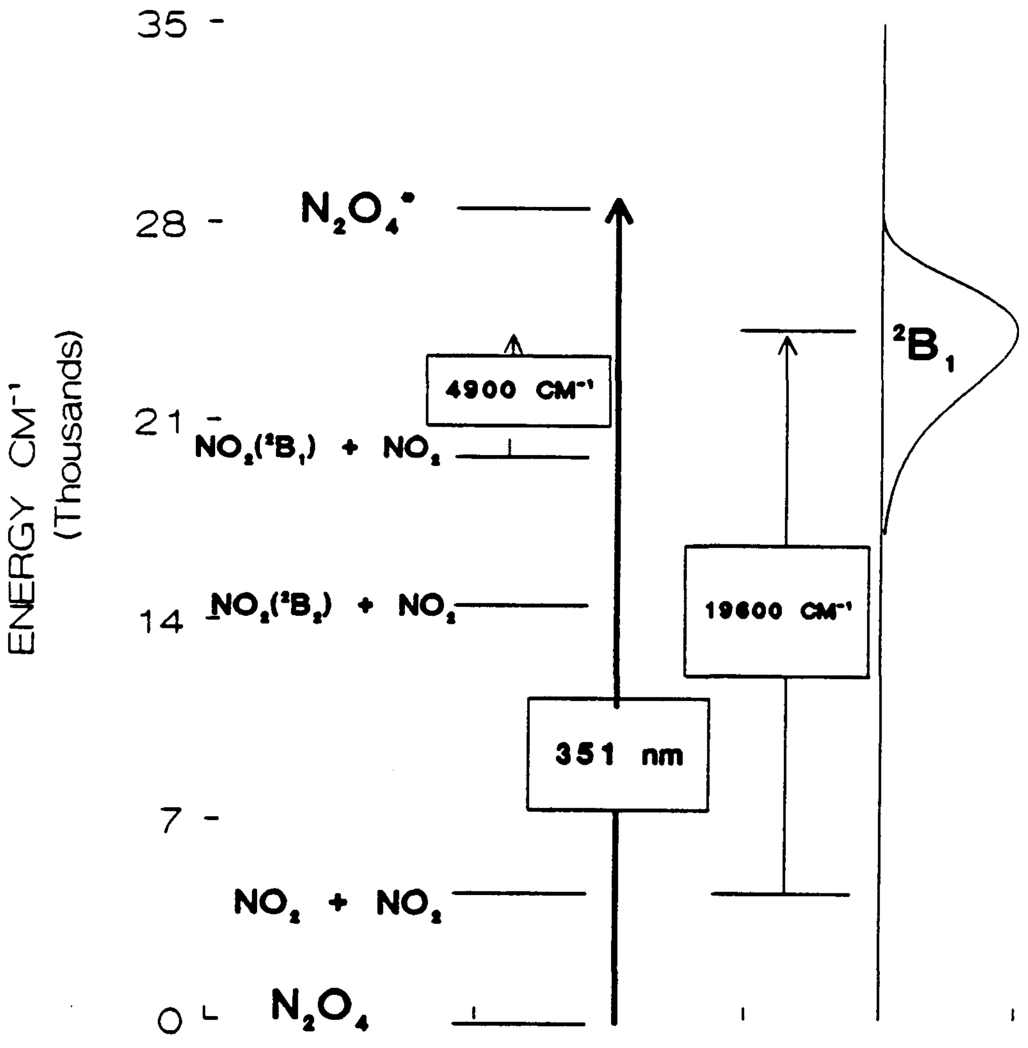

N2O4 351 nm PIF

Figure 1.32

Figure 1.33

N_2O_4 193 nm PIF comprehensive energy diagram

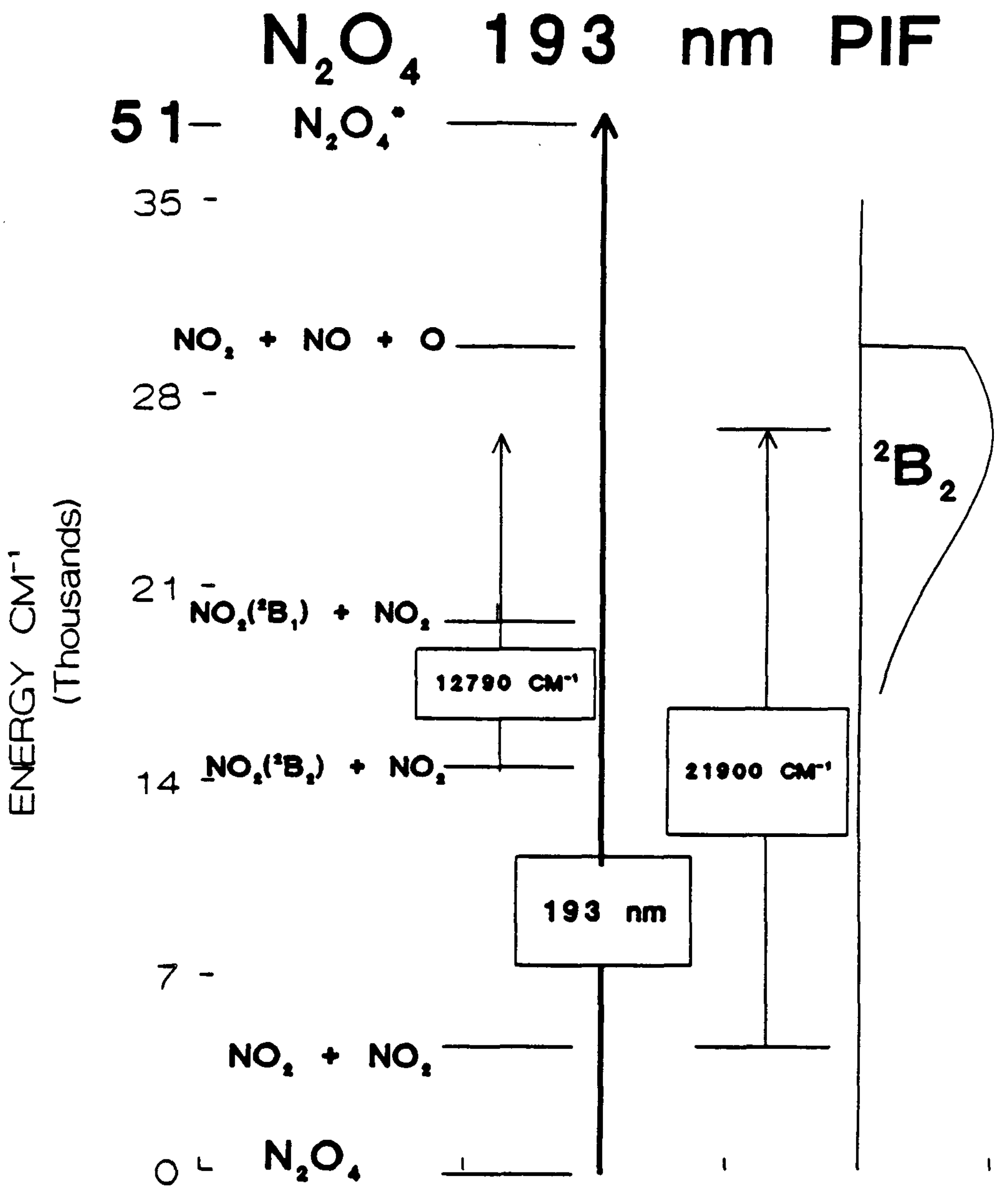
N2O4 193 nm PIF
ENERGY CM-1 (Thousands)
51
35
28
21
14
7
0
N2O4*
NO2 + NO + O
NO2(2B1) + NO2
NO2(2B2) + NO2
NO2 + NO2
N2O4
12790 CM-1
21900 CM-1
193 nm
2B2

Figure 1.33

Figure 1.34

N_2O_4 248 nm PIF comprehensive energy diagram

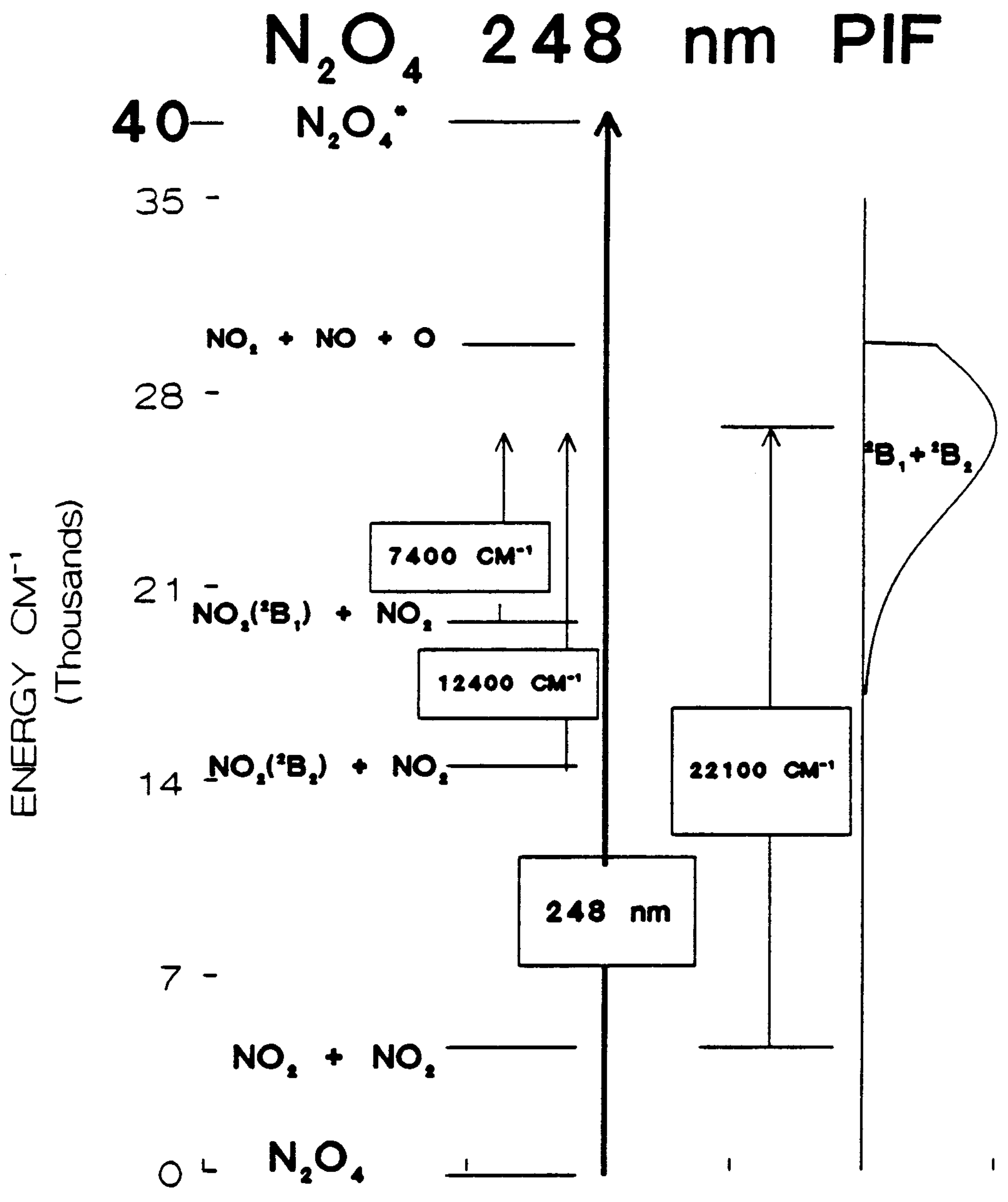
N_2O_4 248 nm PIF
ENERGY CM^{-1}
(Thousands)
40
35
28
21
14
7
0
$N_2O_4^*$
NO_2 + NO + O
$NO_2(^2B_1)$ + NO_2
$NO_2(^2B_2)$ + NO_2
NO_2 + NO_2
N_2O_4
7400 CM^{-1}
12400 CM^{-1}
248 nm
22100 CM^{-1}
$^2B_1 + {}^2B_2$

Figure 1.34

CHAPTER 2. NO_2Cl Photolysis Induced Fluorescence in a Supersonic Jet at 248 nm

ABSTRACT

The photolysis of NO_2Cl at 248 nm resulting in NO_2 fluorescence was analyzed by the PIF (Photolysis Induced Fluorescence) deconvolution scheme and these results were compared to and Time-of-Flight/Mass Spectrometry (TOF/MS) performed previously in Y.T. Lee's lab by Oh and Coworkers.[1] The results from the pulsed beam PIF agreed with the TOF/MS results leading to 5 product channels in NO_2Cl photolysis.

INTRODUCTION

The ultraviolet photolysis of NO_2Cl at 248 nm has been carried out previously in room temperature flow cell experiments and the resulting NO_2^* spectrum analyzed by the PIF deconvolution scheme.[2] The Time-of-Flight/Mass spectrometry (TOF/MS) has also been carried out previously for the 248 nm photolysis of NO_2Cl.[1] The present experiment carries out the PIF of NO_2Cl after having undergone cooling in a supersonic jet, yielding an energy distribution for the resultant fluorescent NO_2^*. The comparison between the NO_2^* energy distribution from the PIF method and the NO_2 energy distribution from the TOF/MS method may be carried out to better define the product channels. The ultraviolet absorption spectra[3] shown in Figure 2.1 is diffuse in the 248 nm region, indicative of direct dissociation. The ground state equilibrium structure is depicted in Figure 2.2.[4]

EXPERIMENTAL

The experimental arrangement is the same as that utilized in chapter 1 (Figure 1.3). The slush bath for NO_2Cl consisted of dry ice and methanol (-80 ∘C) yielding a vapor pressure of ~15 torr. The decomposition rate of NO_2Cl at this temperature is negligible.[3] A 300 torr stream of helium was passed over the sample leading to a seeding fraction of 5% NO_2Cl. These conditions were similar to those of Oh and coworkers who did not observe significant amounts of clusters.[1]

The synthesis of NO_2Cl followed the procedure of Volpe et. al.[5] A stream of anhydrous hydrogen chloride (Matheson Gas Company, 99%) was passed through a 196 K cold trap to remove any traces of water. This was passed through a porous glass bubbler into a solution containing 25 ml 90% nitric acid, 60 ml 95% sulfuric acid, and 70 ml 30% fuming sulfuric acid which was vigorously stirred by a magnetic stirring bar. The resulting mixture of HCl, Cl_2, and NO_2Cl was passed through a 196 K cold trap to collect NO_2Cl. The untrapped gas continued to flow through a calcium sulfate column before entering the atmosphere, to prevent atmospheric water from entering the system. The synthesis was terminated when ˜9 ml of nitryl chloride was collected. This was distilled from a 175 K trap to a 77 K trap with the middle ⅓ fraction retained, thus separating Cl_2 impurities in the first ⅓ distillate and NO_2 impurities in the remaining ⅓ fraction. The sample was checked by ultraviolet absorption in a Cary 14 spectrometer and in conjunction with the absorption cross section of Illies and Takacs[3] the purity was estimated to be 90%.

The Hamamatsu R636 (GaAs) the photomultiplier was used for the NO_2Cl data. As was the case for N_2O_4 in chapter 1 the nonuniform response of the system in regards to the fluorescence wavelength had to be taken into account (see appendix A). The system response for the NO_2Cl data is (filename WSF85AV.SYS) illustrated in Figure A.2 of appendix A. The laser fluence at 248 nm was 31.6 mj/cm^2. The slits had to be opened wider than normal for the low fluorescence of NO_2Cl at 248 nm leading to a data point resolution of 2.91 nm. Once again although signals were collected at 400 and 1500 ns, the 1500 ns were much more reliable due to the absence of RF interference.

RESULTS

The six fluorescence spectra following 248 nm excitation of NO_2Cl with 400 ns delay are presented in Figure 2.3. The subsequent ringing of the PMT due to laser

RF adversely affects the signal to noise at this short delay time so these spectra were averaged together resulting in the spectrum in Figure 2.4. The five fluorescence spectra following 248 nm excitation of NO_2Cl with 1500 ns delay are shown in Figure 2.5. At this longer delay the PMT ringing has subsided and the spectra have a better S/N as compared to the 400 ns delay spectra. Applying the Gamma kernel PIF deconvolution method to the 400 ns spectra we obtain the NO_2 internal energy distribution shown in Figure 2.6. The five 1500 ns spectra lead to populations shown in Figure 2.7. The 400 ns population profile falls within the precision of the 1500 ns population profiles. The steady rise of the population with energy near the dissociation threshold suggests sizable NO production.

The populations derived from the TOF/MS[1] are compared to the PIF population for mass:charge (m/e) 46 (NO_2^+) and the group of masses which gave the same distribution (35 Cl^+, 30 NO^+, 16 O^+) in Figures 2.8 and 2.9. More credence is placed in the distribution presented in Figure 2.9 because the TOF/MS populations are confirmed from 3 different mass:charge ratios (NO^+,Cl^+,O^+), the TOF/MS population from NO_2^+ ion monitoring in Figure 2.8 has some error due to NO_2^* " cracking " in the ionizer, and the resolution in Figure 2.9 is superior as indicated by the more energetic internal energy peak partially resolved into 2 peaks. In Figure 2.9 the low energy TOF peak corresponds to ground state $NO_2(X)$; whereas the high energy peak(s) corresponds to the NO_2 (A^2B_1 + B^2B_2) population. The sum of the overlapped region of the superimposed TOF/MS population indicated by the dashed line in Figure 2.9 looks similar to the supersonic jet PIF population.

The Gamma Kernel fitting parameters for 248 nm supersonic jet PIF of NO_2Cl are listed in Table 2.1. The statistical measures of the population such as the mean, standard deviation, and root mean squared values are tabulated in Table 2.2.

DISCUSSION

A. Photolytic Channels and Quantum Yields

The energetically accessible channels for the 248 nm photolysis of NO_2Cl are:[6]

$$NO_2Cl + h\nu \rightarrow NO_2(X) + Cl(^2P_{3/2}) \qquad \lambda < 842 \text{ nm} \qquad (2.2)$$

$$\rightarrow NO(X) + ClO(X) \qquad \lambda < 665 \text{ nm} \qquad (2.3)$$

$$\rightarrow NO_2(A^2B_2) + Cl(^2P_{3/2}) \qquad \lambda < 462 \text{ nm} \qquad (2.4)$$

$$\rightarrow NOCl(X) + O(^3P) \qquad \lambda < 415 \text{ nm} \qquad (2.5)$$

$$\rightarrow NO_2(B^2B_1) + Cl(^2P_{3/2}) \qquad \lambda < 376 \text{ nm} \qquad (2.6)$$

$$\rightarrow NO(X) + O(^3P) + Cl(^2P_{3/2}) \qquad \lambda < 270 \text{ nm} \qquad (2.7)$$

The TOF/MS experiments by Oh et. al.[1] yielded several time resolved peaks at mass:charge 46 corresponding to NO_2(X,A,B) and several time resolved peaks for mass:charge 35 corresponding to the direct production of Cl and Cl resulting from NOCl " cracking " in the ionizer. These results serve as evidence for channels 2.2, 2.4 , 2.5 and 2.6. The PIF results by the very nature of detecting fluorescence gives support for channels 2.4 and/or 2.6. The sharp cutoff of the PIF population near the NO_2 dissociation serve as evidence for channel 2.7 which is difficult to detect by the TOF due to the low kinetic energy present. Thus these two complementary methods yield 5 product channels (all of the above channels except 2.3).

B. Dissociation Dynamics

As stated earlier the ultraviolet absorption spectra of NO_2Cl is structureless, indicative of a fast dissociation. The assignment for 248 nm excitation for NO_2Cl is not known. The ultraviolet absorption spectra of other NO_2 containing molecules (i.e. nitroalkanes) show two peaks: one strong feature near 186 nm and a less intense ones in the 265-280 range. A $\pi \rightarrow \pi^*$ transition has been assigned to the strong feature whereas $n \rightarrow \pi^*$ and $\sigma \rightarrow \pi^*$ transitions have been assigned to the weaker feature.[7,8] These transitions are said to be localized on NO_2.

C. Time-of-Flight / Supersonic Jet PIF

The internal energy distribution derived from the PIF jet spectrum seems to be consistent with the internal energy derived from the Time-of-Flight spectra at m/e = 35, 30, and 16 given in Figure 2.9. The relative heights of the two NO_2 population curves from the TOF/MS are the same as that observed but the PIF internal energy distribution height relative to these is not absolute. The PIF internal energy height was normalized by requiring its area to be the same as that of the NO_2^* peak of the TOF/MS. This normalization will not give an exact match of the high energy NO_2^* peak from the TOF/MS with the PIF internal energy peak because of the limitations of each method. The TOF/MS detection doesn't detect the slow moving fragments (Cl^+, NO^+, O^+) efficiently leading to a degradation of the high energy side of the NO_2^* peak near D_0. The PIF scheme is not able to resolve different electronic states of NO_2 (two peaked-distribution) due to the nature of the Gamma kernel fitting function which produces a single maximum in the NO_2 internal energy distribution. With these limitations taken into account and a slightly different normalizing constant the internal energy of the PIF peak should have better overlap with the NO_2^* (including vibrationally excited $NO_2(X)$ above the NO_2^* threshold indicated by the dashed line).

CONCLUSION

The NO_2 internel energy distribution from NO_2Cl PIF at 248 nm in a supersonic jet has been compared to the NO_2

inteernal energy distribution from the TOF/MS of NO_2Cl at 248 nm. The two supplementary methods agree very well in the region of energy and lead to five dissociation channels:

$$NO_2Cl + h\nu \rightarrow NO_2(X) + Cl(^2P_{3/2}) \qquad \lambda < 842 \text{ nm} \qquad (2.2)$$

$$\rightarrow NO_2(A^2B_2) + Cl(^2P_{3/2}) \qquad \lambda < 462 \text{ nm} \qquad (2.4)$$

$$\rightarrow NOCl(X) + O(^3P) \qquad \lambda < 415 \text{ nm} \qquad (2.5)$$

$$\rightarrow NO_2(B^2B_1) + Cl(^2P_{3/2}) \qquad \lambda < 376 \text{ nm} \qquad (2.6)$$

$$\rightarrow NO(X) + O(^3P) + Cl(^2P_{3/2}) \qquad \lambda < 270 \text{ nm} \qquad (2.7)$$

REFERENCES

[1] D. Oh, Ph.D. Thesis, University of California, Berkeley, 1988.

[2] D. Oh, W.N. Sisk, K. Patten, H.S. Johnston, manuscript in preparation.

[3] A.J. Illies, G.A. Takacs, J. Photochem. **6**, 35 (1976).

[4] K. Endo, Nippon Kagaku Kaishi, **9**, 1129 (1979).

[5] M. Volpe and H.S. Johnston, J. Am. Soc. **78**, 3903 (1956).

[6] D.L. Baulch, R.A. Cox, R.F. Hampson, Jr., J.A. Kerr, J. Troe, and R.T. Watson, J. Phys. Chem. Ref. Data **9**, 467 (1980).

[7] G.D. Greeenblatt, H. Zuckerman, and Y. Hass, Chem. Physics Letters **134**, 593 (1988).

[8] J.C. Mialocq and J.C. Stephenson, Chem. Phys. **106**, 281 (1986).

Gamma Kernel Fitting Parameter for NO_2Cl 248 nm PIF

File name	Species	λ nm	τ_{ns} DEL	M	n	Y_{max}	SYSTEM RESPON
WSF83F	NO_2Cl	248	1500	28444	7.8125 E-4	1.0529 E1	WSF 85AV
WSF83H					1.5625 E-3	1.8463 E1	
WSF84B					1.5625 E-3	2.3224 E1	
WSF84D					1.5625 E-3	2.3346 E1	
WSF84J					1.5625 E-3	1.6220 E1	

Table 2.1

The Fitting parameters in the Gamma Kernel fitting function are M, the maximum available energy (cm^{-1}), Ymax, and n. τ_{ns} is the boxcar gate delay in nanoseconds. The system response refers to the system repsonse file (see appendix A).

Population Statistics for NO_2Cl 248 nm Gamma Kernel PIF

FILE NAME	SPECIES	λ nm	τ_{ns} DEL	MEAN	MOST PROB	RMS	σ
WSF83F	NO_2Cl	248	1500	1.7923E4	2.5107 E4	1.8295 E4	3.66920E3
WSF83H				1.8062E4	2.5107 E4	1.8435 E4	3.6880E3
WSF84B				1.7828E4	2.5107 E4	1.8199 E4	3.65488E3
WSF84D				1.7824E4	2.5107 E4	1.8195 E4	3.65401E3
WSF84J				1.8222E4	2.5107 E4	1.8595 E4	3.70535E3

Table 2.2

The entries correspond to the mean, most probable, root mean square and standard deviation of the NO_2 internal energy distributions.

Figure 2.1

The NO_2Cl ultraviolet absorption spectrum from Ref. 3.

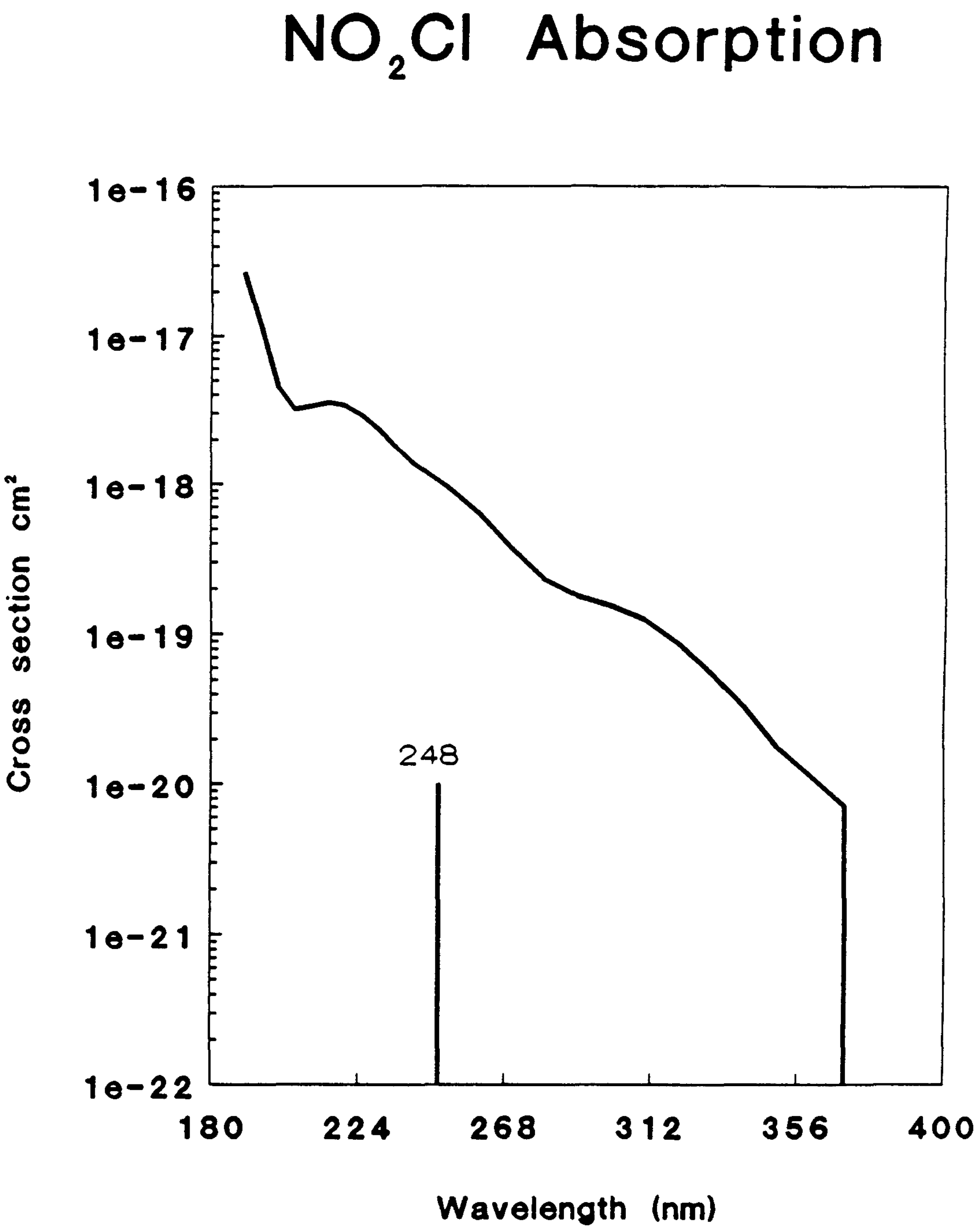
NO$_2$Cl Absorption
Cross section cm^2
1e-16
1e-17
1e-18
1e-19
1e-20
1e-21
1e-22
248
180
224
268
312
356
400
Wavelength (nm)

Figure 2.1

Figure 2.2

Ground state structure of NO_2Cl.

Parameters obtained from Ref. 4.

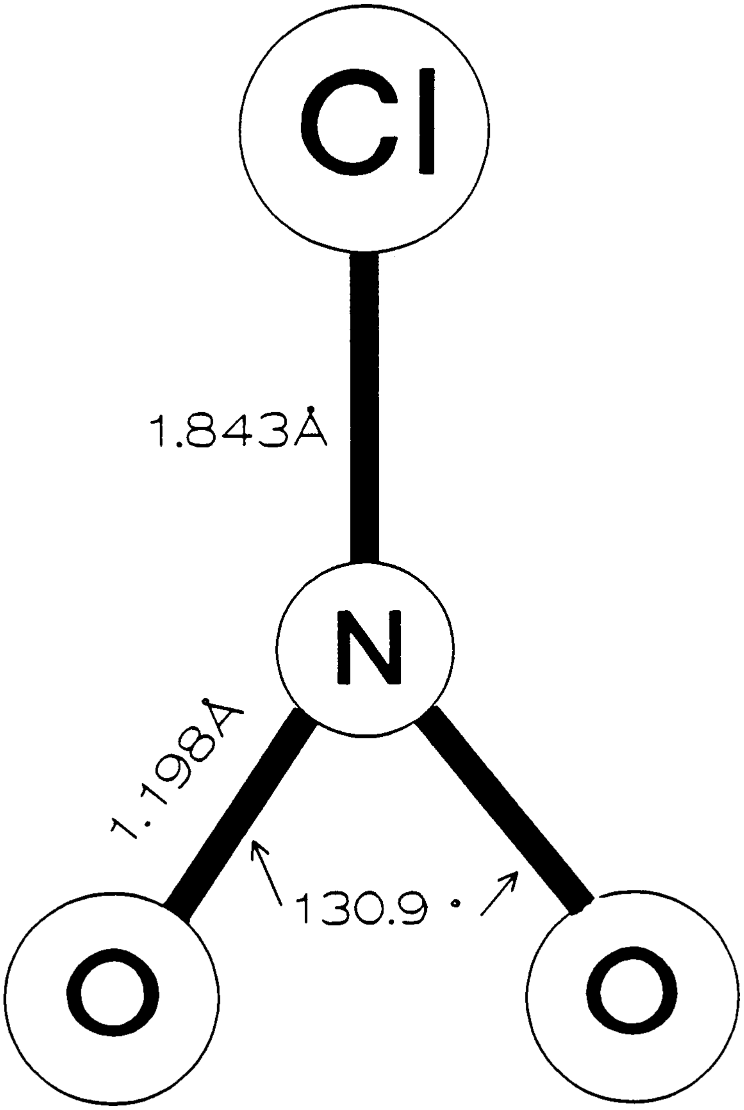

Figure 2.2

Figure 2.3

Reproductions of the 248 nm NO_2Cl PIF spectra corrected for laser power and system response. NO_2 fluorescence observed 400 ns after laser photolysis of a supersonic jet of NO_2Cl.

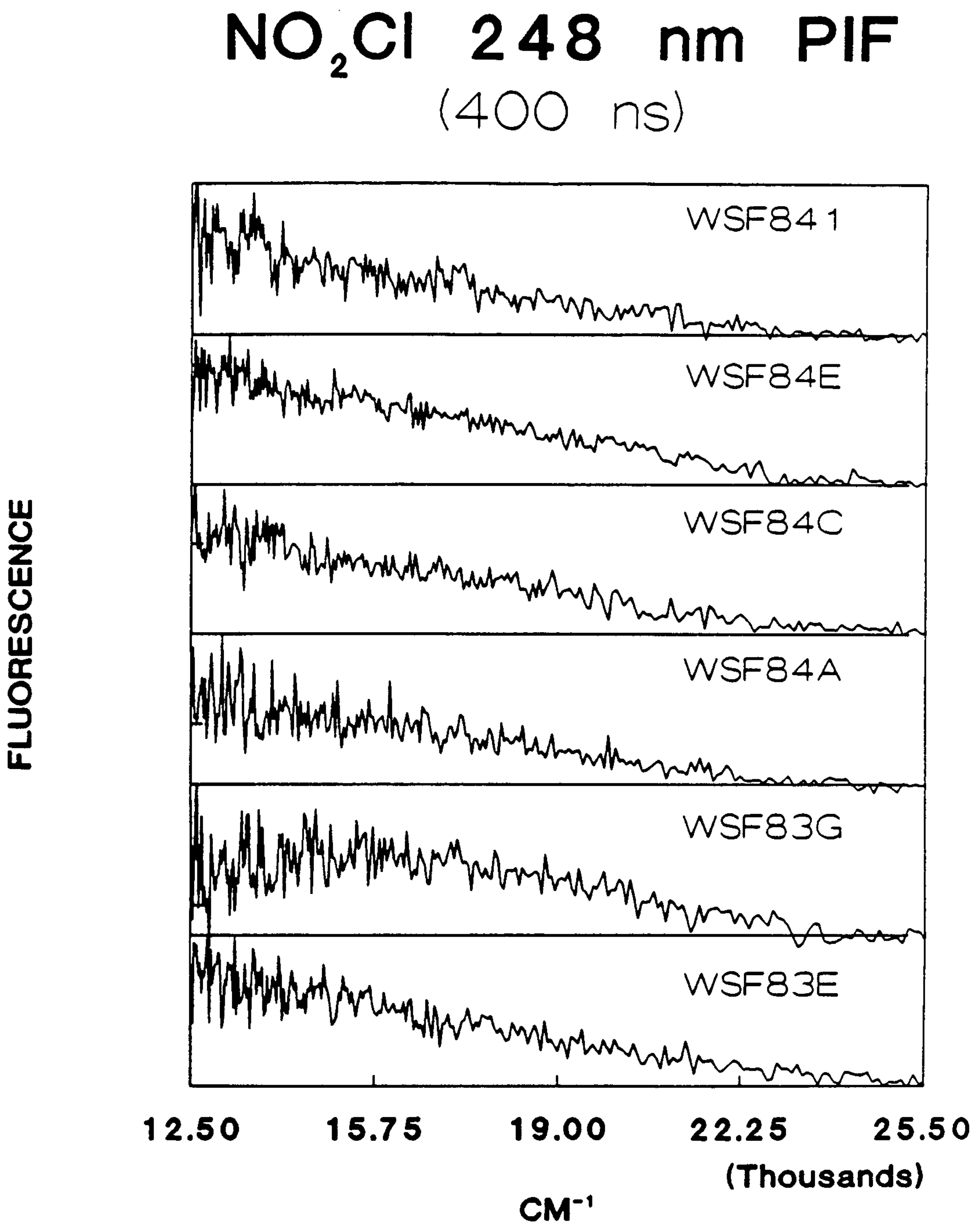
NO$_2$Cl 248 nm PIF
(400 ns)
WSF841
WSF84E
WSF84C
WSF84A
WSF83G
WSF83E
FLUORESCENCE
12.50
15.75
19.00
22.25
25.50
(Thousands)
CM^{-1}

Figure 2.3

Figure 2.4

The resulting averaged NO_2Cl PIF spectrum for 248 nm photolysis at 400 ns delay.

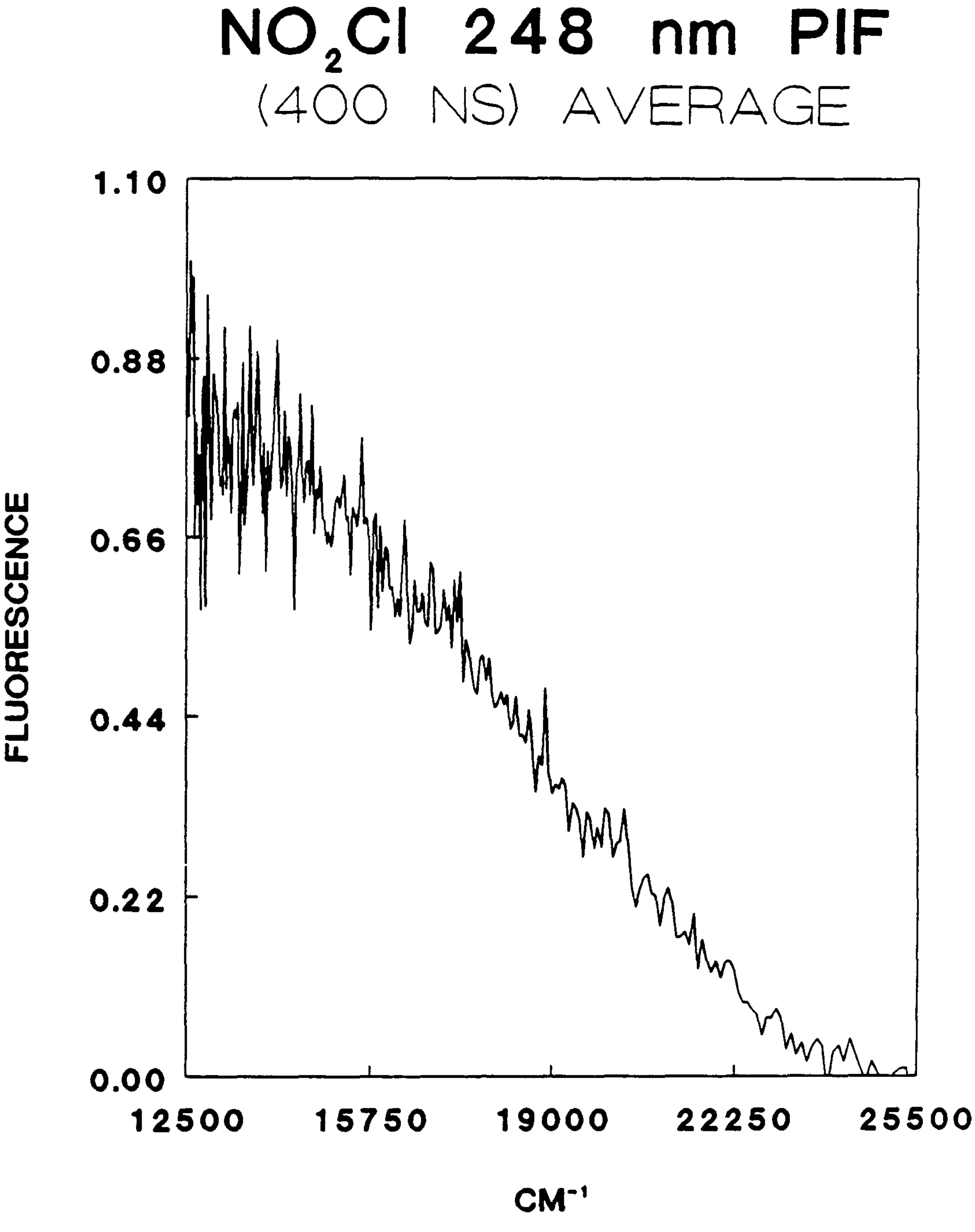
NO_2Cl 248 nm PIF
(400 NS) AVERAGE
FLUORESCENCE
1.10
0.88
0.66
0.44
0.22
0.00
12500
15750
19000
22250
25500
CM^{-1}

Figure 2.4

Figure 2.5

Reproductions of the 248 nm NO_2Cl PIF spectra corrected for laser power and system response. NO_2 fluorescence observed 1500 ns after laser photolysis of a supersonic jet of NO_2Cl.

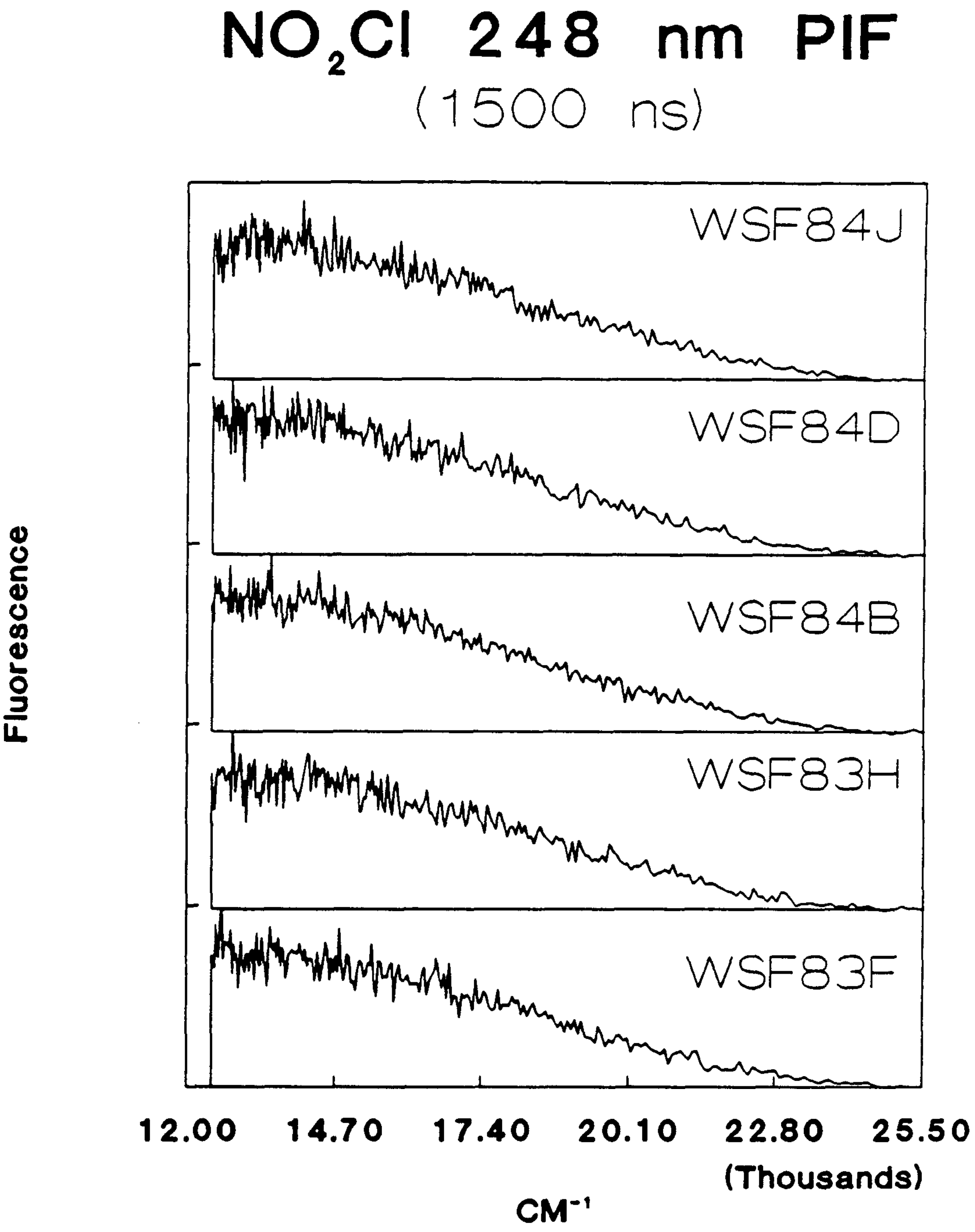
NO_2Cl 248 nm PIF
(1500 ns)
WSF84J
WSF84D
WSF84B
WSF83H
WSF83F
Fluorescence
12.00
14.70
17.40
20.10
22.80
25.50
(Thousands)
CM^{-1}

Figure 2.5

Figure 2.6

The NO_2 energy distribution obtained by applying the Gamma kernel PIF deconvolution scheme to 248 nm photolysis of NO_2Cl at 400 ns delay (Figure 2.4).

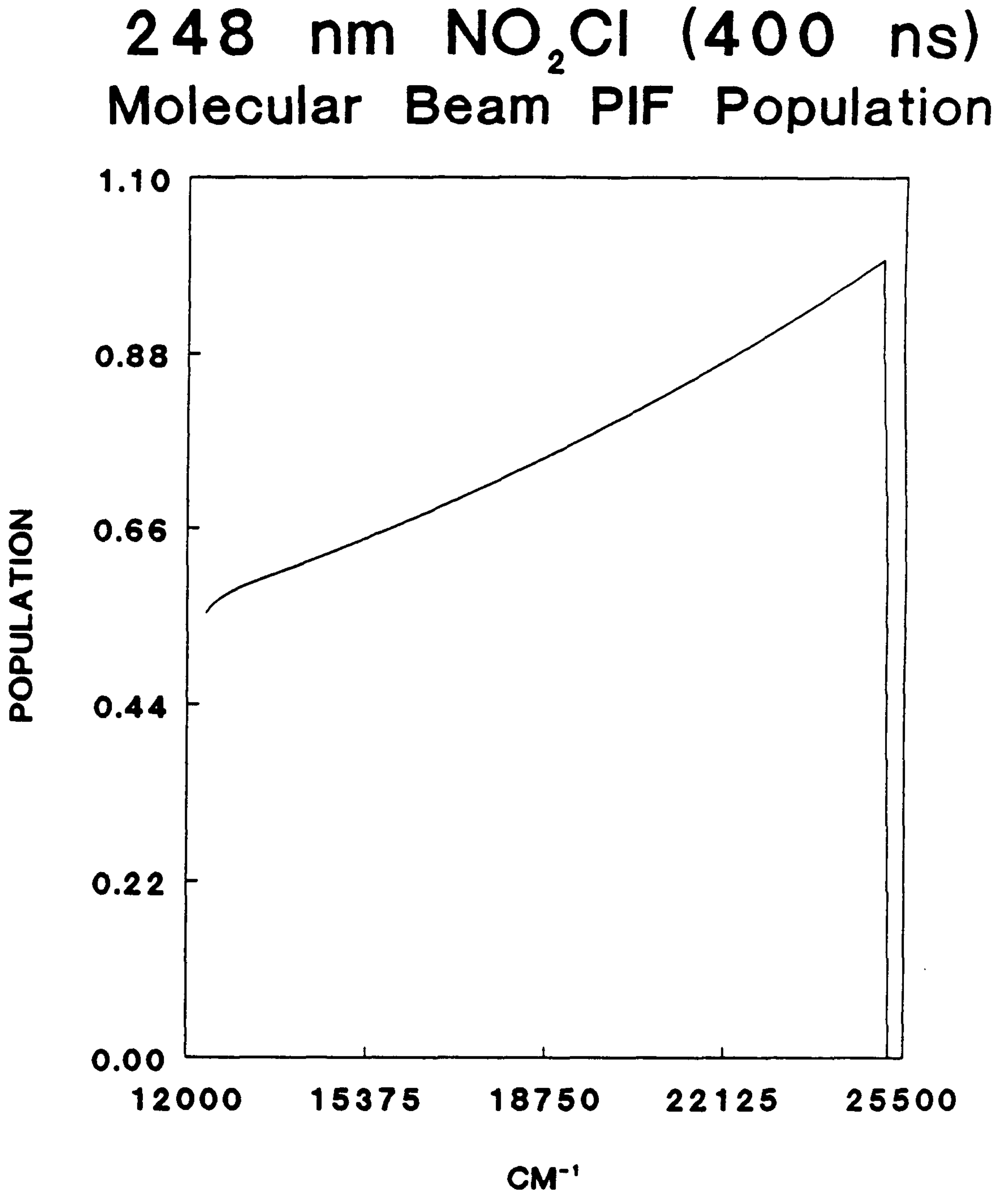
248 nm NO_2Cl (400 ns)
Molecular Beam PIF Population
POPULATION
1.10
0.88
0.66
0.44
0.22
0.00
12000
15375
18750
22125
25500
CM^{-1}

Figure 2.6

Figure 2.7

The NO_2 energy distribution obtained by applying the Gamma kernel PIF deconvolution scheme to 248 nm photolysis of NO_2Cl at 1500 ns delay (Figure 2.5).

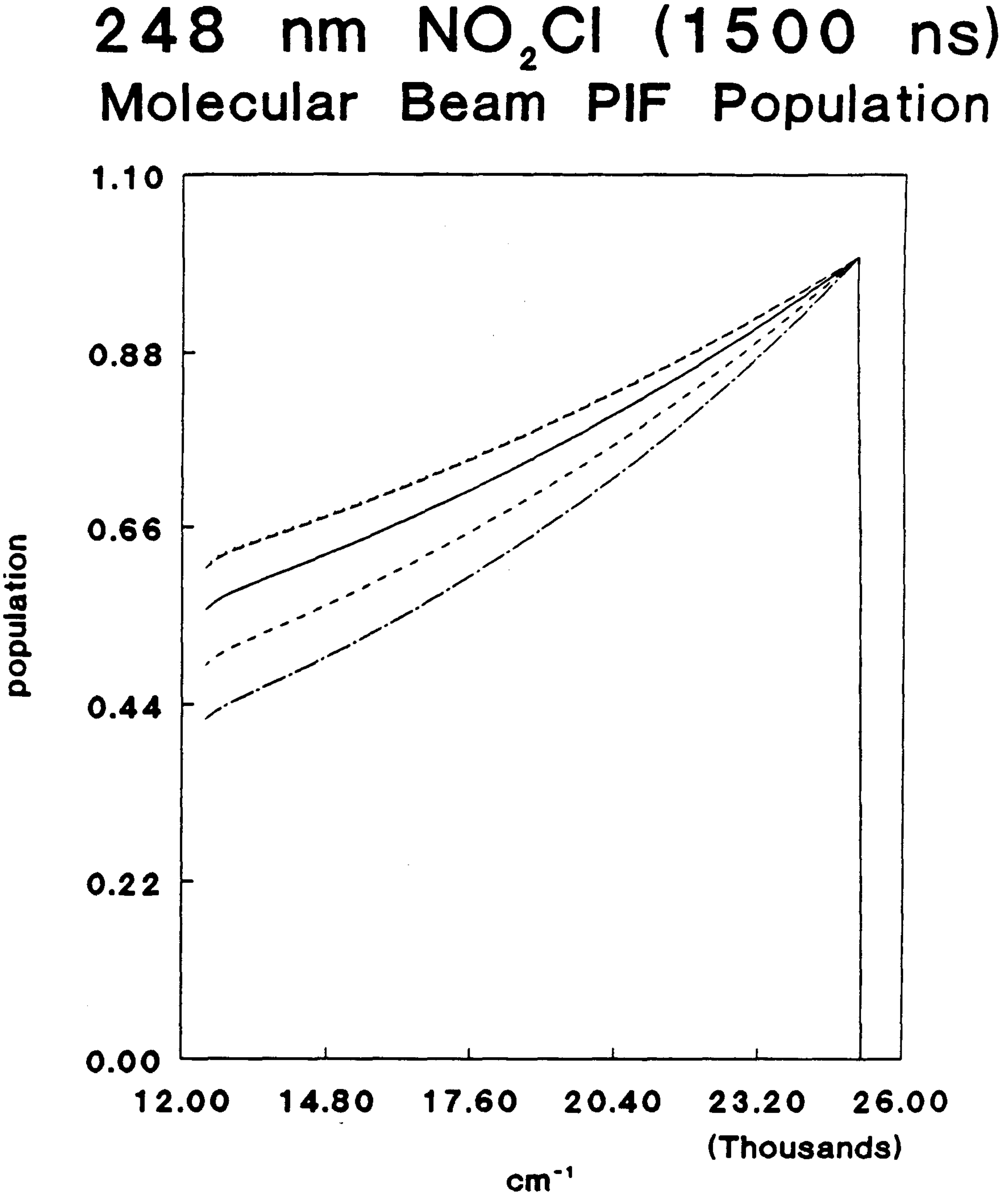

248 nm NO_2Cl (1500 ns)
Molecular Beam PIF Population

Figure 2.7

Figure 2.8

NO_2Cl PIF NO_2 internal energy distribution compared to the Time-of-Flight NO_2 internal energy distribution [Ref. 1] for m/e = 46 detection.

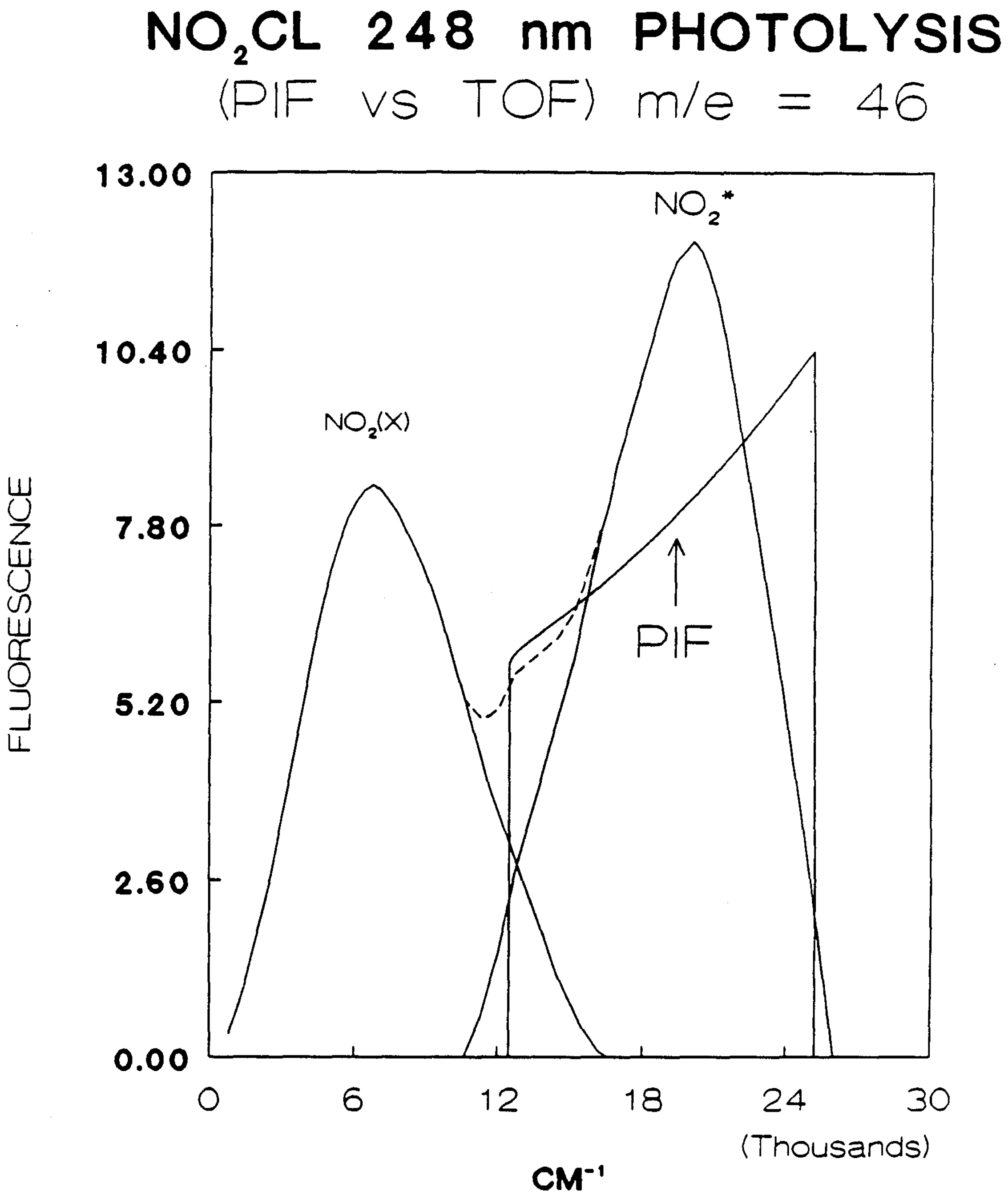
NO$_2$CL 248 nm PHOTOLYSIS
(PIF vs TOF) m/e = 46
NO$_2$*
NO$_2$(X)
PIF
FLUORESCENCE
13.00
10.40
7.80
5.20
2.60
0.00
0
6
12
18
24
30
(Thousands)
CM^{-1}

Figure 2.8

Figure 2.9

NO_2Cl PIF NO_2 internal energy distribution compared to the Time-of-Flight NO_2 internal energy distribution [Ref. 1] for m/e = 30,35,16 detection.

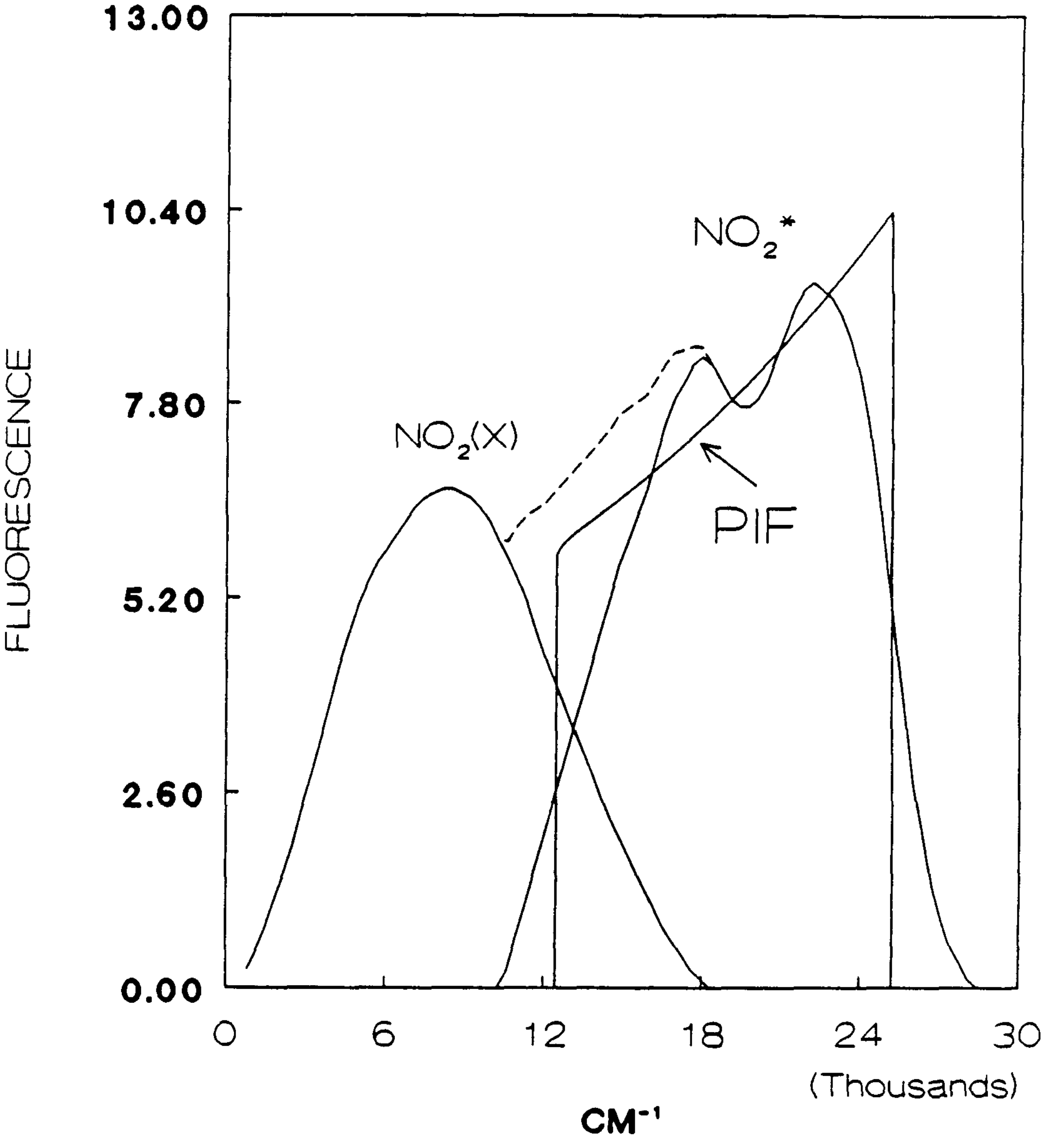

NO$_2$CL 248 nm PHOTOLYSIS

(PIF vs TOF) m/e = 35,30,16

Figure 2.9

CHAPTER 3. NO_2 Fluorescence in the Dissociation Region

ABSTRACT

The undispersed fluorescence of NO_2 is observed following the excitation of NO_2Cl, N_2O_4, and NO_2. The Photolysis Induced Fluorescence Excitation (PIFEX) spectrum of NO_2Cl shows a decrease in the fluorescence quantum yield, ϕ_f, when scanning to shorter wavelength. This decrease in ϕ_f is attributed to the onset of the NO + O + Cl channel. This drop is not observed when exciting N_2O_4 in the energetically possible NO production range. The NO_2 LIF spectra yield information on 3 parallel bands observed near 400 nm as well as a confirmation on D_0, which is found here to be 3978.3±0.03Å (air-calibrated).

INTRODUCTION

When a molecule (ABC) is irradiated with laser light in the vicinity of its dissociation threshold, a competition is established between dissociation (A + BC) and fluorescence ($ABC^* \rightarrow h\nu$). If the fluorescence lifetime is longer than the predissociation lifetime, then the fluorescence is expected to decrease as the excitation energy approaches the dissociation threshold. By noting the wavelength at which attenuation of fluorescence takes place, a bond dissociation energy may be determined if an exit energy barrier does not exist. This effect has been demonstrated for H_2CO[1], SO_2[2], and NO_2[3]. These flow cell experiments provide upper bounds for the bond dissociation energy, D_0, due to the contribution of rotational energy of the ground state, which causes fluorescence to gradually decrease. When these molecules are cooled via expansion in a supersonic jet, the bulk of this rotational energy is removed, and a more accurate determination of D_0 may be obtained. This was the case for NO_2 in supersonic jet fluorescence excitation experiments performed by Chen and Coworkers.[4]

In this experiment we studied three examples of this fluorescence near D_0.

1. $NO_2Cl \rightarrow NO_2^* + Cl \rightarrow NO_2 + Cl + h\nu$

   $\rightarrow NO + O + Cl \quad (\lambda < 267 nm)$[5]

   Range studied, 230 to 290 nm

2. $N_2O_4 \rightarrow NO_2^* + NO_2 \rightarrow 2NO_2 + h\nu$

   $\rightarrow NO + O + Cl \quad (\lambda < 334\text{-}339\ nm)$[6]

   Range studied, 336 to 346 nm

3. (a) NO_2 D_0 determination

   $NO_2 \rightarrow NO_2^* \rightarrow NO_2 + h\nu$

   $\rightarrow NO + O \quad (\lambda < 397.8\ nm)$[4]

   Range studied, 392 to 403 nm

   (b) Three parallel bands were identified in this region and the spectroscopic constants used to describe these bands were determined.

In each case, the photochemical reactant was cooled to about

3 K in a pulsed supersonic molecular beam.

EXPERIMENTAL

The experimental arrangement was the same as that of PIF experiments in chapter 1 (Figure 1.3), with the modification of placing at the exit of the excimer laser a dye laser (Lumonics Hyperdye-300) and a second-harmonic generation system utilizing a beta barium borate crystal (Lumonics Hypertrak-1000). A supersonic beam of sample (NO_2Cl, N_2O_4, or NO_2) seeded in helium was crossed with laser radiation 8 mm downstream. For NO_2Cl the boxcar gate delay was 500 ns, and the two values for the width was 500 ns and 15 μs. For N_2O_4 the boxcar delay values were 500 and 1000 ns with a width of 100 ns. For NO_2 the boxcar delay was 500 ns and the width was 100 ns and 10 μs.The purpose of the two boxcars settings (long & short gates) was to note if temporal degradation occurred.

The dyes used were: Exalite 398 for the NO_2 FEX spectra, P-Terphenyl (λ_{max}= 341 nm , Acton Research) for the N_2O_4 PIFEX work, and Coumarin 540, Coumarin 500, and Coumarin 480 (Acton Research) for the NO_2Cl PIFEX experiments. The dye output was doubled via the beta barium borate crystal only for the NO_2Cl photolysis. The laser energy at the interaction region (8 mm from the jet output) was usually between 0.2 - 1.0 mj/pulse thus minimizing the possibility of multiphoton excitation. The dye laser was calibrated with a neon optogalvanic cell[7], and all the frequencies for the high resolution work (NO_2 FEX, N_2O_4

PIFEX) were specified as vacuum-calibrated whereas the NO_2Cl wavelengths are specified as air calibrated. The reason for this is that the dye laser specifies wavenumbers as vacuum-calibrated and wavelength as air-calibrated.

The NO_2 and N_2O_4 spectra were recorded in an automated fashion by stepping the dye laser and collecting 100 shots per wavenumber setting. The NO_2Cl experiment which required the beta barium borate crystal for doubling the frequency of the dye laser, was performed by a manual adjustment of the angle of the doubling crystal to optimize the power for each datum. The laser power was measured by a photodiode (EG&G GPD100) placed at the exit window of the vacuum chamber.

The fluorescence was collected with the recessed 7.6 cm f/1 lens and focused onto the filtered (Corning 7-52 or 3-72) photocathode of a Hamamatsu R636 or RCA C31034A PMT, for the PIFEX and NO_2 FEX spectra. For NO_2 fluorescence near the dissociation threshold a few spectra were recorded for the strongest parallel band in which the fluorescence was filtered via a synchronously scanned monochromator to a particular vibrational level of the ground state.[8,9] This synchronously scanned fluorescence was focused onto the entrance slit of a 0.3 m McPherson monochromator (model 218) in order to monitor emission to v=1 of ν_1 and ν_2. The slits were set at 1 mm width corresponding to a spectral window of 2.6 nm or less than 160 cm^{-1} in the 400 to 450 nm range. This slit width is 10 times the scan range of 15 cm^{-1} thus there is no need to scan the monochromator synchronously since the fluorescence intensity shouldn't change greatly due to v=1 slightly changing position from the peak position of the slit resolution window. One concern these 160 cm^{-1} wide slits raises is that of distinguishing between fluorescence to $2\nu_2$(1500 cm^{-1}) and ν_1(1320 cm^{-1}). If the slits are set to observe ν_1, the majority of fluorescence viewed is that of 1160 - 1480 cm^{-1}. The 1480 cm^{-1} is very close to 1500 cm^{-1}, thus there could be a minor $2\nu_2$ contribution to the ν_1 filtered fluorescence.

The synthesis of NO_2Cl followed the procedure of Volpe et. al.[10] described in chapter 2.

As stated earlier each sample was seeded in 300 torr helium. The seeding ratio for each was determined by the low temperature bath: a carbon tetrachloride/dry ice bath (-23 °C) for N_2O_4 yielded 50 torr ~15%; an acetonitrile/dry ice bath (-50 °C) for NO_2 yielded 10 torr ~ 3%; and a methanol/dry ice bath (-80 °C) for NO_2Cl yielded to a pressure of 15 torr ~5%.

RESULTS

A. NO_2Cl Pifex

The NO_2Cl PIFEX spectra were reproducible within the spread illustrated in Figure 3.1 for 4 scans in the 244 - 269 nm range. The spectra of Figure 3.1 have been corrected for the dye laser spectrum, but not to absorption cross section. These spectra were normalized to constant area and averaged. The averaged spectra were normalized to absorption cross section[11] and linked to averaged spectra of other dye coverage. The resultant spectrum which gives the relative fluorescence quantum yield from 230 to 290 nm, is illustrated in Figure 3.2. There were no sharp features seen in the spectrum implying a direct dissociation for NO_2Cl. The threshold wavelength (267 nm) for the formation of NO + O + Cl is indicated on the figure by the vertical dotted line. In the lower half of Figure 3.2 are the power profiles of the laser for the 3 dyes. The spectra were linked at laser power greater than ½ the maximum power, to minimize any small nonlinear deviations of fluorescence with respect to laser power. As the wavelength decreases from 290 nm the fluorescence quantum yield initially increases until it reaches a plateau at 268 nm. A steep decrease of 30% in ϕ_f occurs as the excitation is scanned from 268 to 244 nm. When the excitation is scanned below 244 nm, ϕ_f appears to rise again but note the fall-off of the dye yield and the noise of Figure 3.1 below 235 nm.

B. N_2O_4 Pifex

The N_2O_4 spectrum was obtained by scanning the laser from 337 to 348 nm. These spectra, uncorrected for laser power, are presented with the corresponding laser power profiles in Figures 3.3-3.6. The threshold wavelengths for $\underline{NO_2 + NO + O}$ at 298 K (334 nm) and 0 K (338 nm) are indicated by vertical lines in each spectrum.[6] The 0 K threshold should be the more appropriate threshold for the expansion cooled molecules. The fluorescence profile closely follows the laser profile.

The background indicated by a 1:4 ASE (Amplified Spontaneous Emission) to laser ratio indicates an offset in the laser power and fluorescence profile which had to be corrected. One point to keep in mind is the ASE may not remain constant across the scan range as implied in Figures 3.3-3.6. It has been demonstrated by other researchers that the ASE may decrease when lazing occurs because lazing depopulates excited states before ASE may occur.[12]

The offset in the fluorescence (background fluorescence due to ASE) which is readily apparent in the beginning and end of the spectrum when there is no lasing is subtracted from the laser power profile and the NO_2* emission profile. The net emission profile was normalized to the net laser profile and N_2O_4 absorption cross section as specified by Bass et. al.[13]. The resultant spectrum (4 superimposed spectra) is displayed along with a laser power profile in Figure 3.7. The quantum yield does seem to be uniform about some constant value ~0.9 with error bars of ±10%. The quantum yield profile still has a contour mimicking that of the laser power probably due to the nonuniformity of the ASE level across the spectrum.

If the NO_2^* fluorescence following N_2O_4 coincides with the absorption cross section as concluded by Inoue et. al.[14], then the fluorescence quantum yield should remain constant in the absence of dissociation.

C. NO_2 FEX Spectra

1. Dissociation Threshold

The fluorescence of NO_2 near its dissociation threshold produced a very clear determination of the bond dissociation energy. Nine reproducible scans were taken over this region with narrow (100 ns) and wide (10μs) gate widths at 500 ns delay. By noting the wavelength at which the fluorescence terminates, the value of D_0 is obtained. For both gate width settings the wavelength value corresponding to D_0 is 3979.4±.02Å. The 9 reproducible scans and the laser power profile from the photodiode are illustrated in Figures 3.8-3.34. The D_0 values are summarized in Table 3.3. The value of Douglas and Huber[15] of 3979±0.1Å determined from the onset of the diffuse band of NO_2 by high resolution spectroscopy seems to be consistent with our value. The room temperature NO_2 LIF experiment by Uselman and Lee gave a value of 3983Å by noting the disappearance of fluorescence.[3] An improvement of this experiment was carried out by Chen and coworkers[4] in which NO_2 LIF was performed subsequent to supersonic cooling to give a D_0 of 3978.2±0.2Å. Chen's results agrees with ours once the our vacuum-calibrated value of 25129.35 cm^{-1} is converted to give an air-calibrated value of 25136.41 cm^{-1} or 3978.3±0.03Å.

A relatively small amount of continuum fluorescence appeared at energies greater than the dissociation threshold (Figures 3.35-3.37). These spectra show the fluorescence rising as the energy increases from 25137 cm^{-1} to 25500 cm^{-1}. This fluorescence is not corrected for the laser power which decreases with increasing energy. When the fluorescence is corrected for laser power in these 3 reproductions, we obtain spectra which rise in a more exponential fashion (Figures 3.38-3.43).

One possibility is that this fluorescence is attributed to $N_2O_4 + h\nu \rightarrow NO_2^* + NO_2$. The absorption cross section of N_2O_4 is not known above 390 nm. Bass et. al.[13] determines the 390 nm N_2O_4 absorption cross section to be $\tilde{}2.8X10^{-20}$ cm^2. The absorption spectra of Hall and Blacet[16], as read from a small figure, is about $1.8X10^{-20}$ cm^2 at 392 nm (25500 cm^{-1}). The laser fluence of 14.1 mj/(pusle cm^2) is so low that this fluorescence is not 2-photon NO excitation.

Another possible explanation for the slight rise in fluorescence after D_0 is due to laser light ASE (Amplified Spontaneous Emission) tradeoff. The full spectrum and the laser power profile including the ASE contribution are displayed in Figures 3.44 and 3.45. It has been noted from dye laser performance research of past experimenters that the ASE decreases as the laser power increases and vice versa.[12] This is due to the fact that lasing selectively robs the system of excited state dye molecules needed for ASE. The fluorescence doesn't rise above the extrapolated initial ASE level (Figure 3.44). Whether the spectra in Figures 3.35 - 3.37 are due to N_2O_4 PIF or an artifact due to ASE needs to be resolved with future experiments.

2. Spectral Structure Near the Dissociation Threshold

Three parallel bands ($\Delta K = 0$) were also observed in the vicinity of the dissociation threshold. Figures 3.46-3.51 shows the three parallel bands with band origins at 25061.8 cm^{-1}, 24846.6 cm^{-1}, and 24791.0 cm^{-1}. The spectrum in Figure 3.48 is the most convincing case. These bands were determined from term value equations below used to determine the separations of P(4), P(2), R(0), R(2), and R(4).[9,15,17,18,19]

$$F(N'') = T''_v + \overline{B''} N''(N''+1) \; for K = 0 \qquad (3.1)$$

$$\overline{B''} = \frac{B''+C''}{2} \qquad (3.2)$$

F''(N'') is the ground state rovibronic term value, T_ν'' is the ground state vibronic energy, N'' is the quantum number for the total angular momentum apart from spin, and B" and C" are the ground state rotational constants.

$$F_1(N') = T'_v + \overline{B'} N'(N'+1) + \frac{1}{2}\overline{\epsilon_{bb}} \qquad (3.3)$$

for K = 0

$$F_2(N') = T_v'' + \overline{B'} N'(N'+1) - \frac{1}{2}\overline{\epsilon_{bb}}(N'+1) \qquad (3.4)$$

for K = 0

$$\overline{\epsilon'_{bb}} = \frac{1}{2}(\epsilon'_{bb}+\epsilon'_{bb}) \qquad (3.5)$$

$F_1(N')$ and $F_2(N')$ are the high and low energy component rovibronic term values, $\bar{B}'$ is the excited state rotational constant, and ϵ'_{bb} and ϵ'_{bb} are the excited state spin-rotation coupling constants.

By taking the differences of the above equations for different N values one may derive relationships between the difference of the peak positions and the rotational constants.

$$\overline{B''} = \frac{(R(0)-P(2))}{6} \qquad (3.6)$$

$$\overline{B''} = \frac{(R(2)-P(4))}{14} \qquad (3.7)$$

$$\overline{B'} + \frac{\epsilon'}{10} = \frac{(R(2)-P(2))}{10} \qquad (3.8)$$

$$\overline{B'} + \frac{\epsilon'}{18} = \frac{(R(4)-P(4))}{18} \qquad (3.9)$$

The rotational temperature was determined following the prescription of Herzerg.[20]

$$I = C\nu A_{KN} g_{KN} e^{\frac{-F(N,K)}{KT}} \qquad (3.10)$$

I = intensity of fluorescence

C = constant

ν = wavenumber of transition

A_{KN} = rotational linestrength

g_{KN} = statistical weight of the lower state

$$A_{KN}(R) = \frac{[(N+1)^2 - K^2]}{[(N+1)(2N+1)]} \qquad (3.11)$$

$$A_{KN}(P) = \frac{[N^2 - K^2]}{[N(2N+1)]} \qquad (3.12)$$

for parallel transitions

g_{KN} = (rotational weight or degeneracy)(Nuclear statistical weight)

= (2N+1) g_n

Since O atoms are bosons (spin = 0) then

$$g_n = \frac{1}{2}(2(0)+1)[(2(0)+1)+1](2(1)+1) = 3 \qquad (3.13)$$

for Ψ_{symm}

$$g_n = \frac{1}{2}(2(0)+1)[(2(0)+1)-1](2(1)+1) = 0 \qquad (3.14)$$

for $\Psi_{antisymm}$

The Pauli principle leads to:

for symmetric levels of rotation $\Psi_{symm} = 3$

for antisymmetric levels of rotation $\Psi_{antisymm} = 0$

Where for K = 0, even values of N lead to Ψ_{symm} and odd values of N lead to $\Psi_{antisymm}$.

$\therefore g_{Kn} = 2(N+1)3$ for even levels of N in which K = 0.

By taking the ratio of intensities (Equation 3.10) we obtain for the R branch transition of NO_2 the following formulae for rotational temperature.

For R(0) & R(2):

$$T_{ROT[R(0)/R(2)]} = \frac{3.62}{\ln\left(\frac{3R(0)}{R(2)}\right)} \qquad (3.15)$$

For R(0) & R(4):

$$T_{ROT[R(0)/R(4)]} = \frac{12.07}{\ln\left(\frac{5.04R(0)}{R(4)}\right)} \qquad (3.16)$$

The temperature was determined to be 3-5 K from Equations 3.15 and 3.16. The results of reproductions of the 3 B_2 parallel bands near the dissociation region are displayed in Tables 3.1 and 3.2.

The most promising parallel band (T_ν = 24846.6 cm^{-1}, Figure 3.48) was subjected to the synchronous scan method.[8,9] The synchronous scan method collects fluorescence to a particular vibrational level of the ground state (i.e. v_1 of ν_2 mode) as illustrated in Figure 3.52. The difference between the excitation and observation frequency needs to be maintained at some constant value equivalent to the energy of the vibrational state monitored. The monochromator acts as a constant energy difference filter with respect to the excitation frequency, rejecting all radiation outside of the narrow band peaked at $\nu_{excitation}$ - v_1. Since $\nu_{excitation}$ is scanned this requires the monochromator to be scanned synchronously; however as pointed out earlier if the mmonochromator slits are wide enough in relation to the scanning range of the dye laser then the monochromator may remain fixed. The band located at 24846.6 cm^{-1} was scanned while monitoring fluorescence to ν_1 (stretching vibration = E_{photon} - 1321 cm^{-1}) and ν_2 (bending = E_{photon} - 750 cm^{-1}). This was carried out in order to see if the excited state selects a particular vibrational state, and to better determine the symmetry of the excited state to confirm that the band in question is a parallel band. The resultant spectra are shown in Figures 3.53 (ν_1) and 3.54 (ν_2). The spectra are very similar with the exception that the intensity of the P(2) and R(0) peaks is larger than the other peaks in the ν_2 spectrum as compared to the ν_1 spectrum. Another interesting point is that the P(2) and R(0) peaks seem to have grown relative to R(2) in both ν_1 and ν_2 spectra compared to the total fluorescence collection spectra (Figure 3.48). Note that all spectra are normalized to the largest peak intensity.

DISCUSSION

A. Relative Quantum Yield for NO_2 Fluorescence as NO_2Cl is Photolyzed in the Vicinity of the NO + O + Cl Threshold

The manifestation of the onset of the NO + O + Cl channel competing against the fluorescence channel NO_2^* + Cl is seen in the fluorescence quantum yield profile of NO_2Cl (Figure 3.2). The NO_2Cl PIFEX spectrum shows that ϕ_f (Fluorescence quantum yield) increases, decreases, and possibly increases again as the energy increases. The initial increase in ϕ_f as the laser is scanned from 290 to 269 nm is possibly due to the resulting NO_2 fragment usurping a larger amount of energy, thus fluorescing at more energetic (shorter lifetime) frequencies. The fall in ϕ_f from 269 to 244 nm is consistent with the NO production channel (NO+O+Cl) opening while the NO_2^*+Cl channel dampens. The subsequent rise of ϕ_f could be due to experimental error and an artifact due to normalizing over a rapidly decreasing laser power. Thus as $\lambda_{photolysis}$ decreases, two opposing mechanisms are at work, the opening of the NO + O + Cl channel which works to decrease ϕ_f and the decrease in τ_f which strives to bring about an increase the fluorescence. Initially the former mechanism wins out but as $\lambda_{photolysis}$ approaches 267 nm the latter mechanism of dissociation becomes more significant.

Oh[21] compared the NO_2 LIF signal strength at 410.29, 415.76, and 421.0 nm to the room temperature NO_2Cl PIF signal strength at 266, 248, and 193 nm. The fluorescence quantum yield was determined to be $0.9\pm.5(2\sigma)$ at 266 nm, $0.7\pm0.2(2\sigma)$

at 248 nm, and 0.03±0.03(2σ) at 193 nm. These results are consistent with those presented in Figure 3.2 which show a 30% decrease in fluorescence between 267 and 244 nm.

B. Relative Quantum Yield of NO_2 Fluorescence as N_2O_4 is Photolyzed in the Vicinity of NO_2 + NO + O Threshold

The N_2O_4 PIFEX spectra show uniform fluorescence quantum yield as the laser is scanned past the onset of the NO production channel (Figure 3.7). The 0 K threshold value of 338 nm, which is the more appropriate threshold value for expansion-cooled precursors, is very close to the edge of the spectrum. It is possible the laser failed to adequately scan the dissociation threshold.[6] It appears that a decrease in ϕ^f is beginning but it is still within the error bars of the experiment. The scan should have continued further to the lower wavelengths; however the laser stopped lasing in this region.

The N_2O_4 PIFEX spectra shown in Figure 3.7 seems to have a small drop at edges of the spectrum. This may be vestigial structure of the laser power normalization. The laser power as indicated in Figure 3.3 has two components, the true wavelength-dependent laser emission and wavelength-independent ASE. The ASE is the baseline laser power which is seen as the flat region at the beginning and end of the power spectrum. The assumption is made that this ASE stays constant throughout the spectrum such that it may be subtracted from the spectrum leaving a net laser signal. In actuality once the lasing begins some of this ASE is converted to lasing, thus effectively lowering the baseline. The net effect this would have on the power-normalized spectra is to falsely increase it in the middle where the ASE→laser conversion is the greatest.

C. Fluorescence of NO_2 excited in the vicinity of the NO + O Threshold

1. Spectral Features near D_0

The NO_2 FEX spectra provide insight into the nature of the excited states. The rotational constants for the ground state (X^2A_1) and the excited state (A^2B_2) for the 3 parallel bands shown in Figures 3.46-3.51 and Tables 3.1-3.2 are consistent with those of the NO_2 fluorescence excitation experiments near 455 nm Hayashi and coworkers.[9] The B' values are smaller than B'' implying that the excited state has a larger bond angle than the ground state. This seems odd in that the $^2B_2$ equilibrium bond angle is 102°; whereas the ground state equilibrium angle is 134°.[22] One possible solution proposed by Hayashi is that the $^2B_2$ state is perturbed by the high vibrational levels of ground state.[9] The " mean angle " of the $^2A_1$ state when excited by 400 nm radiation is about 180°. Once this couples with the $^2B_2$ state the angle could be > 134° allowing for the B' to be smaller than B''. The $^2B_2$

state may couple with the $^2A_1$ via 3 mechanisms:[23] (1) Coriolis coupling of rotations and vibrations, (2) spin-orbit coupling, and (3) vibronic coupling through ν_3. Since the bands under discussion have low N values then mechanism #1 is ruled out. The lifetime broadening of NO_2 supports the existence of the $^2B_2$-$^2A_1$ coupling referred to as Douglas coupling.[24]

The parallel bands show the rotational temperature determined from R(0)/R(2) to be ~3 K, whereas those from R(0)/R(4) are near 5 K. This could be due in part to incomplete thermal equilibrium of the supersonically expanded NO_2. Another possible cause for these two temperatures is the uncertainty in the intensity values for R(0), R(2), and R(4). The baseline of the system is approximate and the peak intensities were derived solely from peak heights, because the inability to completely resolve peaks made it impossible to integrate the area under a peak. If this is the case more credence should be placed in the 3 K value derived from R(0)/R(2) since the R(2) intensity is greater than R(4) making the baseline error account for a smaller percentage.

2. Synchronous Scan of the T_ν=24846.6 cm^{-1} band

The NO_2 FEX spectra derived from the synchronous scans for the parallel band located at 24846.6 cm^{-1} (Figures 3.53 and 3.54) show a spectral invariance in regards to monitoring ν_1 or ν_2. This rules out the possibility of mode selectivity as observed by Hayashi. The ν_1/ν_2 fluorescence invariance is expected in first order since both ν_1 and ν_2 are symmetric. The ν_2 monitored spectrum seems cleaner than the total fluorescence and the ν_1 monitored spectra. Due to the monochromator slit width the ν_1 monitored band could contain contributions from fluorescence to $2\nu_2$. These spectra do appear different from the NO_2 FEX spectra of the 24846.6 cm^{-1} band with total fluorescence collection (Figure 3.48). This is probably due to the Franck-Condon factors of fluorescence to $2\nu_1$, $2\nu_2$, $3\nu_1$, etc. Based on these observation the 24846.7 cm^{-1} band may be exhibiting a certain amount of mode selectivity. This could be due to the character of the excited state such that the Franck-Condon factor is larger for fluorescence to ν_2 than to ν_1.

One peak which exhibits different relative intensity in the total fluorescence, as opposed to fluorescence monitored to ν_1 and ν_2, is arbitrarily labeled " α ". This peak increases (slower rate of decrease) for the ν_1/ν_2 selected fluorescence with respect to total fluorescence collection. One possible explanation for this is that the α peak has little or no ν_3 contributions, thus when the total fluorescence is observed it doesn't grow as fast at the other peaks. Again it is possible that this may be attributed to better Franck-Condon overlap of the excited state to other vibrational states ($2\nu_1$, $2\nu_2$, $3\nu_1$, ...) which correspond to other peaks.

CONCLUSION

The study of NO_2 fluorescence at energies capable of dissociating NO_2 has been carried out for NO_2Cl, N_2O_4, and NO_2 by laser excitation. The NO_2Cl PIFEX spectrum shows a large drop (~30%) in ϕ_f as $\lambda_{photolysis}$ decreases from 269 to 244 nm indicative of the NO production channel.

The fluorescence excitation spectra for N_2O_4 appear flat in the 336 - 346 nm region capable of producing NO at 336 - 339 nm. This suggests that very little nitric oxide is produced. To better understand the N_2O_4 system, future studies need to be done at slightly shorter wavelengths (325 - 340 nm) utilizing a higher laser:ASE ratio.

The NO_2 dissociation threshold of 3978.3±0.03Å is in accord with the previous supersonic jet determination by Chen (3978.2±0.2Å), with both measures expressed as air-calibrated. A second fluorescence observed beyond D_0 is tentatively attributed to N_2O_4. An investigation of three parallel bands derived from NO_2 FEX experiment near D_0 (25137 cm^{-1}) yielded information on rotational constants. For three different parallel bands B' was less than B'' implying that the excited states' ONO angle was larger than the ground state.

REFERENCES

[1] A.B. Collear and R.E.M. Hedges, Trans. Faraday Soc. **66**, 1618 (1970).

[2] H. Okabe, J. Am. Chem. Soc. **93**, 7095 (1971).

[3] W. Uselman and E.K.C. Lee, J. Chem. Phys. **64**, 3457 (1976).

[4] C.H. Chen, D.W. Clark, M.G. Payne, and S.D. Kramer, Optics

Comm. **32**, 391 (1980).

[5]D.L. Baulch, R.A. Cox, R.F. Hampson, Jr., J.A. Kerr, J. Troe, and R.T. Watson, J. Phys. Chem. Ref. Data, **9**, 467 (1980).

[6]I.C. Hisatsune, J. Phys. Chem., **65**, 2249 (1961).

[7]V. Kaufman, B. Edlén, J. Phys. Chem. Ref. Data **3**, 825 (1974).

[8]N. Sugimoto, S. Takezawa, Chem. Phys. Let. **121**, 367 (1985).

[9]T. Hayashi, T. Imasaka, and N. Ishibashi, Chem. Phys. **109**, 145 (1986).

[10]M. Volpe and H.S. Johnston, J. Am. Chem. Soc. **78**, 3903 (1956).

[11]A.J. Illies, G.A. Takacs, J. Photochem. **6**, 35 (1976).

[12]M.J. Mckee, J. Lobin, and W.A. Young, Applied Optics **21**, 725 (1982).

[13]A.E. Bass, A.E. Ledford, Jr., and A.H. Laufer, J. Res. Natl. Bureau Stands. **80**, 143 (1975).

[14]G. Inoue, Y. Nakata, Y. Usui, H. Akimoto, and M. Okuda, J. Chem. Phys. **70**, 3689 (1979).

[15]A.E. Douglas and K.P. Huber, Can. J. Phys. **43**, 74 (1964).

[16]T.C. Hall, Jr., and F.E. Blacet, J. Chem. Phys. **20**, 1745 (1952).

[17]R.E. Smalley, L. Wharton, D.H. Levy, J. Chem. Phys. **63**, 4977 (1975).

18W.T. Raynes, J. Chem. Phys. **41**, 3020 (1964).

[19]C.C. Lin, Phys. Rev. **116**, 903 (1959).

[20]G. Herzberg, <u>Electronic Spectra and Electronic Structure of</u>

Polyatomic Molecules Volume III, (Van Nostrand Reinhold, New York, 1966).

[21] D. Oh, Ph.D. Thesis, University of California, Berkeley 1988.

[22] G.D. Gillispie, A.U. Khan, A.C. Wahl, R.P. Hosteny, M. Krauss, J. Chem. Phys. **63**, 3425 (1975).

[23] J.C.D. Brand, W.H. Chan, and J.L. Hardwick, J. Mol. Spectrosc. **56**, 309 (1975).

[24] A.E. Douglas, J. Chem. Phys. **45**, 74 (1966).

Intensities and Line Positions for the 3 Parallel Bands of NO_2 Near D_0

Table 3.1

Filename	Energy (CM^{-1})	Intensity	Assignment
CM596H.DAT	25058.018	0.45691	P(4)
	25059.863	0.61766	P(2)
	25062.621	0.64216	R(0)
	25063.951	0.59262	R(2)
CM598C.DAT	25058.018	0.39477	P(4)
	25059.850	0.57414	P(2)
	25062.621	0.63056	R(0)
	25063.854	0.60926	R(2)
CM599C.DAT	25058.018	0.41469	P(4)
	25059.836	0.56597	P(2)
	25062.621	0.61886	R(0)
	25063.938	0.6099	R(2)
	25065.123	0.41663	R(4)
CM598N.DAT	24842.746	0.37131	P(4)
	24844.811	0.92490	P(2)
	24847.410	1.00000	R(0)
	24848.631	0.64721	R(2)
	24849.607	0.24588	R(4)
CM597C.DAT	24842.844	0.43732	P(4)
	24844.822	0.89295	P(2)
	24847.410	1.00000	R(0)
	24848.703	0.74392	R(2)
	24849.438	0.52828	R(4)
CM598Q.DAT	24787.127	0.27406	P(4)
	24789.129	0.40073	P(2)
	24791.814	0.46187	R(0)

Filename	Energy (CM^{-1})	Intensity	Assignment
	24793.023	0.40183	R(2)
	24794.000	0.22842	R(4)
CM597E.DAT	24787.127	0.27675	P(4)
	24789.092	0.37141	P(2)
	24791.814	0.43489	R(0)
	24793.012	0.38887	R(2)
	24793.779	0.21940	R(4)

Table 3.1

NO_2 Parallel Band Spectroscopic Constants

Table 3.2

FILNAME	B'' R(O) P(2) a	B'' R(2) P(4) b	B' R(2) P(2) c	B' R(4) P(4) d	T R(0) R(2) e	T R(0) R(4) f	T_v g
CM596H	0.464	0.425	0.412		3.071		25061.797
CM598C	0.462	0.417	0.40		3.195		25061.821
CM599C	0.464	0.423	0.410	0.395	3.252	5.99	25061.816
CM598N	0.433	0.420	0.382	0.381	2.360	4.00	24846.647
CM597C	0.431	0.419	0.388	0.366	2.596	5.35	24846.655
CM598Q	0.448	0.421	0.389	0.382	2.924	5.20	24791.043
CM597E	0.454	0.420	0.392	0.370	2.990	5.24	24791.052

a - ground state rotational constant derived from R(0) and P(0) Eq. 3.6

b - ground state rotational constant derived from R(2) and P(4) Eq. 3.7

c - excited state rotational constant derived from R(2) and P(2) Eq. 3.8

d - excited state rotational constant derived from R(4) and P(4) Eq. 3.9

e - rotational temperature derived from R(0) and R(2)

f - rotational temperature derived from R(0) and R(4)

g - vibronic band origin

NO_2 Dissociation Threshold

Table 3.3

Filename	D_0 (cm^{-1}) (gate width 100 ns)	D_0 (cm^{-1}) (gate width 10 μs)
CM592D	25129.52	25129.43
CM592E	25129.43	25129.43
CM592F	25129.43	25129.43
CM595A	25129.53	25129.43
CM595B	25129.34	25129.34
CM595C	25129.43	25129.21
CM595D	25129.20	25129.20
CM596A	25129.20	25129.43
CM596B	25129.24	25129.24
MEAN	25129.36±0.13	25129.35±0.10

Figure 3.1

4 reproductions of NO_2 fluorescence from NO_2Cl Photolysis in a supersonic Jet as the photolyzing wavelength is scanned from 244 to 269 nm. This fluorescence is corrected for the laser power profile but not for the absorption cross section.

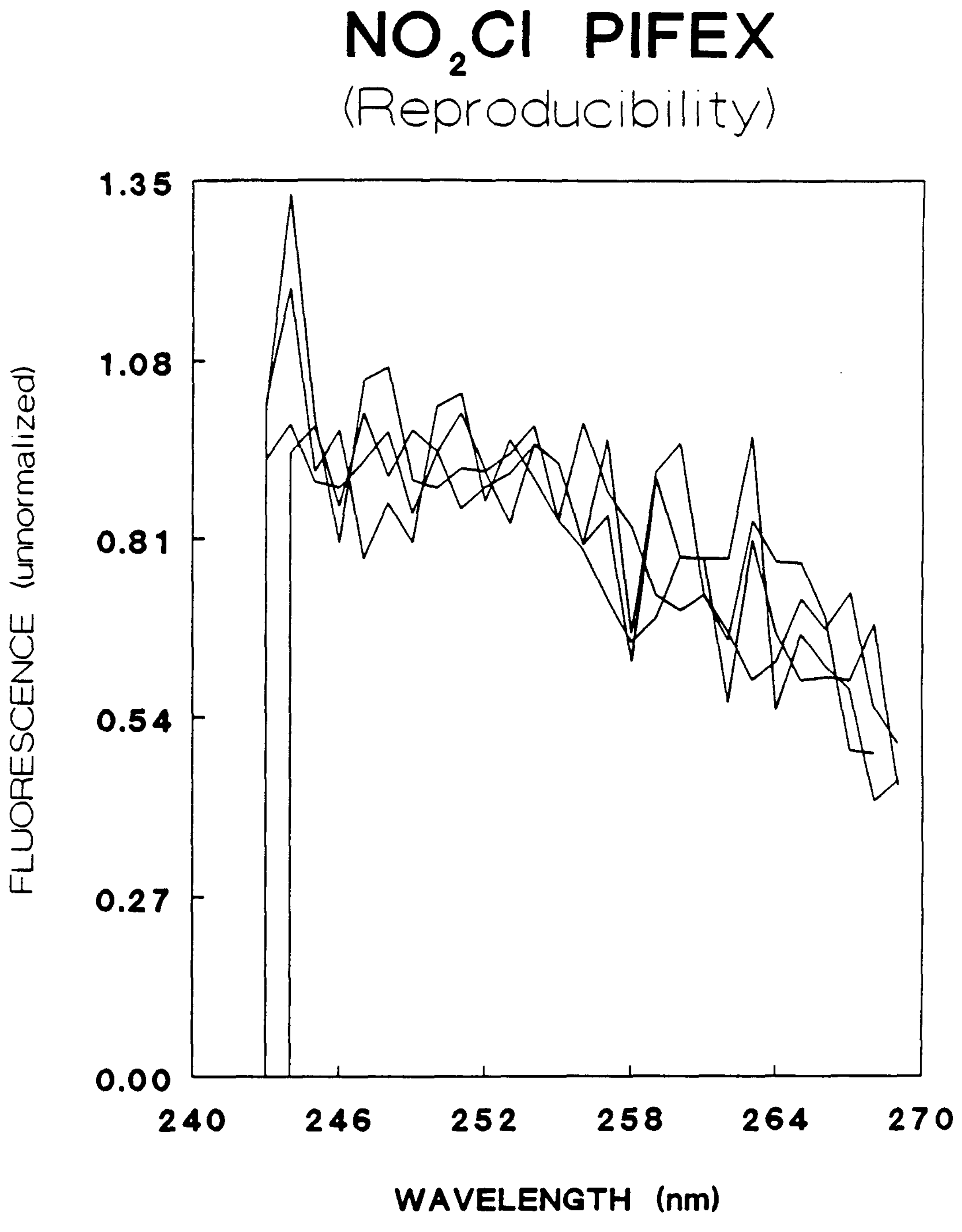

NO_2Cl PIFEX
(Reproducibility)
1.35
1.08
0.81
0.54
0.27
0.00
FLUORESCENCE (unnormalized)
240
246
252
258
264
270
WAVELENGTH (nm)

Figure 3.1

Figure 3.2

Relative fluorescence quantum yield spectrum of NO_2 following NO_2Cl Photolysis in the 230 to 290 nm range (upper solid curve). The lower dashed curves represent the dye laser (doubled) power profiles. The dashed vertical line represents the energetic barrier for the NO + O + Cl channel.

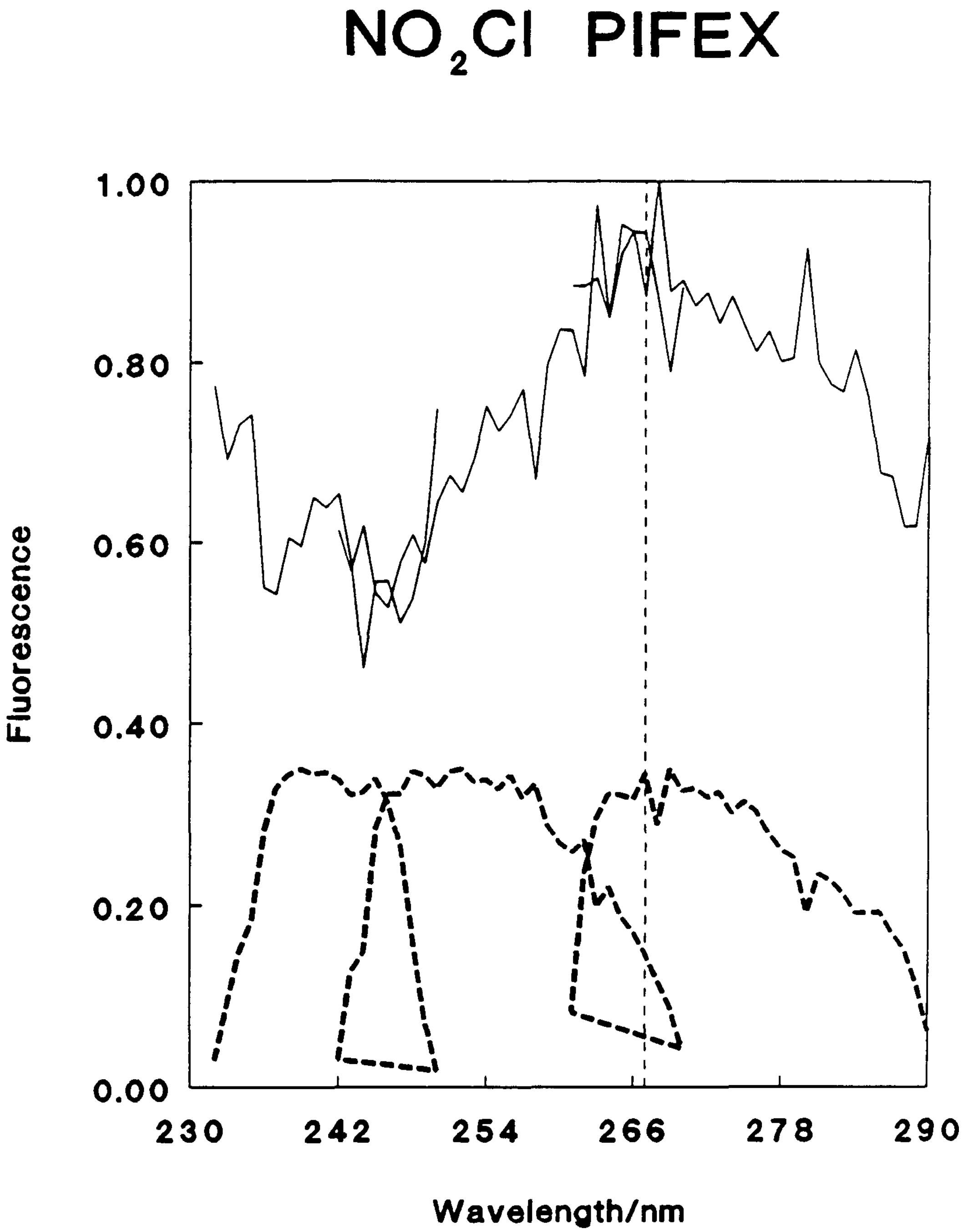
NO$_2$Cl PIFEX
Fluorescence
1.00
0.80
0.60
0.40
0.20
0.00
230
242
254
266
278
290
Wavelength/nm

Figure 3.2

Figures 3.3 - 3.6

The Photolysis Induced Fluorescence (PIFEX) spectra of N_2O_4 (solid curve). These NO_2 fluorescence spectra have not been corrected for the laser power profile or the absorption cross section. The dashed curve is the laser power profile including the Amplified Spontaneous Emission (ASE) which is seen as a broad band background fluorescence accompanying the laser light. The dashed vertical lines represent the threshold for the NO_2 + NO + O channel at 298 K (334 nm) and 0 K (338 nm).

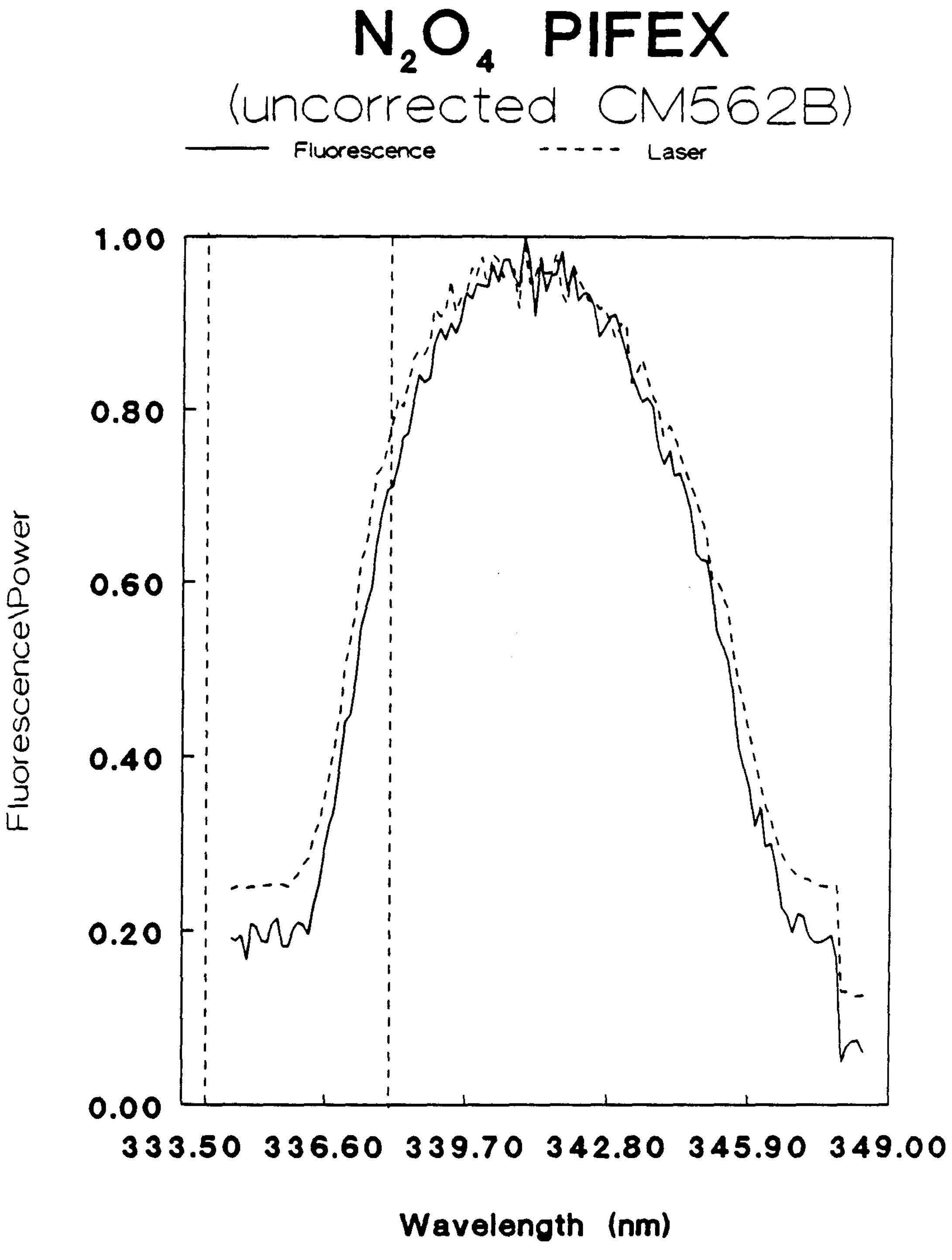
N_2O_4 PIFEX
(uncorrected CM562B)
Fluorescence
Laser
Fluorescence\Power
1.00
0.80
0.60
0.40
0.20
0.00
333.50
336.60
339.70
342.80
345.90
349.00
Wavelength (nm)

Figure 3.3

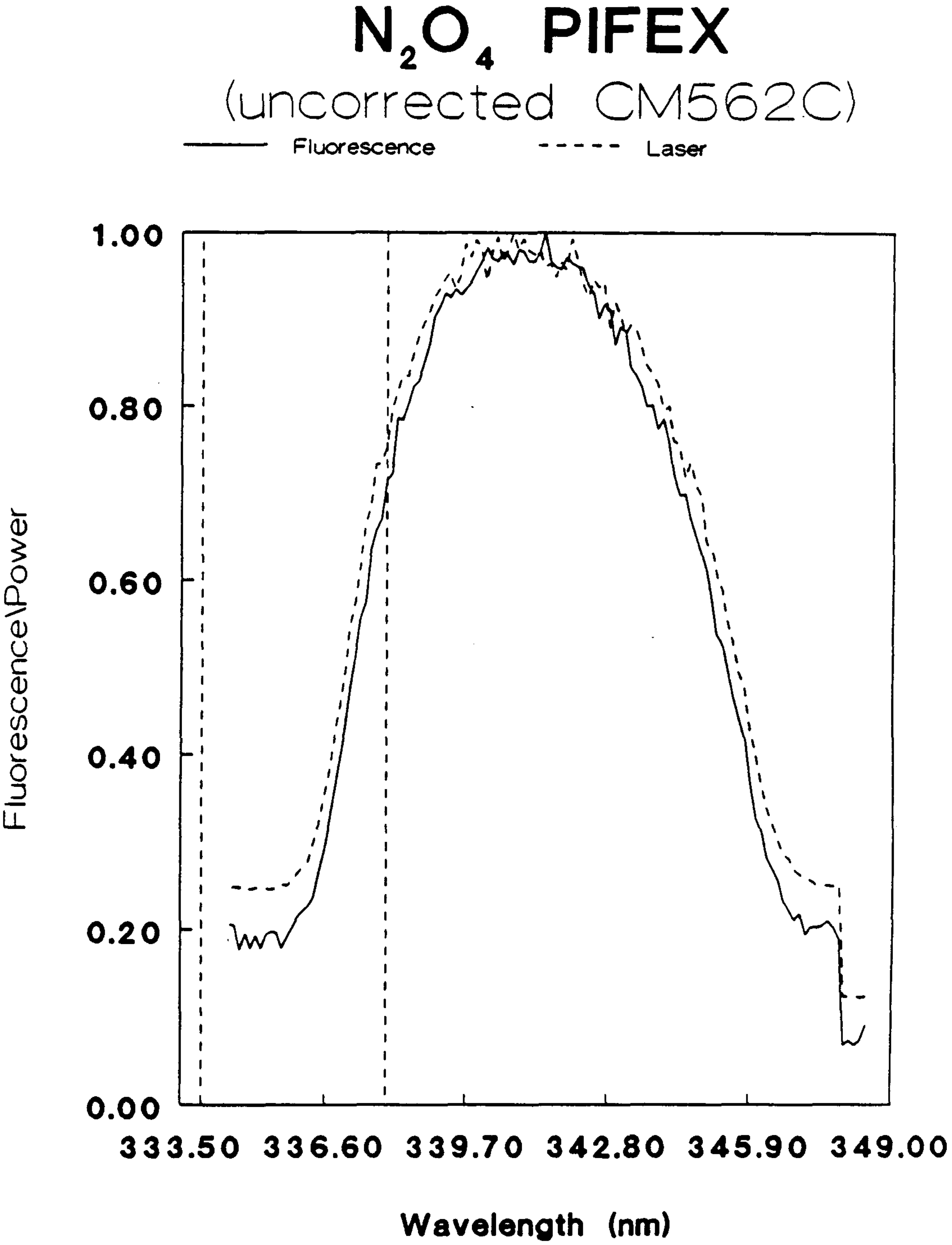
N$_2$O$_4$ PIFEX
(uncorrected CM562C)
Fluorescence
Laser
Fluorescence\Power
1.00
0.80
0.60
0.40
0.20
0.00
333.50
336.60
339.70
342.80
345.90
349.00
Wavelength (nm)

Figure 3.4

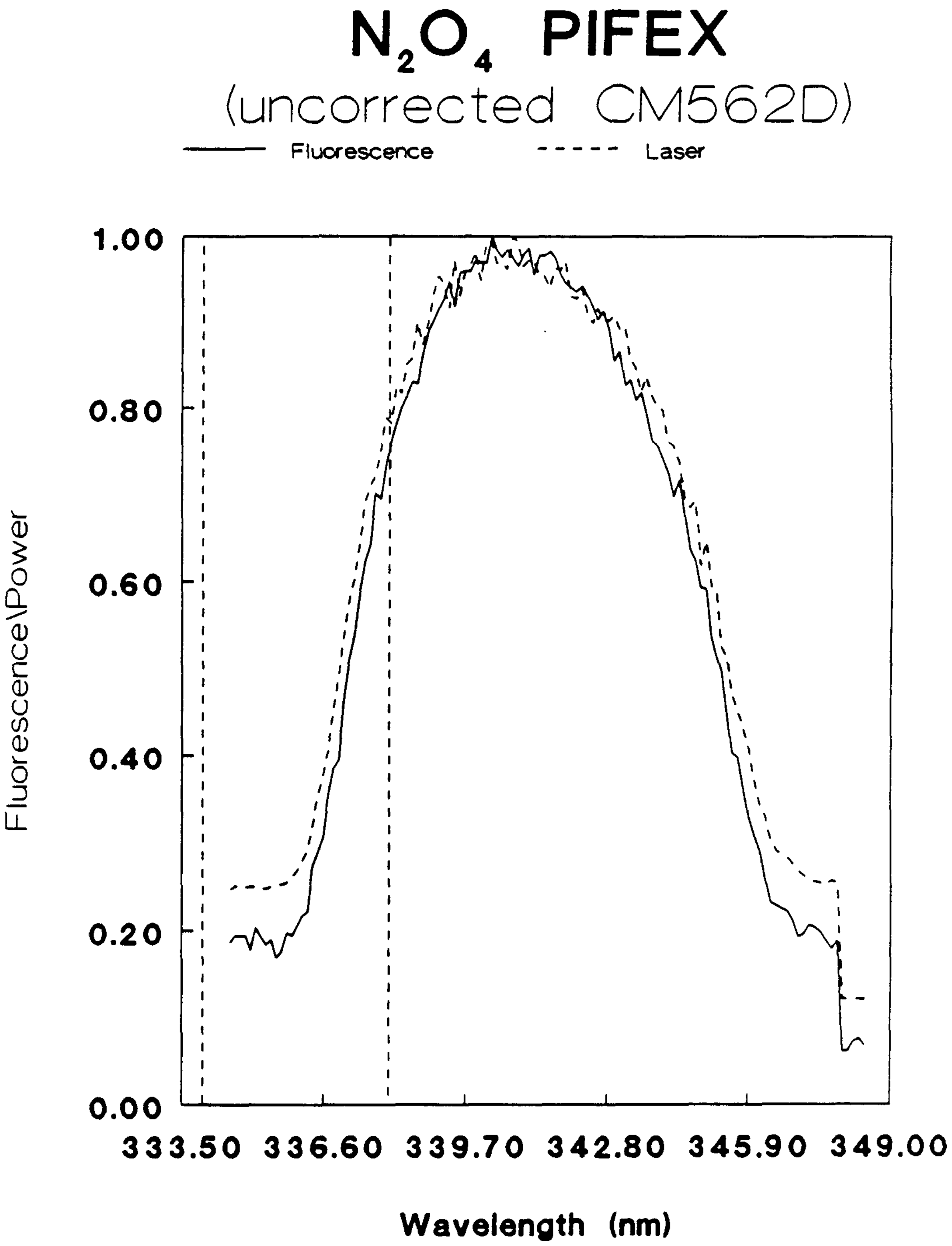
N_2O_4 PIFEX
(uncorrected CM562D)
Fluorescence
Laser
1.00
0.80
0.60
0.40
0.20
0.00
Fluorescence\Power
333.50
336.60
339.70
342.80
345.90
349.00
Wavelength (nm)

Figure 3.5

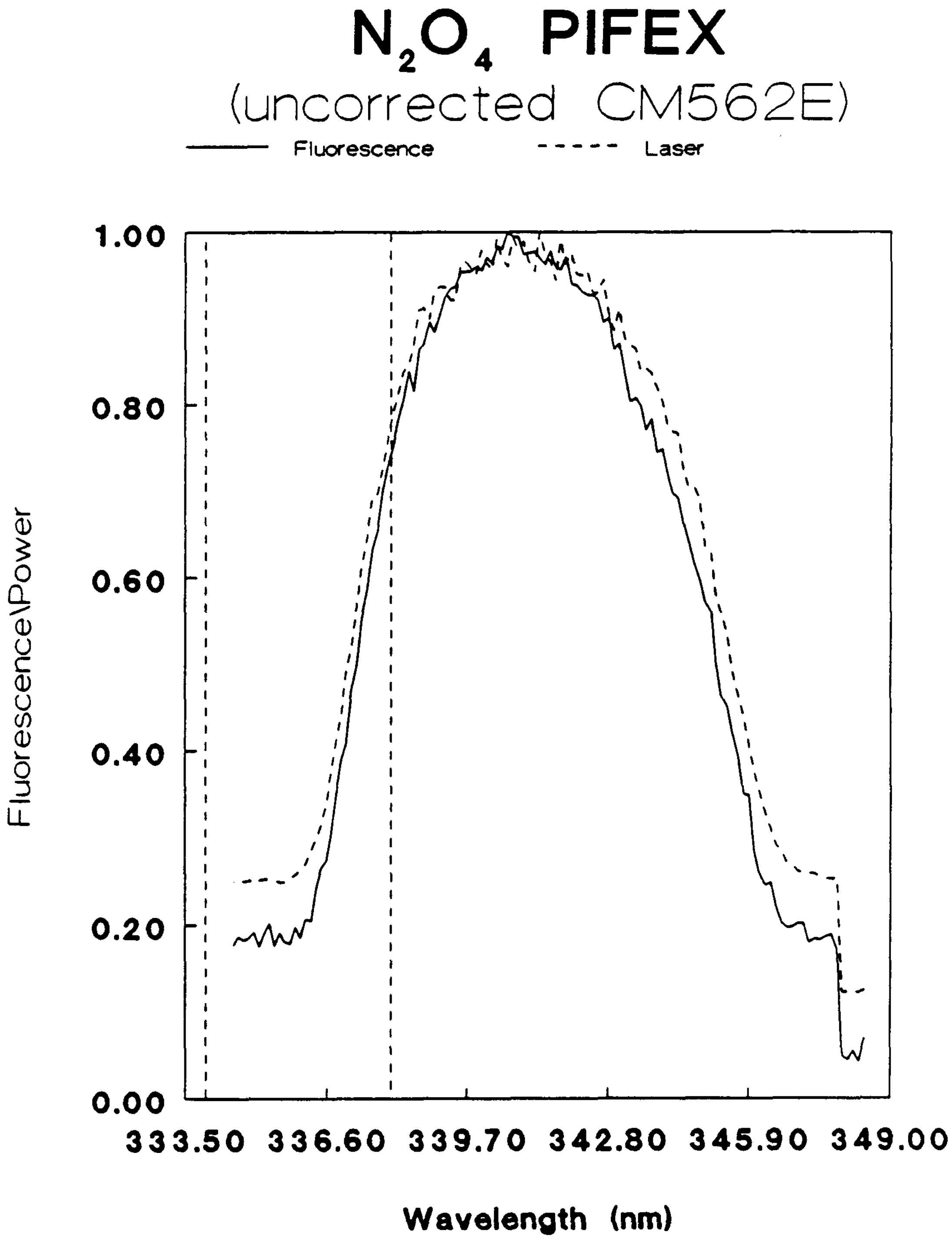
N2O4 PIFEX
(uncorrected CM562E)
Fluorescence
Laser
1.00
0.80
0.60
0.40
0.20
0.00
Fluorescence\Power
333.50
336.60
339.70
342.80
345.90
349.00
Wavelength (nm)

Figure 3.6

Figure 3.7

The relative quantum yield of NO_2 fluorescence following N_2O_4 photolysis. The dashed line at 338 nm marks the threshold for the NO_2 + NO + O channel at 0 K.

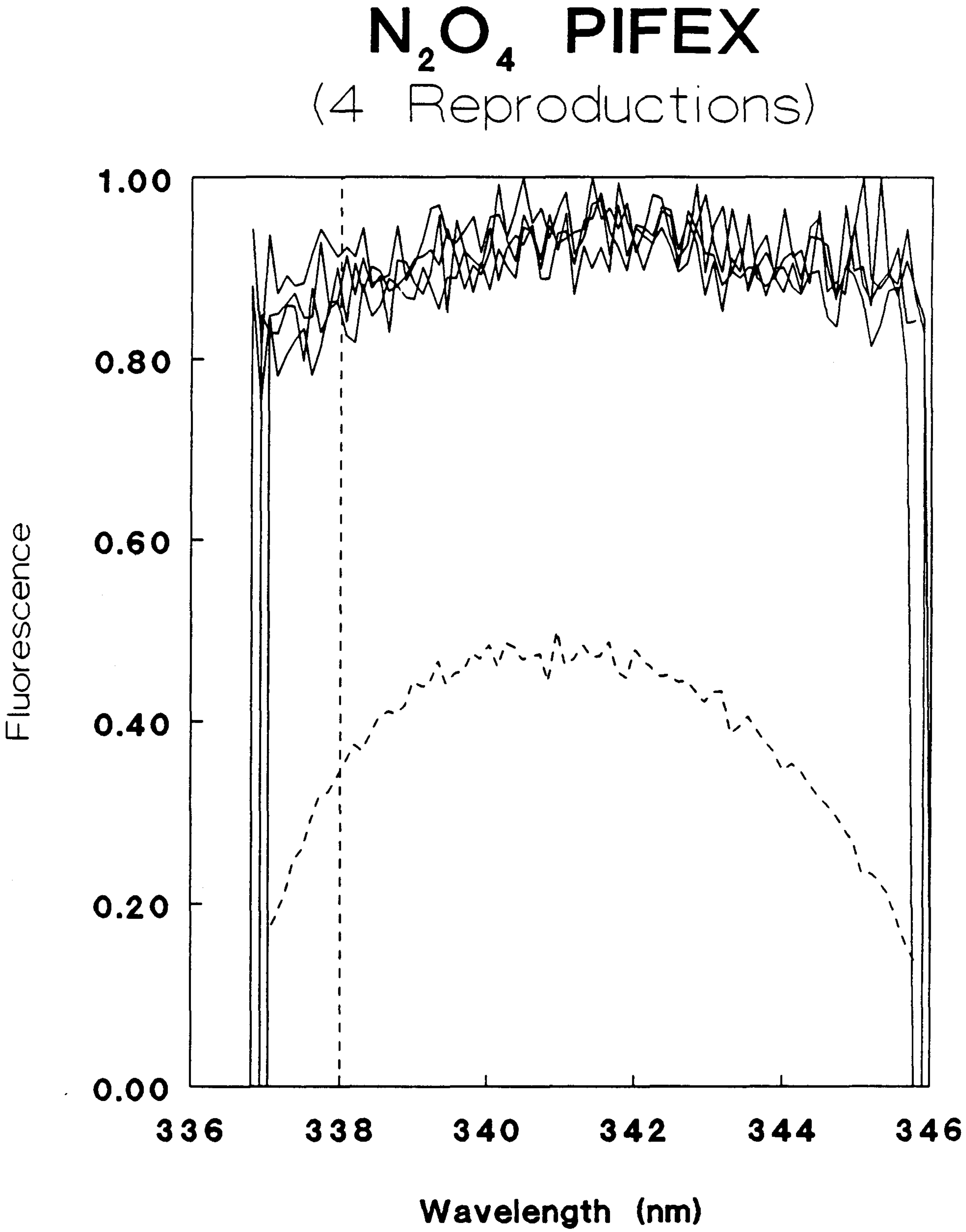

N_2O_4 PIFEX
(4 Reproductions)
Fluorescence
1.00
0.80
0.60
0.40
0.20
0.00
336
338
340
342
344
346
Wavelength (nm)

Figure 3.7

Figures 3.8 - 3.34

NO_2 fluorescence excitation scans at narrow (100 ns) and wide (10 μs) gate widths in the vicinity of D_0. The vertical line marks the D_0 determination ($NO_2 \rightarrow NO + O$). The laser power profile follows each pair of FEX spectra. The numbers given as the threshold (D_0) are observed for the figures presented.

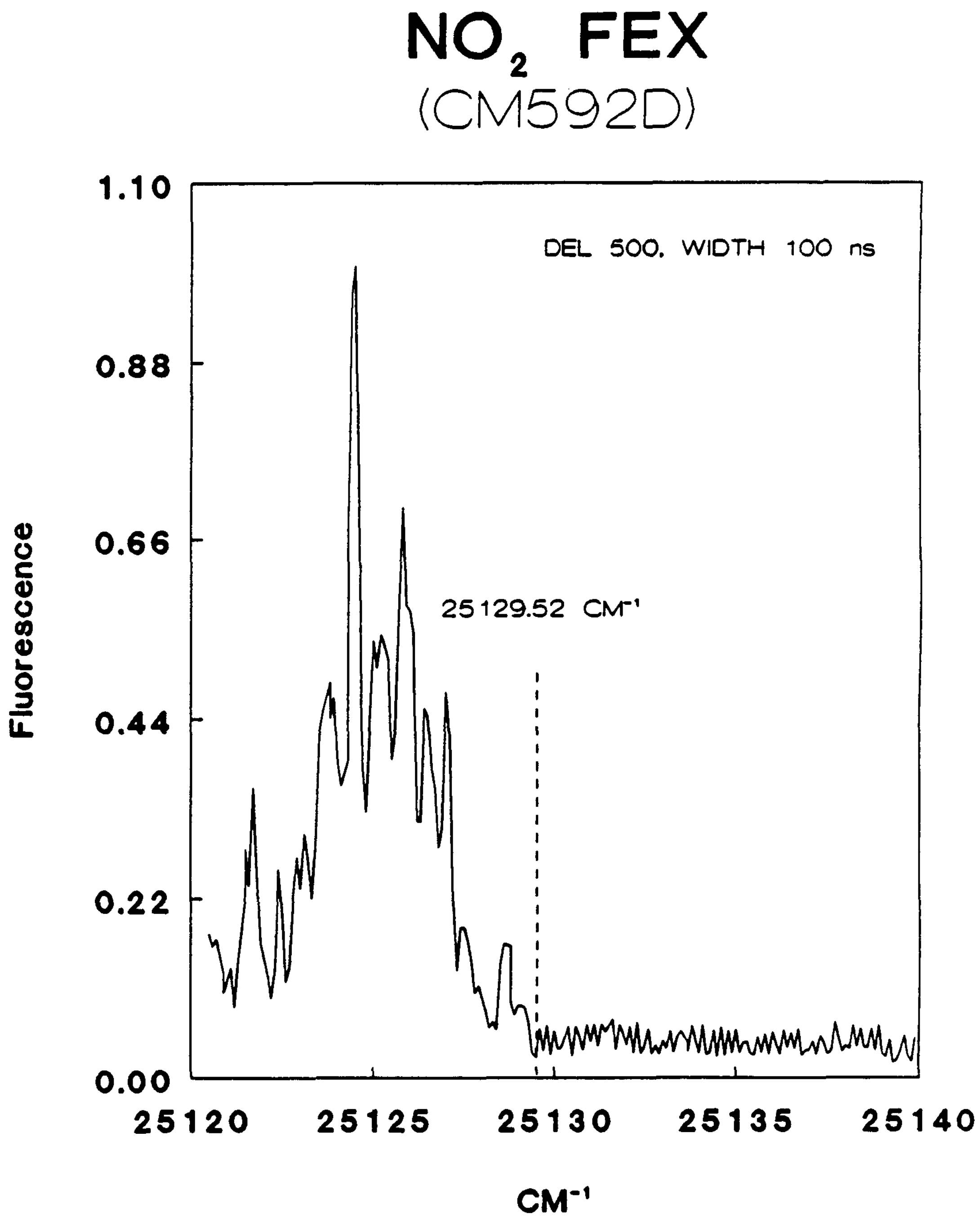
NO_2 FEX
(CM592D)
DEL 500, WIDTH 100 ns
25129.52 CM⁻¹
Fluorescence
1.10
0.88
0.66
0.44
0.22
0.00
25120
25125
25130
25135
25140
CM⁻¹

Figure 3.8

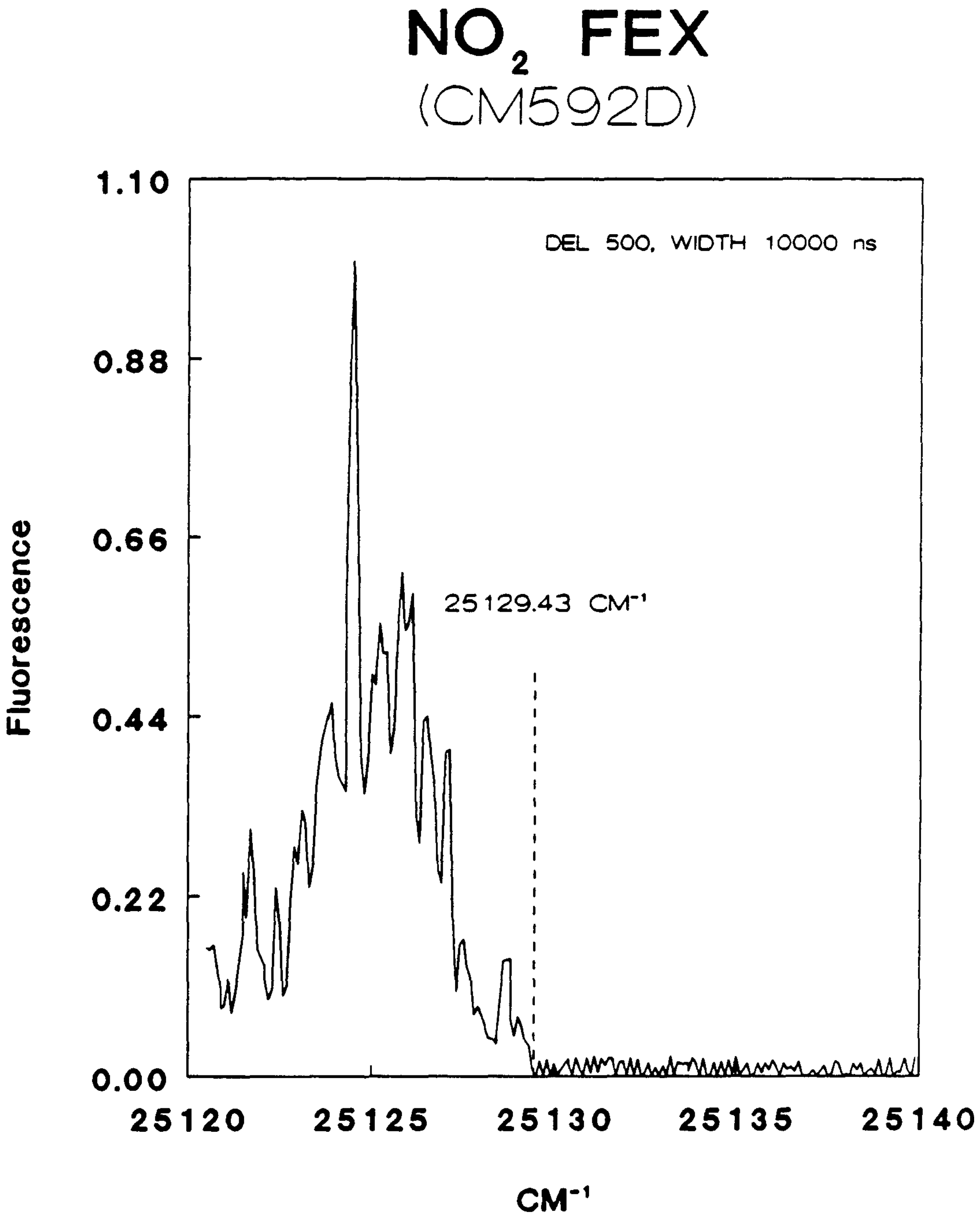
NO$_2$ FEX
(CM592D)
DEL 500, WIDTH 10000 ns
25129.43 CM^{-1}
Fluorescence
1.10
0.88
0.66
0.44
0.22
0.00
25120
25125
25130
25135
25140
CM^{-1}

Figure 3.9

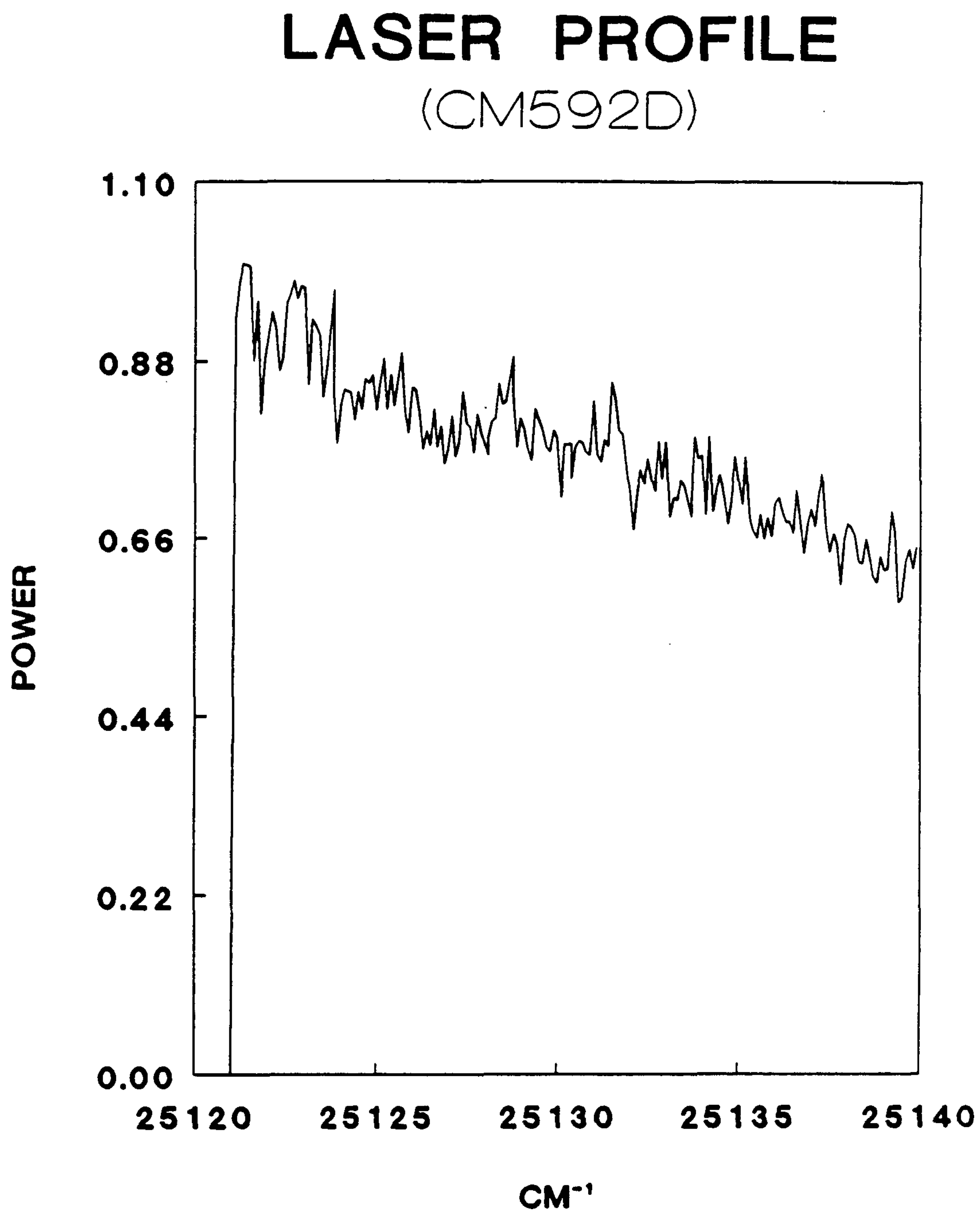
LASER PROFILE
(CM592D)
1.10
0.88
0.66
0.44
0.22
0.00
POWER
25120
25125
25130
25135
25140
CM⁻¹

Figure 3.10

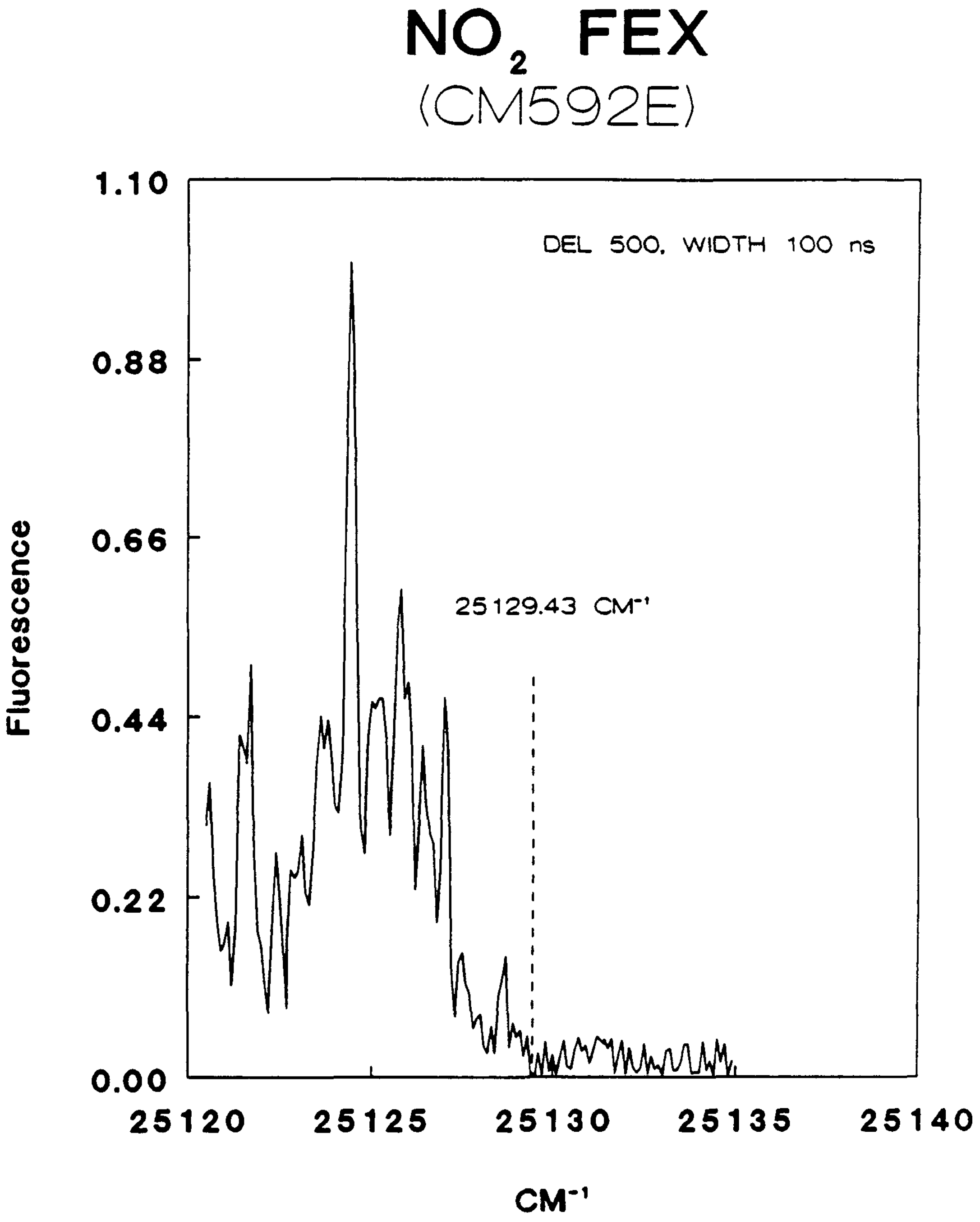
NO$_2$ FEX
(CM592E)
DEL 500, WIDTH 100 ns
25129.43 CM^{-1}
Fluorescence
1.10
0.88
0.66
0.44
0.22
0.00
25120
25125
25130
25135
25140
CM^{-1}

Figure 3.11

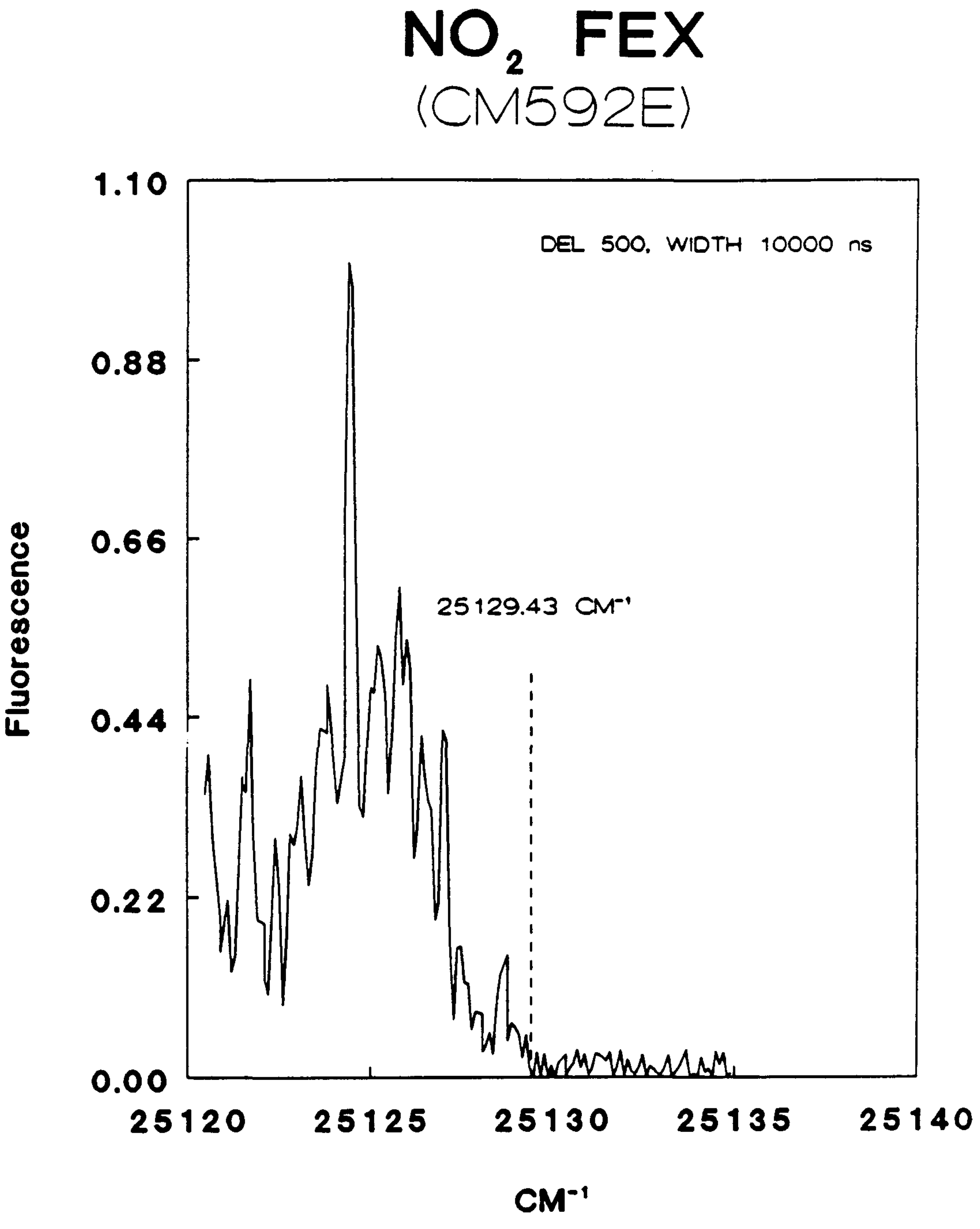
NO$_2$ FEX
(CM592E)
DEL 500. WIDTH 10000 ns
25129.43 CM^{-1}
Fluorescence
1.10
0.88
0.66
0.44
0.22
0.00
25120
25125
25130
25135
25140
CM^{-1}

Figure 3.12

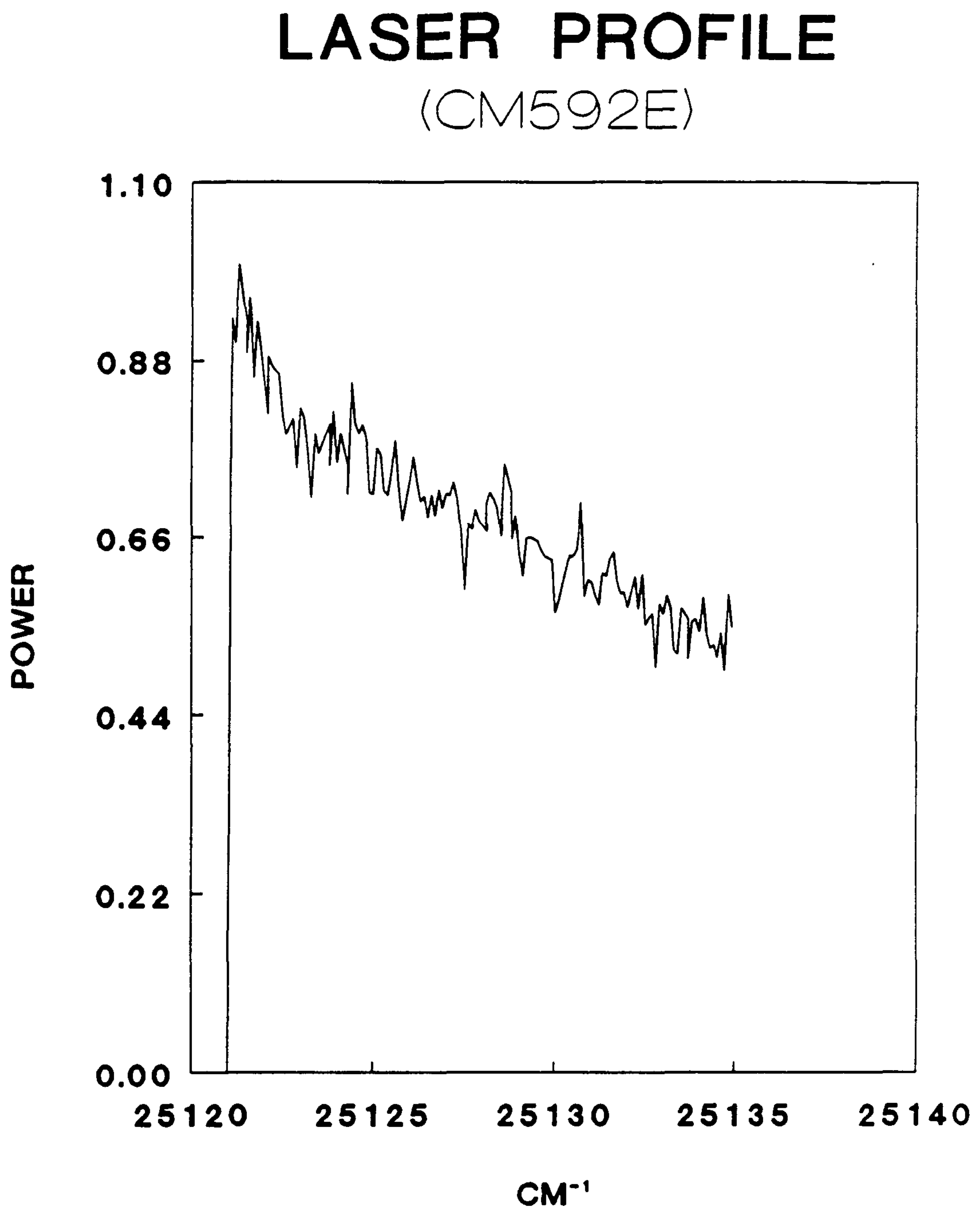
LASER PROFILE
(CM592E)
1.10
0.88
0.66
0.44
0.22
0.00
POWER
25120
25125
25130
25135
25140
CM⁻¹

Figure 3.13

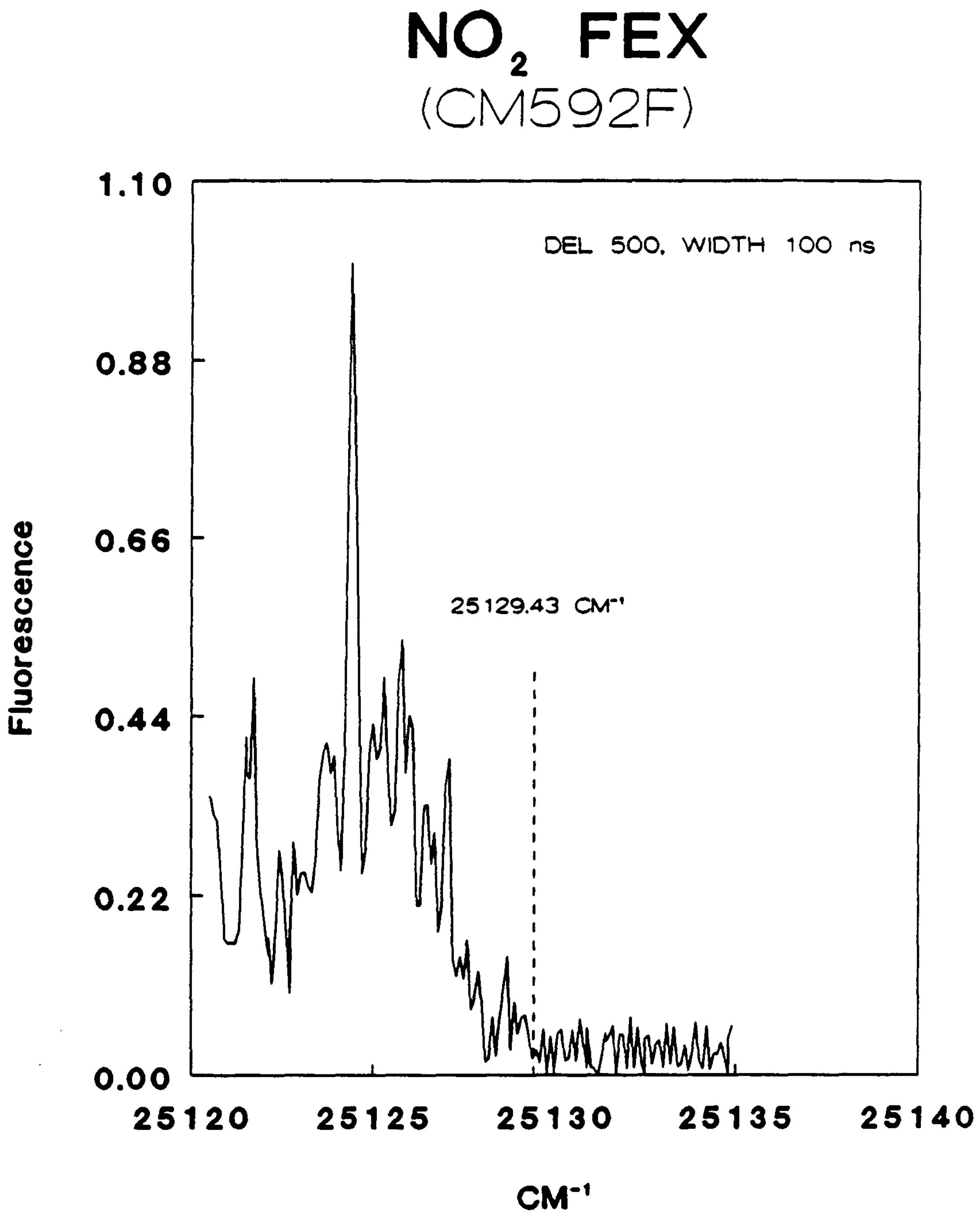
NO$_2$ FEX
(CM592F)
DEL 500, WIDTH 100 ns
25129.43 CM^{-1}
Fluorescence
1.10
0.88
0.66
0.44
0.22
0.00
25120
25125
25130
25135
25140
CM^{-1}

Figure 3.14

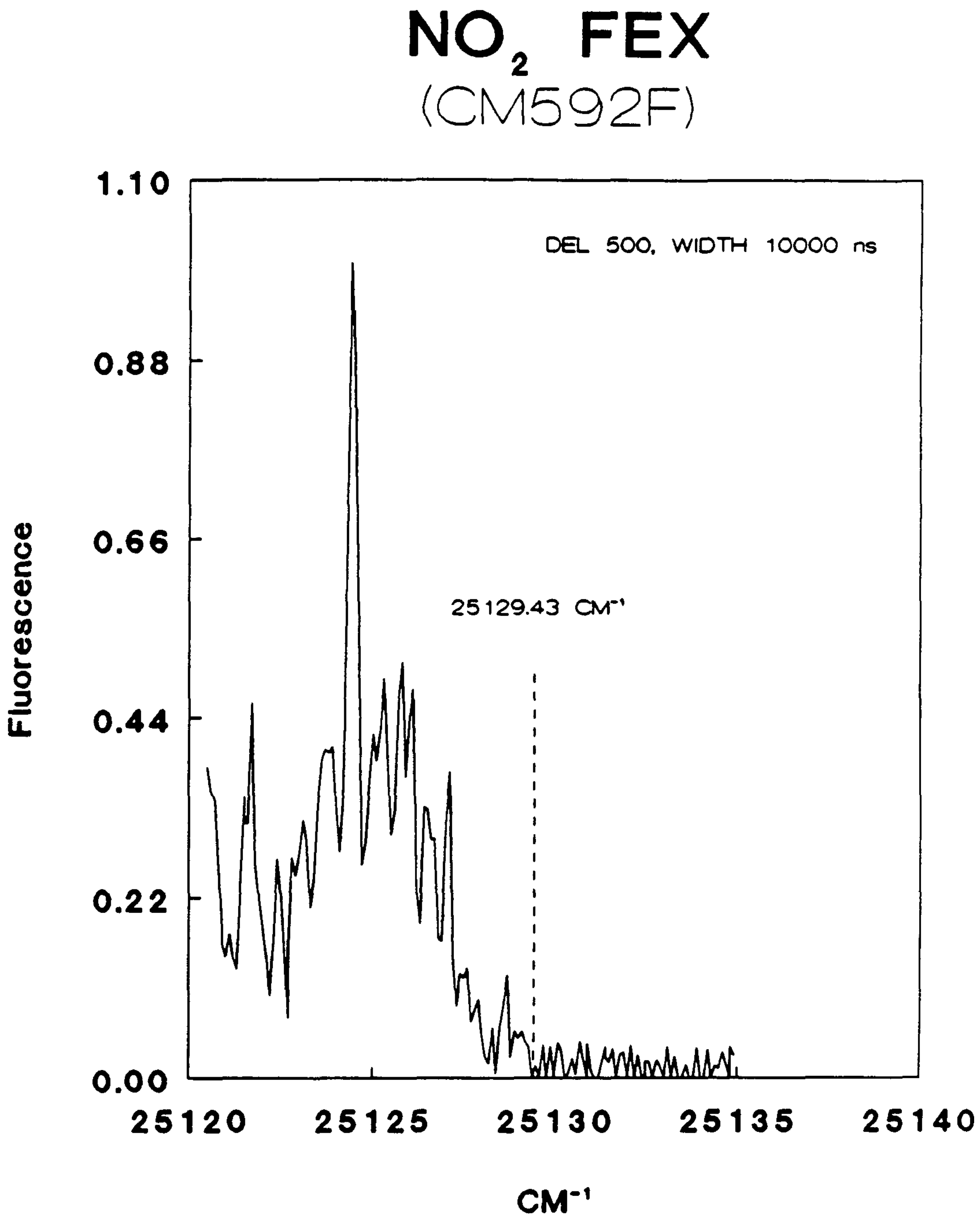

NO_2 FEX
(CM592F)

Figure 3.15

LASER PROFILE

(CM592F)

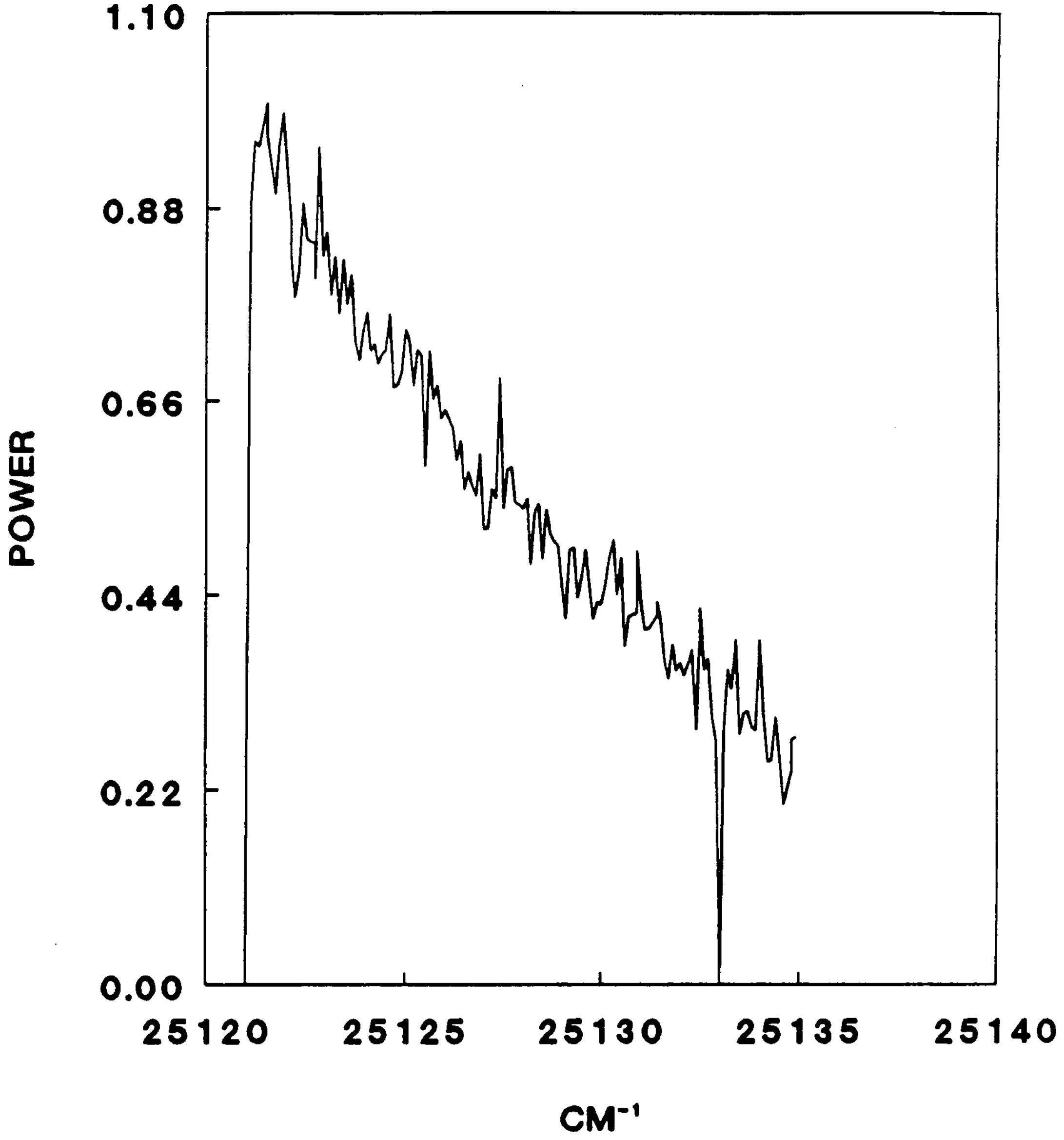

Figure 3.16

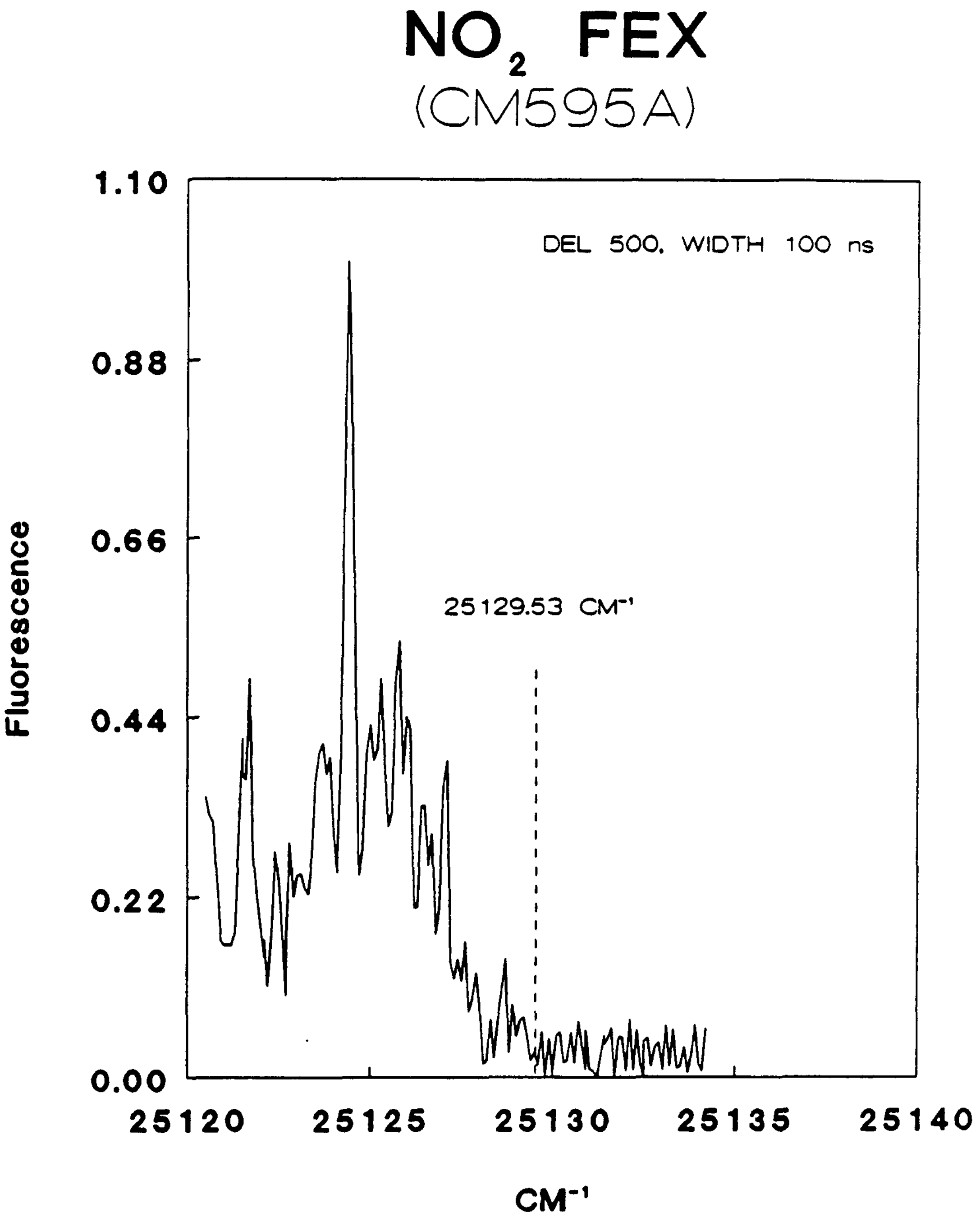
NO$_2$ FEX
(CM595A)
DEL 500. WIDTH 100 ns
25129.53 CM^{-1}
Fluorescence
1.10
0.88
0.66
0.44
0.22
0.00
25120
25125
25130
25135
25140
CM^{-1}

Figure 3.17

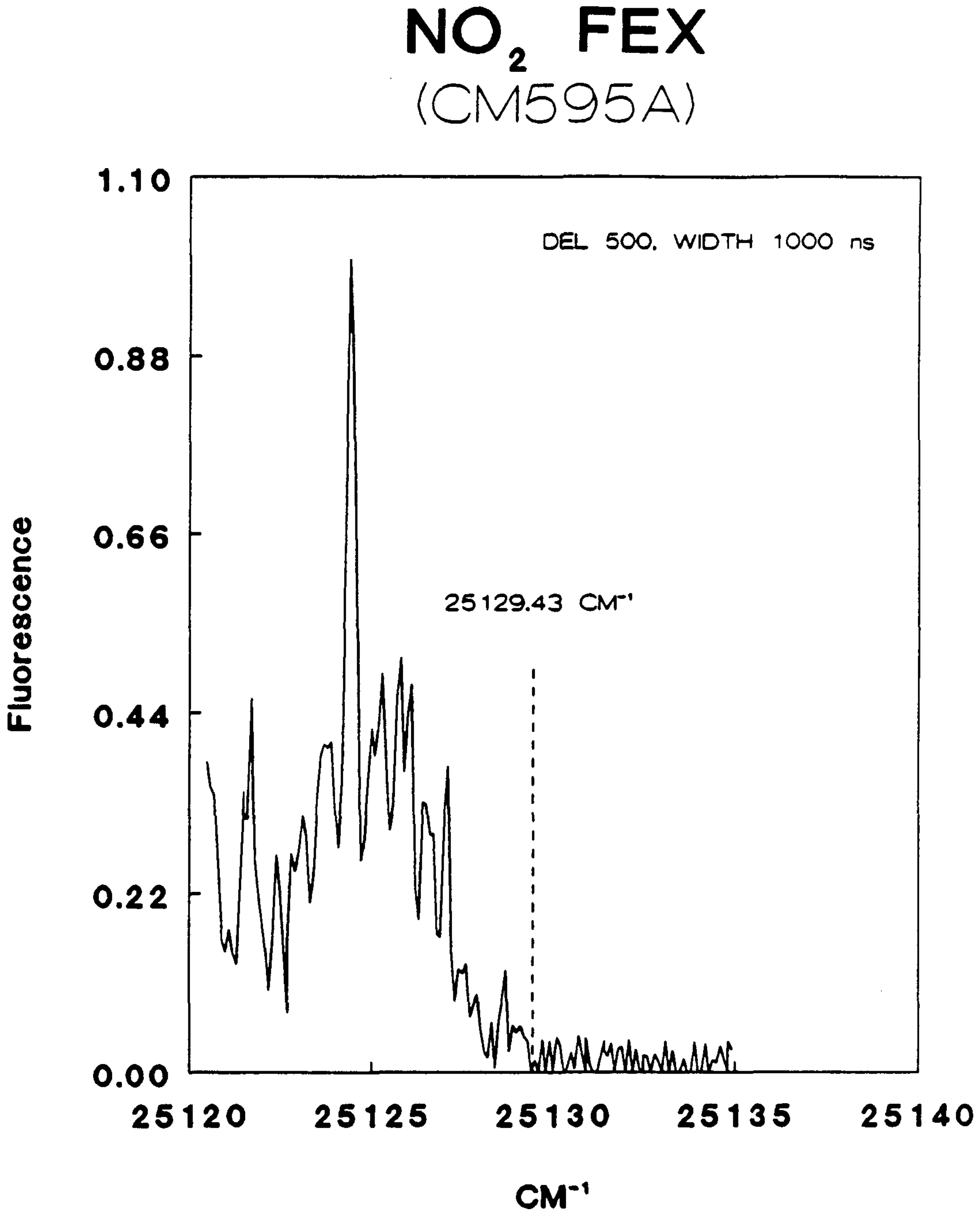
NO_2 FEX
(CM595A)
DEL 500. WIDTH 1000 ns
25129.43 CM^{-1}
Fluorescence
1.10
0.88
0.66
0.44
0.22
0.00
25120
25125
25130
25135
25140
CM^{-1}

Figure 3.18

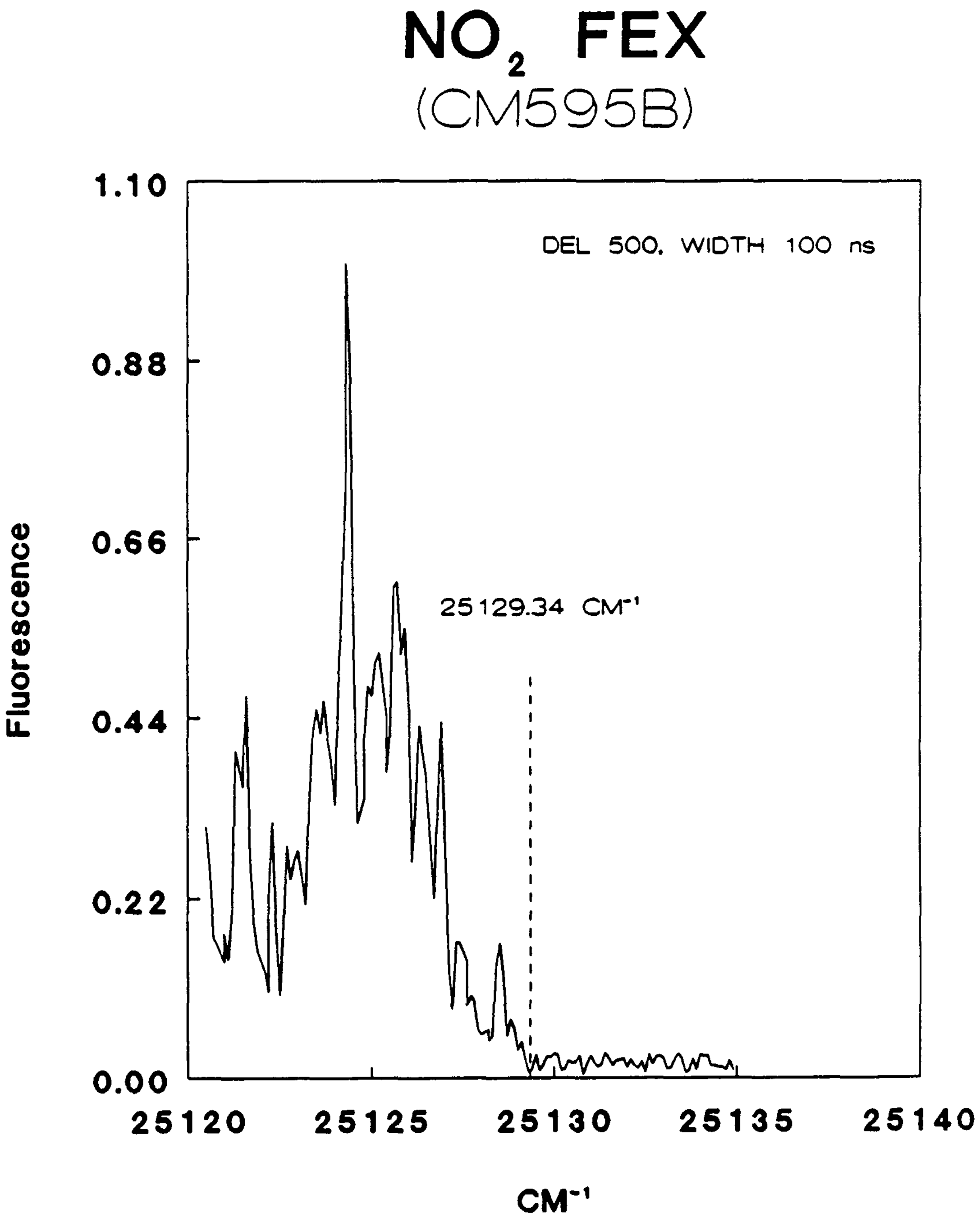
NO₂ FEX
(CM595B)
DEL 500. WIDTH 100 ns
25129.34 CM⁻¹
Fluorescence
1.10
0.88
0.66
0.44
0.22
0.00
25120
25125
25130
25135
25140
CM⁻¹

Figure 3.20

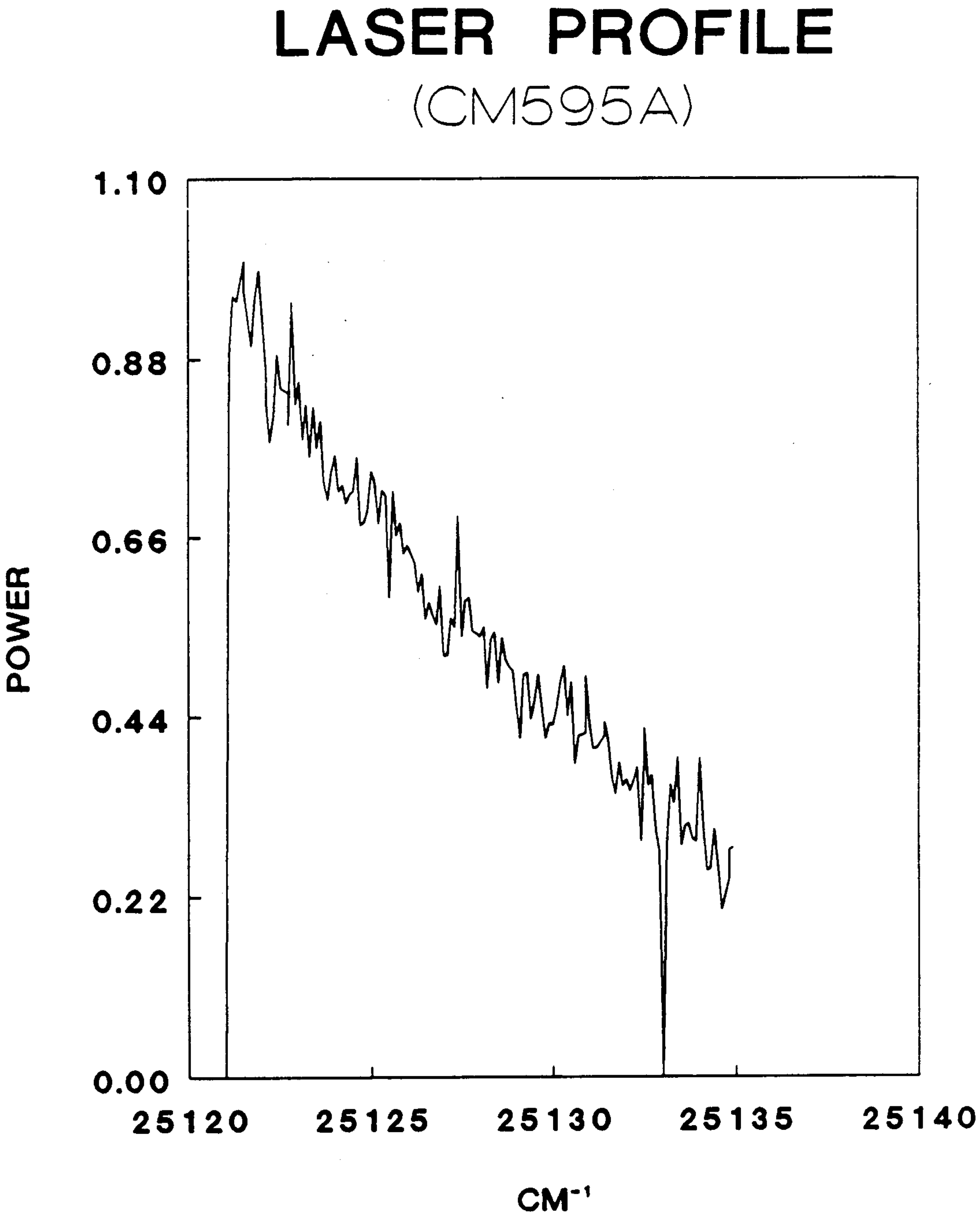
LASER PROFILE
(CM595A)

Figure 3.19

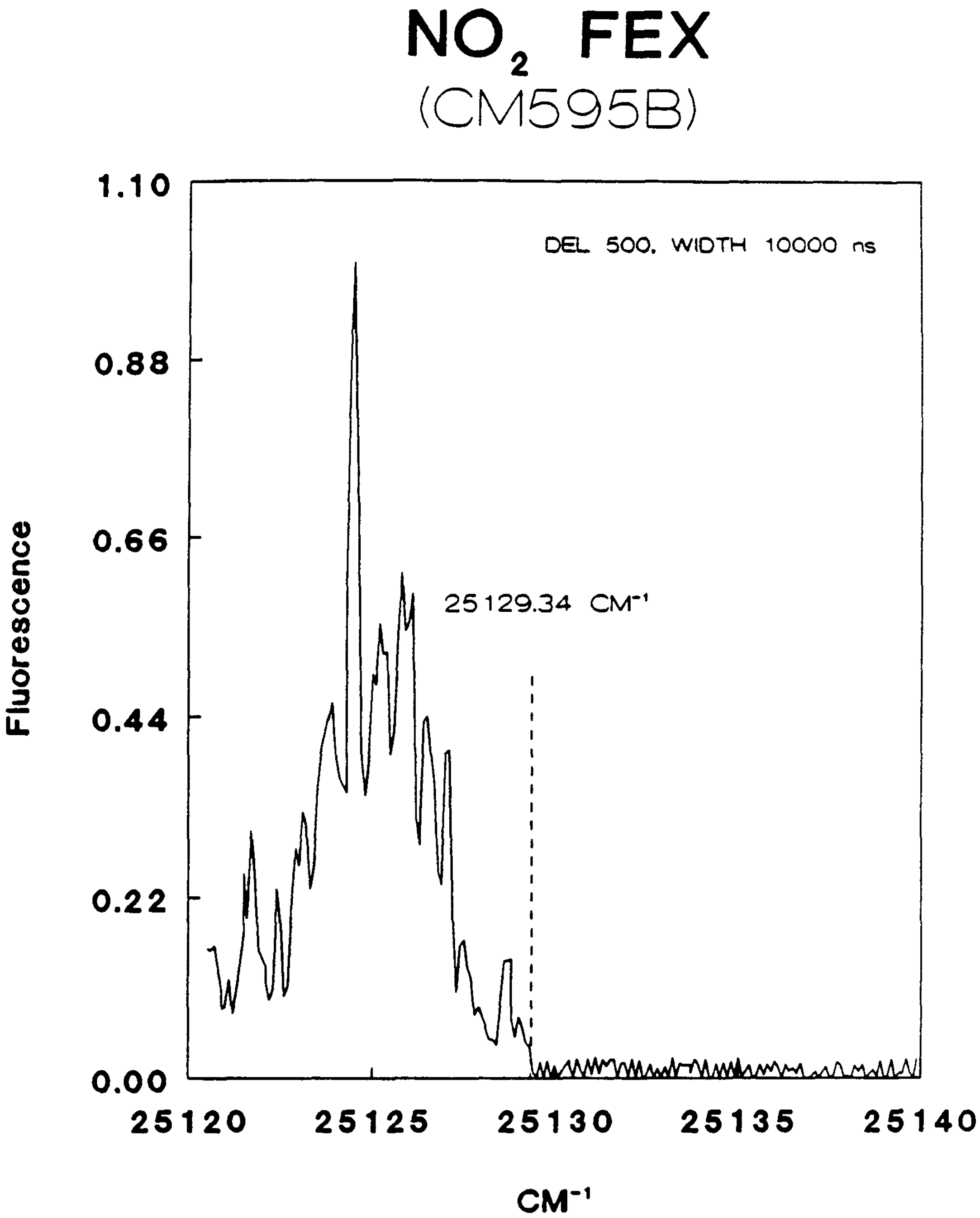
NO$_2$ FEX
(CM595B)
DEL 500, WIDTH 10000 ns
25129.34 CM^{-1}
Fluorescence
1.10
0.88
0.66
0.44
0.22
0.00
25120
25125
25130
25135
25140
CM^{-1}

Figure 3.21

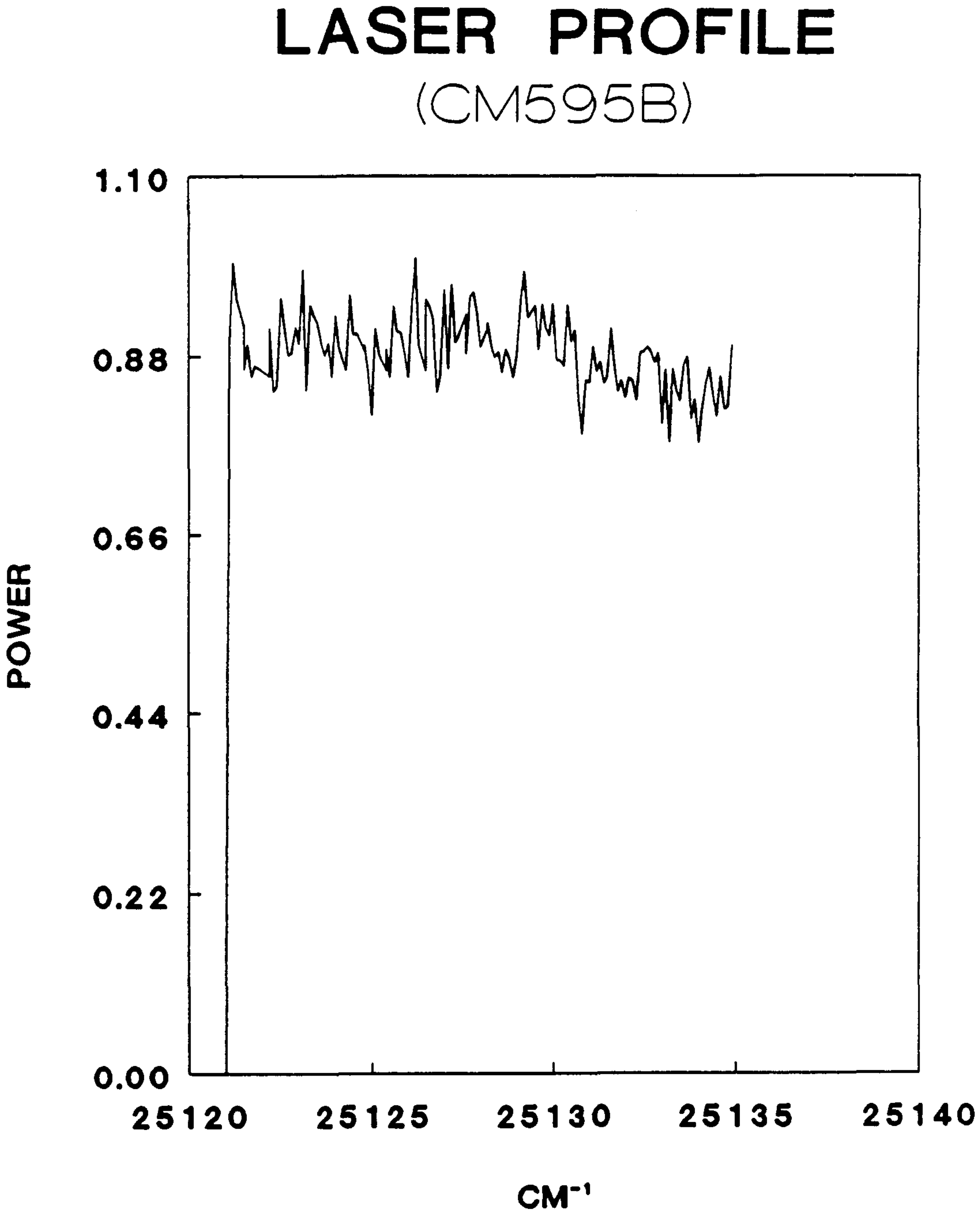
LASER PROFILE
(CM595B)
POWER
1.10
0.88
0.66
0.44
0.22
0.00
25120
25125
25130
25135
25140
CM⁻¹

Figure 3.22

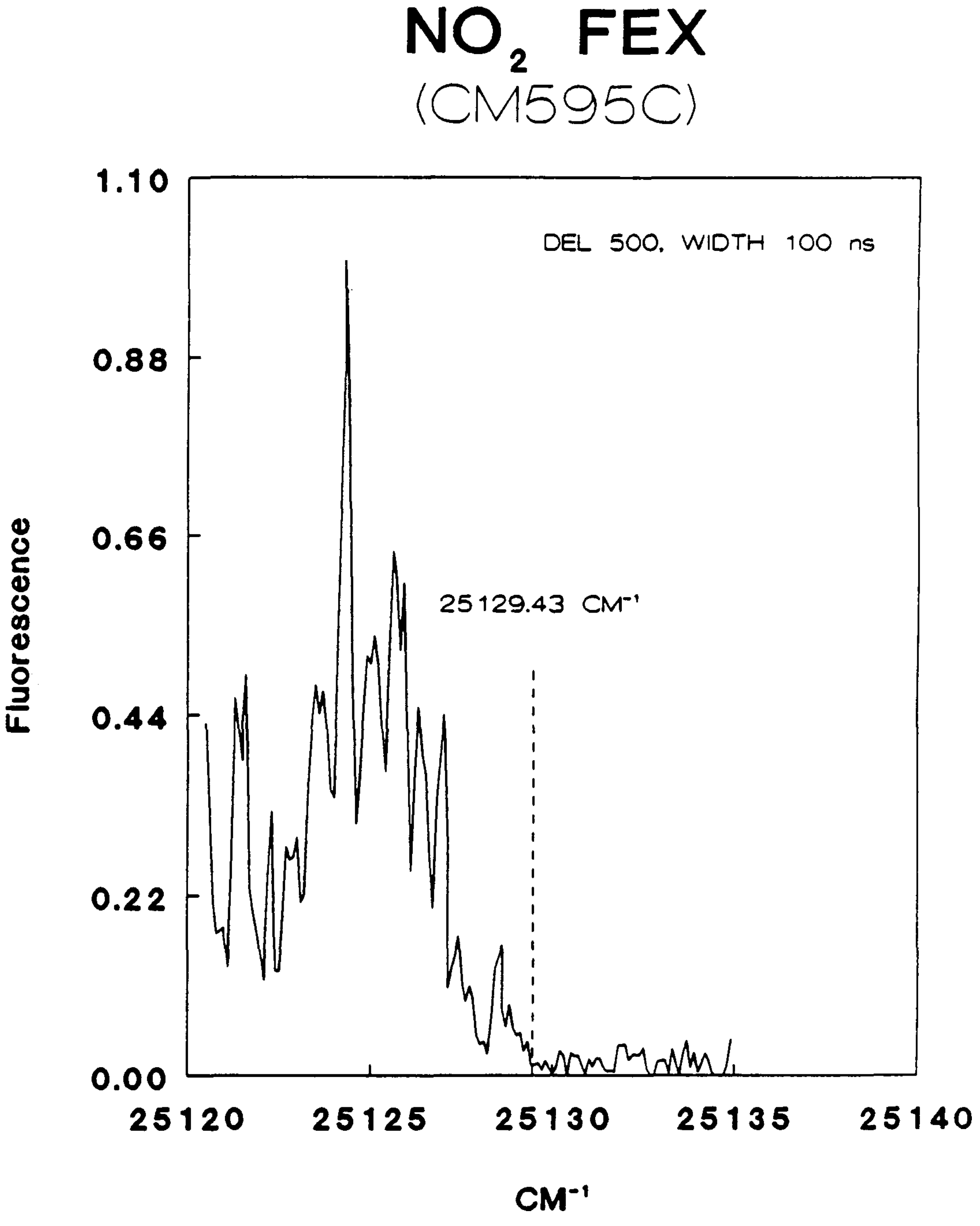
NO$_2$ FEX
(CM595C)
DEL 500, WIDTH 100 ns
25129.43 CM^{-1}
Fluorescence
1.10
0.88
0.66
0.44
0.22
0.00
25120
25125
25130
25135
25140
CM^{-1}

Figure 3.23

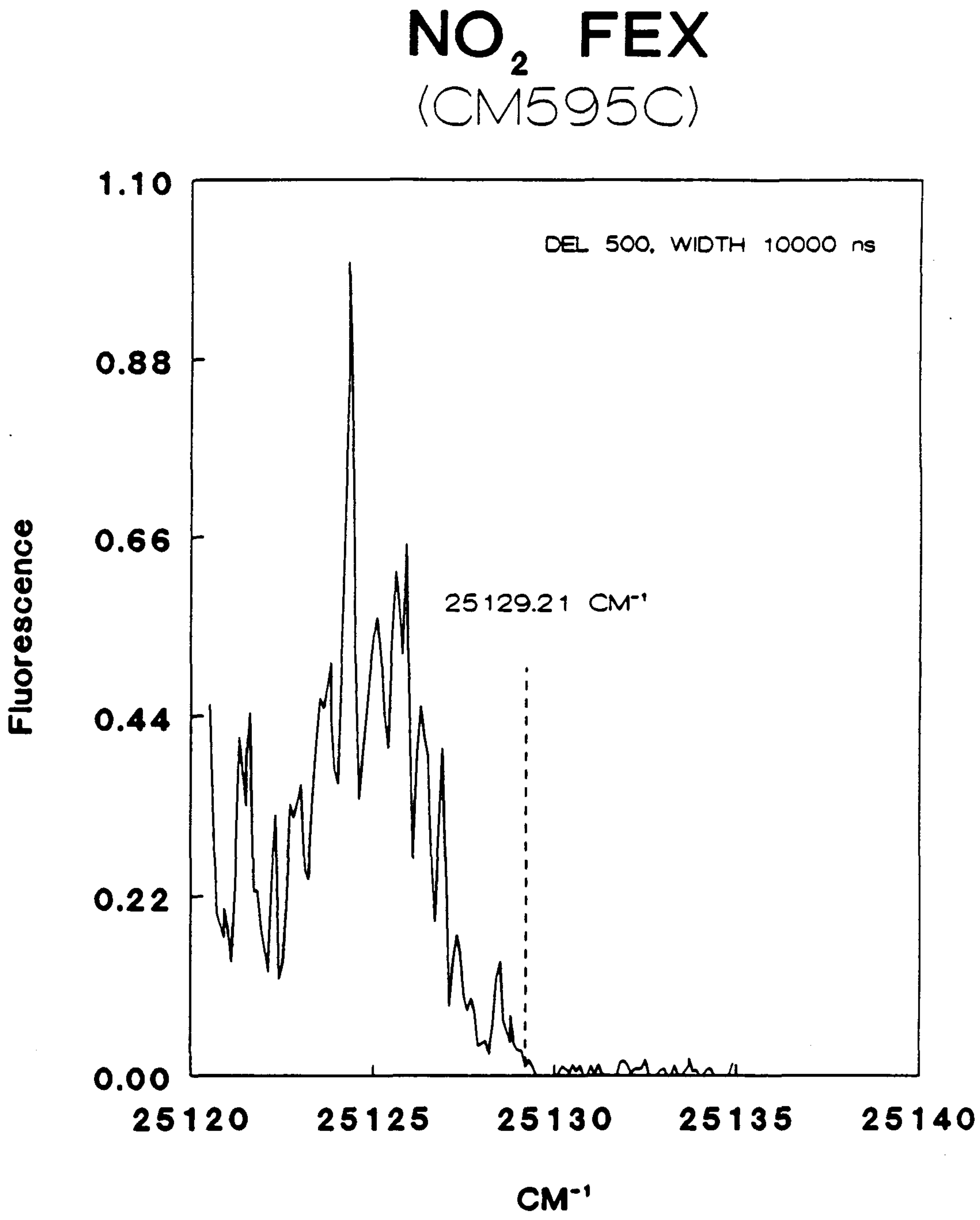
NO$_2$ FEX
(CM595C)
DEL 500. WIDTH 10000 ns
25129.21 CM^{-1}
Fluorescence
1.10
0.88
0.66
0.44
0.22
0.00
25120
25125
25130
25135
25140
CM^{-1}

Figure 3.24

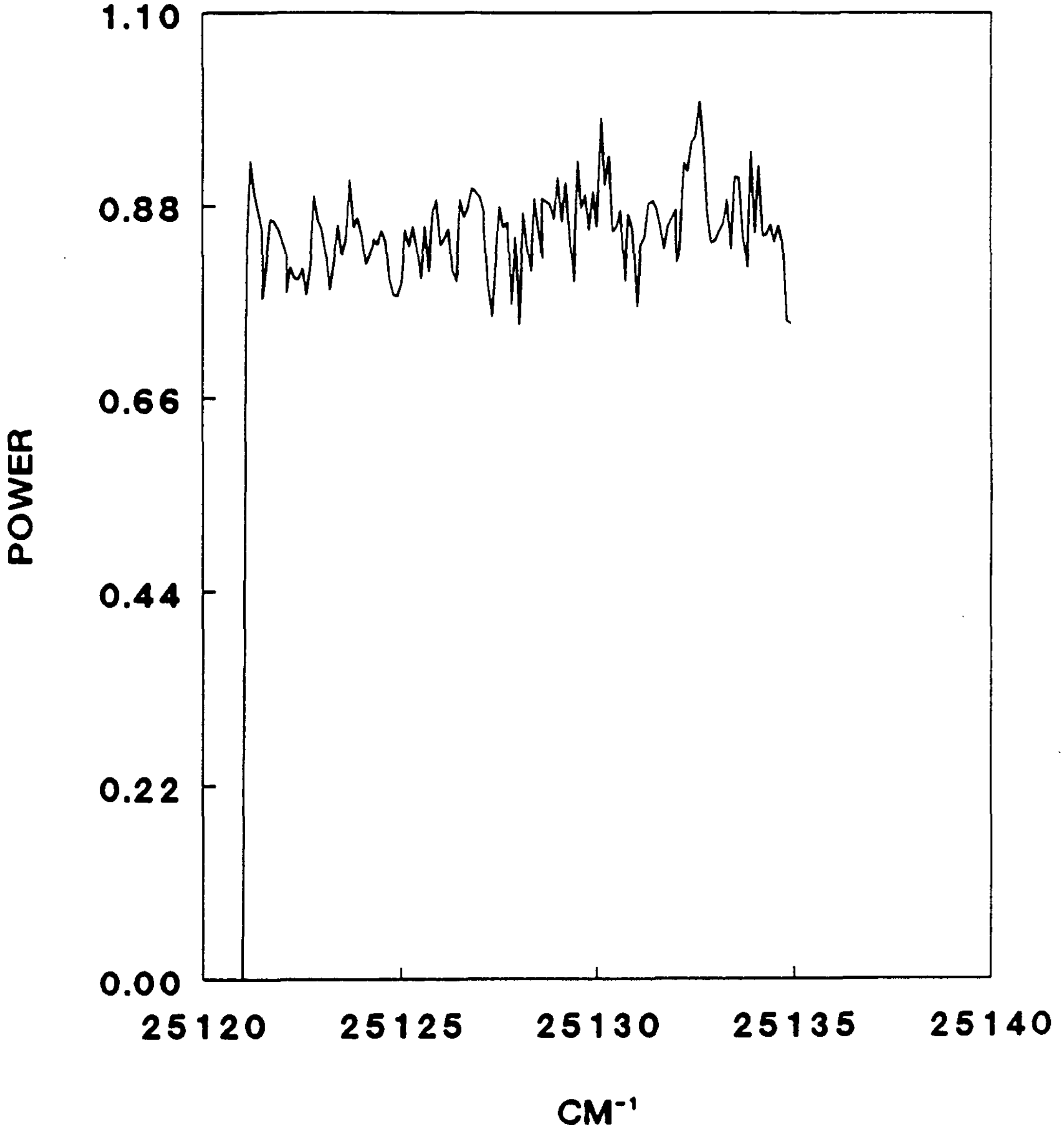

LASER PROFILE

(CM595C)

Figure 3.25

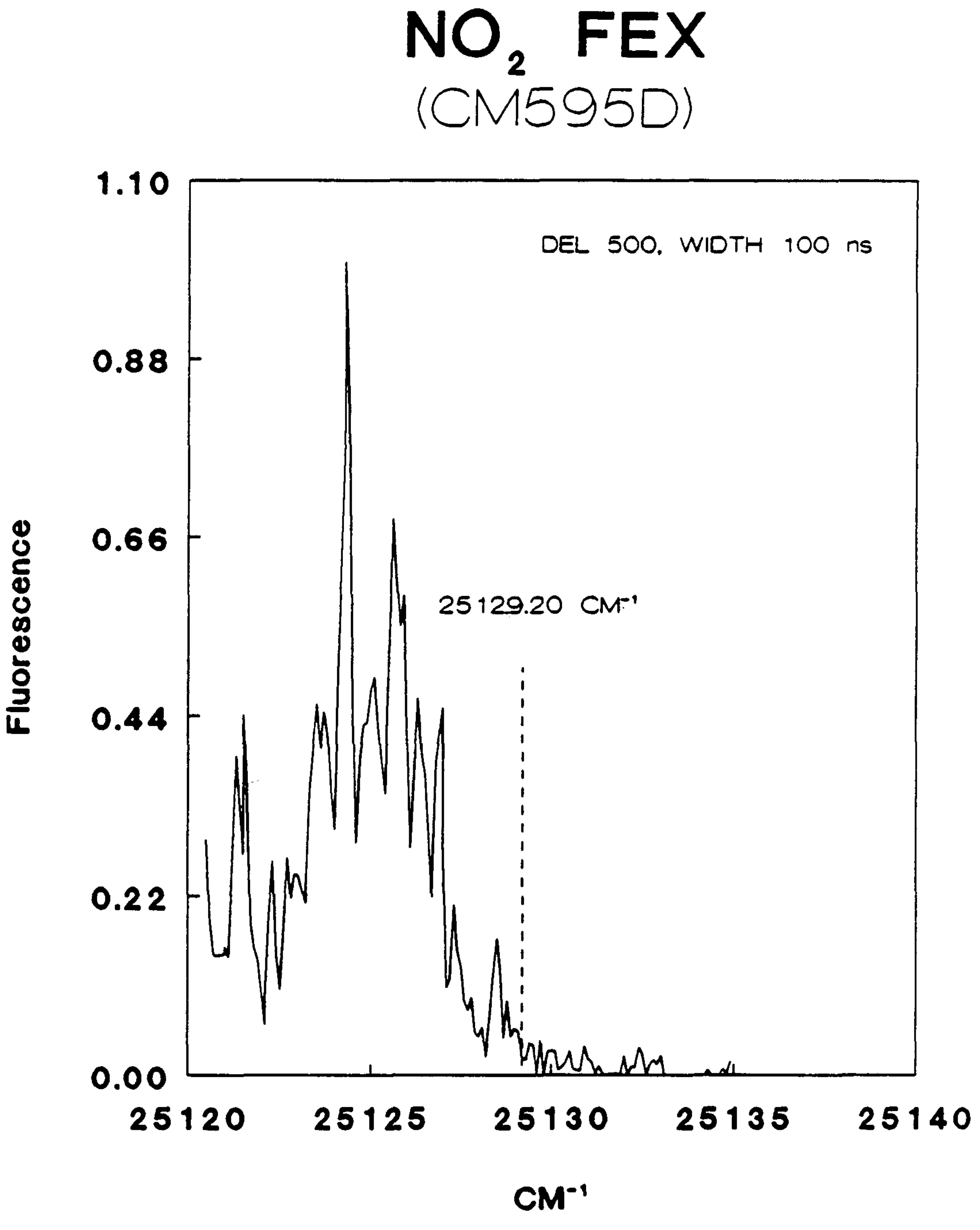
NO$_2$ FEX
(CM595D)
DEL 500, WIDTH 100 ns
25129.20 CM^{-1}
Fluorescence
1.10
0.88
0.66
0.44
0.22
0.00
25120
25125
25130
25135
25140
CM^{-1}

Figure 3.26

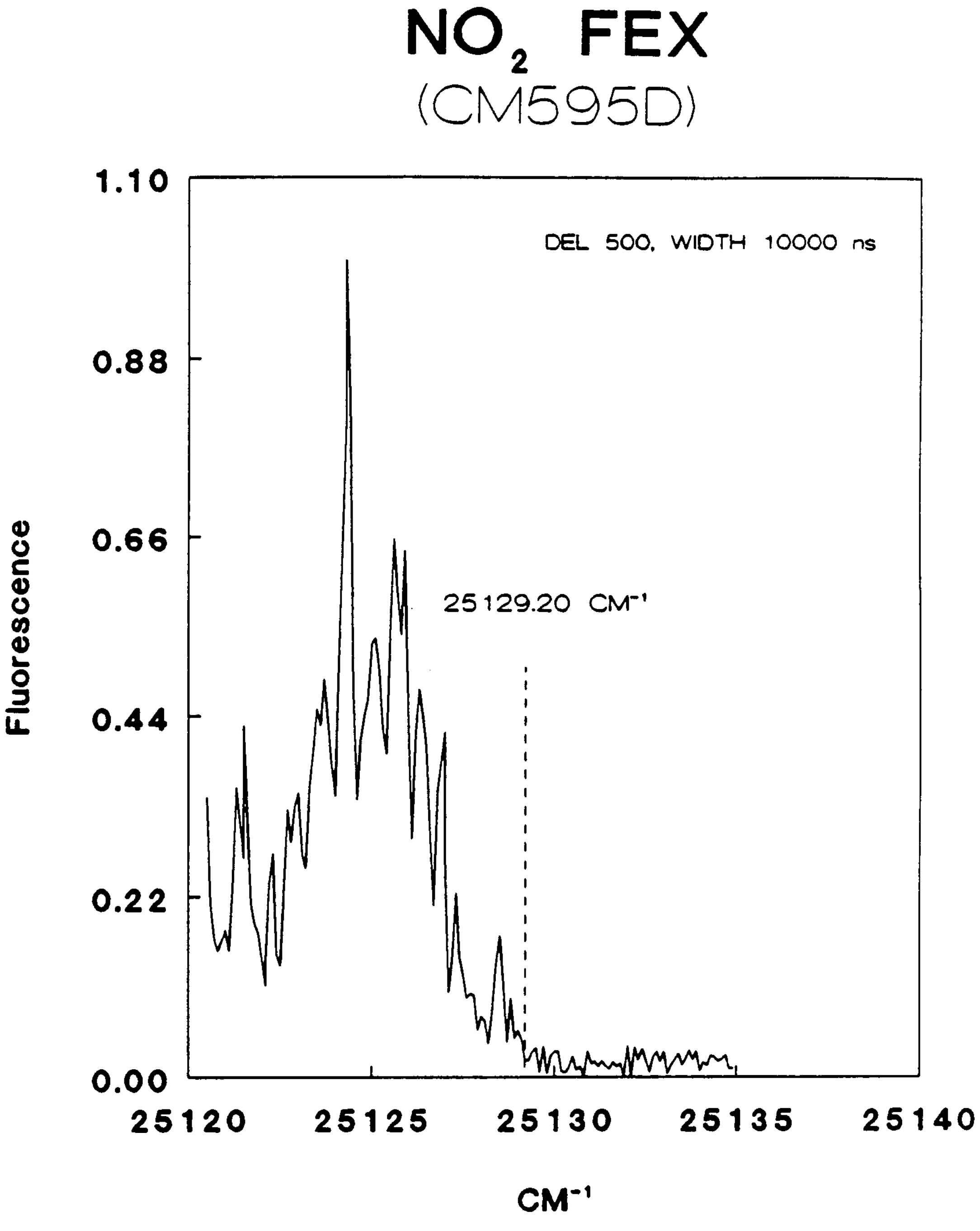

NO_2 FEX
(CM595D)
DEL 500, WIDTH 10000 ns
25129.20 CM⁻¹
Fluorescence
1.10
0.88
0.66
0.44
0.22
0.00
25120
25125
25130
25135
25140
CM⁻¹

Figure 3.27

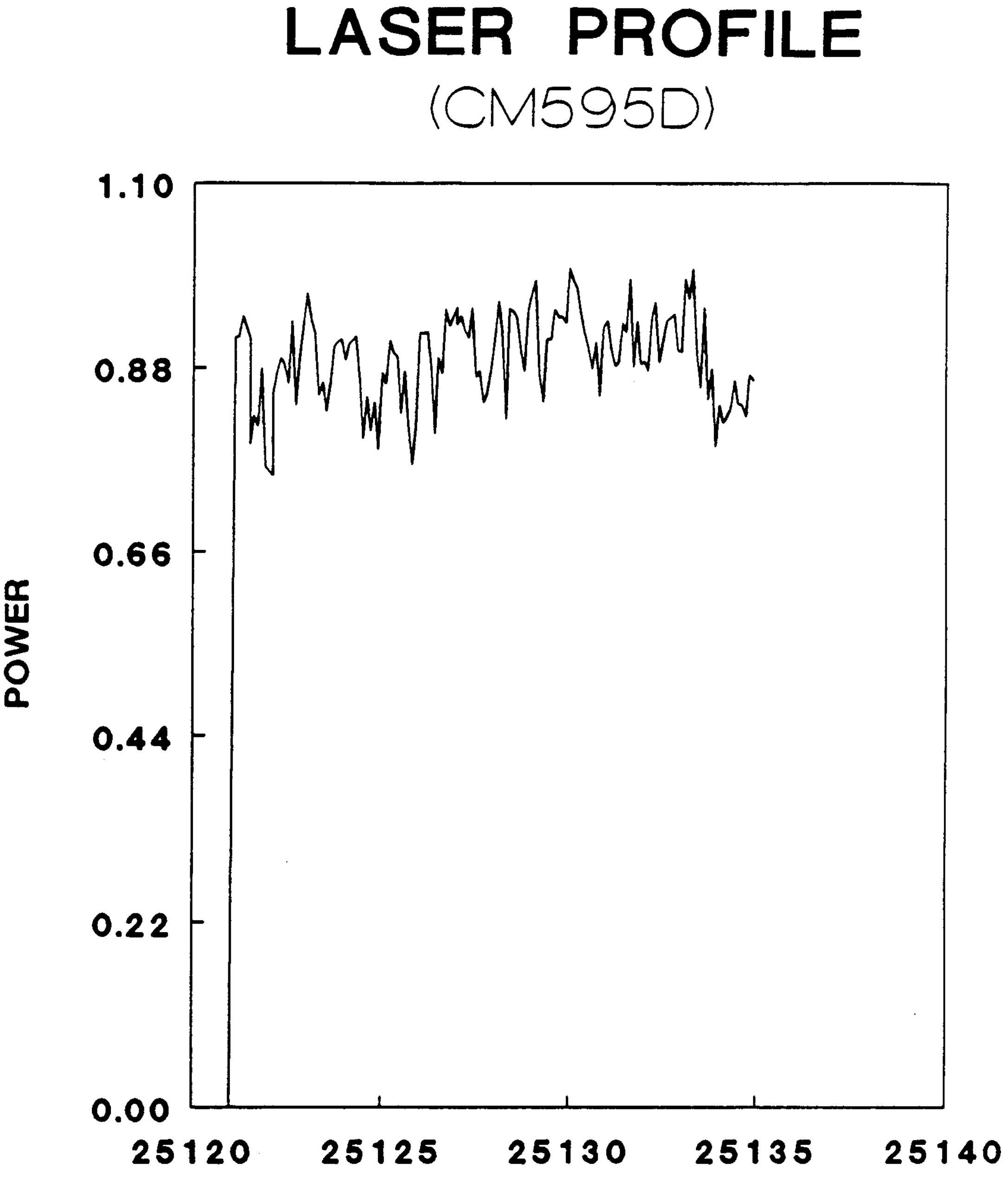
LASER PROFILE
(CM595D)
POWER
1.10
0.88
0.66
0.44
0.22
0.00
25120
25125
25130
25135
25140
CM⁻¹

Figure 3.28

NO_2 FEX
(CM596A)

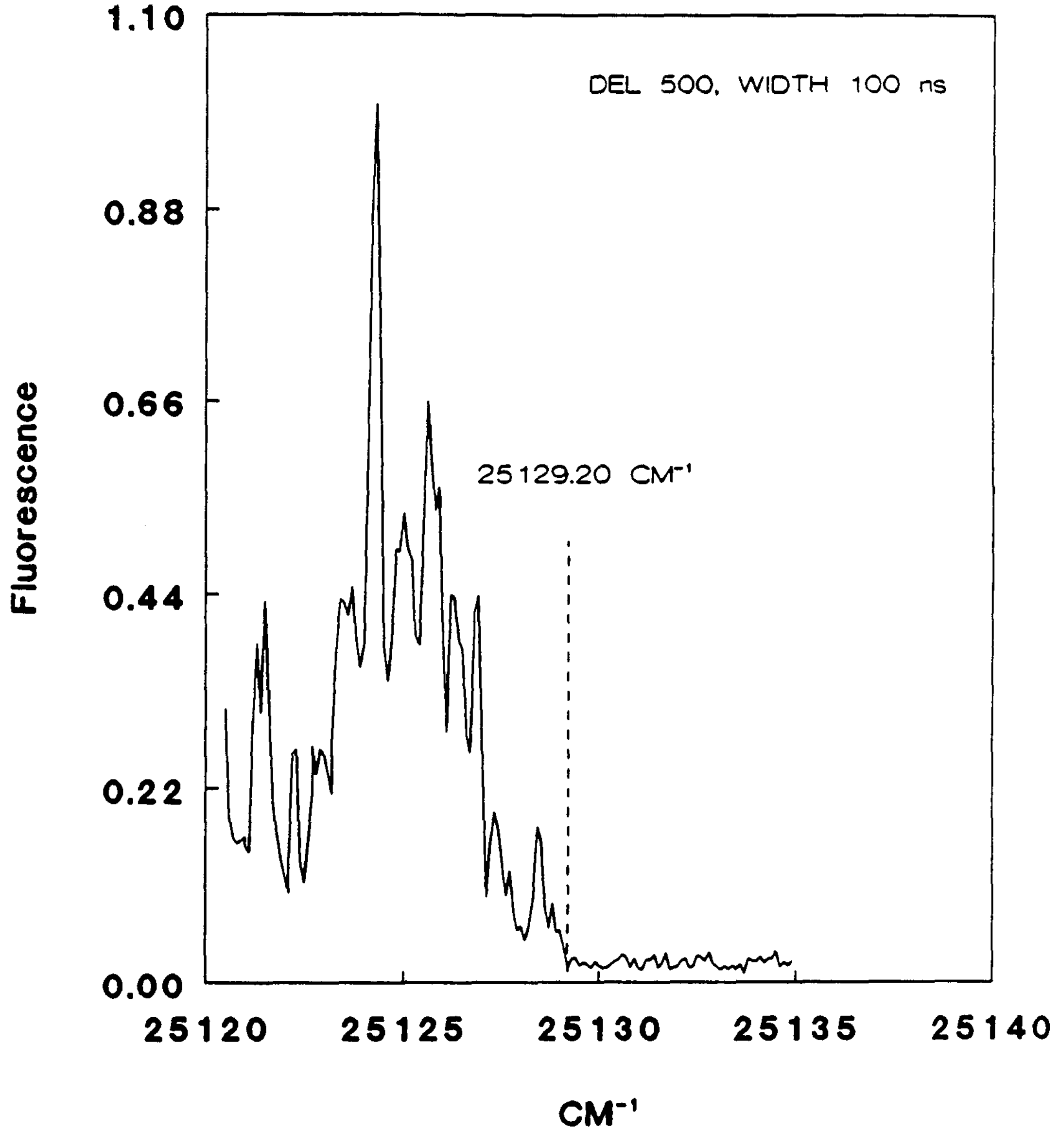

Figure 3.29

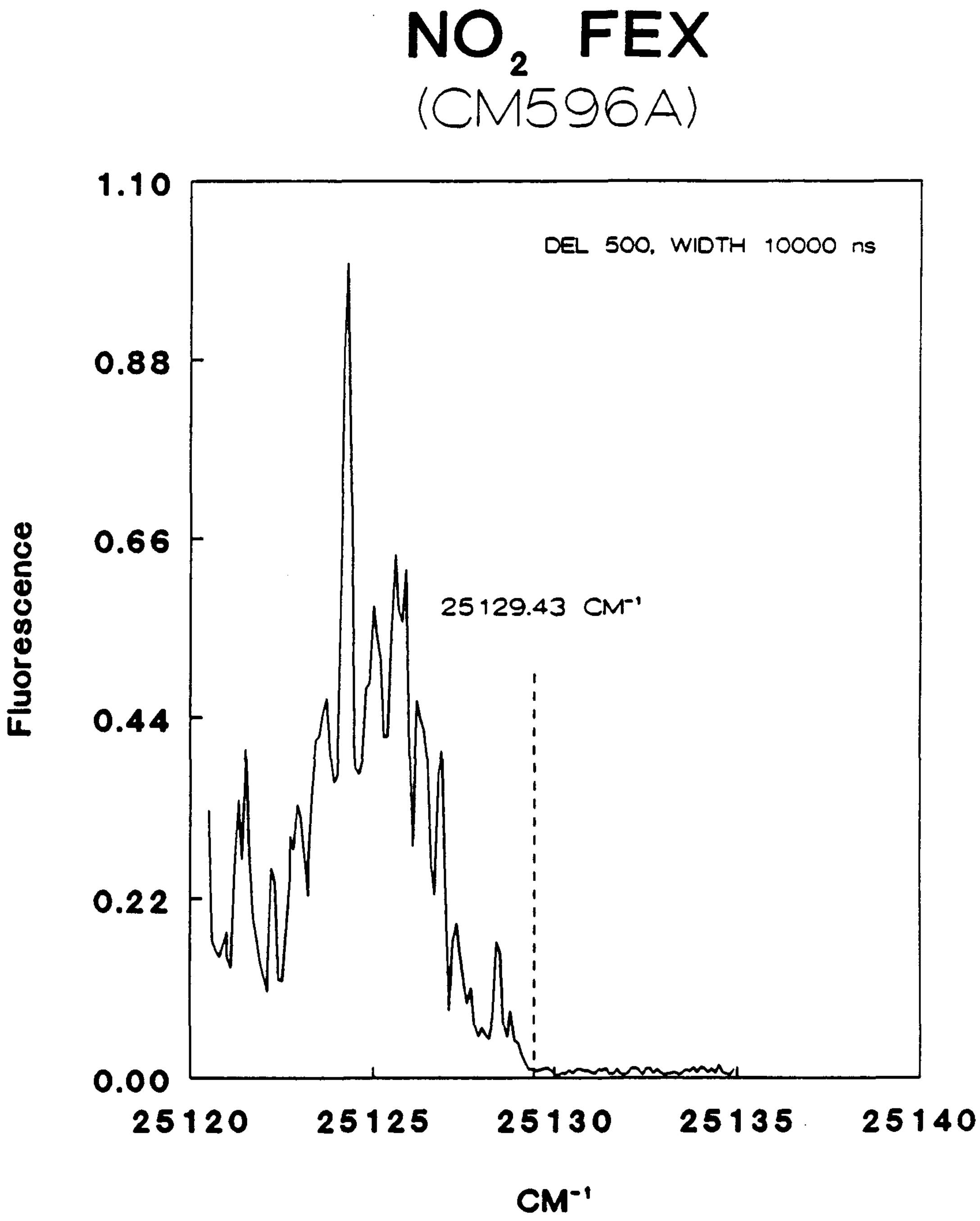
NO$_2$ FEX
(CM596A)
DEL 500, WIDTH 10000 ns
25129.43 CM⁻¹
1.10
0.88
0.66
0.44
0.22
0.00
Fluorescence
25120
25125
25130
25135
25140
CM⁻¹

Figure 3.30

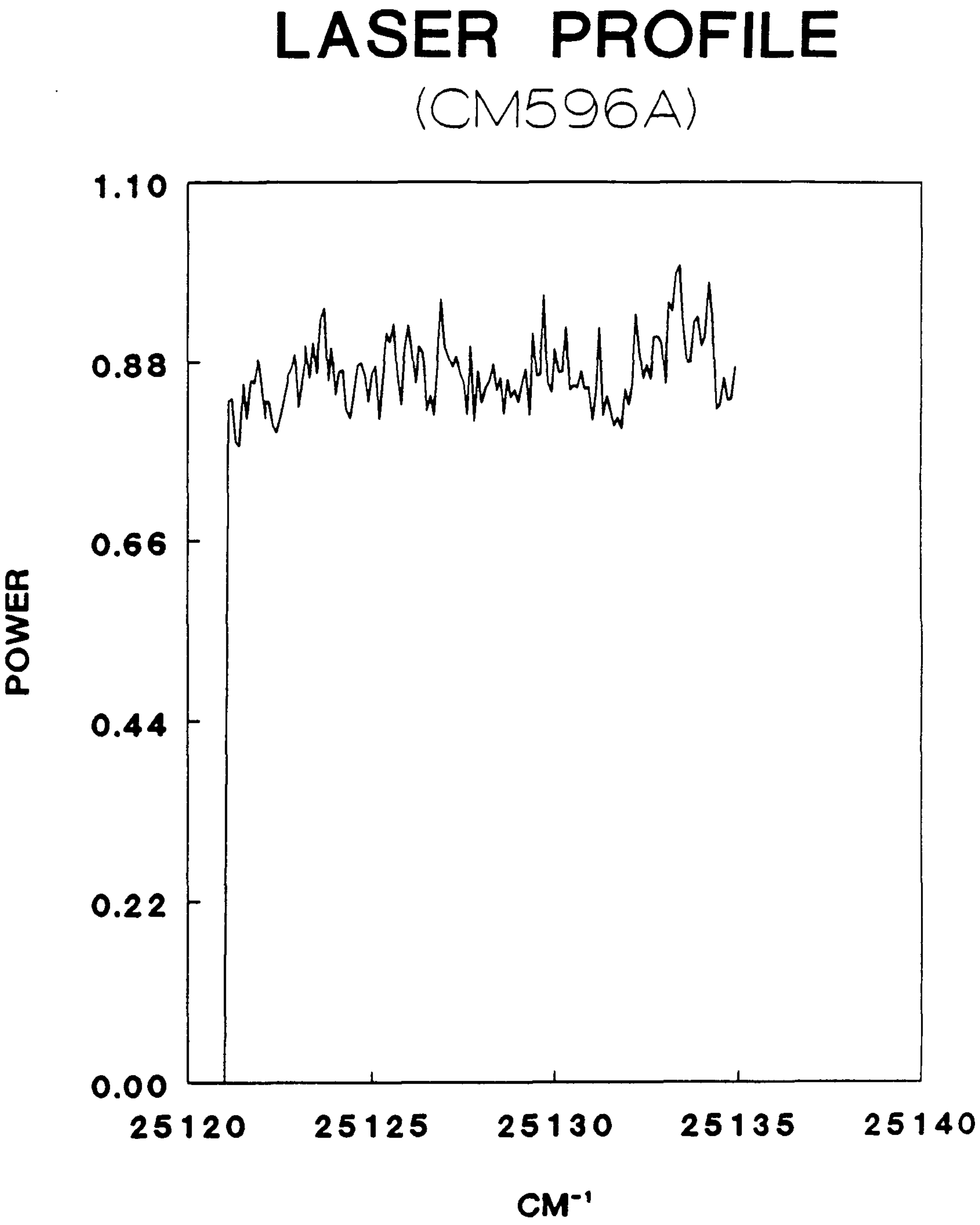
LASER PROFILE
(CM596A)
POWER
1.10
0.88
0.66
0.44
0.22
0.00
25120
25125
25130
25135
25140
CM⁻¹

Figure 3.31

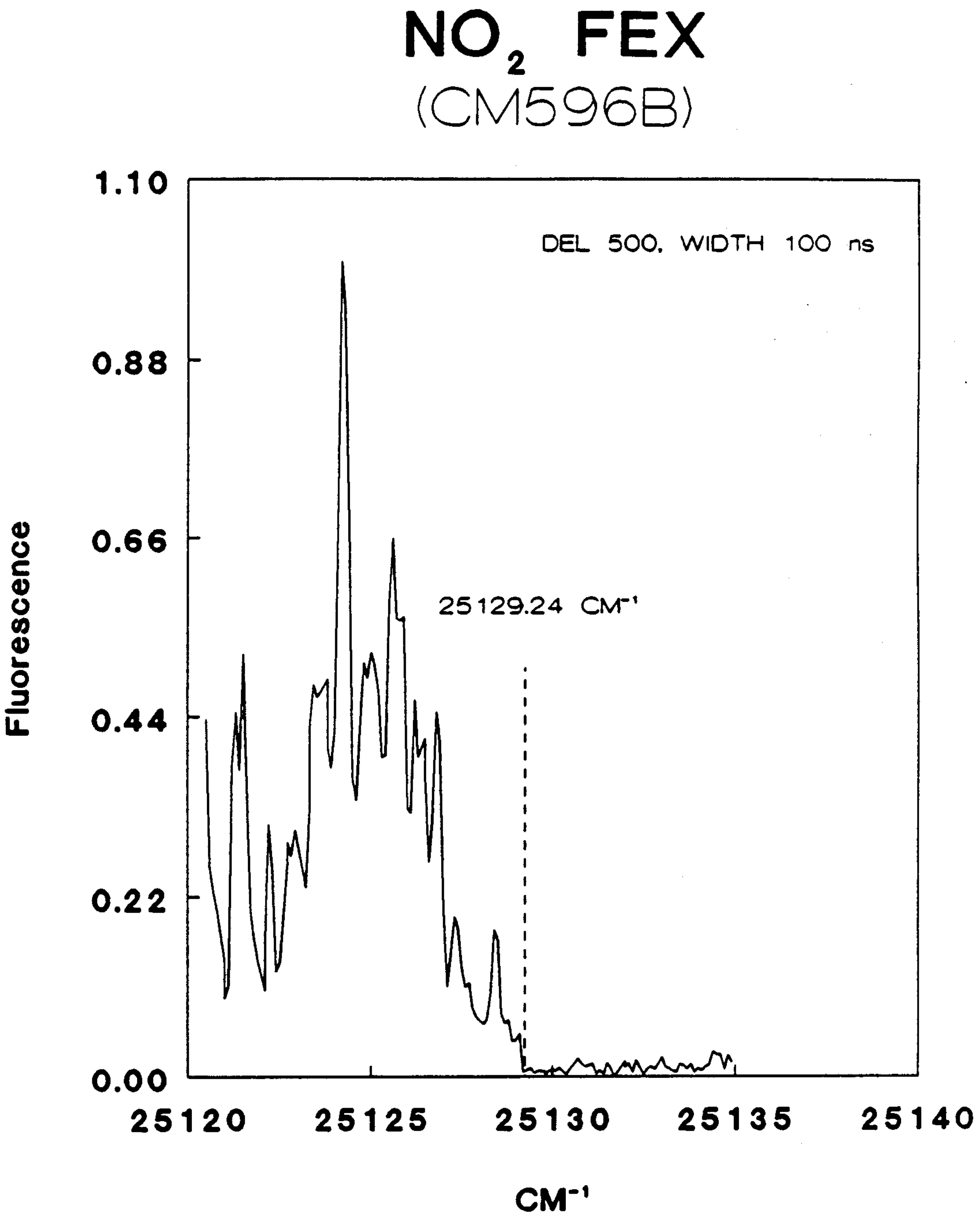
NO₂ FEX
(CM596B)
DEL 500, WIDTH 100 ns
25129.24 CM⁻¹
Fluorescence
1.10
0.88
0.66
0.44
0.22
0.00
25120
25125
25130
25135
25140
CM⁻¹

Figure 3.32

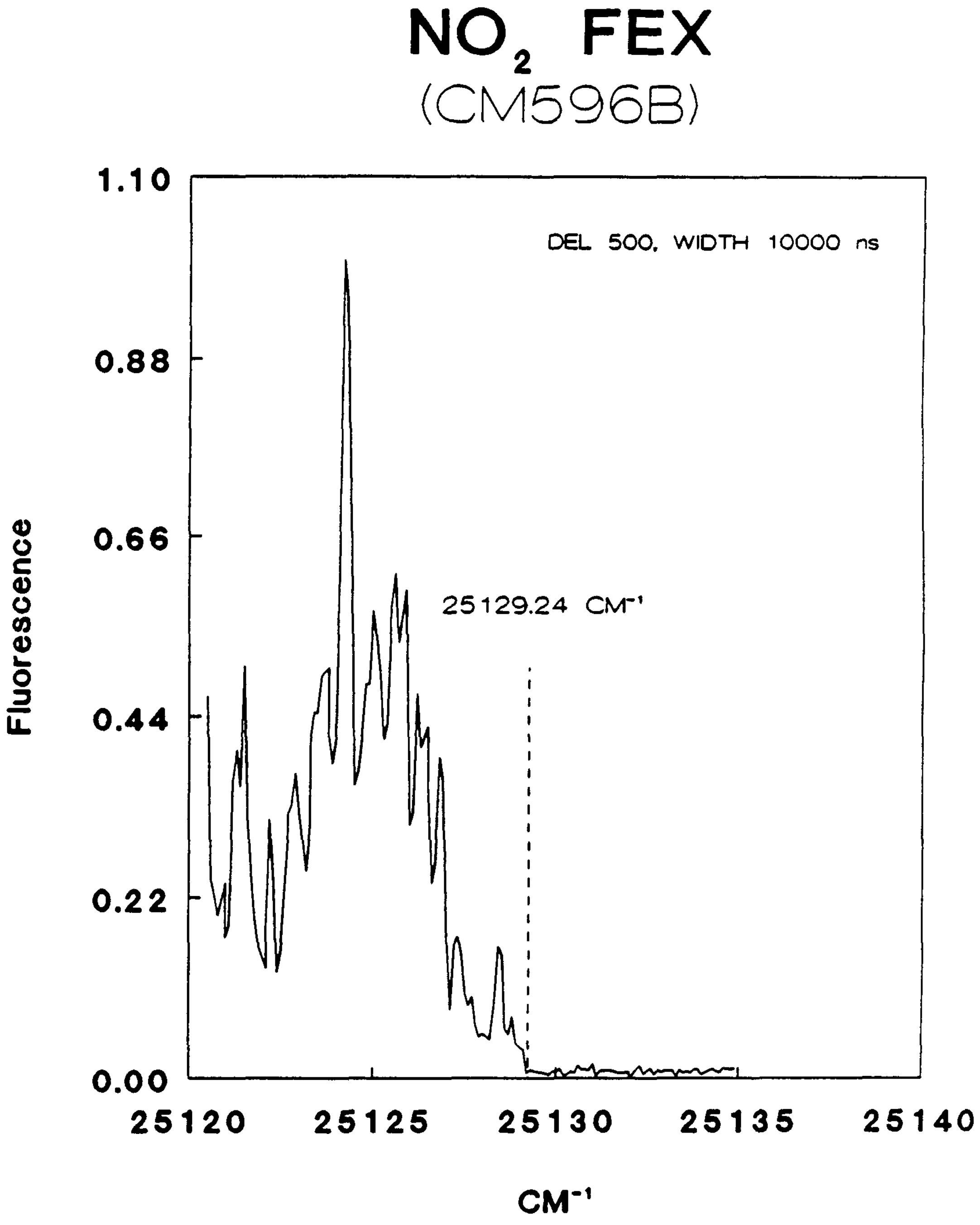

NO$_2$ FEX
(CM596B)
DEL 500, WIDTH 10000 ns
25129.24 CM^{-1}
Fluorescence
1.10
0.88
0.66
0.44
0.22
0.00
25120
25125
25130
25135
25140
CM^{-1}

Figure 3.33

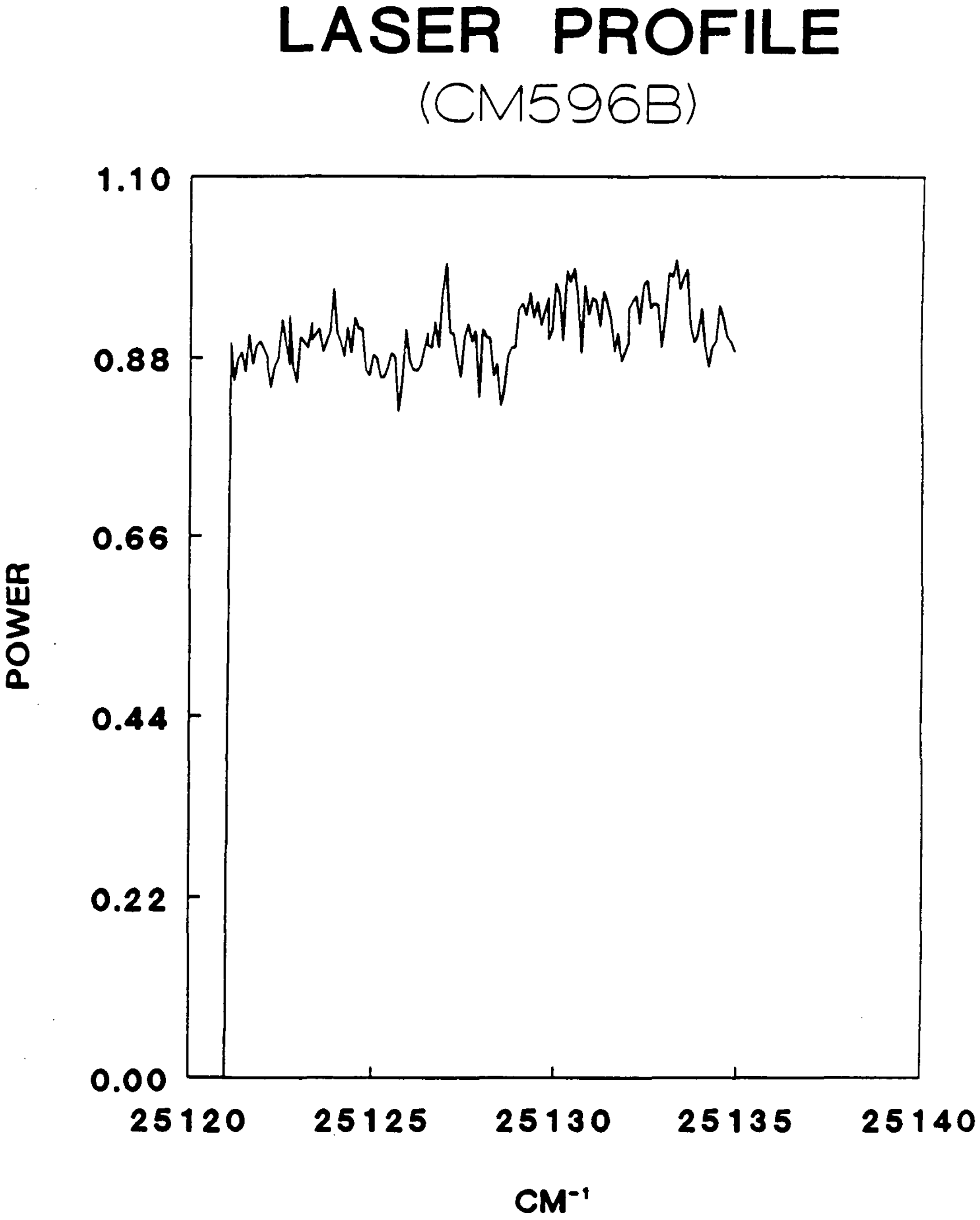
LASER PROFILE
(CM596B)
POWER
1.10
0.88
0.66
0.44
0.22
0.00
25120
25125
25130
25135
25140
CM^{-1}

Figure 3.34

Figures 3.35 - 3.37

3 reproductions of the fluorescence observed beyond the dissociation threshold of NO_2. These spectra are not corrected for laser power or absorption cross section.

Fluorescence > D_0

(CM589A)

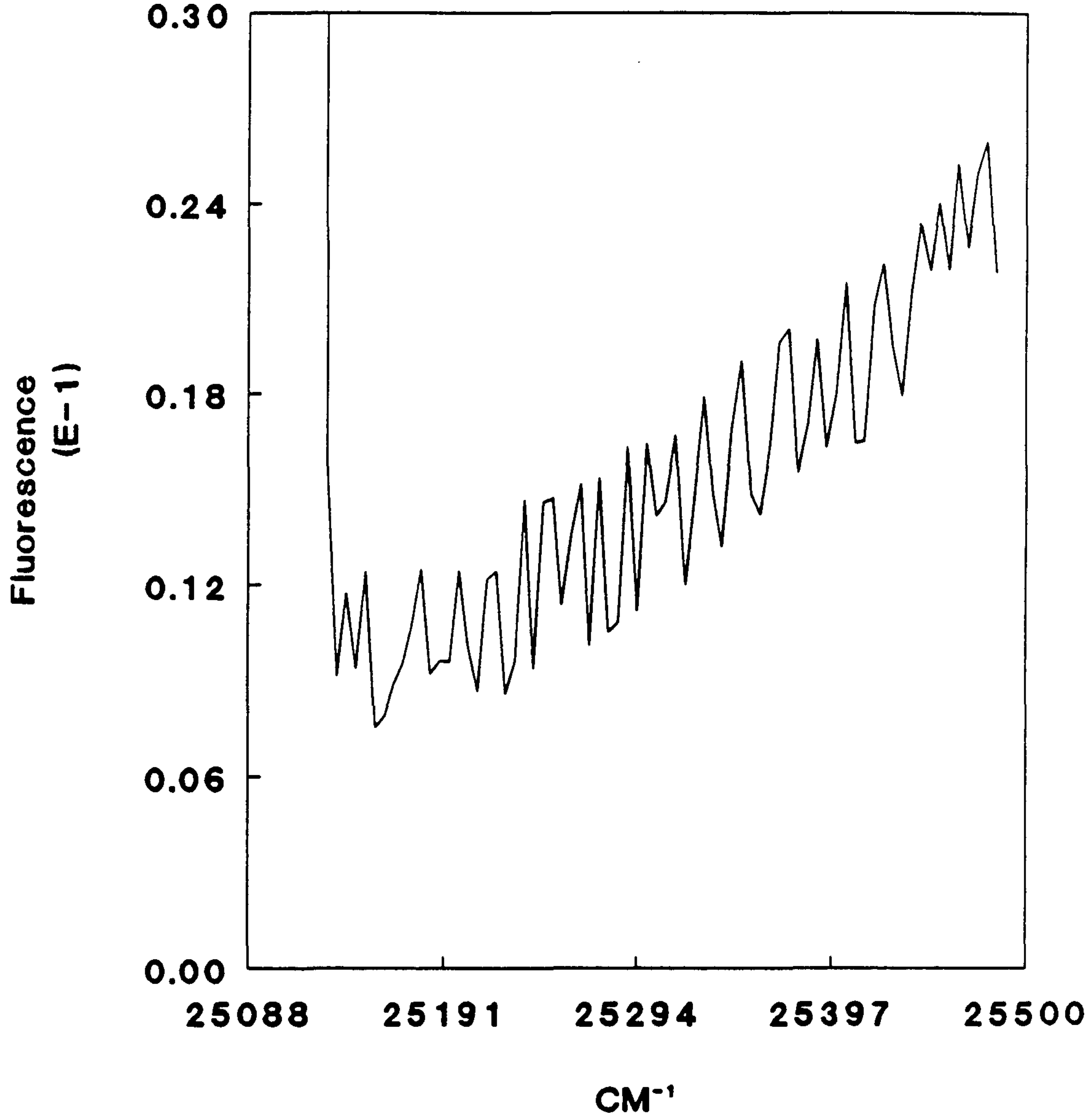

Figure 3.35

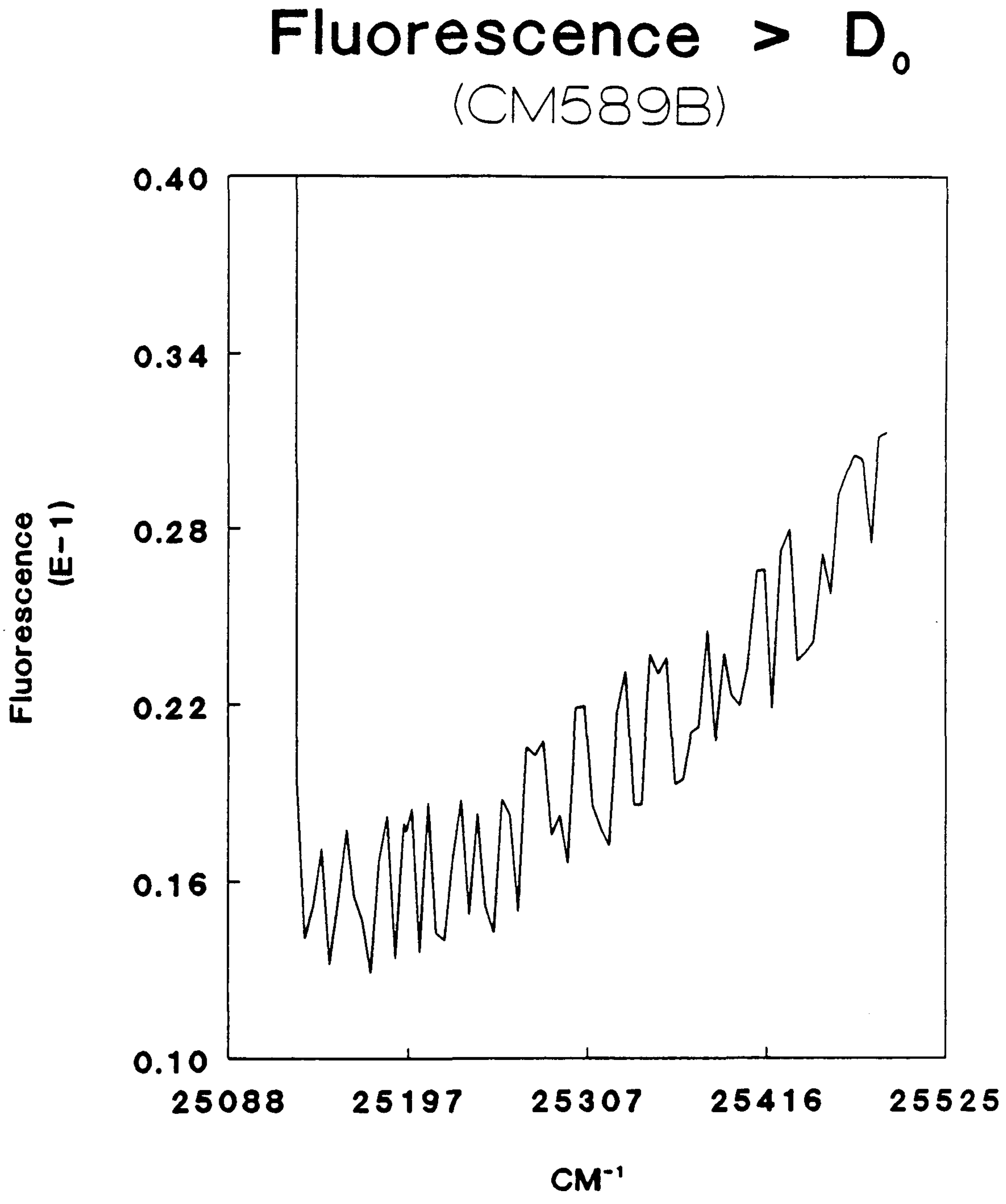
Fluorescence > D₀
(CM589B)
Fluorescence
(E-1)
0.40
0.34
0.28
0.22
0.16
0.10
25088
25197
25307
25416
25525
CM⁻¹

Figure 3.36

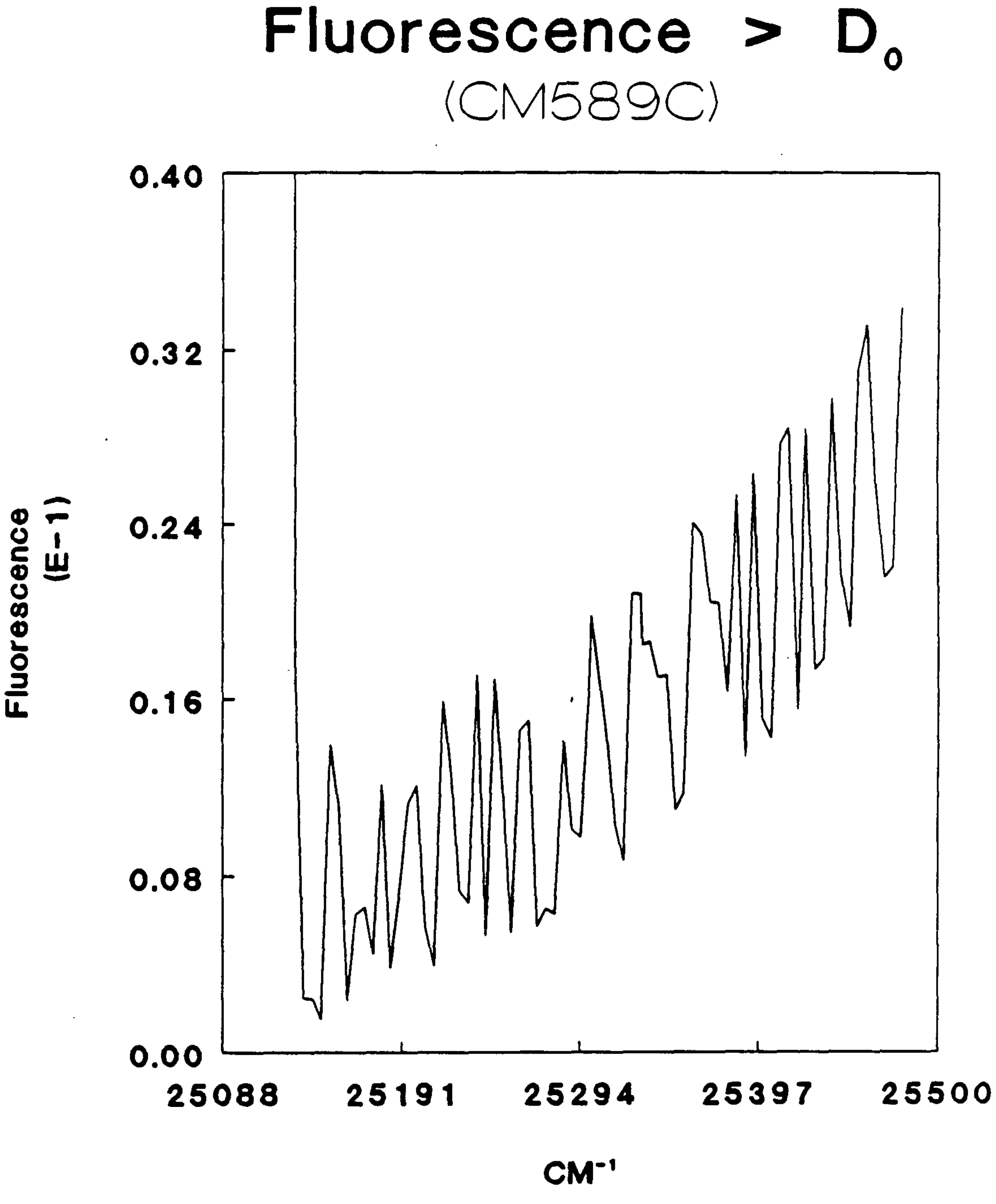
Fluorescence > D$_0$
(CM589C)
0.40
0.32
0.24
0.16
0.08
0.00
Fluorescence (E-1)
25088
25191
25294
25397
25500
CM^{-1}

Figure 3.37

Figures 3.38 - 3.43

3 reproductions of the fluorescence observed beyond the NO_2 dissociation threshold corrected for the laser power profile. The laser power profile follows each fluorescence spectrum.

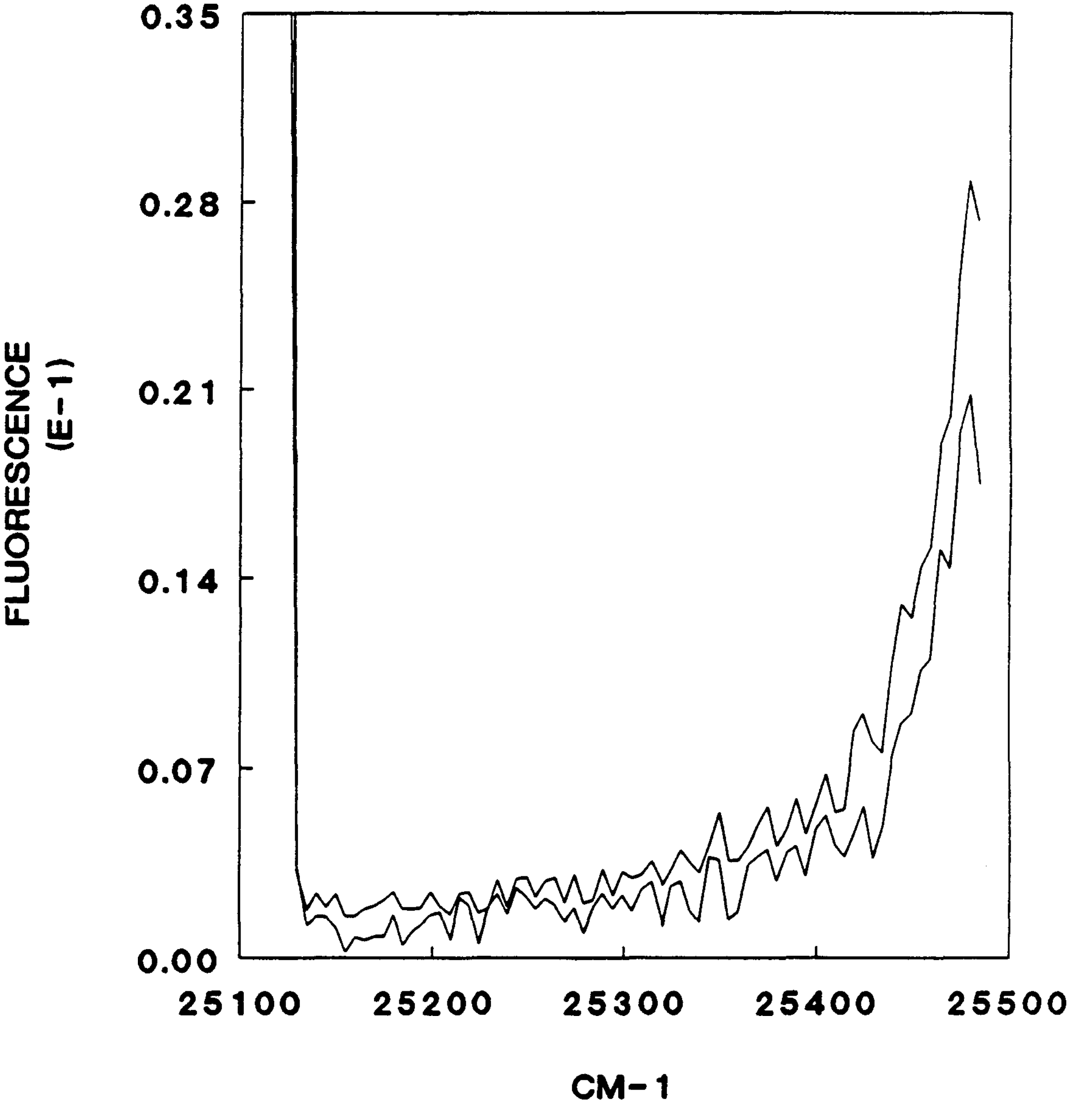

Fluorescence > D_0

(CM589A) Power Normalized

Figure 3.38

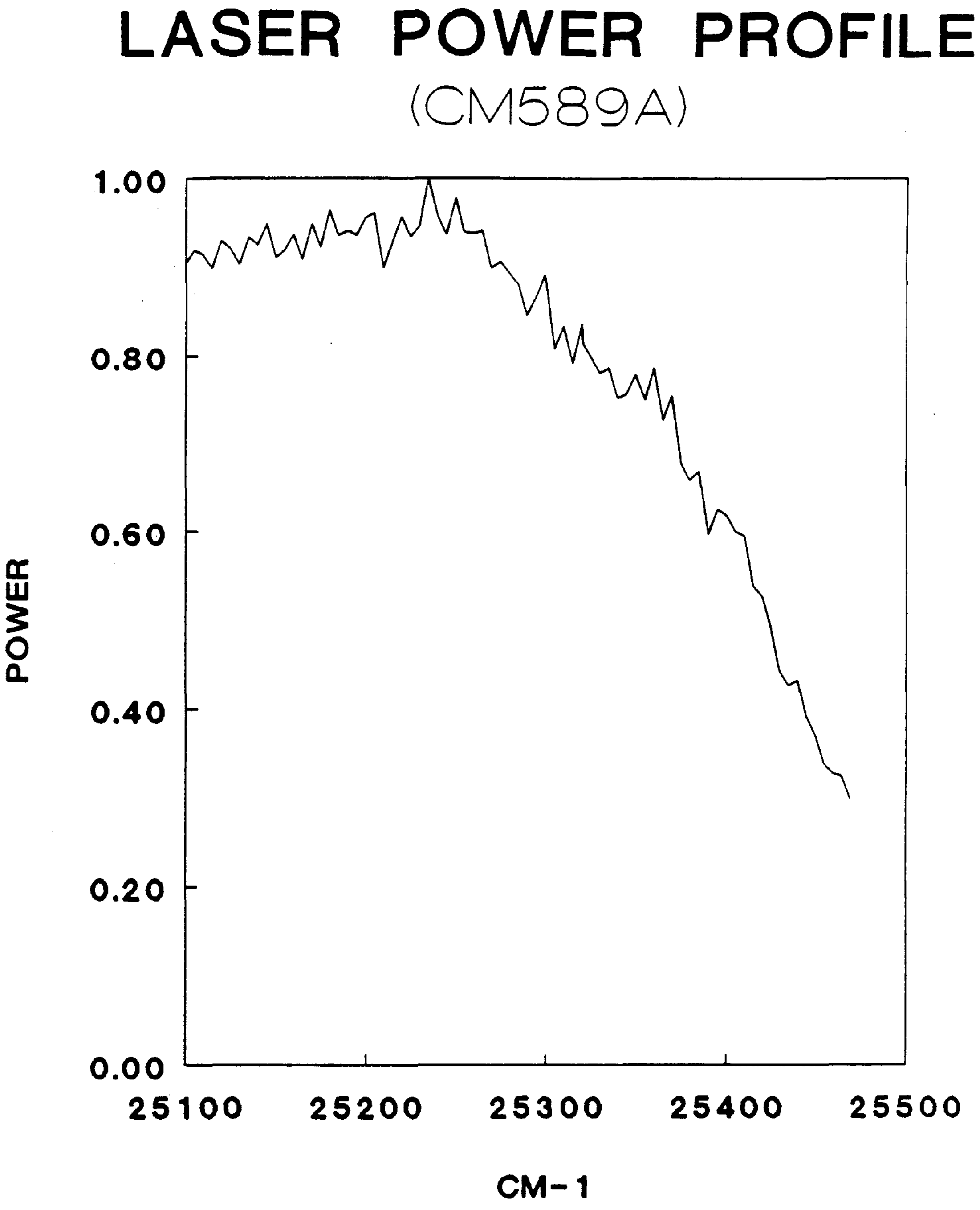
LASER POWER PROFILE
(CM589A)
1.00
0.80
0.60
0.40
0.20
0.00
POWER
25100
25200
25300
25400
25500
CM-1

Figure 3.39

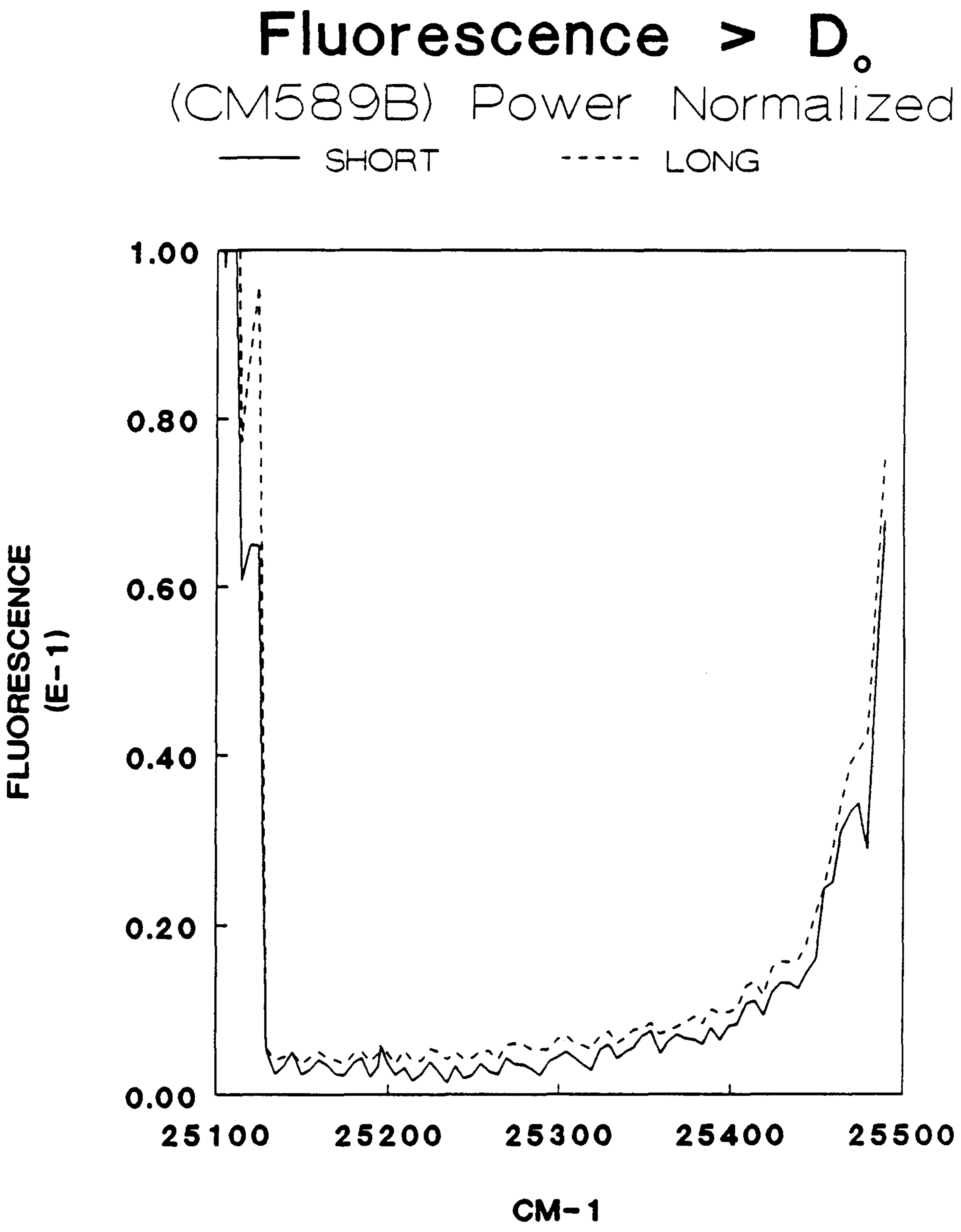
Fluorescence > D$_o$
(CM589B) Power Normalized
SHORT
LONG
FLUORESCENCE (E-1)
1.00
0.80
0.60
0.40
0.20
0.00
25100
25200
25300
25400
25500
CM-1

Figure 3.40

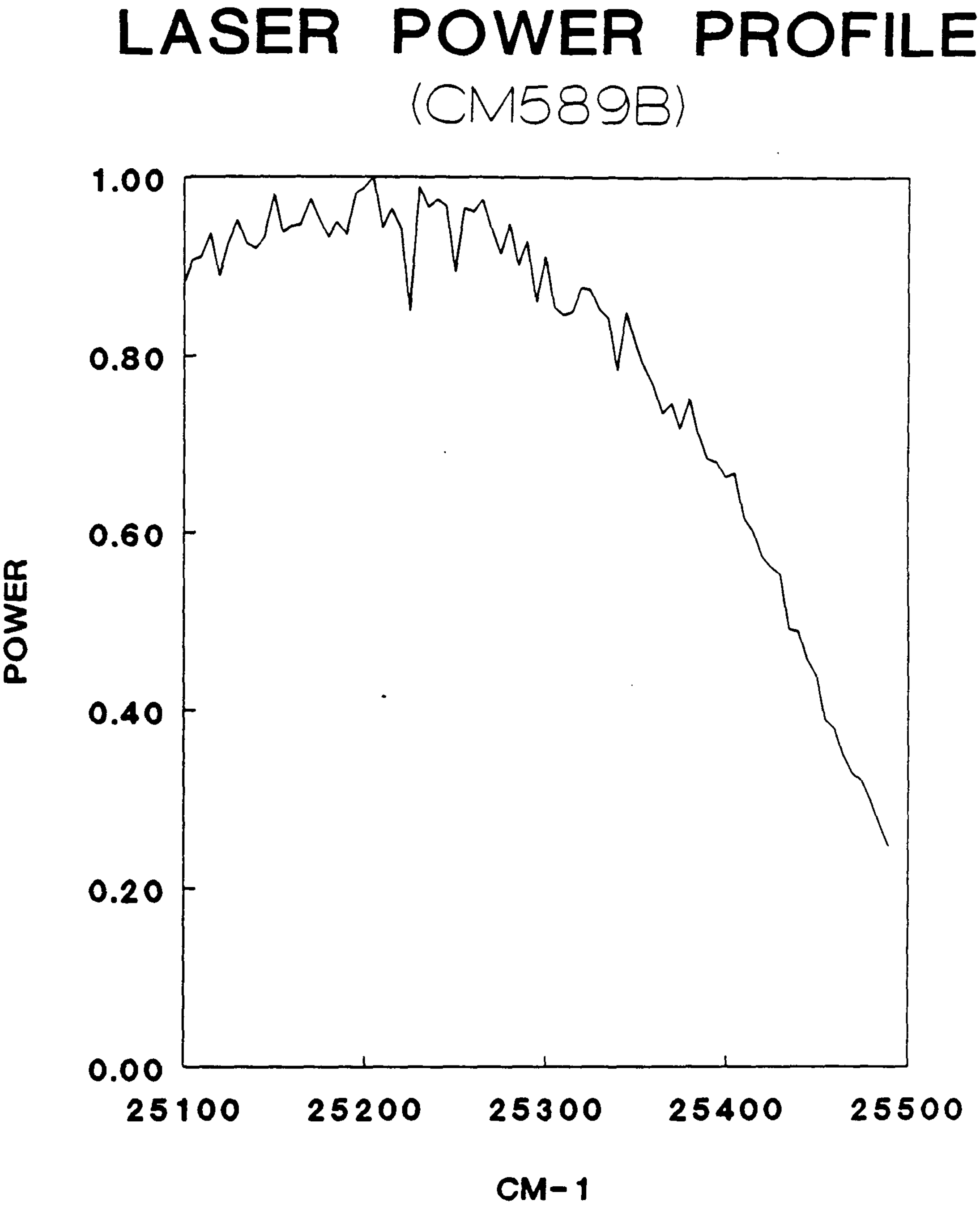
LASER POWER PROFILE
(CM589B)
POWER
1.00
0.80
0.60
0.40
0.20
0.00
25100
25200
25300
25400
25500
CM-1

Figure 3.41

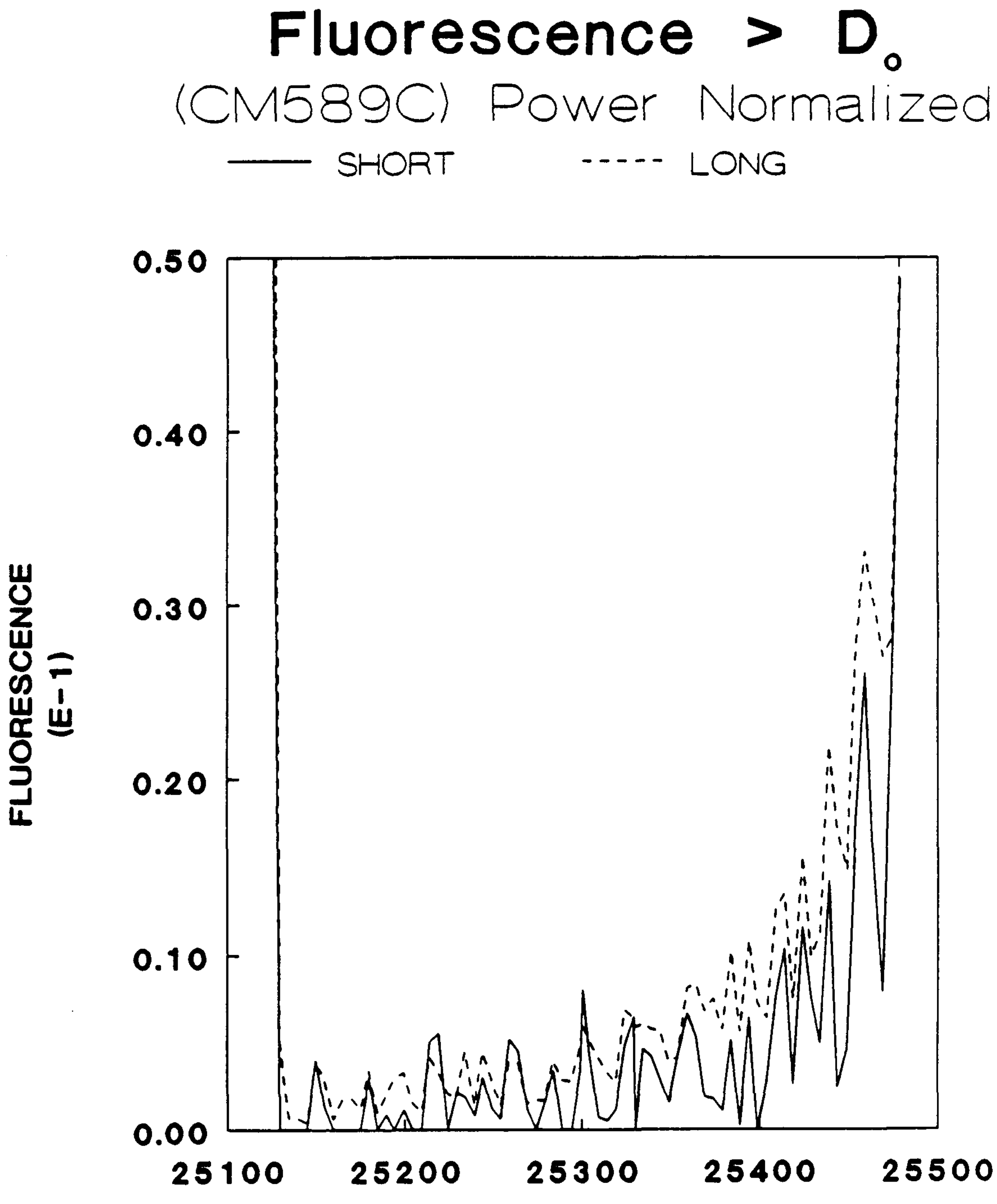
Fluorescence > D_o
(CM589C) Power Normalized
SHORT
LONG
0.50
0.40
0.30
0.20
0.10
0.00
FLUORESCENCE
(E-1)
25100
25200
25300
25400
25500
CM-1

Figure 3.42

LASER POWER PROFILE

(CM89C)

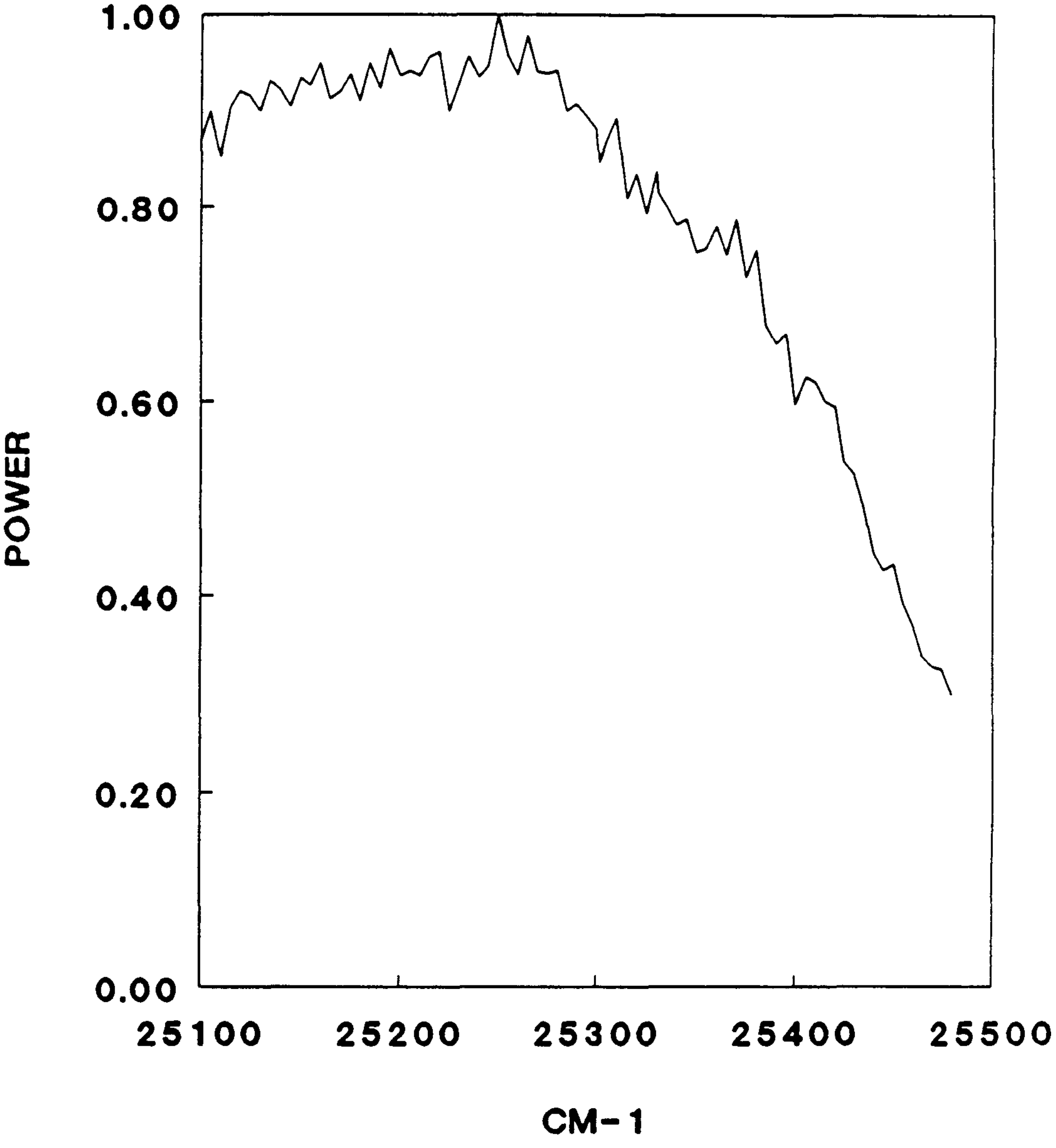

Figure 3.43

Figure 3.44

The NO_2 FEX spectrum observed for the entire dye range. Note the small gradual rise in the signal past D_0.

Figure 3.45

The corresponding laser power profile for the dye (Exalite 398) utilized to obtain the FEX spectrum in figure 3.44. The lasing baseline is given by the dashed line.

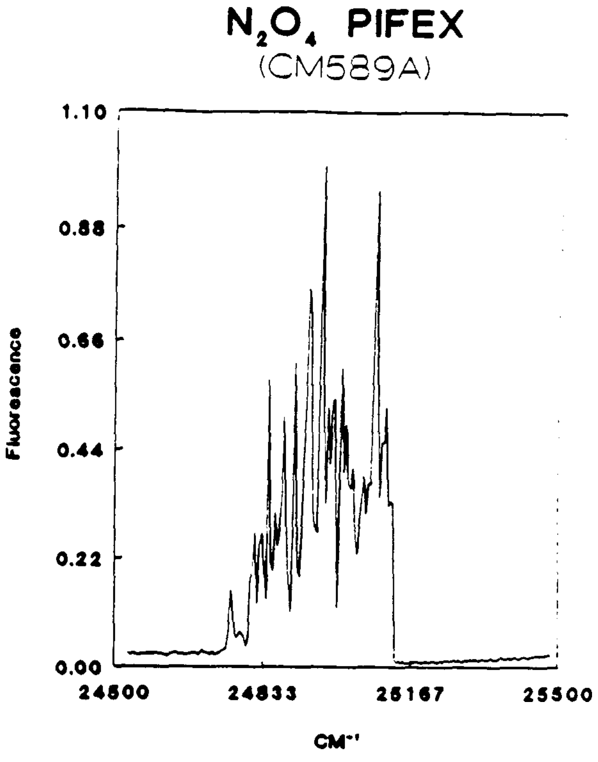

Figure 3.44

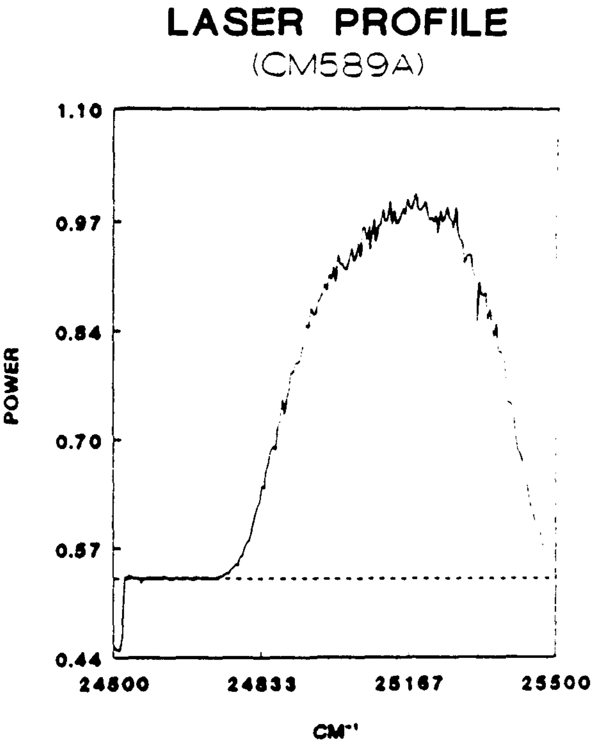

Figure 3.45

Figure 3.46

NO_2 parallel band with orgin = 25062.8 cm^{-1}.

Figure 3.47

The corresponding laser power profile.

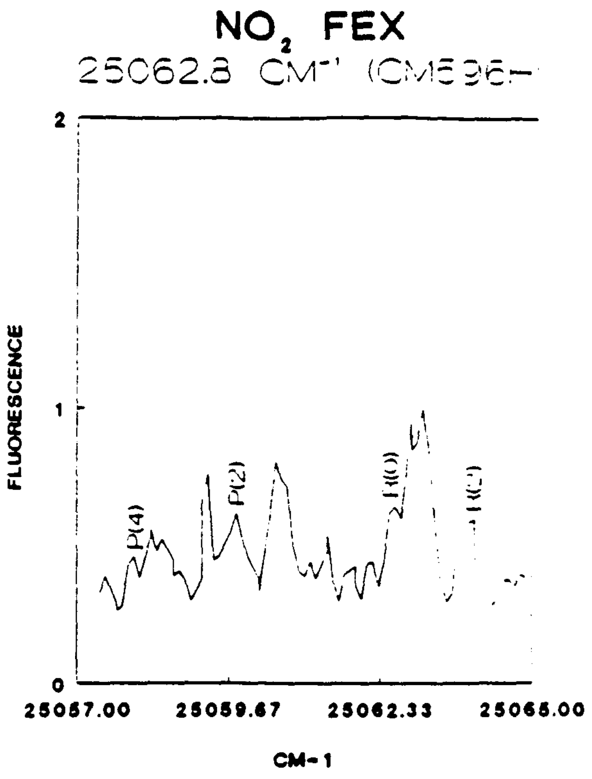

Figure 3.46

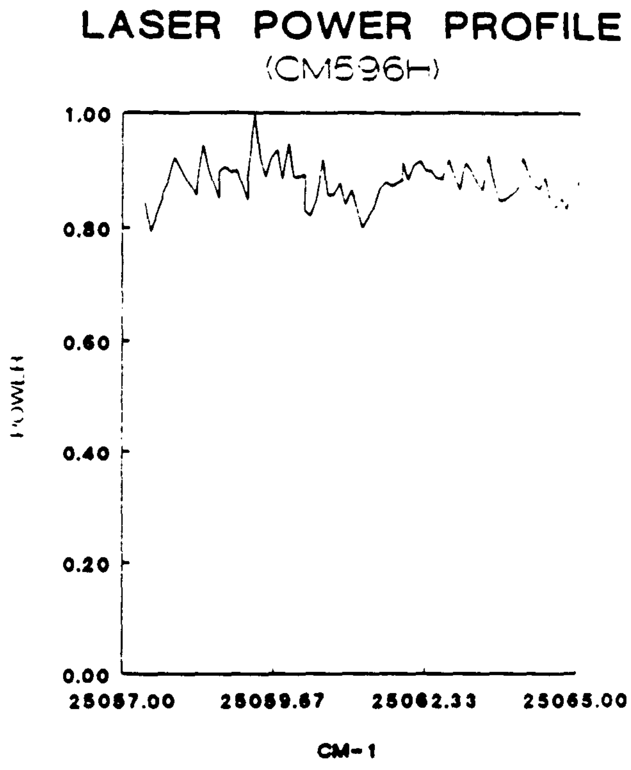

Figure 3.47

Figure 3.48

NO_2 parallel band with orgin = 24846.6 cm^{-1}.

Figure 3.49

The corresponding laser power profile.

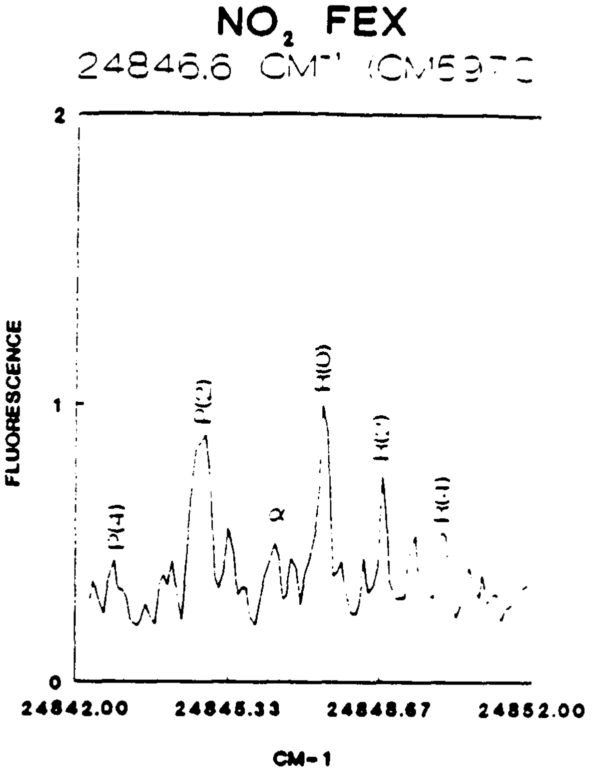

Figure 3.48

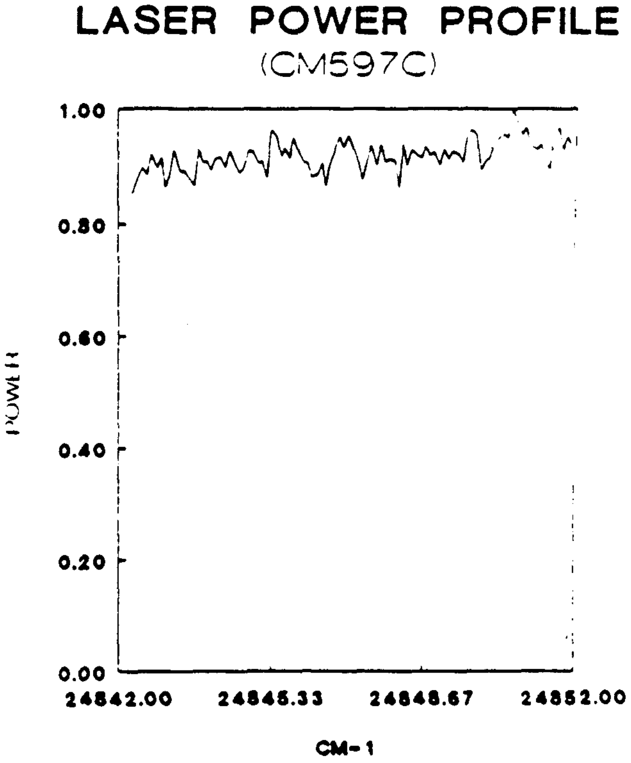

Figure 3.49

Figure 3.50

NO_2 parallel band with orgin = 24791.0 cm^{-1}.

Figure 3.51

The corresponding laser power profile.

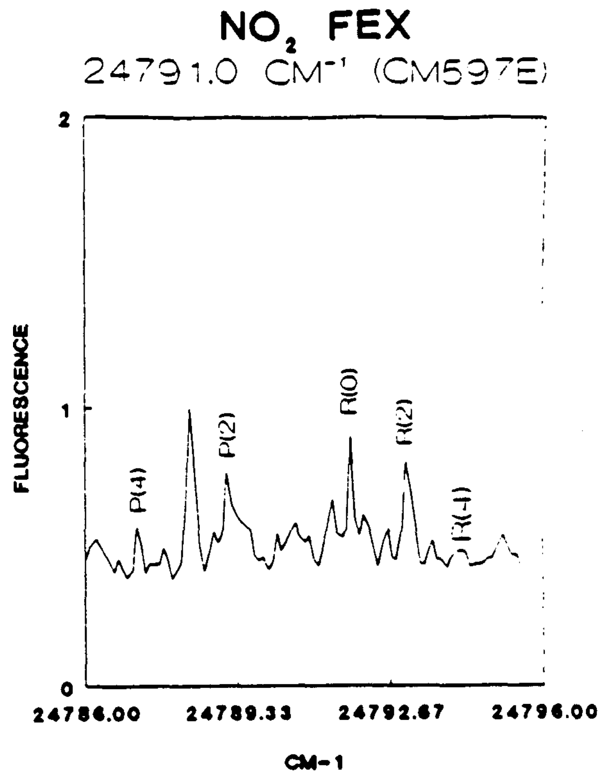

Figure 3.50

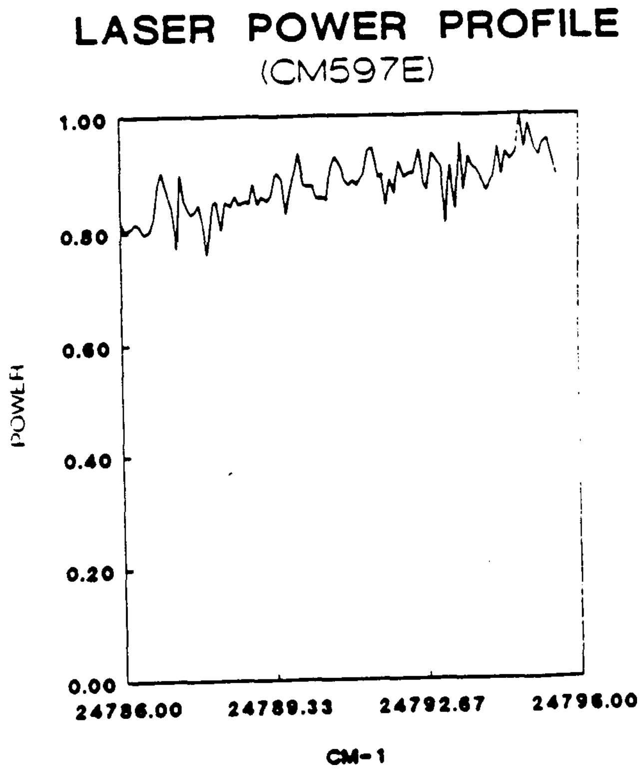

Figure 3.51

Figure 3.52

Schematic of the synchronous scan method for observing fluorescence to the v =1 level. As the excitation (solid) is scanned from start to finish the observed fluorescence (dashed line) is also scanned.

SYNCHRONOUS SCAN

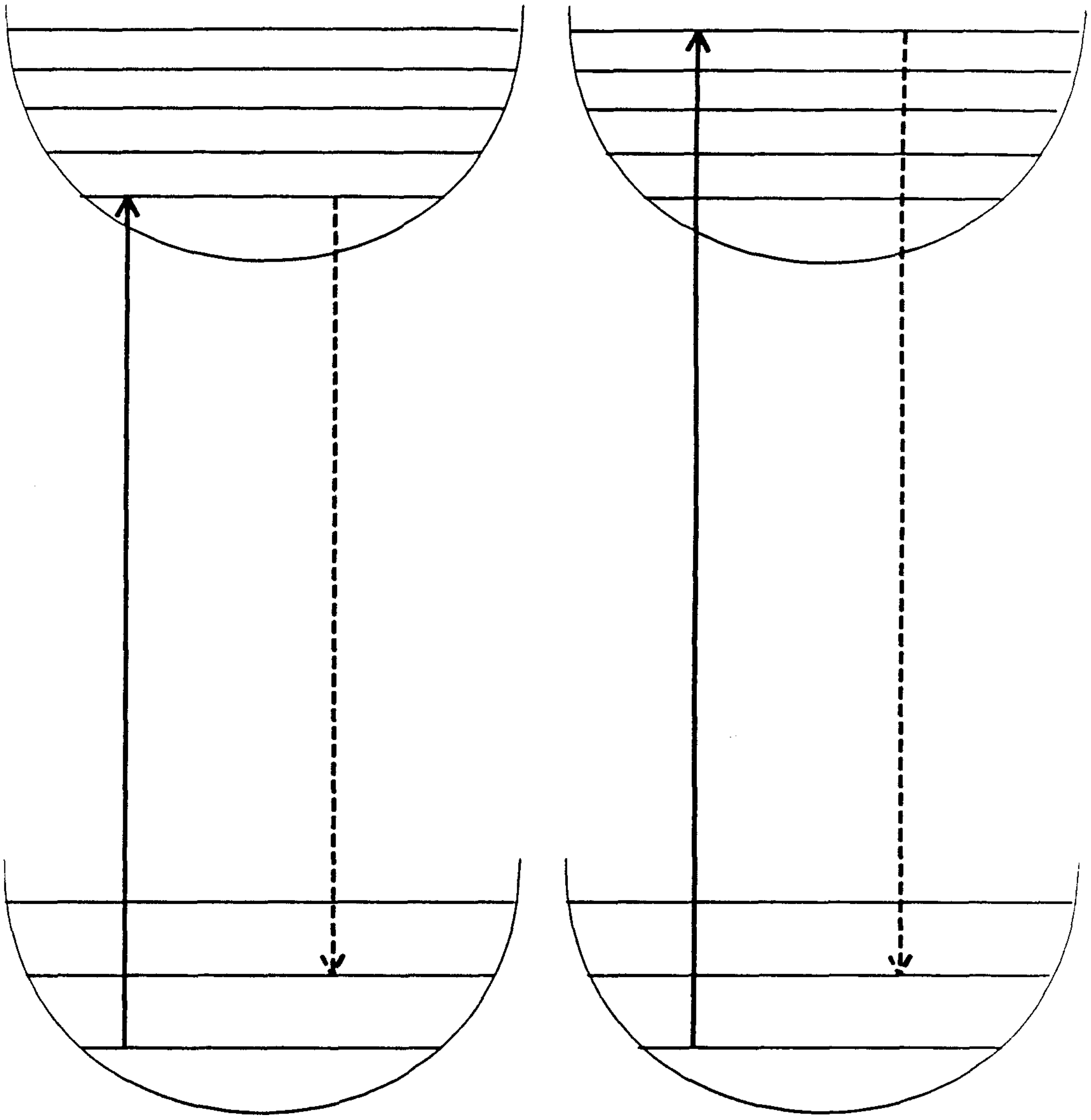

Figure 3.52

Figure 3.53

The ν_1 synchronous scan spectra of the parallel band observed at 24846.6 cm^{-1} (see Figure 3.48).

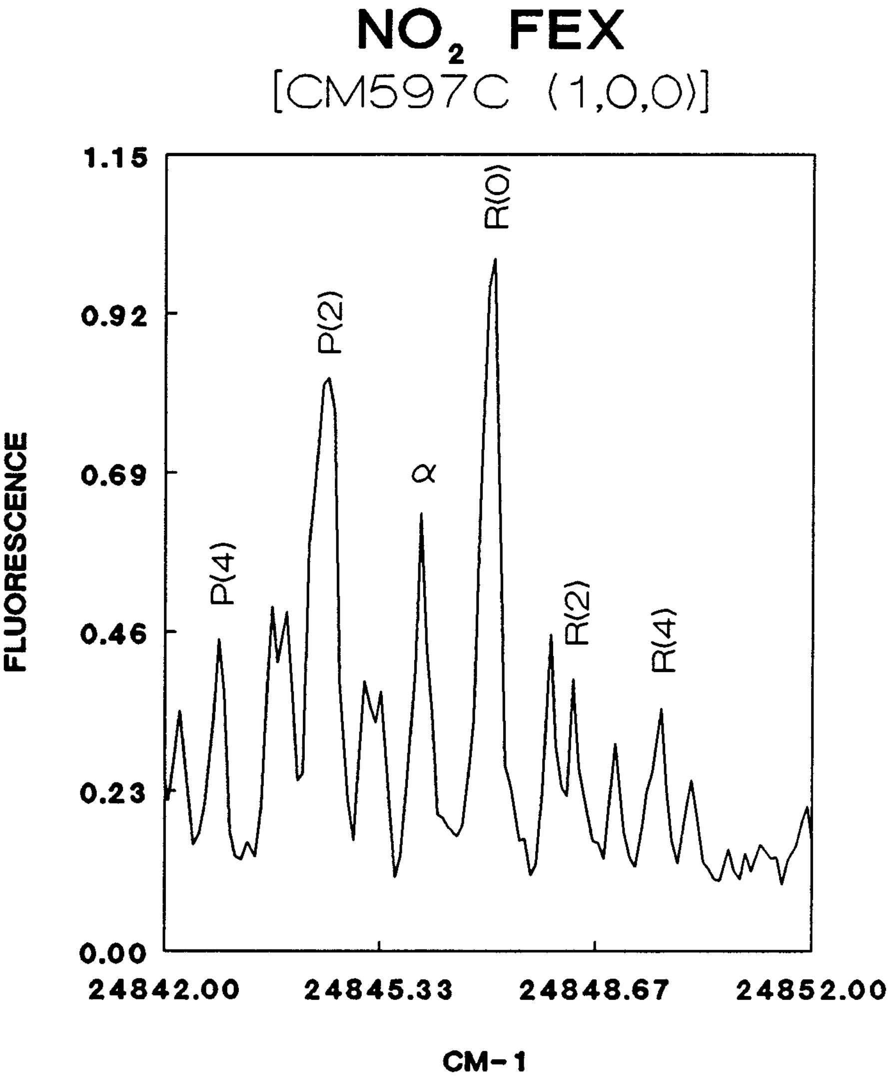
NO2 FEX
[CM597C (1,0,0)]
FLUORESCENCE
1.15
0.92
0.69
0.46
0.23
0.00
P(4)
P(2)
α
R(0)
R(2)
R(4)
24842.00
24845.33
24848.67
24852.00
CM-1

Figure 3.53

Figure 3.54

The ν_2 synchronous scan spectra of the parallel band observed at 24846.6 cm^{-1} (see Figure 3.48).

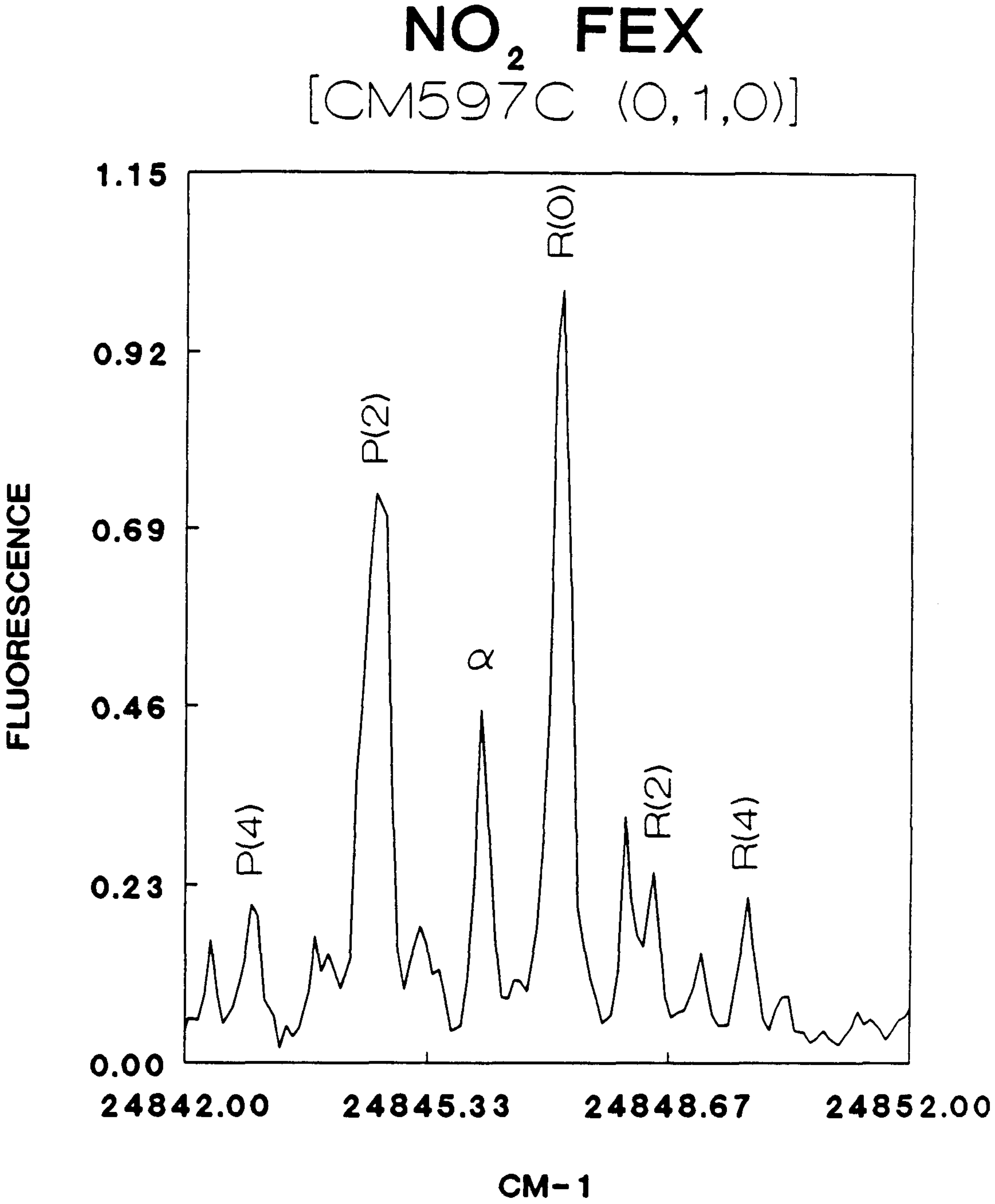
NO2 FEX
[CM597C (0,1,0)]
1.15
0.92
0.69
0.46
0.23
0.00
FLUORESCENCE
24842.00
24845.33
24848.67
24852.00
CM-1
P(4)
P(2)
α
R(0)
R(2)
R(4)

Figure 3.54

APPENDIX A

SYSTEM RESPONSE

The PIF data were corrected to account for the nonuniform response of the system (photocathode of the PMT, the grating of the monochromator, and all optics involved in the fluorescence collection). This was accomplished by a tungsten lamp at a temperature T scanned by a monochromator and collected by the same PMT and collection optics. The ratio of this observed tungsten lamp intensity profile ($I_{\lambda T(OBS)}$) to the true lamp intensity profile ($I_{\lambda T(TRUE)}$) gives the response profile of the system, which we shall refer to as the system response (S_λ). The corrected data are the ratio of the uncorrected data to the system response.

This correction occurs as follows: The true tungsten lamp intensity profile is computed through multiplying the blackbody at temperature T by the emissivity ($e_{\lambda T}$), the ratio of the spectral radiant intensity in a direction normal to the surface of the body at temperature T in the wavelength interval (λ,λ+dλ) to that of a blackbody at the same temperature and in the same wavelength interval. This produces the true tungsten lamp intensity profile.

$$I_{\lambda T(TRUE)} = e_{\lambda T}\, I^{B}_{\lambda T}\, d\lambda \qquad \text{(A.1)}$$

Values of $e_{\lambda T}$ from 230 - 2300 nm at temperatures from 1600° K to 2800° K in intervals of 200° K are tabulated by J.C. DeVos.

$$I^{B}_{\lambda T}\, d\lambda - \frac{8\pi hc}{\lambda^{5}(e^{\frac{hc}{\lambda kT}}-1)}\left(\frac{\lambda}{hc}\right) d\lambda \qquad (A.2)$$

The units of the blackbody in equation a.2 is photon density per wavelength interval.

$$S_{\lambda} - \frac{I_{\lambda T(OBS)}}{I_{\lambda T(TRUE)}} \qquad (A.3)$$

The system response for the different system configuration is illustrated in Figures A.1 - A.4. Note that the RCA 4832 and Hamamatsu R636 PPMTs are equipped with GaAs photocathodes which have a more uniform detection efficiency across the visible spectrum than the Hamamatsu R1477 PMT which is equipped with a multialkali (Na-K-Sb-Cs) photocathode.

REFERENCE: J.C. DeVos, Physica, XX, 690 (1954).

Figures A.1 - A.4

System respose curves illustrating how sensitive the system is to responding to a photon of the particular wavelength computed from Equation A.3. Note that a focusing lens (glass) was placed between the exit slit of the monochromator and the PMT for the experiments corresponding to the system response presented in Figure A.1; this was removed for all other experiments corrresponding to the other system response profiles.

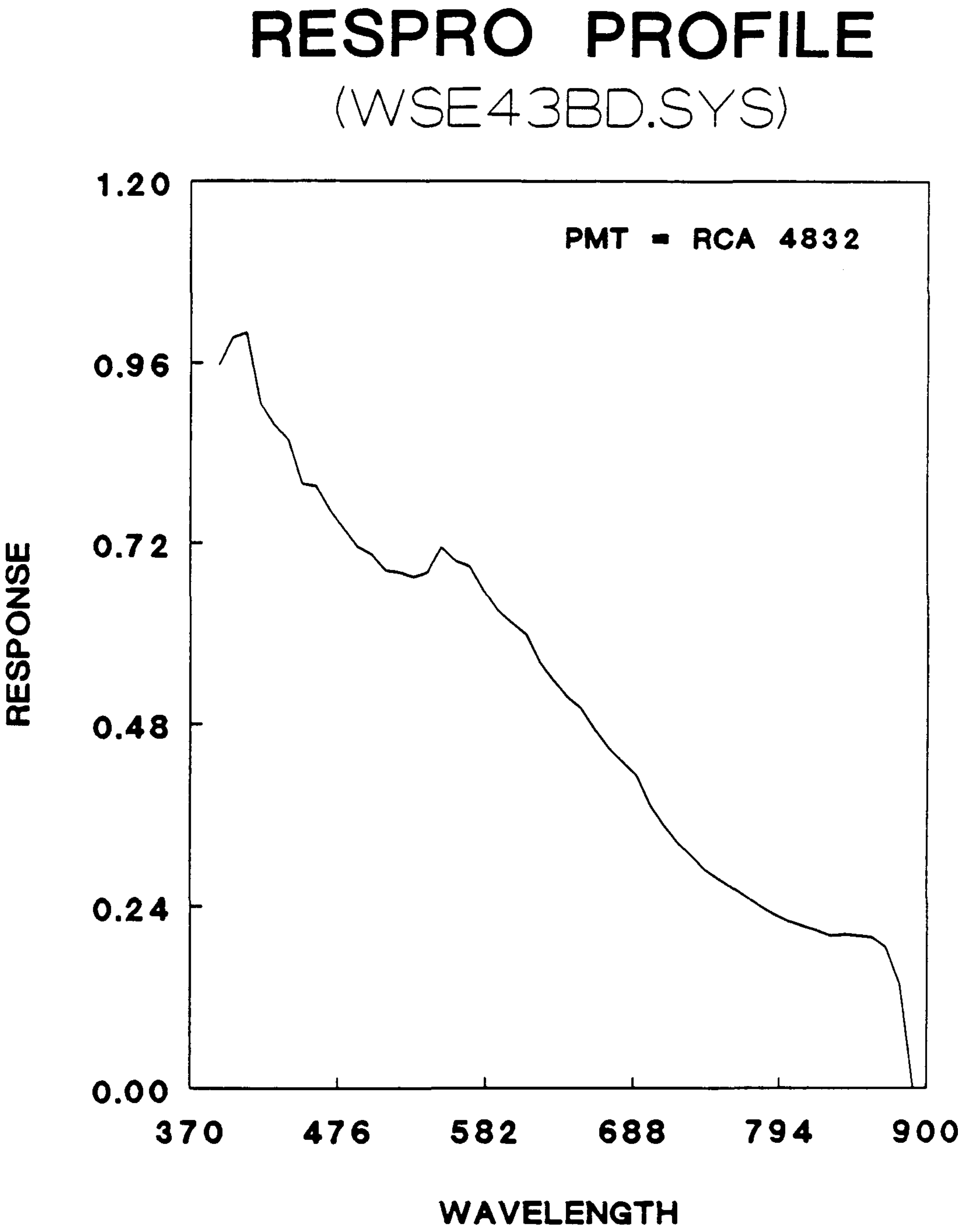
RESPRO PROFILE
(WSE43BD.SYS)
PMT = RCA 4832
1.20
0.96
0.72
0.48
0.24
0.00
RESPONSE
370
476
582
688
794
900
WAVELENGTH

Figure A.1

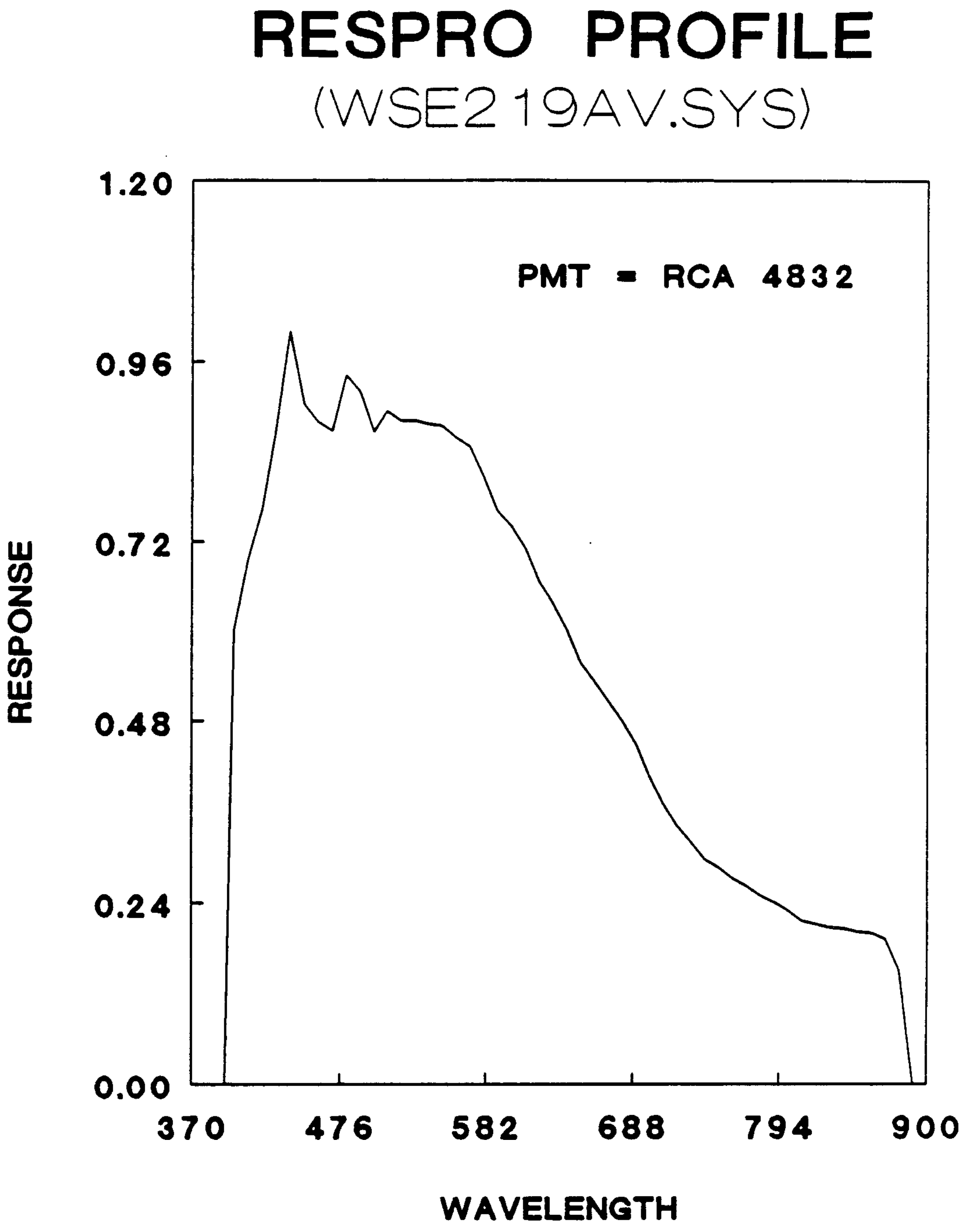

RESPRO PROFILE
(WSE219AV.SYS)

Figure A.2

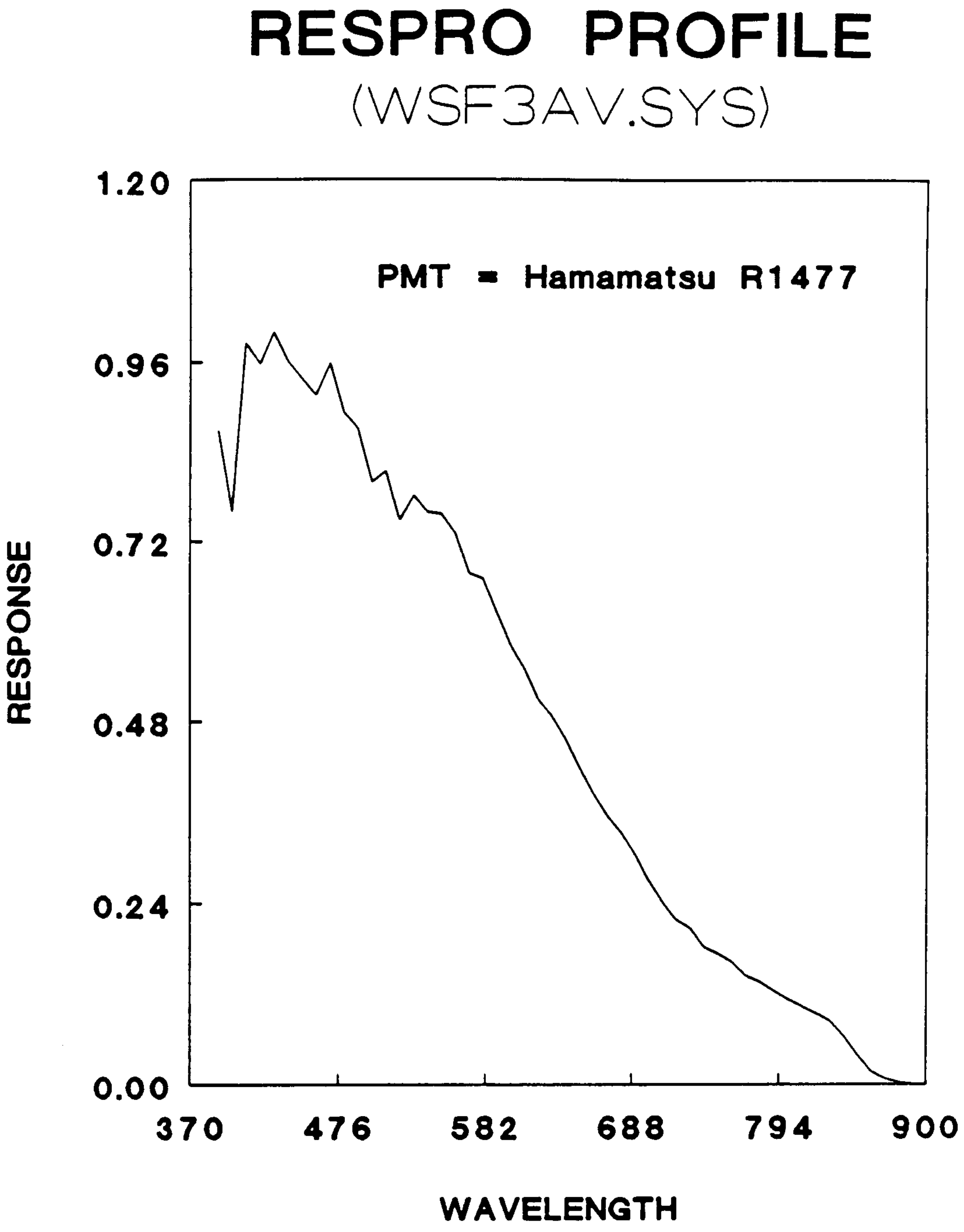
RESPRO PROFILE
(WSF3AV.SYS)
PMT = Hamamatsu R1477
RESPONSE
1.20
0.96
0.72
0.48
0.24
0.00
370
476
582
688
794
900
WAVELENGTH

Figure A.3

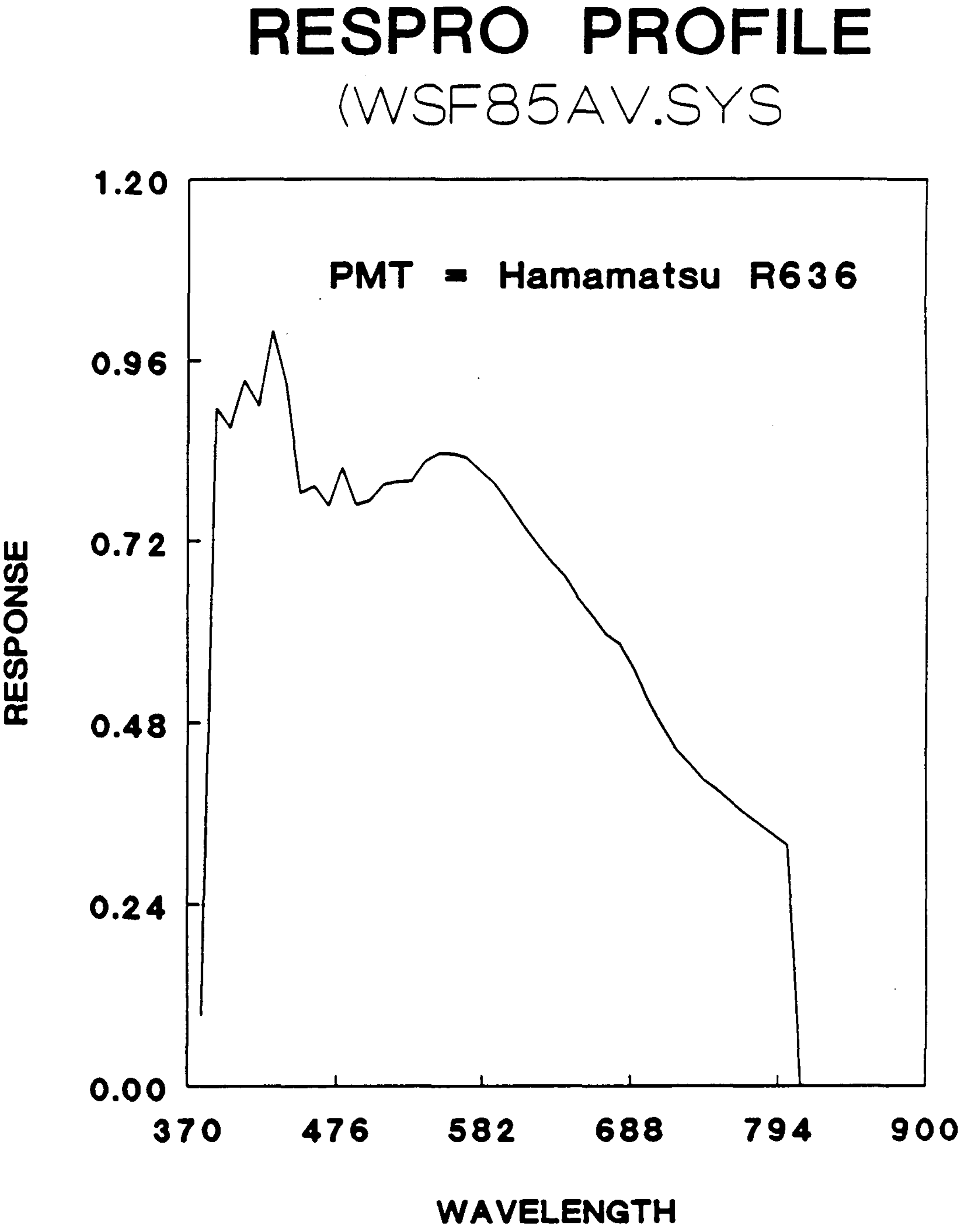
RESPRO PROFILE
(WSF85AV.SYS
PMT = Hamamatsu R636
RESPONSE
1.20
0.96
0.72
0.48
0.24
0.00
370
476
582
688
794
900
WAVELENGTH

Figure A.4

Appendix B

N_2O_4 Fluorescence Threshold

Fluorescence threshold data for three superimposed reproductions at 248 and 351 nm photolysis of N_2O_4 are shown in Figures B.1 and B.2. The thermodynamic threshold of NO_2 dissociation into NO + O is 25137 cm^{-1}; thus no NO_2 fluorescence is observed above this energy.[1] Initially it was deemed possible to obtain the N-N bond dissociation energy by noting the onset of fluorescence. In the absence of thermal energy the fluorescence at 351 nm photolysis should begin near 419 nm indicated by the dotted line assuming a bond dissociation energy of ~4600 cm^{-1}.[2] The 351 nm spectrum shows that a small and relatively insignificant amount of fluorescence still begins near 397.8 nm which corresponds to the $NO_2 \rightarrow NO + O$ dissociation. This fluorescence between 397.8 and 419 nm has a very poor signal to noise ratio. It should also be pointed out that the 248 nm PIF spectrum has a steeper ascent from 397.8 nm than the 351 nm spectrum. The area encompassed in the 351 nm spectrum from 397 to 419 nm ratioed to the total fluorescent area accounts for a smaller fraction than the equivalent ratio for the 248 nm spectrum. According to the vibrational partition function at 300 K approximately only 13% of the N_2O_4 molecules are in the vibrationless state; thus a significant fraction of N_2O_4 molecules exist in a vibrationally excited state. During the expansion only a small fraction of this vibrational energy is removed. The energy transfer effectiveness depends on the number of collisions and deactivation cross sections. The rotational-translational deactivation cross section, σ_{rot}, is much larger than the deactivation cross section for vibrational-translational or vibrational-rotational transfer, σ_{vib}. This makes vibrational cooling less effective than rotational cooling.[3] This vibrational excitation of the precursor most likely manifests itself in the fluorescence of the NO_2 fragment allowing fluorescence to begin at 397.8 nm instead of near 419 nm. The liberal seeding conditions (45 torr of N_2O_4 in 300 torr of helium) in addition to the significant number of low frequency vibrational modes in N_2O_4 obviate effective vibrational cooling. The significant fraction of fluorescence, greater than 99%, following 351 nm photolysis does agree well with the 419 nm threshold.

References

[1] C.H. Chen, D.W. Clark, M.G. Payne, and S.D. Kramer, Optics Communications, **32**, 391 (1980).

[2] I.C. Hisatsune, J. Phys. Chem., **65**, 2249 (1961).

[3] W. Demtröder, R. Duchowicz, J. Gress, H.J. Forth, R. Kullmer, G. Persch, and M. Schwarz, Physica Scripta., **T23**, 176 (1988).

Figure B.1

Illustration of the onset of NO_2 fluorescence following N_2O_4 photolysis at 248 nm for 3 superimposed spectra.

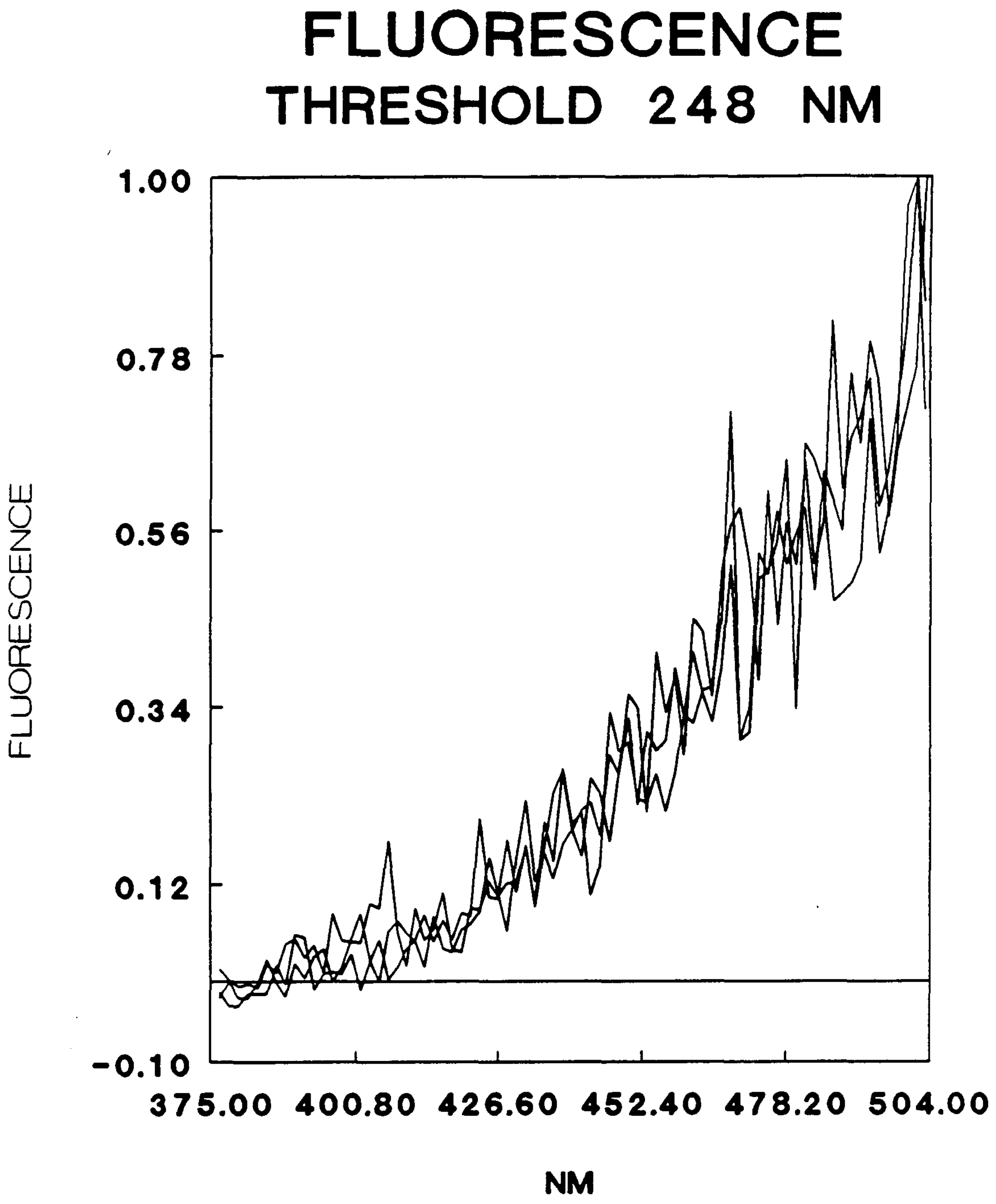

FLUORESCENCE
THRESHOLD 248 NM

Figure B.1

Figure B.2

Illustration of the onset of NO_2 fluorescence following N_2O_4 photolysis at 351 nm for 3 superimposed spectra. The dotted lines correspond to the threshold of NO_2 dissociation (397.8 nm) and the maximum available internal energy of NO_2 following 351 nm photolysis of N_2O_4.

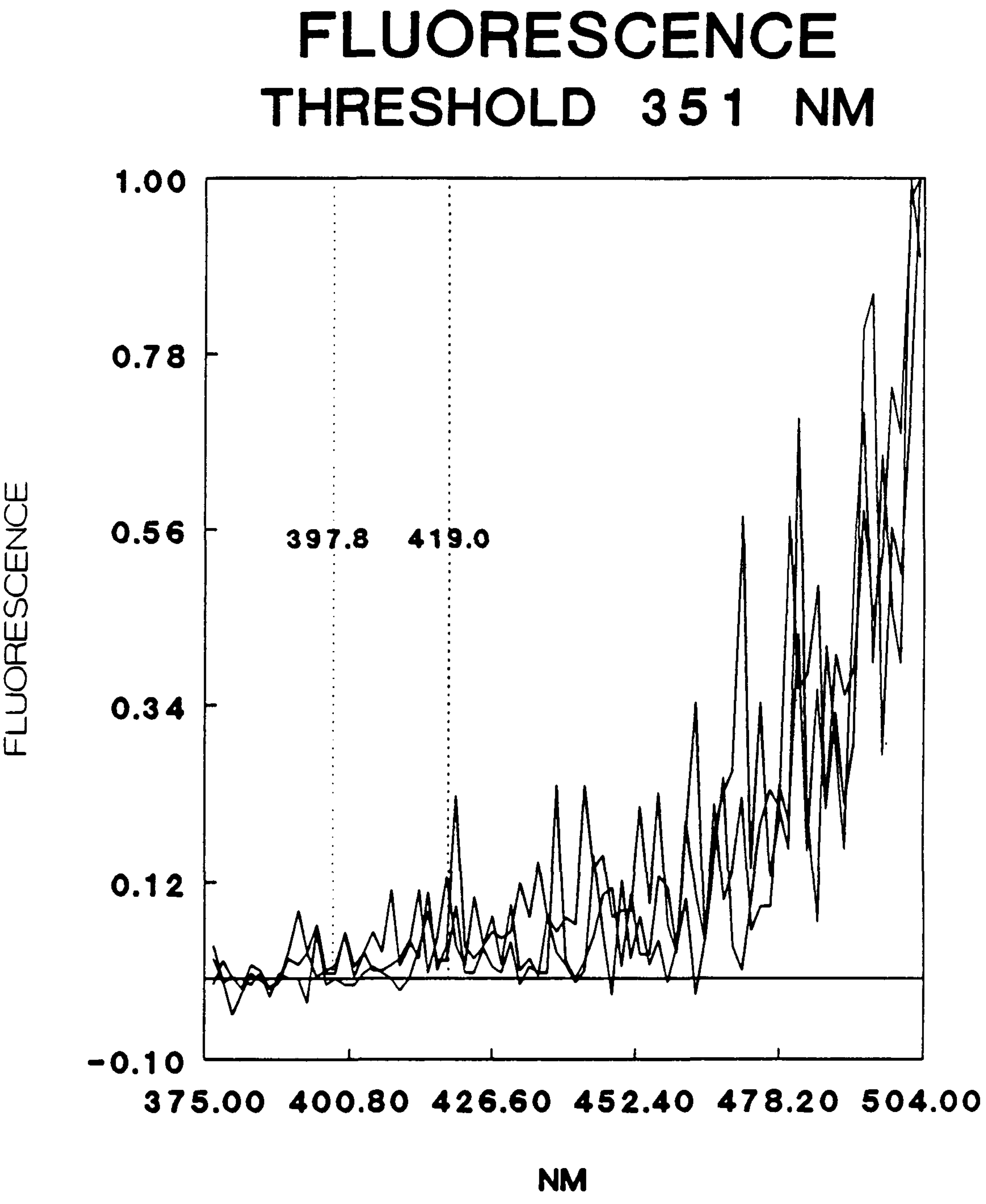
FLUORESCENCE
THRESHOLD 351 NM

Figure B.2

Appendix C

N_2O_4 Discrete Features

The 248 nm and 351 nm N_2O_4 PIF spectra illustrated in Figure C.1 show discrete features which are tabulated in Tables C.1-C.4. There were 83 and 35 reproducible features at 400 ns delay for the 351 and 248 nm PIF spectra respectively in the 404 - 807 nm range. When the delay time of data collection increases to 1500 ns the number of peaks falls to 64 for 351 nm and 31 for 248 nm PIF. Approximately 55% of the 1500 ns delay and 351 nm peaks appear at 400 ns delay; whereas 25% of the 1500 ns delay 248 nm peaks appear in the 400 ns delay PIF spectra. The absolute intensities of these peaks could not be obtained due to the poor signal to noise which caused the peak heights to change. The peak positions were constant within 5Å with a slit resolution of 20Å. These peaks could not be assigned particular state-to-state transitions due to complexities of the NO_2 LIF spectra and the nature by which the electronically excited NO_2 was produced. This is the first published report of such peaks at 248 and 351 nm. Kawasaki[1] did not report the observation of discrete features in his emission spectra of N_2O_4 possibly due to utilizing a very long observation time in which post photolysis collisions may degrade the spectrum. Another reason why Kawasaki may not have seen these discrete features may be due to his utilization of a neat beam as opposed to a seeded beam as was utilized in this experiment. There has been some speculation that the discrete features are due to multiphoton excitation with subsequent NO β band (B→X) emissions which extend into the visible for when it fluoresces to the high vibrational levels of the ground state. The fluorescence lifetime of such emission is 50 - 100 μsec.[1] The results of this experiment do not support this claim due to: (1) the first order dependence of the fluorescence with laser power and (2) the spectral range of the sharp features not extending below the dissociation threshold of NO_2. These features are not due to due to multiphoton excitation of NO_2 followed by the visible emission of $2^2B_2 \rightarrow 1^2B_2$, because the lifetime of such transitions is less than 10 ns.[2]

It is believed that these features are due to N_2O_4 photolyzing to produce a much more narrow distribution of excited state NO_2 relaxing to particular ground vibrational states and emitting a photon corresponding to this energy difference. Donnelly and coworkers have carried out studies of low pressure NO_2 laser induced fluorescence.[3] They observed a low pressure (0.01-0.1 mTorr) collision free continuum which is of increasing importance as excitation energy increases. This also is the case for the N_2O_4 photolysis wavelength in that the continuum is dominant at 193 nm, but not so pronounced at 248 and 351 nm excitation in which the sharp features are apparent. This is based on the PIF analysis showing higher NO_2 internal energy for photolysis at 193 nm than at 248 or 351 nm. Donnelly concluded that the sharp features are attributed to the vibrational levels of the optically allowed excited electronic states ($^2B_1$,$^2B_2$) fluorescing to various vibrational levels of the ground electronic state ($^2A_1$). The density of $^2A_1$ vibrational levels is very large in the region of the $^2B_1$ and $^2B_2$ electronic origins; thus, accounting for an apparent " continuum of emission. "

Eventually these discrete features might be assigned specific quantum states. Recent work by Persch and coworkers[4] demonstrated the existence of 407 vibronic band origins with B_2 symmetry in the spectral range from 13277-24565 cm^{-1}. By adding or subtracting quanta from the observed peaks, both the 351 and 248 nm data, these band origins could be obtained as shown in Table C.5. This would seem to suggest that the NO_2^* is fluorescing from the $^2B_2$ state. This could be the case; however this doesn't negate the possibility of NO_2^* being born in the $^2B_1$ state, curve crosssing to the $^2B_2$ state and subsequently fluorescing.

References

[1] H.Dunnwald, E. Siegel, W. Urban, J.W. Rich, G.F. Homicz, and M.J. Williams Chem. Phys. **94**, 195 (1985).

[2] K. Tsukiyama, J. Chem. Phys. **82**, 1147 (1985).

[3] V.M. Donnelly, D.G. Keil, and F. Kaufman, J. Chem. Phys. **71**, 659 (1979).

[4] G. Persch, E. Mehdizadeh, W. Demtröder, Th. Zimmermann, H. Köppel, and L.S. Cederbaum, Ber. Bunsenges. Phys. Chem., **92**, 312 (1988).

Table C.1
Energy Locations for Fluorescent Discrete Features Following the Photolysis of N_2O_4 at 351 nm Delay 400 ns

No.	Energy[cm^{-1}]	No.	Energy[cm^{-1}]
1.	24325.	42.*	16162.9
2.	23946.4	43.*	16033.3
3.	23485.4	44.	15992.3
4.	22779.0	45.*	15908.4
5.	22527.	46.*	15745.6
6.	22281.6	47.	15664.2
7.*	22119.0	48.*	15583.6
8.*	21958.7	49.	15501.5
9.	21575.0	50.*	15363.3
10.	21222.4	51.	15260.2
11.	20929.3	52.	15178.4
12.	20785.7	53.	15061.8
13.	20439.4	54.*	14926.0
14.	20169.4	55.*	14798.8
15.	19841.3	56.*	14671.4
16.	19712.2	57.*	14573.6
17.	19586.0	58.*	14490.0
18.*	19153.4	59.	14426.5
19.	19096.7	60.#	14363.1
20.*	18801.6	61.	14299.0
21.	18684.6	62.*	14245.0
22.*	18516.1	63.	14186.4
23.*	18349.6	64.#	14128.3
24.*	18183.5	65.*	14098.4
25.	17972.7	66.	14017.4
26.*	17815.8	67.*	13861.6
27.*	17711.7	68.*#	13708.0
28.	17608.7	69.	13596.7
29.	17559.3	70.	13505.7
30.	17458.1	71.	13397.1
31.	17409.7	72.	13328.5
32.*	17259.2	73.*	13232.8
33.	17164.4	74.*	13061.7
34.	16972.2	75.*	12951.7
35.	16923.3	76.	12841.9
36.	16784.2	77.*	12708.1
37.	16691.7	78.	12655.03
38.	16556.3	79.	12577.0
39.	16380.0	80.	12347.2
40.	16292.0	81.*	12448.6
41.	16204.8	82.	12397.7

* Feature also seen at 351 nm 1500 ns delay

\# Feature also seen at 248 nm 400 ns delay

Table C.2
Energy Location for Fluorescent Discrete Features Following the Photolysis of N_2O_4 at 351 nm delay 1500 ns

No.	Energy[cm^{-1}]	No.	Energy[cm^{-1}
1.	24721.9	32.	16334.5
2.	^{2}4420.0	33.*	16162.9
3.	24230.7	34.	16118.6
4.	23849.3	35.*	16033.3
5.	23041.5	36.	15951.5
6.	22779.0	37.*	15908.4
7.	22696.3	38.*	15745.6
8.*	22119.0	39.*	15583.6
9.*	21958.7	40.*	15363.3
10.	21802.6	41.	15183.7
11.	21647.4	42.*	14926.0
12.	21367.5	43.*	14799.5
13.	20999.6	44.*	14671.4
14.	20859.4	45.*	14573.6
15.	20104.5	46.*	14490.0
16.	19906.4	47.	14423.5
17.	19399.9	48.	14330.8
18.	19154.5	49.*	14245.0
19.	18977.1	50.*	14098.4
20.	18800.5	51.	14011.5
21.	18630.6	52.*	13869.6
22.*	18516.8	53.*	13708.0
23.*	18348.6	54.	13587.0
24.*	18183.3	55.	13495.3
25.*	17815.8	56.	13406.6
26.*	17711.7	57.	13290.8
27.	17661.6	58.*	13232.8
28.	17507.0	59.*	13061.7
29.*	17259.2	60.*	12951.7
30.	16466.3	61.	12815.6
31.	16423.1	62.*	12708.1
		63.	12551.8
		64.*	12448.6

* Feature also seen at 351 nm 400 ns delay
# Feature also seen at 248 nm 1500 ns delay

Table C.3
Energy Location for Fluorescent Discrete Features
Following Photolysis at 248 nm delay 400 ns

No.	Energy[cm^{-1}]	No.	Energy[cm^{-1}]
1.	20483.4	19.*	15633.5
2.*	20008.0	20.	15392.9
3.	18935.8	21.*	15084.1
4.	18758.2	22.	15009.4
5.	18583.9	23.	14934.3
6.	18357.0	24.	14823.6
7.	18032.6	25.#	14362.7
8.	17917.9	26.	14678.9
9.	17758.8	27.#	14127.3
10.*	17500.9	28.	14028.2
11.*	17299.5	29.	13930.5
12.*	17199.9	30.	13771.3
13.	17102.8	31.#	13707.1
14.	16957.8	32.	13431.8
15.	16675.0	33.	13224.0
16.*	16447.4	34.	13080.4
17.*	16224.5	35.	12966.8
18.	15881.8		

* Feature also seen at 248 nm 1500 ns delay
\# Feature also seen at 351 nm 400 ns delay

Table C.4
Energy Location for Fluorescent Discrete Features Following Photolysis of N_2O_4 at 248 nm delay 1500 ns

No.	Energy[cm^{-1}]	No.	Energy[cm^{-1}]
1.	23719.2	18.	16815.2
2.	22818.1	19.*	16447.4
3.	22563.2	20.*	16224.5
4.	22391.4	21.	15756.7
5.	21057.1	22.*	15633.5
6.	20911.8	23.	15198.7
7.*	20008.0	24.*	15084.1
8.	19550.3	25.	14608.1
9.	19425.0	26.	13645.4
10.	19177.3	27.	13584.1
11.	18758.2	28.	13522.7
12.	18583.9	29.	13081.3
13.	18357.0	30.	13024.2
14.	18135.7	31.	12430.9
15.*	17500.9		
16.*	17299.5		
17.*	17199.9		

* Feature also seen at 248 nm 400 ns delay
\# Feature also seen at 351 nm 1500 ns delay

Correlation of NO_2 Fluorescent Peaks With $^2B_2$ Orgins of Persch

$\omega_1 = 1321$ $\omega_2 = 750$ $\omega_3 = 1617$

ENERGY IN CM^{-1}

351 NM BANDS

REF ν	Δv_1	Δv_2	Δv_3	Resultant ν	True ν
19841.3	−1	+3	−1	19153.3	19153.
	0	−1	0	19091.3	19096.7
	−1	0	0	18520.3	18516.1
	0	−2	0	18341.3	18349.6
	−1	+2	−2	16786.3	16784.2
	−1	+1	−2	16036.3	16033.3
	−2	0	−1	15582.3	15583.6
	−1	+1	−3	14419.3	14426.5
	0	−3	−2	14357.3	14363.1
	−3	+1	−2	13394.3	13397.1
17815.8	−2	+4	−1	16556.8	16556.3
	−1	+2	−1	16377.8	16380.0
	−1	−1	0	15744.8	15745.6
	−2	0	0	15173.8	15178.4
	−2	+2	−1	15056.8	15061.8
	−3	+3	−1	14485.8	14490
	−2	−1	0	14423.8	14426.5
	−1	−3	0	14244.8	14245.
	−2	+3	−2	14189.8	14186.4
	−1	−1	−1	14127.8	14128.3

Table C.5

Figure C.1

Illustration of the N_2O_4 PIF spectra (not corrected for the system response) at 351, 248, and 193 nm excitation.

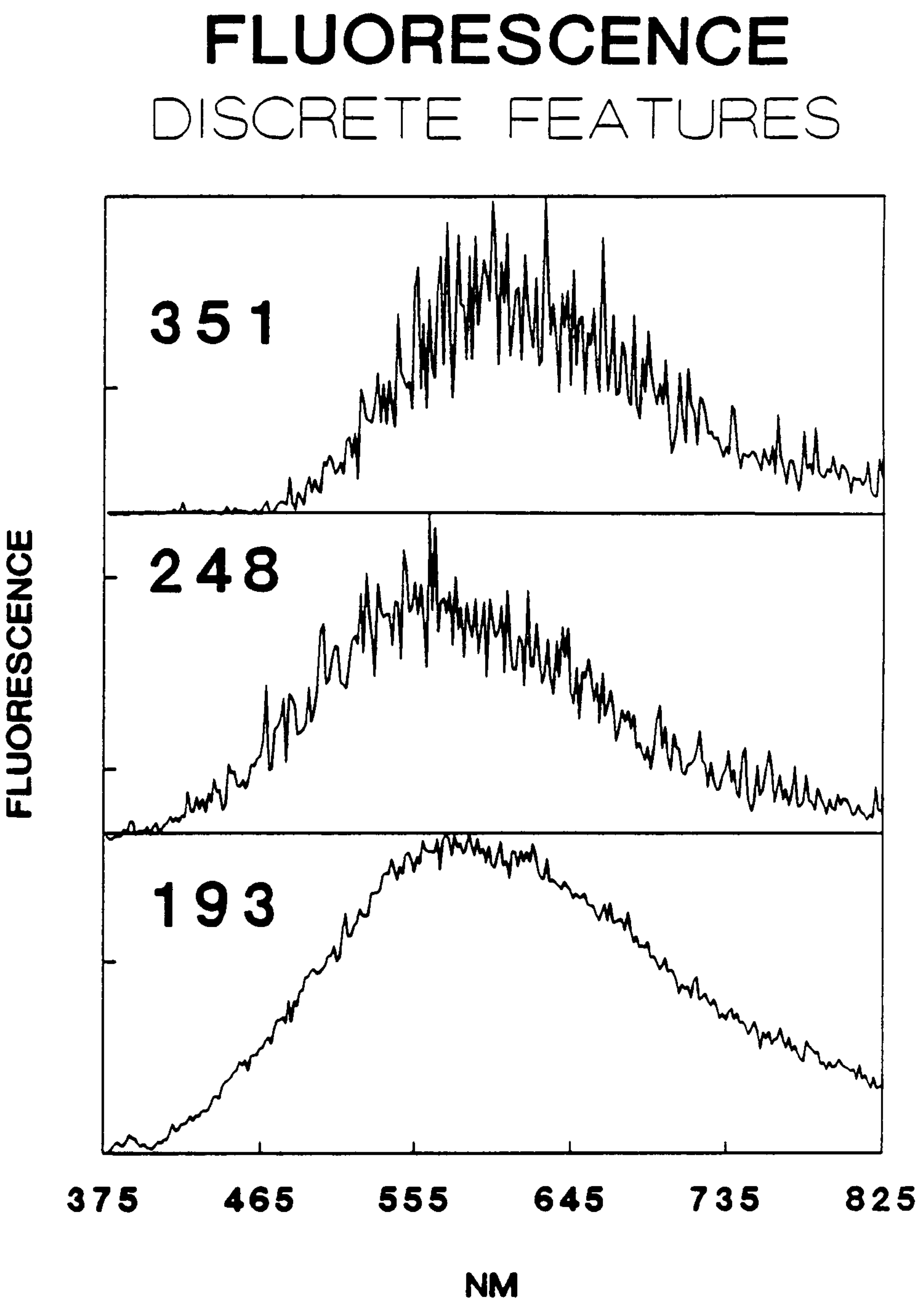
FLUORESCENCE
DISCRETE FEATURES
351
248
193
FLUORESCENCE
375
465
555
645
735
825
NM

Figure C.1

Appendix D

Comparison of Room Temperature and Low Temperature PIF of NO_2Cl at 248 nm

A. NO_2 LIF (Flow Cell / Expansion-cooled

The effect of temperature depression of the precursor on the spectrum is illustrated for NO_2 LIF spectra recorded in this lab in Figures D.1-D.4. The room temperature LIF spectra for λ = 399.8 and 402.9 nm show a broad fluorescence spectrum; whereas the expansion cooled LIF spectra for λ = 398.0 and 402.8 nm show a fluorescence that falls off much more sharply in the red implying a narrow distribution. This may be explained by noting that the room temperature NO_2Cl has a larger spread of J (quantum number for angular momentum) values which may allow the excited states NO_2 to access more rotational phase space. This may lead to a broad fluorescence profile. The constrained initial energy distribution of the expansion-cooled NO_2 leads to a narrow distribution of the excited state molecules. This narrow distribution will in turn produce a narrow fluorescence profile relative to the room temperature results due to the rotation / vibration selection rules.

B. NO_2Cl PIF (Flow Cell / Expansion-cooled)

As shown in Figure D.5 the NO_2Cl PIF NO_2^* energy distribution, P(E_{NO2}), for the supersonically cooled sample has a broader NO_2 internal energy distribution than the that derived from the flow cell. The fact that the supersonic jet results seem to be consistent with the supersonic jet TOF/MS results; whereas the room temperature flow cell results disagrees with both seem to suggest that the temperature, by increasing the rotational angular momentum, of NO_2Cl plays an important role in the dissociation dynamics.

Figure 2.9 which shows the NO_2Cl 248 nm PIF population with the population derived from the TOF/MS suggests that the two electronic states of NO_2 (B_2 and B_1) may be helpful in explaining the observed difference between the room temperature and jet cooled NO_{2Cl} PIF populations. In the bulb the high temperature of NO_2Cl gives rise to a high range of J values in the excited state of NO_2Cl; whereas the supersonice jet has a low temperature distribution of NO_2Cl which gives rise to a low range of J vaues in the excited state of NO_2Cl. The populations of Figure D.5 may be possibly explained by the $^2B_1$ electronic state of NO_2 being favored over the $^2B_2$ state (see Figure 2.9) for large values of J in the excited state of NO_2Cl excited at room temperature. The supersonic jet with its low values of j in the excited state of NO_2Cl may lead to NO_2 fragments with approximately equal branching ratios for being born in the $^2B_1$ or $^2B_2$ state.

Allowing for a certain amount of extrapolation, Figure D.5 suggests that the flow cell photolysis produces more NO than the jet photolysis. This may be verified by determining the absolute quantum yield of NO. Plans are underway to conduct such an experiment in our laboratory.

REFERENCES

[1] D. Oh, W.N. Sisk, K. Patten, H.S. Johnston, manuscript in preparation.

Figure D.1

NO_2 Lif at $\lambda = 399.8$ nm for room termperature flow cell (5 mtorr 30 ns delay).[1]

Figure D.2

NO_2 Lif at $\lambda = 402.9$ nm for room termperature flow cell (5 mtorr 30 ns delay).[1]

NO$_2$ 399.8 nm LIF

(Flow Cell)

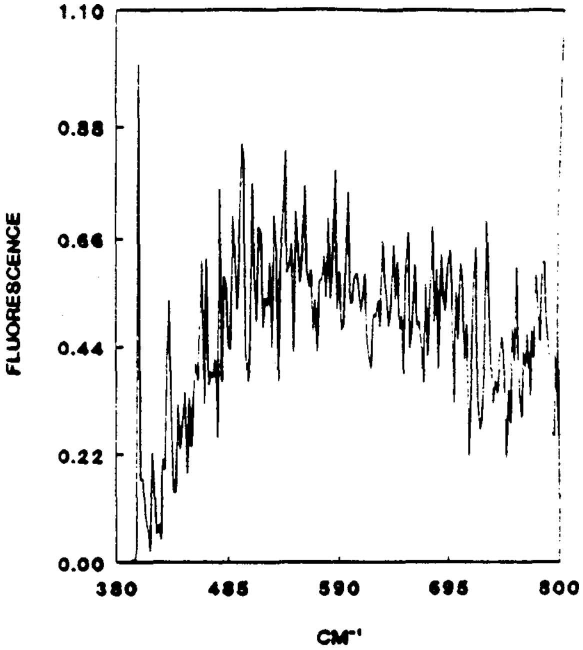

Figure D.1

NO$_2$ 402.9 nm LIF

(Flow Cell)

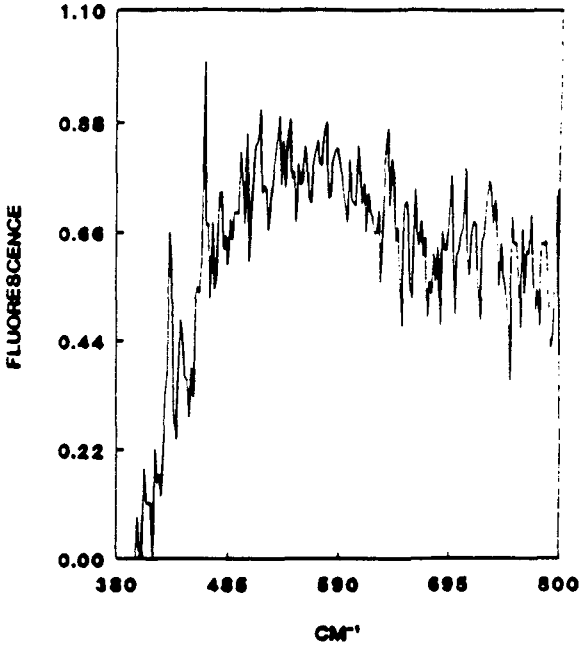

Figure D.2

Figure D.3

NO_2 Lif at λ = 398.0 nm for supersonic jet, performed in same experimental setup presented in chapter 1.

Figure D.4

NO_2 Lif at λ = 402.8 nm for supersonic jet, performed in same experimantal setup presented in chapter 1.

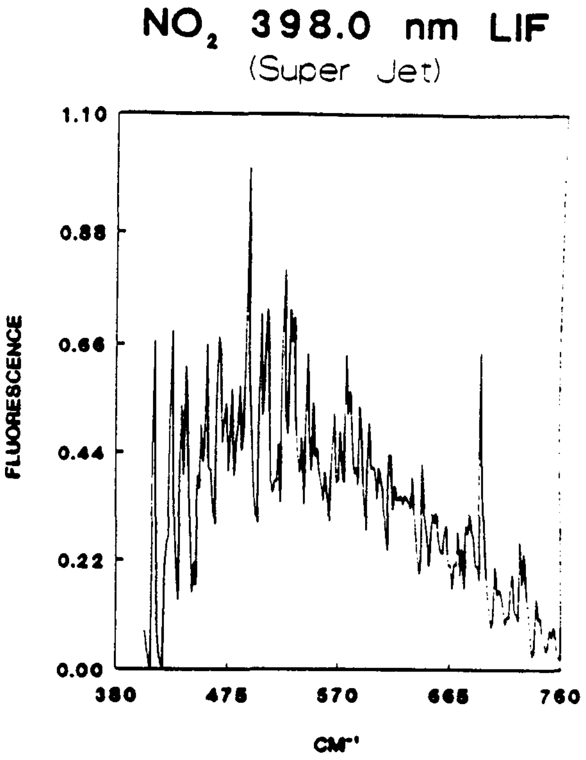

Figure D.3

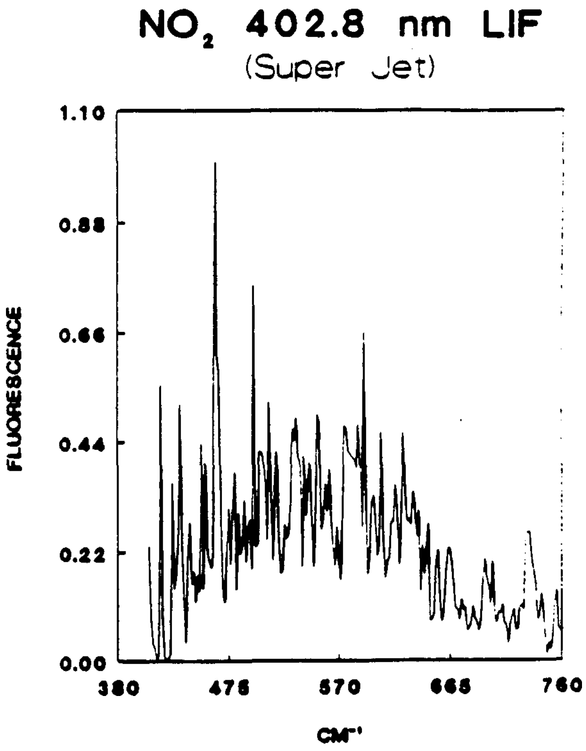

Figure D.4

Figure D.5

Comparison of the Gamma Kernel PIF NO_2 internal energy distributions for NO_2Cl photolysis at 248 nm for the flow cell (298 K) and the supersonic jet (5 K).

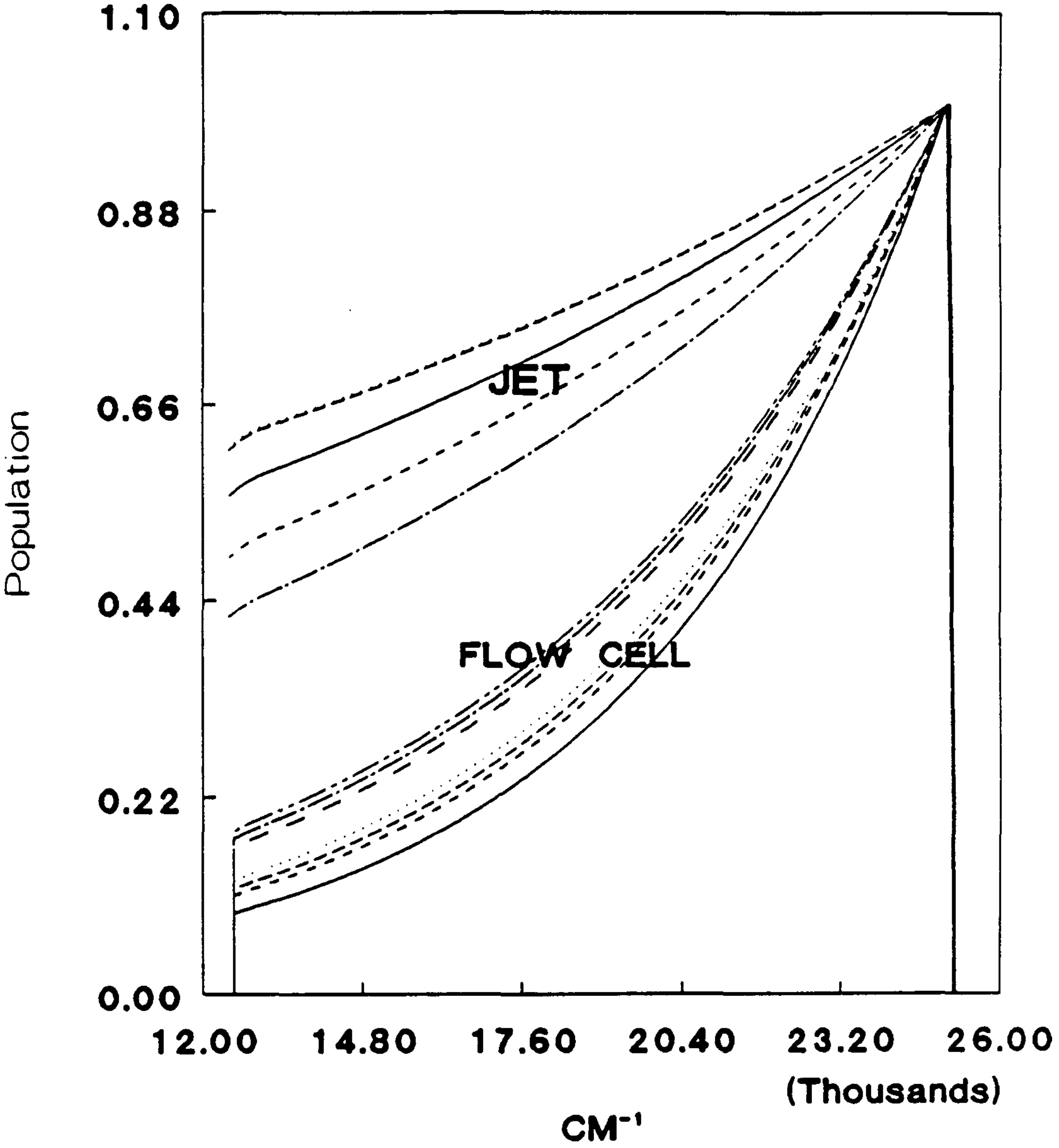

NO_2Cl 248 nm PIF
Flow Cell / Supersonic Jet)

Figure D.5

Appendix E

Clusters

A. NO_2Cl

The cluster content expected from the NO_2Cl (5% in helium) supersonic beam is expected to be small compared to the monomer. The conditions utilized in this experiment are similar to those used by Oh and coworkers in Y.T. Lee's laboratory[1], where the dimer content was negligible.

The manifestation of the clusters in the PIF would to place a red shift in the fluorescence, thus causing the NO_2 energy distribution to be higher than it should be at the lower energies. A plausible mechanism for this phenomenon occurs as follows: (1) Laser excitation localized on the NO_2 group in the NO_2Cl cluster promotes the molecule to the electronic excited state. (2) Intramolecular vibrational energy relaxation occurs and some of this energy flows along the van der Waals coordinate. (3) The van der Waals coordinate ruptures, and in doing so causes a fraction of this initial vibrational energy to be released as translational energy. (4) The excited molecule/cluster $(NO_2Cl)_{n-1}$, now missing one of its groups, fluoresces possiblly at a lower energy than it would have in the absence of IVR and v→t transfer.

B. N_2O_4

For N_2O_4 the idea was to purposefully form N_2O_4 instead of

NO_2 . This was done in chapter 1 by utilizing large pressures of N_2O_4 and therefore large seeding ratios. The possibility of higher order clusters dependends on the number of three-body collisions. The degree to which these three-body collisions occur manifests as the change, upon expansion, in the compositon of the dimer to monomer (N_2O_4:NO_2). In the room temperature cell before the jet formation, the partial pressures were 14 torr NO_2 and 2.8 torr N_2O_4 (Figure 3.44), and the ratio NO_2/N_2O_4 was 5. After the supersonic expansion, the ratio of NO_2/N_2O_4 was 1.7, whereas all NO_2 would be converted to N_2O_4 at equilibrium at the temperature of the beam. These results show that the number of three-body collisions, which are required for cluster formation) were limited, and the molecular bonded N_2O_4 probably greatly exceeded higher clusters based on van der Waals or dipole-dipole interaction. This was computed from a comparison of the absorption coefficents of Bass2 and Hall3, laser intensities, and signal intensities of NO2 and N_2O_4 in figure 3.44. This calculation did involve approximating the N_2O_4 absorption cross section at 392 nm, which has not been measured, from the cross section below 390 nm, which has been measured.

A better way to determine if the higher order clusters have a significant effect on the spectrum is to perform the N_2O_4 PIF experiment in the range 295 to 365 nm. Inoue and coworkers[4] have determined that the NO_2 fluorescence following N_2O_4 photolysis at room temperature in this wavelength range follows the absorption cross section profile for N_2O_4. In chapter 3, Figure 3.3 - 3.6, the N_2O_4 PIFEX spectrum is shown from 336 to 346 nm, which varies linearly with the laser power. The absorption cross section for this region (336-346 nm) is constant within 5%. This shows that the N_2O_4 supersonic PIFEX spectrum obtained for the limited range in this laboratory is similar to the room temperature N_2O_4 PIFEX and the absorption cross section profile. This shows that the NO_2 fluorescence following photolysis is not perturbed very much by the fluorescence of the higher order clusters, since the spectrum appears to be very much like the room temperature $N_{20}4$ PIFEX. Plans are under way to conduct the N_2O_4 PIFEX experiment over the entire 295 to 365 nm range to test for evidence of cluster formation. Before this material is submitted for publicaton, we will make these checks for higher cluster formation.

Previous researchers, Kawasaki[5] and Wren[6], have attempted to determine the composition of higher order clusters in a neat beam of $(NO_2)_n$. They were able to observe the $N_2O_4^+$ ion but not any ions of higher order due to the relative concentration and the dissociative ionization of the these higher order van der Waals complexes. The N-N bond energy in the dimer is 13 Kcal[7] much stronger than the van der Waals bonds of the higher order clusters. The exothermicity of forming this bond for NO_2 to make covalently bonded dimers is energetically favored over NO_2 binding to N_2O_4 to form higer order clusters. If these higer order clusters do persist and yield NO_2 fluorescence after photolysis, a red shift in the fluorescence may be expected as indicated above giving rise to an NO_2 internal energy distribution having more weight at the lower energies than than the distribution from the pure dimer photolysis.

References

[1] D. Oh, Ph.D. Thesis, University of California, Berkeley 1988.

[2] A.E. Bass, A.E. Ledford, Jr., and A.H. Laufer, J. Res. Naatl. Bureau Stands. **80**, 143 (1975).

[3] T.C. Hall, Jr., and F.E. Blacet, J. Chem. Phys. **20**, 1745 (1952).

[4] G. Inoue, Y. Nakata, Y. Usui, H. Akimoto, and M. Okuda, J. Chem. Phys. **70**, 3689 (1979).

[5] M. Kawasaki, K. Kasatani, and H. Sato Chemical Physics **78**,65 (1983).

[6] D.J. Wren, Applied Spectroscopy **34**, 627 (1980).

[7] I.C. Hisatsune, J. Phys. Chem. **65**, 2249 (1961).